Magmatism and rifting at the South Atlantic margin: Magma transport and emplacement mechanisms of mafic dykes from magnetic studies

Zur Erlangung des akademischen Grades einer
DOKTORIN DER NATURWISSENSCHAFTEN
von der Fakultät für
Bauingenieur-, Geo- und Umweltwissenschaften

des Karlsruher Instituts für Technologie (KIT)

genehmigte
DISSERTATION
von

Dipl.-Geol. Miriam Wiegand
aus Zeulenroda

Tag der mündlichen
Prüfung: 22.12.2016

Referent: Prof. Dr. Reinhard O. Greiling
Korreferentin: PD Dr. Agnes Kontny
Korreferent: Prof. Dr. Heinz-Günter Stosch

Karlsruhe 2016

It doesn't matter so much where you stand.
What matters is where you are going.

-Swedish proverb-

Abstract

The Henties Bay Outjo Dyke swarm (HOD) in NW Namibia is part of the early Cretaceous Paraná-Etendeka Large Igneous Province, which originated during the early Cretaceous breakup of western Gondwana into Africa and South America. The basaltic dykes consist dominantly of dolerites, which are compositionally equivalent to the erupted lava series and thus the HOD provides a look at the feeder systems of a flood basalt province. The dyke orientations are subvertical and most have NE-SW and minor NW-SE oriented strike directions parallel or perpendicular to the Neoproterozoic Damara Belt in which they intruded.
A petrofabric study is presented for 41 HOD dykes using the anisotropy of low-field magnetic susceptibility (AMS) with the aim to derive magma flow directions and thus better constrain emplacement mechanisms within the dyke swarm. Additionally, the anisotropy of the anhysteretic remanent magnetization (AARM) is applied to a subset of theses samples in order to detect disturbances by grain size effects on the magnetic fabric due to single-domain titanomagnetite. For individual samples also the shape-preferred orientation of plagioclase was determined for comparison with the magnetic fabric.

At the contact with the country rock, the HOD dykes have fine-grained, vitrophyric to intersertal or glassy textures. A more or less strong preferred orientation of the phenocrysts can be recognized microscopically and is interpreted as a magmatic flow fabric. The microfabrics of the dykes are characterized by intergranular to ophitic or subophitic intergrowths of plagioclase and clinopyroxene, locally with minor contents of olivine and/or hornblende. The magnetic susceptibility (κ) in the dyke rocks is predominantly controlled by late-crystallized titanomagnetite (tmt; used for solid solutions between the end members ulvospinel and magnetite), which is associated and locally intergrown with ilmenohaematite. Tmt is the main carrier mineral of the AMS, but also of the AARM in most of the HOD rocks. Strong variations of the magnetic susceptibility are attributed to subsolidus processes during magma cooling such as high- and low-temperature oxidation of tmt. High-temperature (deuteric oxidation) is indicated by lamellae of ilmenite whereas low-temperature oxidation (maghemitization) is obvious from irreversible κ-T curves. Both types of alteration are typically accompanied by grain size reduction of tmt. Secondary minerals such as carbonate, sericite or pseudomorphic replacement of tmt and ilmenite by leucoxene are frequent and regarded as the product of hydrothermal alteration. From hysteresis properties, alternating field demagnetization and from the comparison of AMS and AARM fabric ellipsoid orientation it is concluded that tmt occurs in various domain states within the samples from single-domain over pseudo-single domain to multi-domain states.
Magnetic susceptibility and its anisotropy in the dykes is mainly controlled by distribution anisotropy of titanomagnetite grains at boundaries and interstices of the flow-oriented silicate phenocrysts (plagioclase and pyroxene). The anisotropy is mainly due to magnetostatic interaction between very closely-spaced tmt grains. The degree of anisotropy is low in most samples with less than 10% ($P' < 1.1$), supporting a primary magmatic origin. This is in accordance with the lack of evidence for metamorphic or brittle tectonic overprint.
In 66 of 110 investigated samples the AMS fabric is "normal", with the long and intermediate fabric axes (= plane of magnetic foliation) within the dyke plane. These rock fabrics are interpreted as flow fabrics where early crystallized minerals are oriented by magma flow. Therefore, the magma flow direction is inferred from the orientation of the long magnetic fabric axis (κ_{max}) in samples with fabric type I taken from the dyke margin. The flow directions are mostly vertical to subvertical regardless of location near or distant from the former rifted margin. This implies generation of mantle melts beneath the entire HOD region (c. 300 x 100 km). Horizontal κ_{max} orientation is less frequent and is interpreted

as local variation of the magma flow direction (horizontal) within the dyke segments or at the segment tips.
The "anomalous" magnetic fabrics of the remaining 38 samples, where the magnetic foliation is non-parallel with the dyke plane, are attributed to two mechanisms. One is the pure single-domain effect of very fine-grained titanomagnetite, which was found in 6 cases by reorientations of anomalous AMS fabrics to normal-type AARM fabrics.
The more common cases of anomalous fabric are probably related with rotation of the AMS axes by tectonic shear at the dyke walls during magma emplacement. Dyke-internal shear, generated by the velocity gradient of the magma flow between dyke walls and centre, produces symmetric imbrication of long AMS fabric axes κ_{max} on opposite dyke walls (observed in 3 dykes). The dyke-external tectonic shear is transferred to the magma, deforming the symmetric imbrication and producing an asymmetric one. Field support for syn-emplacement tectonic shear is given by dyke segmentation geometries including locally curved segments, en-echelon arrangements, left/right-stepping displacements and lineation at the dyke walls. In the regional context, syn-emplacement shear is consistent with the observed reactivation during Gondwana breakup of Neoproterozoic transcrustal shear zones in the Damara mobile belt.

Provided that both the NE- and the NW-striking dykes intruded during early Cretaceous times, which is suggested by radiometric dating and the age relations of mutually cross-cutting NE- and NW-dykes, crustal extension must have occurred at least in two perpendicular directions to emplace them: NW-SE and NE-SW. Magma overpressure in the intruding dykes is suggested to have caused additional stresses in the country rock that influenced the orientation of adjacent dyke fissures. The dyke orientations and timing are consistent with a three-armed rift system (triple junction geometry), where the Damara Belt as the NE-striking inland arm becomes inactive while dyking and rifting continued along the coast-parallel Gariep and Kaoko Belts, finally opening the South Atlantic Ocean. Pre-existing NE-striking Panafrican structures of the Damara-Orogen likely facilitated magma intrusion in the early Cretaceous which may explain the predominance of the NE dykes.
The dominance of vertical and subvertical magma flow orientation suggests magma sources existed over a wide area beneath the dyke swarm. Published pressure estimates from clinopyroxene-melt thermobarometry of HOD dykes suggest reservoir depths of 11 to 17 km. From these mid-crustal reservoirs magma ascended steeply in propagating main fissures up to the present outcrop level (and beyond), which was then in a brittle environment at 4 to 5 km of depth. While propagating, individual dyke segments inflated due to continued magma injection. The less common horizontal κ_{max} orientation near the segment tips is interpreted as lateral propagation of one dyke segment to the adjacent one leading to their final merging. Field observation of overlapping segment tips or broken country rock "bridges", which previously separated two dyke segments supports this mode of dyke propagation.

Zusammenfassung

Kern dieser Arbeit ist eine Studie der Gesteinsgefüge mafischer Gänge des Henties Bay-Outjo Gangschwarms in NW-Namibia, hauptsächlich über die Anisotropie der magnetischen Suszeptibilität (AMS) und ergänzend über die Anisotropie der anhysteretischen remanenten Magnetisierung (AARM). Ziel war das Bestimmen von Magmafließrichtungen innerhalb einzelner Gänge, um darüber Fließmuster im gesamten Gangschwarm abzuleiten und schließlich die Platznahmemechanismen des Gangschwarms zu verstehen. Der Henties Bay-Outjo Gangschwarm (HOD) intrudierte während der frühen Kreidezeit in den neoproterozoischen Damara-Gürtel, der zu dieser Zeit als einer von drei Riftarmen im Zuge des auseinanderbrechenden Gondwanakontinentes reaktiviert wurde. Während die Extension entlang des Damara-Arms bald wieder zum Erliegen kam, entwickelten sich passive Kontinentalränder östlich von Südamerika und westlich von Afrika, entlang des sich öffnenden Südatlantischen Ozeans. Begleitet wurde das Auseinanderbrechen Gondwanas von intensivem Vulkanismus, dessen Erscheinungen zur Paraná-Etendeka Flutbasaltprovinz gezählt werden. Dazu zählen neben seewärts einfallenden Reflektoren (SDR), kontinentalen Flutbasalten, Intrusiva und Lagergängen, auch mafische Gänge, wie die des HOD.
Die überwiegend steil einfallenden HOD-Basaltgänge sind doleritisch ausgeprägt und im Kontakt zum Nebengestein feinkörnig vitrophyrisch bis intersertal oder glasig. Submikroskopisch ist oft eine mehr oder weniger starke Vorzugsorientierung der Einsprenglinge erkennbar, die als magmatisches Fließgefüge interpretiert wird. Die Mikrogefüge der Dolerite sind charakterisiert durch intergranular bis ophitisch oder sub-ophitisch miteinander verwachsene Plagioklase und Klinopyroxene, gelegentlich mit geringem Olivin- und/ oder Hornblendeanteil. Die magnetische Suszeptibilität (κ) in den Ganggesteinen wird vorwiegend kontrolliert von spät auskristallisiertem Titanomagnetit (Tmt; Terminus wird verwendet für alle Mischkristalle zwischen den Endgliedern Ulvöspinell und Magnetit), der mit Ilmenohämatit gelegentlich verwachsen ist. Tmt bildet damit das Hauptträgermineral der AMS, aber auch der AARM in den meisten HOD-Gesteinen. Starke Variationen der magnetischen Suszeptibilität werden oft hervorgerufen durch Subsolidusprozesse, wie hochtemperierte deuterische Oxidation während der Abkühlvorgänge im Magma (Anzeiger dafür sind gitterartig angeordnete Entmischungslamellen von Ilmenit in Tmt-Kristallen.) und tiefer temperierte Oxidation (Maghemitisierung), die sich hauptsächlich aus irreversiblen κ-T Kurven ableiten lässt. Beide Arten der Alteration sind typischerweise verbunden mit einer Korngrößenverkleinerung des Tmt. Sekundärminerale wie Karbonat, Serizit oder verschieden starke Pseudomorphosen von Tmt und Ilmenit nach Leukoxen sind häufig anzutreffen und werden als Produkte von hydrothermaler Überprägung angesehen. Aus Hystereseeigenschaften, Wechselfeldabmagnetisierung und dem Vergleich von AMS und AARM-Gefügeorientierung wird geschlussfolgert, dass Tmt in unterschiedlichen Domänenzuständen innerhalb einer Probe vorliegt, von Einbereichs- (Single-Domain) Körnern über kleine Mehrbereichs- (Pseudo-Single Domain) Teilchen bis hin zu größeren Mehrbereichs- (Multi-Domain-)Tmt in jeweils unterschiedlichen Anteilen.
Aufgrund der Vorzugsorientierung von Tmt entlang von zuvor auskristallisierten Silikatphasen (Plagioklas und Pyroxen) und aufgrund seiner Akkumulation in ihren Zwickeln, wird die gemessene magnetische Gesteinsanisotropie hauptsächlich als eine Verteilungsanisotropie angesehen. Sie wird verursacht durch magnetostatische Wechselwirkungen zwischen einzelnen, sich (fast) berührenden Tmt-Körnern. Im Durchschnitt wurden niedrige Anisotropiewerte der magnetischen Suszeptibilität von unter 10 % ($P' < 1.01$) gemessen, passend zu den primär-magmatischen Gesteinsgefügen, die weder Anzeichen für metamorphe noch für spröd-tektonische Überprägung aufweisen. 66% der untersuchten 111 Proben zeigen normale AMS-, also Typ I-Gefüge, deren lange und mittlere Gefügeellipsoidachsen κ_{max} und κ_{int} in der Gangebene liegen. Diese Gefüge werden als konservierte Fließgefüge interpretiert, bei denen früh aus der Schmelze kristallisierte Minerale durch das Magmafließen eingeregelt wurden. Nur von den vom Gangrand stammenden Gefügetyp-I-Proben wurde die Magmafließrichtung für den jeweiligen Gang von der Orientierung der κ_{max}-Achse abgeleitet. Vertikale bis subvertikale κ_{max}-Richtungen dominieren über den gesamten Gangschwarm hinweg und werden interpretiert als mehr oder weniger steiler Magmenaufstieg. Auf steile Fließrichtungen weist auch Gangsegmentierung hin, die in steil angeschnittenen Geländeaufschlüssen beobachtet wurde. Weniger häufig kommt horizontale κ_{max}-Orientierung vor und wird als lokale Variationen der Magmafließrichtung (hier horizontal) innerhalb der Gangsegmente oder an den Segmentenden gedeutet.

Um die Entstehung der 38 anomalen, nicht gangparallelen AMS-Gefüge (Typen II-IV) zu verstehen, wurden verschiedene potentielle mineralogische und geologische Ursachen überprüft. Die anomalen AMS-Gefüge der 6 Proben (4 davon nahe dem Gangkontakt), die normale (Typ I) AARM-Gefüge zeigen, werden auf einen höheren Einbereichs-(Single-Domain, SD) Tmt-Anteil zurückgeführt, also auf den SD-Effekt im klassischen Sinn. In diesen 4 Fällen wurde die Magmafließrichtung schließlich von der Orientierung der langen Achse der AARM-Gefüge abgeleitet, da bei dieser Methode ausschließlich die Kornform der Tmt (und die Form der Tmt-Cluster) relevant ist, ungeachtet ihres Domänenzustandes. Das überraschend hohe Auftreten anomaler AARM-Gefüge unter den AMS Typ I - Proben ist möglicherweise dem Vorhandensein von sekundärem Tmt geschuldet, der keine Ausrichtung im fließenden Magma erfahren hat und deshalb nicht gangparallel orientiert ist.
Für die meisten anderen Proben mit anomalen AMS-Gefügen konnten weder Zusammenhänge mit der Alteration von Tmt gefunden werden, noch mit Beiträgen anderer Minerale zur AMS außer von Tmt, bis auf einzelne Ausnahmen**.**
Für eine alternative Interpretation der Magmenfließrichtung ist die Orientierung der Gesteinsgefüge in einem Profil über die Gangmächtigkeit interessant, besonders die Orientierung von κ_{max} an beiden Gangkontakten, wo die Intrusionsrichtung der ersten Magmenschübe konserviert ist. In einem Vergleich des Winkels zwischen κ_{max} und der Gangfläche in Proben nahe beider Kontakte wurde im Bezug auf die Gangwand bei 16 von 41 Gängen eine Asymmetrie des AMS-Gefüges festgestellt. Innerhalb des Probensatzes gibt es lediglich 3 Gänge mit nahezu symmetrischer (konjugierter), dachziegelartiger Anordnung der κ_{max}-Achsen an gegenüberliegenden Gangrändern - die Symmetrieebene ist gangparallel und im Gangzentrum. Es wird angenommen, dass die Asymmetrie der κ_{max}-Orientierung auf tektonische Scherung an den Gangwänden während der Magmenintrusion zurückzuführen ist. Satellitenbilder und Geländebeobachtungen segmentierter Gänge mit teils gebogenen Segmentenden, enechelon Anordnung und rechts-/linkstretendem Lateralversatz der Segmente sprechen ebenfalls für den Einfluss einer lokalen Scherkomponente zusätzlich zur regionalen Extension in der Unterkreide. Auch im großregionalen Maßstab kam es zur Zeit der Gangintrusionen und des Auseinanderbrechens von Gondwana zu Scherbewegungen, die tiefkrustale neoproterozoische Scherzonen im Gebiet des HOD im Damaragürtel reaktivierten.

Im HOD-Gangschwarm dominieren NE-SW-streichende Gänge, die parallel zum Damara-Gürtel intrudierten. Deutlich weniger, aber als Untergruppe abgrenzbar, kommen NW-SE-Gänge vor und untergeordnet auch andere Richtungen. Vorausgesetzt, dass alle Gänge frühkreidezeitlich intrudiert sind - und Beziehungen sich gegenseitig schneidender NE und NW-Gänge belegen keinen generellen streichrichtungsgebundenen relativen Altersunterschied -, muss die Extension der Kruste damals entlang mindestens 2 verschiedener, zueinander senkrechter Richtungen stattgefunden haben: NW-SE und NE-SW-orientiert. Magmenüberdruck in den intrudierenden Gängen induzierte wahrscheinlich zusätzlich lokale Spannungen im Grundgebirge und beeinflusste damit die Orientierung benachbarter Gangspalten. Diese Vorstellung passt zum Modell eines 3-armigen Riftsystems (triple junction), bei dem der Damara-Inlandarm inaktiv wurde, während die Gangplatznahme und das Rifting entlang der beiden übrigen Arme (Gariep und Kaoko-Gürtel) fortschreitet und sich schließlich der Südatlantik öffnet. Präexistierende panafrikanische Krustenstrukturen des alten Damaraorogens haben wahrscheinlich als Wegsamkeiten für die Magmenintrusion in der Unterkreide gedient, was das Vorherrschen des NE-Gangstreichens erklären könnte.

Das Vorherrschen vertikaler und subvertikaler Magmafließrichtungen ist ein Hinweis auf Magmaquellen unterhalb, die über den gesamten HOD-Gangschwarm verteilt sind. Thermometriedaten von Klinopyroxenen sprechen für Reservoire in Krustentiefen von 11 bis 17 km. Von diesen mittelkrustalen Magmenzwischenspeichern stieg das Magma steil bis halbsteil innerhalb von propagierenden Hauptspalten bis zum heutigen Aufschlussniveau (und weiter) auf, was zu dieser Zeit in sprödem flach-krustalen Bereichen von 4-5 km Tiefe lag. Während der Propagation verbreiterten sich die einzelnen Segmente der Aufstiegsspalten (Gänge) und blähten sich durch fortdauernde Magmeninjektion auf. Horizontale κ_{max}-Orientierung nahe den Segmentenden wird als laterales Propagieren eines Gangsegmentes hin zum benachbarten Segment gedeutet, was schließlich mit deren Vereinigung endet. Überlappende Segmentenden oder zerbrochene Nebengesteins-"Brücken", die zwei Gangsegmente zuvor separiert haben, sind jeweils Zeugen und Überbleibsel dieser Art der Gangpropagation.

Contents

1 Introduction 1

2 Geological setting 1

2.1 Geological evolution and setting of the study area 1

2.1.1 Evolution of the basement 1

2.1.2 Breakup of Gondwana and Post-breakup evolution 2

2.2 Tectonic structures in the study area 4

2.3 Breakup-related mafic dyke swarms 6

3 Fundamentals of rock magnetism 11

3.1 Magnetization, magnetic susceptibility and remanence 11

3.2 Types of magnetism 13

3.3 Magnetic domains 14

3.4 Internal demagnetizing field 16

3.5 Magnetic anisotropy and anisotropy energy of particles 16

3.6 Magnetic hysteresis and hysteresis loop 17

3.7 Magnetic mineralogy in basalts 19

3.7.1 Magnetite and titanomagnetite 20

3.7.2 Haematite and ilmenohaematite solid solutions 21

3.7.3 Iron oxyhydroxides and iron sulfides 22

3.7.4 High temperature oxidation/ deuteric oxidation of Fe-Ti-oxides 22

3.7.5 Low temperature oxidation/ maghemitization of titanomagnetite 22

4 Methods 24

4.1 Anisotropy of low-field magnetic susceptibility 24

4.1.1 Historical account of AMS application to magma flow in dykes 25

4.1.2 Measuring procedure 30

4.2 AARM – Anisotropy of anhysteretic remanent magnetization 32

4.3 Image analysis 33

4.4 Methods for analysing the magnetic mineralogy 35

4.4.1 Temperature-dependent magnetic susceptibility 35

4.4.2 Transmitted- and reflected-light microscopy 36

4.4.3 Alternating field demagnetization and median destructive field 36

4.4.4 Hysteresis measurements 37

4.5 Other measurements 38

4.5.1 Natural remanent magnetization and Koenigsberger ratio 38

4.5.2 Geochemical analysis 38

5 Field studies of dykes 40
6 Geochemical classification of the dyke rocks 56
7 Results 58
7.1 Petrography of the samples 58
7.2 Magnetic mineralogy 60
7.2.1 Reflected-light microscopy 60
7.2.2 Temperature-dependence of the magnetic susceptibility 65
7.2.3 Hysteresis measurements 68
7.3 Natural remanent magnetization and Koenigsberger ratio 70
7.4 Alternating field demagnetization 71
7.5 Magnetic susceptibility and its anisotropy 73
7.6 Anhysteretic remanent magnetization and its anisotropy 80
7.7 The silicate rock fabric 84
8 Comparison of rock fabrics 88
8.1 Magnetic fabrics: AMS versus AARM 88
8.2 AMS fabrics before and after alternating field demagnetization 91
8.3 Magnetic versus silicate fabrics 92
9 Discussion 96
9.1 Magnetic mineralogy 96
9.2 Rock magnetic fabrics 99
9.2.1 Anomalous fabrics due to magnetic minerals other than tmt 100
9.2.2 Is there a single-domain effect? 101
9.2.3 Influence of Natural Remanent Magnetization on AMS - NRM, Q and AMS_{AFD} 107
9.2.4 Anomalous grain orientation 109
10 Interpretation 115
10.1 Magma flow directions and paleostress field 115
10.2 Dyke emplacement model 118
11 Conclusions 121
11.1 Magneto-mineralogy and magnetic fabric in the HOD dykes 121
11.2 Tectonic interpretation and dyke emplacement 121
12 References 123
13 Appendices 134

Acknowledgement/Danksagung

Zuerst möchte ich mich herzlich bei meinem Betreuer Prof. Reinhard O. Greiling bedanken, der mir mit seinem reichen Erfahrungsschatz und mit seiner Übersicht über weite Bereiche des Projektes beratend zur Seite stand und mir in Problemfällen den Rücken freigehalten hat.

Mein tiefer Dank gebührt Dr. Agnes Kontny, die mir als Zweitbetreuerin durchgehend, aber besonders in der Endphase mit viel Geduld, Zeit und Motivation geholfen hat, den roten Faden im Auge zu behalten. Mit ihren guten Ideen, aber auch ihrer Menschlichkeit und ihrem Verständnis war sie mir eine wesentliche Stütze.

Meine außerordentliche Dankbarkeit gebührt überdies Dr. Robert (Bob) Trumbull vom GFZ Potsdam, der mich als Projektpartner von Beginn an tatkräftig begleitet hat, sei es bei der Geländearbeit wie auch bei organisatorischen Fragen. Ganz besonders zu schätzen weiß ich seine inhaltlichen Anmerkungen während meiner Schreibphase sowie sprachlichen Korrekturen als Englisch-Muttersprachler. Bob war mir ein unglaublich hilfsbereiter und zuverlässiger Partner in allen Belangen und für seine aufbauende Motivation im Endstadium des Schreibens bin ich sehr dankbar.

Weiterer Dank gilt einer Reihe von Helfern, die mir bei Probennahme und -präparation zur Hand gingen und mir viel Arbeit abgenommen haben, unter ihnen ganz besonders meinem lieben Freund Maximilian Zundel, mit dem ich unvergessliche Erlebnisse in der Namib teilen durfte.

Auch Oliver Frei von der Universität Freiburg danke ich für das Mitwirken an diesem Projekt über Geländearbeit bis hin zu thermobarometrischen und Luftbildstudien im Rahmen seiner Masterarbeit, sowie anregenden Gesprächen.

Many thanks are given to Dr. Martin Chadima and Prof. František Hrouda from Agico Inc., Brno, for the possibility and assistance to conduct the AARM measurements there and for fruitful discussions and comments.

Ich möchte mich ebenso bei Prof. Appel und seinen Mitarbeitern im Magnetiklabor der Geophysik-Arbeitsgruppe, Universität Tübingen, für die Bereitstellung der Geräte und Betreuung der Hysteresemessungen bedanken.

Gedankt sei darüberhinaus der DFG, die mir mit der dreijährigen Finanzierung dieses Projektes überhaupt diese Entwicklungsmöglichkeit geboten hat.

Ausserdem möchte ich mich gern bei den Kollegen meiner Arbeitsgruppe bedanken für das sehr angenehme, sich gegenseitig helfende Miteinander und den Austausch, besonders meinem Zimmerkollegen Boris Reznik, sowie Ulrike Brecht, Jens Grimmer und Frank Dietze und bei meinen anderen Kollegen am Institut für Angewandte Geowissenschaften des KIT Karlsruhe, wo ich bei Fragen stets Offenheit und Hilfsbereitschaft antraf.

Abbreviations

AC	alternating current
(A)ARM	(anisotropy of) anhysteretic remanent magnetization
AF(D)	alternating field (demagnetization)
A/m	Ampere per metre
AMS $AMS_{INITIAL}$	low field anisotropy of magnetic susceptibility, measured on pristine sample
AMS_{AFD}	low field anisotropy of magnetic susceptibility, measured after alternating field de-magnetization
cpx	clinopyroxene
DC	direct current
Fe	iron
H	magnetic field
H_{AARM}	field applied when imparting a remanent magnetization during AARM measurement
H_C	coercive force
H_{CR}/	remenent coercive force
hem	haematite
H_{Max}	maximum applied magnetic field
HOD	Henties Bay-Outjo Dyke swarm
ilmhm	ilmenohaematite = haemoilmenite = titanohaematite
ilm	ilmenite
ImA	Image Analysis
κ (kappa)	magnetic susceptibility
κ_m	mean or bulk magnetic susceptibility
κ_{max}, κ_{int}, κ_{min}/ κ_1, κ_2, κ_3	maximum, intermediate , minimum axis of magnetic susceptibility
κ(T) or κ-T	temperature-dependent susceptibility, kappa(T)
M	magnetization
MD	multi-domain
MDF	median destructive field, in [mT]
mgh	maghemite
M_R or M_{RS}	saturation remanent magnetization
M_S	saturation magnetization

MS	magnetic susceptibility
mt	magnetite
mT	millitesla
NRM	natural remanent magnetization
Pj or P’	degree of anisotropy of AMS or AARM
plag	plagioclase
pyrrh	pyrrhotite
pyr	pyrite
RM	remanent magnetization
tmt	titanomagnetite (includes all solid solution members from ulvospinel to pure magnetite)
PG	Ponta Grossa (dyke swarm in Brazil)
PSD	pseudo single-domain
SD	single-domain
SI	International System of Units (Système international d’unités)
T	shape factor of AMS or AARM ellipsoid
T_C	Curie temperature
thm	titanohaematite
Ti	titanium
Tmgh	titanomaghemite
tmt	titanomagnetite
T_N	Néel temperature
TRM	thermoremanent magnetization
T_V	Verwey transition of magnetite
vol%	volume percent
VRM	viscous remament magnetization
wt%	weight percent

1 Introduction

During the Cretaceous break-up of western Gondwana, a south to north propagating rift initiated the birth of the South Atlantic Ocean. At its eastern side, the passive continental margin offshore of Southern Africa is one of the classical examples of a volcanic rifted margin. At the continent–ocean transition the African Plate thins out to the west with half-grabens and seaward dipping reflectors and finally gives way to much younger oceanic crust.
Contemporaneous with rifting in early Cretaceous times, the Tristan hot spot was active under today's northwestern Namibia/southwestern Angola, creating the voluminous volcanic rocks of the Parana-Etendeka Large Igneous Province with continental flood basalts, intrusive complexes, sills and dykes. Among the most prominent magmatic features is the Henties Bay-Outjo dyke swarm (HOD), which was emplaced into and parallel with the NE trending Panafrican Damara Belt in northwestern Namibia. Dykes intruded over a vast area extending up to 300 km from the coast and about 100 km in NW-SE extension. The basaltic dykes of the HOD swarm are relatively well exposed and they shape the landscape locally as the so-called "dolerite hills".
One of the outstanding questions regarding this and similar large dyke swarms such as the contemporary Ponta Grossa swarm in Brazil, concerns the magma generation and emplacement scenario and mechanism: is magma generated mainly at the continental margin and dykes propagate laterally through the continental crust; or is dyke propagation and magma flow mainly vertical throughout the dyke swarm, implying that magma is generated in the mantle even far inland from the rift?
A second issue of this study is the paleostress-field at the time of dyke intrusion in relation to the variability in dyke strike. While the majority of the dykes intruded along NE striking, obviously reactivated Proterozoic basement structures that are perpendicular to the coastline of the South Atlantic, a remarkable subset of dykes strikes roughly parallel to the coast.

An analysis of anisotropy of the rock fabric was undertaken in locations located throughout the HOD, with the assumption that early crystals will orient preferentially with their long axes parallel with the magma flow direction. Three different methods of petrofabric analysis were applied. The main method is the anisotropy of low-field magnetic susceptibility (AMS) measurement, which is a relatively fast, non-destructive and very sensitive method. It has been used to infer magma flow directions in several dyke swarms (e.g. Archanjo and Launeau, 2004; Canon-Tapia, 2004 and references therein; Ernst and Baragar, 1992; Knight and Walker, 1988; Raposo and Berquó, 2008; Raposo and Ernesto, 1995). The character, domain state and alteration of magnetic carrier phases were investigated with microscopy and complementary magnetomineralogic methods, including the temperature dependence of the magnetic susceptibility, hysteresis measurements and alternating field demagnetization (AFD). In basaltic rocks generally, and in most of the HOD dykes as well, the magnetic susceptibility is controlled by titanomagnetite (used in the broad sense for all solid solutions between ulvöspinel and magnetite). Magnetic anisotropy of titanomagnetite (tmt) can arise from preferred orientation of unequant grains, and/or by anisotropic distribution of isometric grains and their magnetostatic interaction. Because the standard AMS method provides an integrated result over all the rock's minerals, it is commonly difficult to intepret because of the complexities of the specific magnetic mineralogy including factors related to grain size, alteration, metamorphic or tectonic overprints (e.g. Tarling and Hrouda, 1993). Indeed, in a preliminary study of the HOD dykes (Wiegand et al., 2011), about 59 % of the samples were found to show anomalous AMS fabric orientations, i.e. apparent flow directions not in the plane of the host dyke. To a minor degree, this is confirmed by the new results too, and to better understand and interpret anomalous AMS patterns, the anhysteretic remanent magnetization (AARM) response of a subset of samples was also measured. In contrast to AMS, the AARM method images the preferred orientation of titanomagnetite and/or its clustered grains independent of grain size (Potter, 2004). Furthermore, the AARM signals are given exclusively by remanently magnetizable minerals, such as titanomagnetite, pyrrhotite, haematite and iron hydroxides, so possible effects of paramagnetic silicate minerals are avoided. Finally, for three samples, the magnetic fabric analysis is augmented with a study of shape-preferred orientation of plagioclase from image analysis of three oriented, mutually perpendicular thin sections.
In a late stage of the study the influence of the natural remanent magnetization (NRM) on the AMS fabric was tested on a subset of samples. For this samples were demagnetized partially in alternating

magnetic fields in order to minimize the NRM vector, then their AMS was measured again (AMS_{AFD}) and compared with the initial AMS fabric orientation.

2 Geological setting

2.1 Geological evolution and setting of the study area

2.1.1 Evolution of the basement

Large parts of the study area belong to the intracontinental Damara Orogen (s.s.), but the most northwesterly region belongs to the coastal Kaoko Belt (Figure 2-1). Both orogenic belts evolved at the northwestern margin of the Kalahari Craton in late Neoproterozoic (Panafrican) times. Damara Belt evolution started with the breakup of the supercontinent Rodinia (de Wit, 2008; Frimmel et al. 2010 etc.) c. 900 Ma ago. Multiple rifting separated the Kalahari and Congo-São Francisco Cratons, and also fragmented the northwestern Kalahari Craton (Frimmel et al. 2010). During this period, several small cratonic blocks were split off from the latter craton. The largest fragment is suspected to be the Angola Block (Frimmel et al. 2010), which was previously assumed to be a separate craton, termed Angola or Congo Craton (e.g. Porada, 1989; Miller 1983; Figure 2-1). Northeast-trending parallel rifts developed in this area and a stepwise opening of three initial rift structures occurred (Miller, 1983). While Miller (1983) distinguished three parallel rifts, Frimmel and others (2010) only focus on two: the northern and the southern Nosib Rifts. After opening the Outjo Sea the northern rift failed. In contrast, the southern Nosib Rift developed into an ocean basin, the Khomas Sea, with the eruption of mid ocean ridge basalts (Miller, 1983; Frimmel et al., 2010) and other ocean floor lithological forma-tions. Relics of these rocks crop out as the so-called Matchless Amphibolite Belt (Figure 2-4).

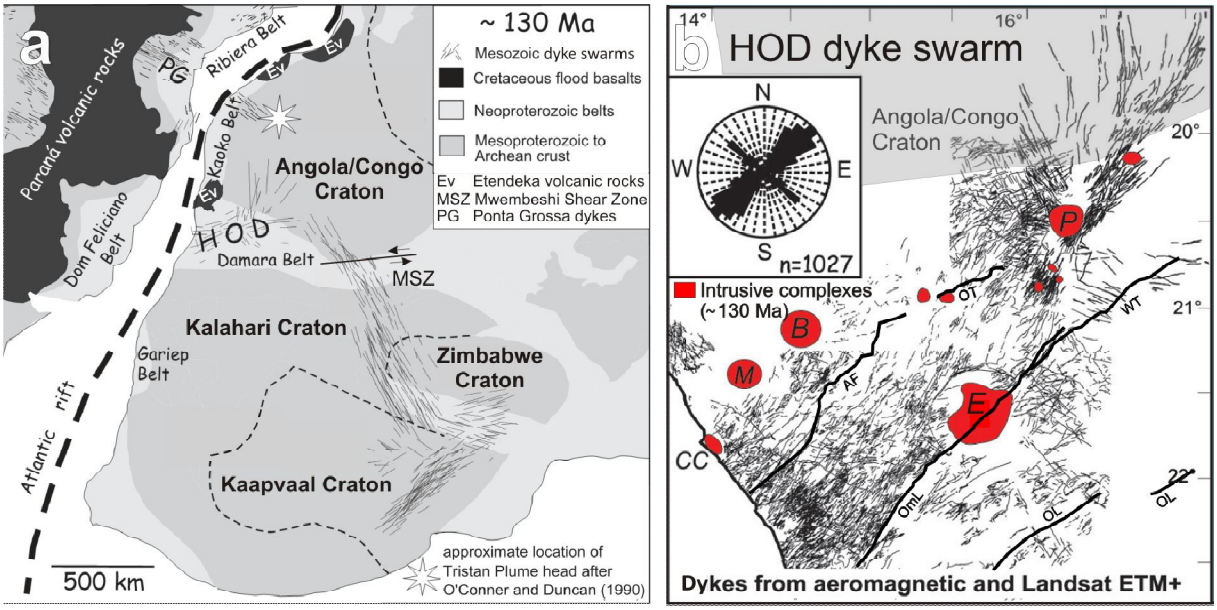

Figure 2-1. a) Map of southwestern Gondwana at Lower Cretaceous times (130 Ma) showing the position of Neoproterozoic fold belts including the Damara and Kaoko Belts between the cratonic blocks. Important features of the Paraná-Etendeka Igneous Province with the HOD dyke swarm are outlined (modified after Trumbull et al., 2004). b) Map of dykes picked from aeromagnetic and Landsat ETM+ images (Hahne, 2004) and rose diagram with dyke trends in the HOD. Area of aeromagnetic survey delineated in Figure 2-3. Abbreviations: AF- Autseib Fault; OL- Okahandja Lineament; OmL- Omaruru Lineament; OT- Otjohorongo Thrust; WT- Waterberg Thrust; Intrusive Complexes: B- Brandberg; E- Erongo; M- Messum; P- Paresis (modified after Wiegand et al., 2011).

As the spreading phase was constrained only to a relatively short time interval of about 35 million years, Frimmel and others (2010) assume the development of only a narrow sea with 700 km maximum width of oceanic crust. Between 780 and 750 Ma another rifting episode at the western margin of

the Kalahari Craton led to the opening of the Proto-South Atlantic, the Adamastor Ocean (e.g. Stanistreet al. 1991).

The Outjo and Khomas Seas merged to form the Damara Ocean. In Neoproterozoic and early Palaeozoic times (450-600 Ma.), the Damara Ocean, was closed by the northeast directed subduction of the Kalahari plate beneath the Angola Block (Frimmel et al., 2010). The Okahandja Lineament is considered as the leading edge of the northern block during collision and amalgamation of the two blocks (Frimmel et al., 2010; see profile in Figure 2-4). Platformal and ocean floor sediments were folded, overthrusted, and built up the Damara Belt. Involved rocks experienced different degrees of metamorphism and anatexis, and the collision zone and the overriding plate were variously intruded by granitic melts (Stanistreet et al., 1991, Frimmel et al. 2010 etc). However, the position and course of the main suture between the Kalahari and Congo-São Francisco Cratons still remains unclear. Frimmel et al. (2010) speculate about its course between the West Congo Belt and the Lufilian/Zambesi Belts covered beneath younger deposits. At the same time or somewhat later than the Damara Orogeny, the sutured cratons collided with the Río de la Plata Craton in the west, which completed the Panafrican Orogeny: a three-armed fold-belt system was formed as part of the Pan-African Mobile Belt: a S trending southern and NNW trending northern coastal branch, Kaoko and Gariep Belt, respectively; its third one is the ENE trending Damara Belt that extends across Namibia into Botswana and links with other Panafrican orogens there (Gray et al 2008). The Panafrican Orogeny led to the birth of the Gondwana continent (Pisarevsky et al. 2008).

2.1.2 Breakup of Gondwana and Post-breakup evolution

The break-up of Gondwana started in Late Jurassic times (Clemson et al. 1997), when extension led to rifting in the southernmost part of South America. The opening of the South Atlantic Ocean was initiated and propagated in time from south to north. Rifting at the incipient Namibian margin started in Early Cretaceous times. At the same time the Tristan mantle plume was active and slightly predated or accompanied the rifting by strong effusive volcanic activity on both sides of the rift. Classical features of volcanic rifted margins were produced along the continental margin of southern Africa: Over a short period of time at 133-131 Ma (Renne et al., 1992; 1996; Stewart et al., 1996) the Paraná-Etendeka Large Igneous Province (LIP, Figure 2-2) formed with bimodal extrusive and intrusive volcanism. Huge amounts of continental flood basalts and quartz latites erupted (Erlank et al., 1984; Milner and Ewart, 1989). Beside the lavas, sills and dykes, large intrusive anorogenic complexes were also formed, like the Cape Cross, Erongo, Messum or Brandberg plutons (both A-type granites) among others (Figure 2-1). Seaward dipping reflectors (SDRs) at both ocean margins are interpreted as subaerial basalt flows, which submerged and were tilted by subsidence of the margin (Hinz, 1981; Gladczenko et al. 1997

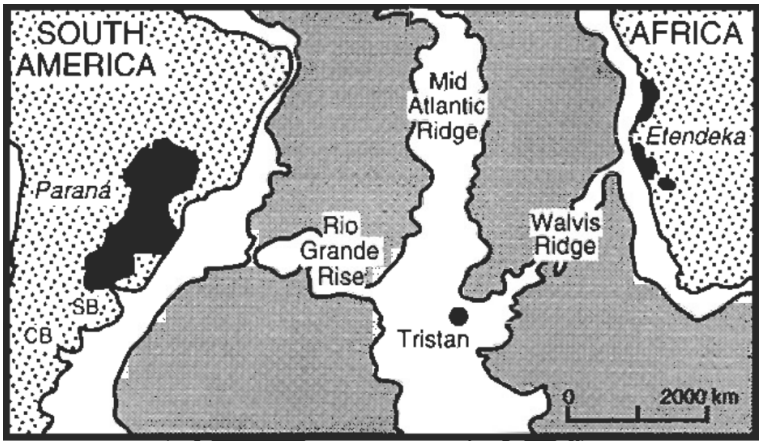

Figure 2-2. Rio Grande Rise and Walvis Ridge plume tracks linking the Large Igneous Provinces Paraná and Etendeka (black) with the Tristan da Cunha Islands, the location of the active plume; after Peate (1997).

and references therein). High p-wave velocities at the continent-ocean transition are interpreted as underplated igneous lower crust (Bauer et al., 2000; Mohriak et al., 2002; Trumbull at el., 2002, Heit

et al., 2013). The submarine paired mountain chains Rio Grande Rise and Walvis Ridge in the South Atlantic Ocean are interpreted as the plume trace. They connect the recent magmatic activity at Tristan da Cunha Islands and Gough with flood basalt exposures of the LIP on each side of the Atlantic (Figure 2-2).

Pre-existing N-S oriented lithospheric structures of the Gariep and Kaoko Belt in Namibia have been reactivated (Clemson et al. 2013) during rifting. Light et al. (1993) observed N-S oriented west-dipping extensional faults to have evolved from the reactivation of Pan-African thrusts. Dyking occurred along the passive continental margins. In NW-Namibia, a large dyke swarm has been emplaced in the area of the Damara Belt. It has been named "Henties Bay-Outjo Dyke swarm" HOD (Trumbull et al., 2004; Hahne 2004), according to its geographic extension between the homonymous settlements and is the study object here. The HOD trends NE, at high angles to the S-Atlantic coast and parallel with the Damara Belt. The dykes are supposed to represent magma conduits for lavas which are now eroded (Trumbull et al. 2004). Figure 2-3 presents the geological setting of northwestern Namibia delineating the major geological units.

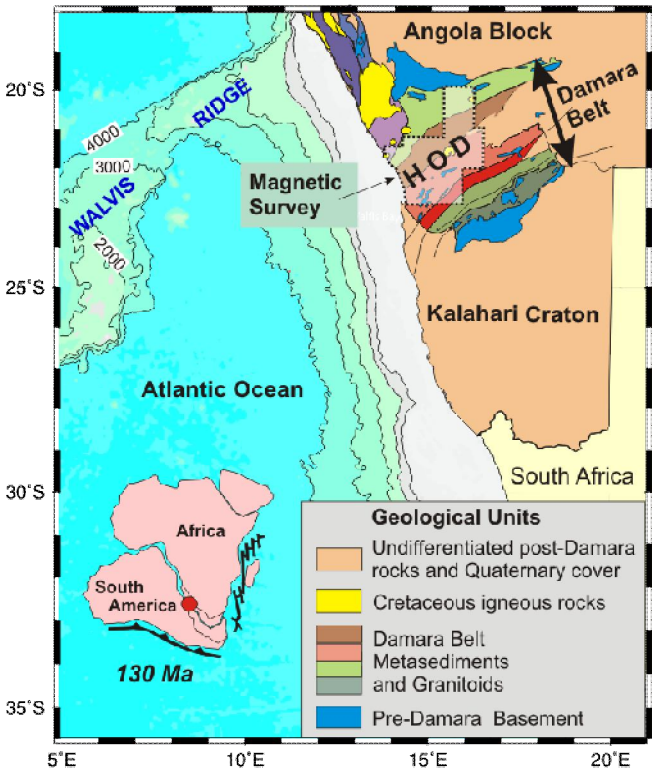

Figure 2-3. Geological setting of the study area in NW Namibia: Damara Belt sutures the Kalahari Craton and the Angola Block; note the position of Henties Bay-Outjo Dyke swarm HOD; area covered by magnetic survey is marked; left inset shows position of Tristan da Cunha mantle plume (red circle) at early Cretaceous times; modified from Hahne (2004). Inset marks area of the magnetic survey shown in Figure 2-1 b.

Since the Cretaceous rifting no major tectonic or magmatic event affected the study area. Fission track data of ^{238}U in apatites give a post-rift denudation and erosion of 4 km (Okenyenya) to 5 km (Brandberg) for central Damaraland (Raab et al. 2005). Peak erosion rates of 0.2 to 0.125 km per Ma are reached in the Upper Cretaceous between 80 and 60 Ma and coincide with a high influx of clastic sediment to offshore basins (Raab et al. 2005). Due to the increased erosional exhumation of the elevated rift shoulders, an escarpment formed between the coastal plain and the inland plateau more than 1000 m above present sea level (Moore et al. 2009). This Great Escarpment along South Africa`s passive margin is diminished and eroded for a length of more than 160 km in the area of Damaraland (Raab et al., 2002 and 2005).

2.2 Tectonic structures in the study area

The regional structure of the Damara Belt is very complex. After Miller (1983) and Daly (1986; 1989) it is subdivided into seven NE striking tectonostratigraphic zones, which are, from north to south: Northern Platform and Foreland, Northern Zone, Central Zone, Okahandja Lineament Zone, Southern Zone, Southern Margin Zone and Southern Foreland and Platform. They are separated by NE-striking (semi-) ductile shear zones and thrusts. A modified map of the tectonic zones and geological units is shown in Figure 2-4. Except one dyke in the Northern Zone of the Damara Belt and three dykes and

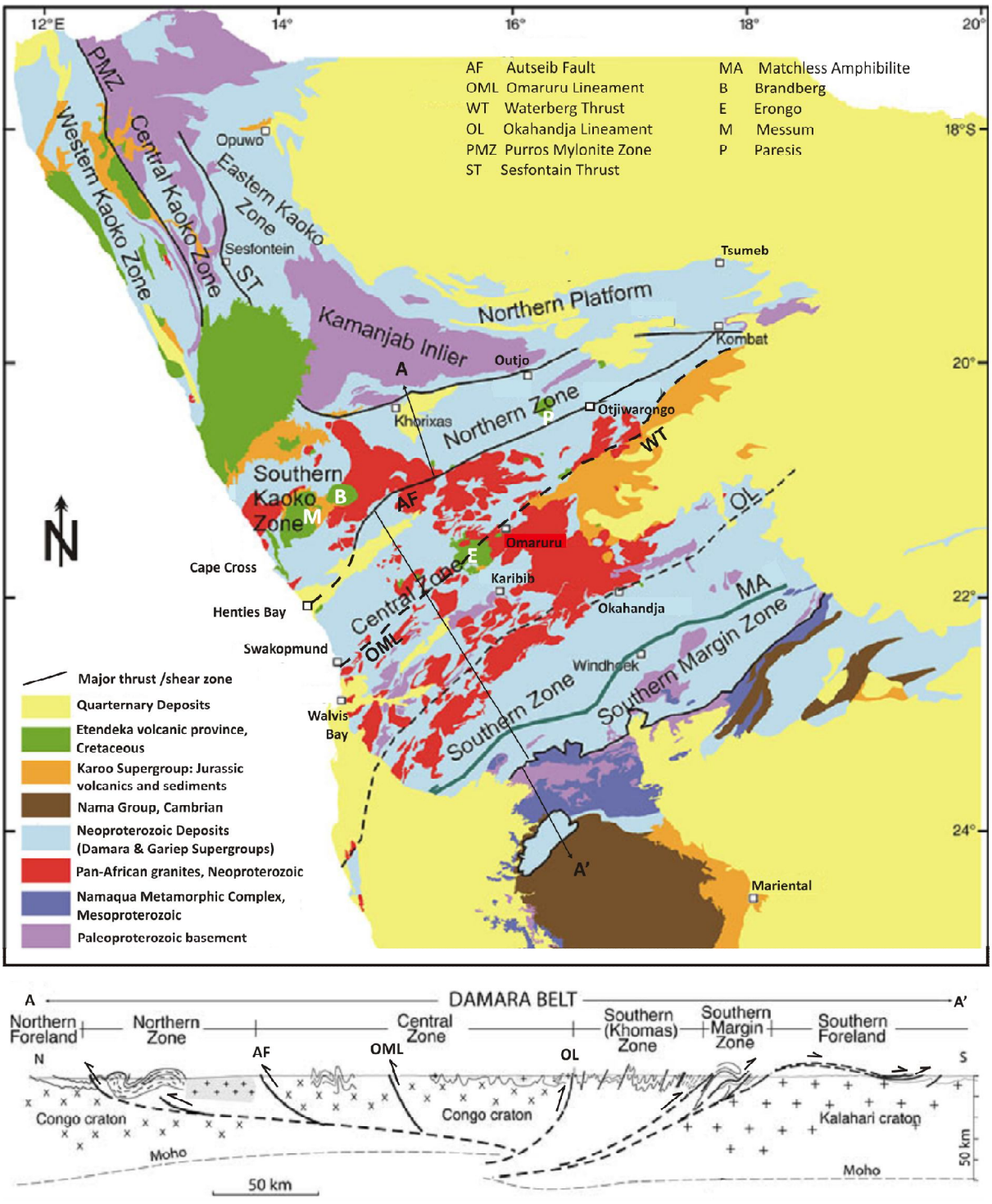

Figure 2-4. Tectonic zones and geological units of the Damara and Kaoko Orogens; modified from Frimmel et al. (2011) and simplified structural profile across the bivergent Damara Orogen (modified after Gray et al. 2008 from Miller & Grote 1988: profiles on Damara Orogen 1:500,000 Map sheets).

one sill in the Southern Kaoko Zone (SKZ) all the other dykes of the Henties Bay-Outjo Dyke swarm studied here are hosted by the Central Zone.

The ***Central Zone (CZ)*** is separated from the Northern Zone by the south dipping Autseib Thrust, called Otjihorongo Thrust in its easterly part. It cuts through Neoproterozoic deposits and Pan-African granites that make up vast parts of this zone. In the south, the Okahandja Lineament (OL) separates the CZ from the Southern Zone. Along the OL the CZ has been uplifted for as much as 20 to 25 km (Miller, 1983). A deeper structural level is cropping out in the CZ, as compared to the Northern Zone (Nagel 1999). Another prominent fault, the Omaruru Lineament-Waterberg Fault (OML-WF), strikes through the centre of the CZ. The OML-WF is delimiting crustal blocks with different lithology and metamorphic grade. There are medium-grade Neoproterozoic Damara sequence metasediments intruded by Cambrian granites north of the lineament, and to the south the metasediments show upper amphibolite to granulite facies, and pre-Damara gneisses occur in cores of deeply-eroded structural domes (Trumbull et al. 2004). Both the OML-WT and the Autseib Fault originated during late convergence stages of Kalahari Craton and Angola Block (Miller, 1983) and were reactivated in the Mesozoic (compare chapter 2.1.1). In Cretaceous times the OML was intruded by the Erongo intrusive complex, whose relics now tower over the peneplains of the Damara Orogen. South of the OML-WT also Palaeoproterozoic basement rocks are cropping out. Further to the east, the Jurassic Karoo Supergroup deposits now form mesas, such as the Waterberg and Mt. Etjo.

The ***southern CZ*** shows the highest uplift and is deeply eroded down to pre-Damara basement inliers (Nagel 1999). NE striking dome structures occur and are interpreted as being created by a ductile sinistral transpression during the collision of the Kalahari and Congo Cratons (Oliver 1994). Folds in this area are east verging to flat-lying and associated with high angle reverse faults (see also Hahne 2004). In the northern CZ rocks of the Kuiseb Formation (Damara Sequence) enclose NE trending dome structures of older formations. Rocks of dome-free areas are folded isoclinally and show a schistosity that is overprinted by a N to NW striking crenulation cleavage (Miller, 1983).

The ***Southern Kaoko Zone (SKZ)*** comprises turbidite rocks (Miller et al. 1983b) arranged in west-vergent structures that were produced during a single deformation phase (Jeppe, 1952; Miller 1973, Weber 1983). The Cretaceous Intrusion complexes Cape Cross, Messum and Brandberg perforate the basement and lavas cover eolian Jurassic sandstones (Etjo Formation) or Pan-African crystalline rocks (Renne et al. 1996).

Meso- and Cainozoic reactivation of Neoproterozoic faults

The Damara Belt as the suture zone between the Kalahari Craton and Angola Block contains Panafrican, Neoproterozoic NE striking crustal scale ductile shear zones: the Autseib Fault-Otjohorongo Thrust (AF-OT), the Okahandja Lineament (OL), and the Omaruru Lineament-Waterberg Thrust (OML-WT) as the most prominent one. The latter is intruded by the Erongo complex (Figures 2-1 b, 2-4 & 2-5). Various researchers found evidence or hints on their reactivation in Mesozoic times:

Studies of Clemson and others (1997, 1999) demonstrate the segmentation of the continental margin offshore Namibia by the named shear zones into discrete zones, each with a different rift evolution. Reactivation of these lineaments during the Cretaceous rifting is suggested therefore. They can be traced from the inland at least 150 km offshore and are orthogonal to the rift axis. Coward and Daly (1984) consider the lineaments to be the continuation of the Mwembeshi Shear Zone (MSZ; Figure 2-1 a), which extends from northern Namibia through Botswana, Zambia and Malawi (Daly, 1986, 1989) with a similar trend.

Several workers found evidence for the reactivation of the Autseib and the Waterberg Thrust at various times during the Phanerozoic (Raab et al. 2002), in particular during the Triassic and during the Early Cretaceous.
The Autseib Fault has obviously been reactivated in the Mesozoic, probably in the Cretaceous, as a reverse fault. Clemson et al. (1997) observed it to cut Triassic sedimentary Karoo Supergroup rocks and also the ring dyke of the Otjohorongo granite complex – one of the 20 Damaraland Complexes- that intruded during the Cretaceous rifting of the South Atlantic. Miller (1980) acknowledges the reactivation of the Autseib Fault during late Karoo- (early Jurassic) and Post-Karoo-Supergroup (after early

Jurassic) times as well. Miller (2008) describes the Mesozoic reactivation of the AF-OT in the north and OmL-WT in the south as overthrusts of the central Damara block onto the adjacent northern and southern blocks, causing uplift of the Damara Belt between them as a "pop-up" structure.
When attempting correlations in Karoo sediments of the Erongo area Hegenberger (1988) recognized two approximately coeval clastic formations that were separated during deposition by an active fault which is part of the Omaruru Lineament Zone. One of the formations was correlated with the Triassic Omingonde Formation. Consequently, they concluded the Triassic reactivation and extension of the Omaruru Lineament zone northeastward as the Waterberg Trust. Also, Holzförster et al. (1999) explain sedimentary and stratigraphic features of late Early Triassic to Early Jurassic deposits in the Waterberg-Erongo area with a synsedimentary, sinistral, oblique-slip motion of the OML-WT. The offshore lateral displacement of the magnetic anomalies M2 and M4 confirms this shear sense (Bauer et al., 2000; Corner, 2002 in Hahne, 2004) besides the vertical/high-angle shear movements ("pop-up") mentioned previously. Dingle et al. (1983) also found that the Waterberg Fault has been reactivated as Karoo (Upper Carboniferous to Lower Jurassic) extensional fault. The Waterberg Fault is described to thrust basement rocks at least 700 m upwards against Lower Jurassic (220-180 Ma) Karoo Supergroup sediments (Schneider, 2008).

Raab et al. (2002) have found strong evidence for a reactivation of the Omaruru-Lineament-Waterberg-Thrust at approximately 70 Ma from onshore apatite fission track data. These data are consistent with offshore seismic stratigraphy within the Walvis Basin (Clemens et al., 1997). The southerly block was moved upward with a late Cretaceous net vertical displacement of about 2 km. For the Autseib Thrust, however, Raab's fisson track data cannot prove a Mesozoic offset. A reactivation of the AF-OT and OL basement structures is attributed to a change in spreading geometry in the South Atlantic and South West Indian Oceans (Raab et al. 2002). However, these authors raise doubts about the reactivation of the offshore segments of the Omaruru and Autseib Faults during late Cretaceous time.

Another coincidence, advertising to a post-breakup reactivation of some of these shear zones is given by a morphological aspect: Raab et al. (2005) point to the fact that onshore Namibia is often referred to as an "example of a high-elevation passive margin, with a generally well-defined coast parallel escarpment some 50-100 km inland from the coast". But it is exactly between the Autseib Fault-Otjihorongo Thrust and Okahandja Lineament where the prominence of the continental margin escarpment is diminished over a zone of ca. 160 km. In that zone, deep erosion and reactivation of the faults have levelled the escarpment to a smooth regional ramp of less than 1° today (Raab et al., 2002).

2.3 Breakup-related mafic dyke swarms

Continental breakup and the birth of the South Atlantic Ocean were accompanied by the installation of extensive mafic dyke swarms on both sides of the rift. On the South American side, in southern Brasil, for example, there is the Florianópolis swarm (Raposo, 1997) on Santa Catarina Island, the Ponta Grossa (PG) swarm (Raposo & Ernesto, 1995), ca. 250 km to the northwest of the former, and a dyke swarm 200 km northeast of the PG swarm, extending between Santos and Rio de Janeiro. The Ponta Grossa dyke swarm is the most prominent one of the named, trending NW-SE at a high angle to the coastline in Paleozoic sediments and Precambrian crystalline rocks of the Ponta Grossa Arch. $^{40}Ar/^{39}Ar$ dating constrains PG dyke emplacement to slightly after the peak volcanism of the Paraná-Etendeka continental flood basalts, with ages from 131.5 ± 0.5 to 129.2 ± 5 Ma and minor subsequent intrusions until 120 Ma (Renne et al., 1996). Also, paleomagnetic data confirm that the PG dykes postdate the major part of the LIP volcanics in the Paraná basin (Raposo & Ernesto, 1989; Raposo, 1992). The latter authors also report some dykes that cut acic and basic lava flows mainly in the northern part of the Paraná basin. Ages from Turner et al. 1994 and Regelous (1993; in Turner et al., 1994) give a somewhat wider age range of 134 ± 1.3 Ma to 130.5 ± 2.8 Ma and 133.3 ± 1.7 to 129.4 ± 0.6 Ma. For the coast-parallel Rio de Janeiro dyke swarm, Turner et al. (1994) give $^{40}Ar/^{39}Ar$ spot fusion ages between 132 and 119 Ma, and Deckart et al. (1998), despite some data ambiguity, concluded mini-plateau ages of 130.6 ± 0.6 to 129.8 ± 0.2 Ma. $^{40}Ar/^{39}Ar$ plagioclase dating was also applied the Florianopolis dykes by Raposo et al. 1998), who yield plateau ages for 5 samples within two ranges from 119-122 Ma and 126-128 Ma. One other sample of their set yielded an isochron age of 121.5 Ma. They argue that due to the small data set it remains unclear, if dyke intrusion was episodic or continuous, but the ages are coeval with the final stages of rifting at this latitude and, therefore, dyke em-

placement appears to be a consequence of crustal extension and subsequent ocean floor spreading. It is argued, therefore, that the Florianopolis dykes correspond to feeders of the surface Paraná lavas. However, recent dating with U-Pb TIMS (Thermal Ionization Mass Spectrometry) on baddeleyite and zircon from mafic and intermediate dykes by Florisbal (2013) supply crystallization ages of 134 ± 0.5 Ma. Accordingly, a much earlier emplacement is suggested for some dykes, coinciding with the main phase of LIP magmatic activity.

On the conjugate margin of southern Africa, LIP-contemporaneous Cretaceous dyke swarms hosted by Pan-African belts have been found along the coast from the Cape Peninsula to NW Namibia. Trumbull et al. (2007) give an overview of their location as well as orientation, intrusion ages, and compositions. Starting in the the Cape Peninsula of South Africa, there is the False Bay dyke swarm (Reid et al., 1991; Backeberg et al., 2011) hosted by the Saldanha Belt. The nearly coast-parallel False Bay dykes have been dated by whole-rock K-Ar at 132 ±6 Ma (Reid et al., 1991), and by ^{40}Ar-^{39}Ar plagioclases at 131.3 ±1.3 Ma (Stewart et al., 1996). About 50 to 100 km inland in the western Cape in the Cedarberg area (Hunter and Reid, 1987) is a group of northwest to southeast-trending dykes. The Cedarberg dykes have not yet been dated, but field relations indicate a post-Karoo age (Chevallier and Woodford, 1999). Farther north, the coast-parallel early Cretaceous Mehlberg dyke swarm is hosted in the coastal Namibian Gariep Belt (Reid and Rex, 1994) and the prominent Henties Bay Outjo Dyke swarm (HOD; Vietor and Weber, 1999; Trumbull et al., 2004, Hahne, 2004) lies within the NE-SW trending Damara Belt. Age determination of the HOD by K-Ar from Siedner and Mitchell (1976), Erlank and others (1984) and Hunter & Reid (1987) scatter between 116 to 143 Ma. Ongoing dating studies by ^{40}Ar/^{39}Ar on plagioclase have yielded a narrower age range of 127 to 135 Ma (R. Trumbull, pers. communication, 2013). Other coast-parallel mafic dykes with LIP-contemporaneous emplacement ages are observed in the NW Namibian Kaoko Belt (Horingbaai dykes) and in the West-Angolan Kwanza basin (Marzoli et al. 1999). The latter are slightly younger than the peak LIP volcanism with ages of 126.1±1.4 Ma. In the compilation of Trumbull et al. (2007) other dykes between the Cape and the HOD are reported, but without age information. The Henties Bay-Outjo and Ponta Grossa dyke swarms are the only large ones on the South Atlantic margin that differ essentially in orientation from the direction of the South Atlantic rift axis. Instead, the HOD and PG dyke swarms strike nearly perpendicular to the coast and extend for about 300 km inland along Panafrican belts.

HOD - The Henties Bay-Outjo Dyke swarm and previous work on it

The Henties Bay-Outjo dyke swarm trends NE-SW parallel with, and within the Neoproterozoic Damara Belt. A pilot study on the distribution of its mafic dykes was first done by Hahne (2004), where dykes were mapped based on high resolution aeromagnetic data recorded in the years from 1994 to 1996 under supervision of the Geological Survey of Namibia. For comparison and because of limited coverage of these data, geologic maps, air photos and Landsat TM and ETM+ satellite images were utilised. The studies demonstrate that the dyke swarm extends for about 300 km SW-NE from the coastal settlement of Henties Bay inland past Outjo and beyond, or 500 km from the continent-ocean boundary as geophysical data suggest (Bauer et al. 2000). The swarm's lateral extension is at least 100 km, but dyke occurrence continues to the NW and SE. However, area-wide detection is difficult because of local Quarternary covers and the restricted availability of high-resolution aeromagnetic surveys in coastal vicinity between Walvis Bay and Lüderitz (Trumbull et al., 2007). With growing distance from the coast, dykes become increasingly discordant to the Damara Belt until they leave it entirely and fan out to the north to intersect the Angola/Congo craton. From there they continue for about 200 km more to the north past the area of high-resolution aeromagnetic data (Trumbull et al., 2004). Hahne (2004) and Trumbull et al. (2004) revealed that dyke density is highest within 100 km from the coastline. One remarkable sharp cut in dyke frequency is made by the Omaruru Lineament in the area between the coastline and the Erongo intrusive complex, where to the south of the Lineament the abundance of dykes abruptly reduces at a fraction.

Figure 2-5, including the stereonets, shows that the abundance of mafic dykes is highest in a narrow area of about 70 km between the Omaruru river and the Omaruru Lineament. The overall major dyke trend is NE, as underlined by the stereonet in the upper left, but also NW, that is to say coast-parallel ones and a few other orientations are present. Especially near the coastline, the NW trend is encoun tered more often (Hahne, 2004; Wiegand 2011) and east of the Omaruru Lineament, this coast trend is

actually prevailing (rose diagram at lower right). Hahne (2004) studied the thickness of 210 dykes along profiles and calculated an average value of 2.9 m with a range of 0.01 m to 45 m. Some of the

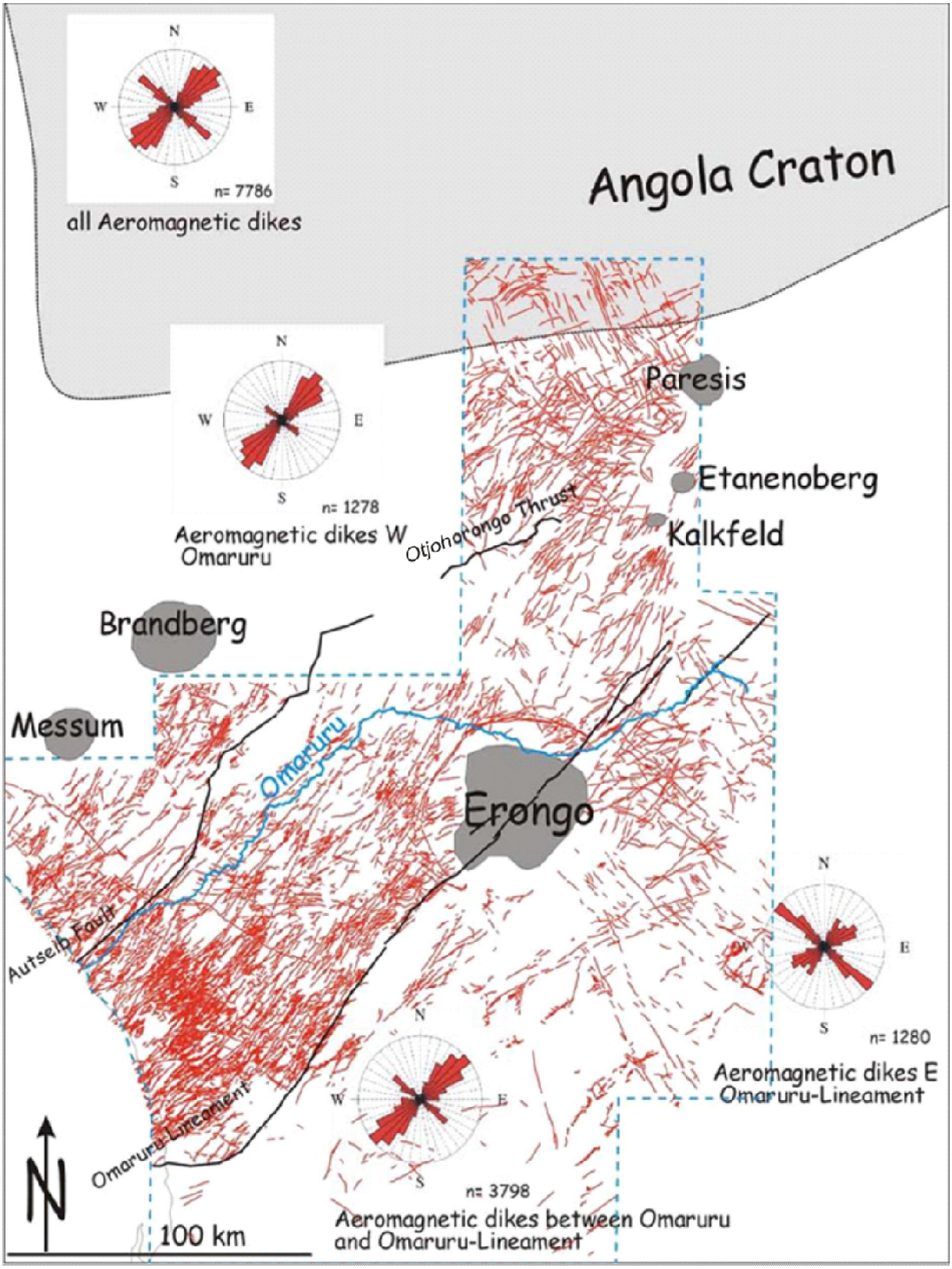

Figure 2-5. Selected mafic dykes from an aeromagnetic anomaly map and orientation distribution of dyke trends in different areas (Hahne, 2004). Coverage of this map delineated in Figure 2-3.

mafic intrusions like the Okombahe or Schwarze Spitzkoppe have a high thickness-to-length ratio with a length of 1.5 to 3 km and a thickness of about 80 to 500 m. They form morphological summits above the plain landscape and are referred to as dolerite plugs. According to the same author, dyke dips are often vertical to moderately inclined (40-80°). Hahne (2004) further states that vertical dykes prevail in coastal areas while progressively inclined dykes occur with increasing distance to the coast. In places, he observed features of a flatter crustal intrusion levels like bifurcations and vesicles. The flat paleo-intrusion depth is confirmed by Raab et al. (2005) who state 4-5 km, or even less, of erosion/ denudation of the plains from the Brandberg area as far as 300 km south since the Upper Cretaceous.

Trumbull and others (2004, 2007) investigated the dyke rocks geochemically. The results show that most of the mafic dykes are tholeiitic and equivalent to the low-Ti series of the Etendeka flood basalts, but less geochemically evolved. They also encountered silicic dykes, but most of them between 80 and 120 km from the coast (Trumbull 2004). Petrographic studies of about 140 mafic dyke samples of the HOD define them as fine to medium-grained basalts, also termed dolerites with intersertal to subophitic and ophitic textures, mainly composed of plagioclase and clinopyroxene and subordinate opaque minerals (Fe-Ti oxides and sulphides), and occasional olivine and amphibole (Wiegand et.al 2011). Alkaline dykes with trachybasalt and tephrite as well as andesite also occur (see also Trumbull et al., 2004).

Age determinations of the HOD dykes are rare. Absolute intrusion ages of the dykes have been constrained by Siedner and Mitchell (1976), Erlank and others (1984) and Hunter & Reid (1987) who determined K-Ar intrusion ages of 116-143 Ma. Erlank (1984) reported $^{39}Ar/^{40}Ar$ ages of 125–130 Ma for dykes near Horingbaai, Renne et al. (1996a) obtained an $^{39}Ar/^{40}Ar$ age of 132±0.7 Ma for gabbroic sills from the Huab area, and Wigand et al. (2004) determined an $^{39}Ar/^{40}Ar$ age of 132±1 Ma for mafic alkaline dykes and small stocks from the Erongo complex. From these few data together with field relations and the compositional similarity with Etendeka volcanic and Damaraland intrusions it is assumed that they were emplaced between 125 and 135 Ma (Trumbull et al., 2004).

During a master thesis study of petrological and geochemical features of the HOD, Frei (2011) also included an extra study of cross-cutting relationships between HOD dykes of different orientations. He investigated a possible correlation between their emplacement age and orientation. This work was done on satellite images with a resolution of 2.5 m (taken in 2010) using GoogleEarth (http://www.google.com/intl/en/earth/index.html for English version). The investigated area extends from 21°36' S to 22°40' S and 14°24' E to 14°52' E. Of 205 intersection points where the order of intrusion was unambiguous, 85 show that NE striking dykes are younger and cut across NW striking ones while the opposite case was recorded 55 times. It was concluded that the NE striking dykes both postdate and partly also intrude synchronously with coast-parallel ones.

Frei (2011, M.sc.thesis) and Keiding et al. (2013) performed mineral chemistry and thermobarometric studies of of the HOD dyke samples, using clinopyroxene compositions to place constraints on the pressure conditions of crystallization, which they interpreted as the depth of magma ponding. Keiding et al. (2013) envisage locally variable and transient magma conduits for the HOD with ponding within the crust based on the scarcity of geochemically primitive dykes in their sample set and of olivine-phyric, Mg-rich Tafelkop magma type in the Etendeka province (Marsh et al., 2001). The barometric results suggest crystallization pressures of 3-5 kbar, which corresponds to a magma emplacement depth of 11-17 km. The depth of emplacement of some dyke magmas is shallower, since they are observed to cut lava flows. The thickness of overlying and now eroded rock may have been as much as 3-4 km based on fission track studies of Raab and others (2005). Frei (2011) also used variations in mineral compositions from HOD dyke samples as evidence for multiple magma intrusions (recharge) by primitive melts. Examples are reverse zoning in clinopyroxene and olivine (more magnesian/Mg-rich rims) and oscillatory zoned plagioclase xenocrysts in the dyke rocks. Similarly, Keiding et al. (2011) point out the occurrence of "ultramagnesian" olivine xenocrysts, which represent unerupted picritic melts.

Of special relevance to the magnetic mineralogy of the HOD dykes, Frei (2011) revealed two compositional types of titanomagnetite: one titanium-poor type with a high FeO/TiO_2-ratio of 4 to 5 (samples 2, 5, 13, 45) and a titanium-rich type with a low FeO/Ti-ratio of 2 to 3 (sample 51 and others SW of

Outjo; compare: ratio 1 = ilmenite). The latter ratio corresponds to an ulvospinel component of 70% (TM70). He also noticed a non-stoichiometry and a systematic cation excess of 15 to 20 % for both titanomagnetite and ilmenite, which is difficult to explain. Oxidation or maghemitisation, which would be expected as common alteration of these minerals, should produce cation deficiency and not excess. It is speculated that the cation excess might have been generated by oxygen vacancies due to a high oxygen fugacity conditions throughout the HOD. Frei (2011) described the current Fe-Ti oxide phases as titanomaghemite and locally hemo-ilmenite, having been altered from the primary phases ilmenite and Ti-magnetite.

3 Fundamentals of rock magnetism

The following introduction to the fundamentals of magnetism basically refers to the textbooks of Soffel (1991), Butler (1992), Tarling & Hrouda (1993) Dunlop & Özdemir (1997) and Tauxe (2002).

3.1 Magnetization, magnetic susceptibility and remanence

All materials have magnetic properties at temperatures above zero degree Kelvin. Magnetism is caused by the motion of electrically charged particles and is a product of the electron`s axial spin and the orbital motion of electrons around the atomic nucleus. The orbital motion can be neglected in ferritic solids. Dependant on the electron configuration of its atoms/ions, in particular paired/unpaired electrons, complete/incomplete electron shells and on the existence of transition elements with unfilled 3d electron shells, materials respond differently to magnetization. Magnetic responses are grouped into three different types: diamagnetic, paramagnetic and ferromagnetic behavior, see Figure 3-7.

The type and strength of the magnetization (M) of any substance depends on two factors: the strength of the applied magnetic field (H) and the magnetic susceptibility (κ, Kappa) of the material being magnetized. This dependence is expressed by the following equation:

$$M = \kappa * H$$

with κ being dimensionless, H in A/m and M in A/m as the magnetic dipole moment per unit volume. Consequently, the magnetic susceptibility determines the magnetizability of a material in an external magnetic field. The magnetic susceptibility is dependant on temperature as well as on the strength, frequency and direction of the applied field and the domain states of the magnetized material. Since the MS in a material is strongly coupled to magnetostatic (grain shape) and/or magnetocrystalline energy (crystal structure, Tauxe, 2002), it is most commonly anisotropic.

Magnetization is composed of an induced and a remanent component: $M = M_{ind} + M_{rem}$. The remanent magnetization remains after the removal of the applied magnetic field. Which one of the two components dominates a rock's magnetization can be determined by calculating the Koenigsberger ratio (Q):

$$Q = M_{rem} / (\kappa * H_{Earth}) \quad .$$

H_{Earth} is the total intensity of the earth's magnetic field at the sample site and at the timeof sampling. The product of susceptibility (κ) and H_{Earth} is the induced magnetization in the current earth magnetic field and M_{rem} is the natural remanent magnetization (NRM). The NRM in a rock is due to ferro(i)-magnetic (chapter 3.2.) minerals and can consist of several components generated by various physico-chemical effects. One of the most important components in natural basalts is the thermoremanent magnetization (TRM), also termed "primary" remanence, imparted by the earth's magnetic field. The TRM normally preserves the direction (and internsity) of the earth's magnetic field at the time of magma cooling. The NRM depends on the amount and type of the carrier minerals, their domain state and on the age of the rock, since the remanence weakens and decays as a function of time. This magnetic decay is termed relaxation time. Secondary remanence is acquired after magma cooling and may alter the magnitude and orientation of the NRM vector, since they can be imparted by a different magnetic field than the one having acted during rock formation. Examples for secondary remanences are a lightning-imparted isothermal remanence, or a viscous remanence acquired at ambient temperatures, for example in the earth's magnetic field.

Both magnetic susceptibility and remanence are usually anisotropic in rocks, reflecting their primary or secondary petrofabrics. Therefore, the anisotropy of magnetic susceptibility (AMS) and the anisotropy of remanence (ARM) are utilized in order to reveal a rock's history by investigation of its magnetic fabric and the preferred orientation of its components (see chapters 4.1 and 4.2). The anisotropy may be due to a large number of sedimentary, igneous, metamorphic and/or tectonic processes. Its orientation can be described mathematically and graphically by tensors or triaxial anisotropy ellipsoids, respectively.

TRM acquisition in magmatic rocks

Schoebel et al. (2013) reason: When magmatic rocks are cooled below the Curie temperature and further down, a thermoremanent magnetization is acquired. This process is observed to be an iterative process of domain wall nucleation and displacement/adjusting domains width (Dunlop & Özdemir, 1997). Energetically, there is a competition between the aligning forces of the external/earth magnetic field and the low energy-directions of the grain's easy axes, where the easy axis direction depends upon the dominant anisotropy energy: grain shape/anisotropy or crystallographic anisotropy. In anisotropic grains the easy axis is the longest grain axis and in isotropic grains the body diagonal [111]. Consequently, when passing through the blocking temperature the magnetic domains and moments will arrange parallel with the easy axes within the grain (Figure 3-6, point 2), and those domains with a minimum angle with the direction of the earth's magnetic field will enlarge relative to the others (Schoebel & De Wall 2013) and dominate the NRM vector. Size and degree of parallelism of the enlarged domains correlate positively with the field's magnitude. When isotropic single-domain grains cool below the blocking temperature, their magnetic moments will get locked and point with a statistical bias into the direction of the acting field (Figure 3-6, point 3; Tauxe, 2002). At room temperature, the so acquired thermoremanent magnetization (TRM) is stable in SD and PSD particles for geological

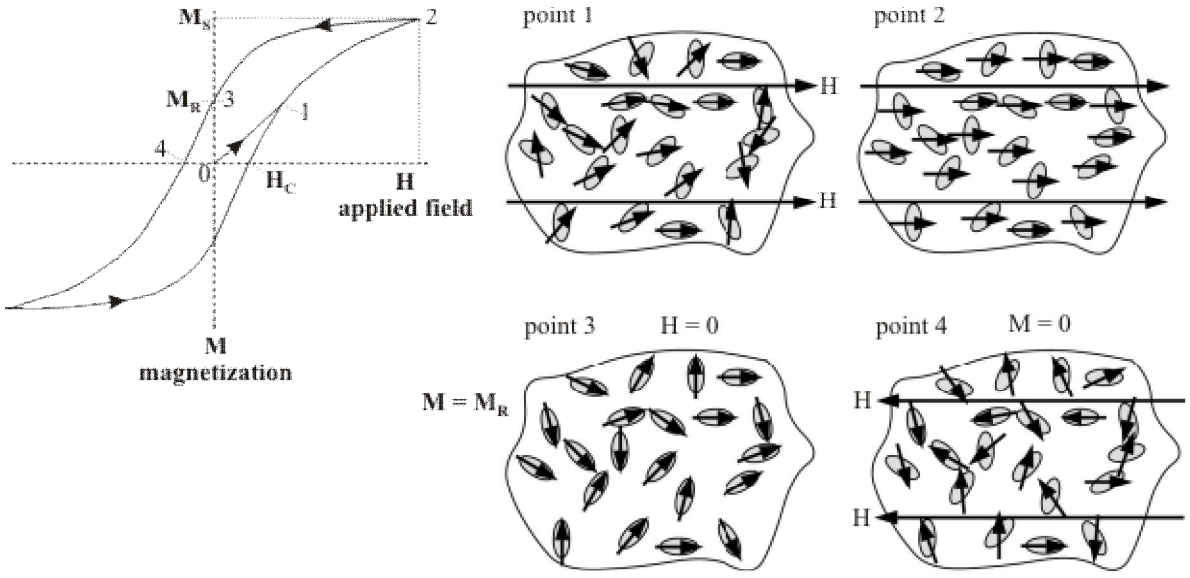

Figure 3-6. Left: Hysteresis loop containing 5 vol.% of dispersed elongate single-domain (SD) magnetite particles. M_S = saturation magnetization, M_R = remanent magnetization, H_C = coercivity. Points labeled are illustrated on the right. Point 1: Magnetization directions within SD grains at point 1 on hysteresis loop. Grey ellipses represent elongate SD magnetite grains. Arrow indicates direction of the (saturated) magnetization (m_S) for each SD grain. Point 2: m_S are rotating towards the direction of H. m_S within the SD grains are aligned parallel with H. Sample is at saturation magnetization M_S. Point 3: After the removal of H the sample retains a remanent magnetization M_R. Note that m_S of each grain has rotated back to the long axis closest to the previous direction of H, to the right. Point 4. The sample has no net magnetization (M = 0). Note that every grain has been slightly rotated toward H, now to the left. Modified after Butler (1992).

times. SD and PSD particles are, therefore, referred to have a long relaxation time. In MD grains, however, energy barriers between the different easy axes are much lower and easier to overcome than the shape anisotropy in the SD grains. Therefore, the TRM decays rapidly in MD grains over the first 10 million years after magma cooling, being partially replaced by a viscous remanent magnetization (VRM) parallel with the actual external magnetic field. Consequently, the NRM vector is composed of at least two components with mostly different direction: the VRM and the NRM (e.g. Dunlop & Özdemir, 1997).

3.2 Types of magnetism

The different types of magnetism, which are presented in the following, are classified according to their states of magnetic ordering, as illustrated in Figure 3-7.

Diamagnetism

Diamagnetism occurs in substances with compensated atomic magnetic moments and complete electron shells. When such a solid is exposed to a magnetic field, orbital electron motion is disturbed. Electrons thus precess and a weak magnetization M is induced anti-parallel to the applied field H. This kind of response is shown by all substances, but it is masked in those with atomic magnetic moments. Induced magnetization is linearly dependent on the applied field and disappears when the field is removed. The magnetic susceptibility (see below) of diamagnetic solids is always negative because of the anti-parallel character of the induced M and does not depend on temperature.

Paramagnetism

Paramagnetic (and ferromagnetic) substances possess incomplete electron shells and atomic magnetic moments do not interact. The induced magnetization is linearly dependent on and parallel with the applied field, which results in a positive magnetic susceptibility. However, the alignment of magnetic moments is disturbed by rising temperatures, because magnetic energy competes with thermal one. This is described by the Curie-Law: $\kappa_{para} = C / T$,

with κ_{para} being the paramagnetic susceptibility, C the Curie constant and T the temperature. As in diamagnetic materials magnetization reduces to zero when the field is removed. Magnetic moments then are randomly oriented again.

Ferromagnetism (sensu lato)

All substances whose atomic magnetic moments interact strongly are referred to as ferromagnetic, sensu lato. This interaction is the result of overlapping electron orbitals of adjacent particles due to short interatomic distances. Thus, electrons can be shared and atomic moments of adjacent particles become strongly coupled because of quantum mechanical exchange energy. The electron spin coupling is also termed ***spontaneous magnetization*** which is a property of the first transition series of elements. The 3d orbital in these elements is particularly prone to exchange interactions because of its shape and potential high number of unpaired spins. Magnetization in ferromagnetic materials is several orders of magnitude stronger than in paramagnetic ones. For this reason, magnetic behaviour in substances composed of ferro- and paramagnetic particles is dominated by ferromagnetic response, as long as these particles make up at least 5% of the volume. In contrast to the other types of magnetization, the alignment of the magnetic moments is preserved after the removal of the externally applied field. Therefore, a ferromagnetic substance is able to record the direction of an applied field. Such a retained magnetization is termed ***remanence***.

Temperatures higher than the *Curie-Temperature* T_c increase the interatomic distance and consequently the spins become disordered, the remanence gets lost and the material becomes paramagnetic. This change in magnetic behaviour is called “phase transition”.

Ferromagnetism (s.l.) can be subdivided into three subtypes due to the form of quantum-mechanical coupling force (exchange and superexchange forces) and the internal structure/unit cell constitution of the material: ferromagnetism (sensu stricto), antiferromagnetism and ferrimagnetism.

A direct coupling of electron spins of adjacent cations happens within the metallic transition elements such as iron, nickel, cobalt and their compounds. In ***ferromagnetic*** (s.s.) substances exchange forces act to align all magnetic vectors in the same direction parallel with the applied field. Superexchange forces operate in more complex compounds such as oxides of the first transition series of elements, where electron spins of cations are shared via an intermediate anion (in oxides: oxygen). Electron spins of two adjacent cations are reversed which creates two oppositely magnetized lattices within the same material. If the magnetization in the two lattices is equally strong, magnetic moments compen-

sate each other. This is termed ***antiferromagnetic*** behaviour. Haematite, for examples, is an antiferromagnetic mineral, but a special case. On the one hand, its magnetic moments are not perfectly antiparallel. In addition, crystal impurities or lattice defects lead to a certain net magnetization, creating a weak ferromagnetism. Haematite, therefore, is known as a canted or imperfect antiferromagnet (see Butler, 1992) whose magnetism is stronger than paramagnetism but much weaker than that of ferromagnetic minerals. Above the *Néel temperature* T_N *(*the T_C equivalent), the ferromagnetic ordering gets lost and the material becomes paramagnetic. This temperature-dependence is described by the Curie-Weiss Law: $\kappa_{anti} \sim 1 / (T-T_N)$ for $T > T_N$

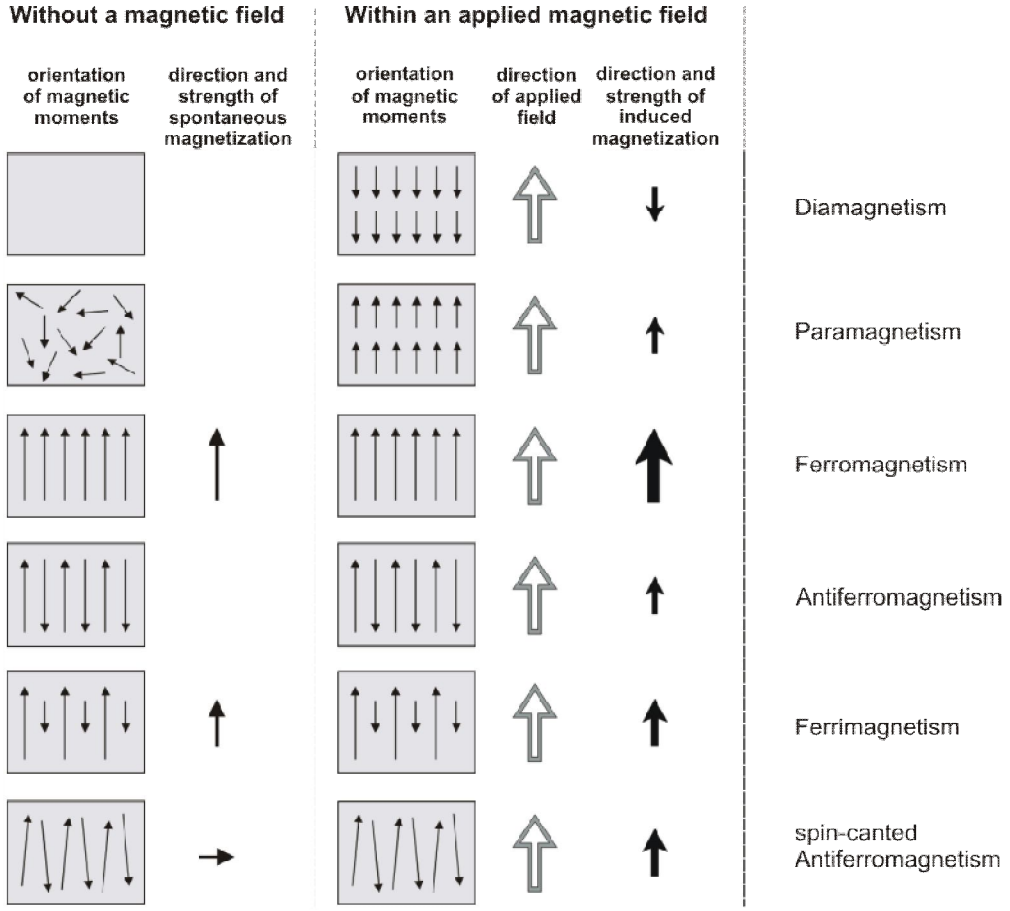

Figure 3-7. States of magnetic ordering, modified after Günther (2003).

An unequal magnetization of the two lattices yields a net magnetization, which defines the substance as ***ferrimagnetic***. This kind of magnetism is stable below T_C and is found in magnetite, for instance (for details see chapter 3.7). For temperatures above T_C, analogous to T_N, spin coupling gets lost: $\kappa_{ferri} \sim 1 / (T-T_C)$ for $T > T_C$.

3.3 Magnetic domains

A ferromagnetic (s.l.) particle that is sufficiently small behaves as a single isolated magnetic dipole with magnetostatic energy stored by the charge separation. Such grains are referred to as ***single domain (SD)*** grains. With increasing grain size also magnetostatic energy grows which is an unfavorable state that reduces grain stability. Therefore, at some particle size termed the *single-domain threshold* d_0, the grain is subdivided into multiple regions of more or less uniform magnetization, magnetic domains, thereby reducing its energy. D_0 strongly depends on the grain`s habit and the saturation magnetization M_S amongst others. Very elongate minerals with a certain length can still be SD, while cubic/isometric grains may be structured with two or more domains. An euhedral magnetite crystal, for

example, is SD only below a grain diameter of 0.1 µm, but a needle-shaped SD magnetite can be even 10 times longer (1 µm). In case of titanomagnetite d_0 strongly depends on the proportion of Ti (Butler and Banerjee, 1975). Titanomagnetites with the composition TM60, for example, show SD-particles up to the grain size of 1 µm in experiments (Soffel, 1971). In contrast, haematite shows still SD crystals at 15 µm edge length. Particles with a high M_S reach a high energy level at much smaller grains and tend to subdivide at much smaller diameters compared to low M_S particles. Magnetic domains are separated by the so-called domain or Bloch walls, whose nucleation also stores energy. It is energetically not favourable to subdivide a grain below a certain size, since wall energy at some point exceeds magnetostatic energy, which is just as unfavourable. Furthermore, in a very small/slim grain, the wall itself would occupy all the space. Domain walls are preferentially installed parallel with the grain`s long axis. As a consequence, very slim, but elongate particles are not struck by subdivision.

Particles with two to eight magnetic domains are termed ***pseudo-single domain (PSD)*** grains. Normally they consist of a few larger domains arranged parallel with the grain`s long/easy axis, and at 180° (hem, tmt, mt, mgh, tmgh) to one another. Owing to this (anti-)parallel arrangement of the large domains, PSD grain behaviour largely resembles SD behaviour. A few small "closure"domains link the larger ones (Figure 3-8) with their magnetic moments aligned in that way to form spiral/circular arrangements in combination with the large domains. They have specific angles of 71° and 109° in mt, tmt, mgh and tmgh. PSD grain sizes of magnetite range between 0.1 or 1 and 8 (Moskowitz and Banerjee, 1979) or 10 µm. According to experimental results from Soffel (1971), the PSD size of TM60 particles ranges from about 1 to 7 µm for two-domains up to 40 to 50 µm for 8 domains. Ferromagnetic (s.l.) crystals containing more than eight magnetic domains are termed ***multi-domain (MD)*** grains.

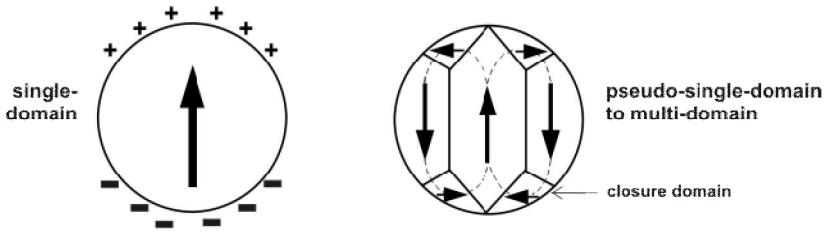

Figure 3-8. Left: Ferromagnetic single-domain particle with surface magnetic charge separation. Arrow inside gives the direction of saturation magnetization. Right: Particle with a few domains, the large ones antiparallel and the small ones perpendicular to these, arranged to "close" the circle with the large domains. Therefore these small ones are termed closure domains. (modified after Butler 1992)

Superparamagnetic particles are smaller than SD ones with only a few nanometres in diameter. They show paramagnetic behaviour since they are not able to store their magnetization after the applied field has been switched off.

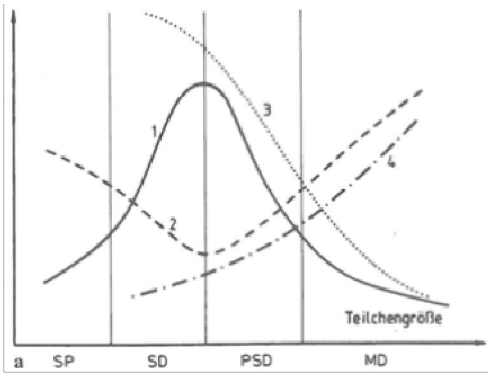

Figure 3-9. Dependence of coercive force (1), susceptibility (2) and the ratios magnetization remanence versus saturation magnetization M_{RS}/M_S (3) and remanent coercive force versus coercive force H_{CR}/H_C (4) from the domain size (Soffel, 1991). For abbreviations see text.

The magnetic properties of particles with different domain states differ substantially, for example the susceptibility and the hysteresis parameters coercive force (H_C), remanent coercive force (H_{CR}), magnetization remanence (M_R), saturation magnetization (M_S) and their ratios H_{CR}/H_C and M_{RS}/MS, as depicted in Figure 3-9 and described in chapter 3.6.

3.4 Internal demagnetizing field

As illustrated by Figure 3-8, surface magnetic grain charges are the consequence of magnetization directed towards the grain surface in a ferromagnet. The resulting external field is a dipole field. If the magnetization direction parallels the long grain axis, the surface charge area is smallest, and vice versa for the short axis. The external or surficial magnetic field induces an internal field inside of the grain which is parallel, but opposed to the external one. Because of opposite sense of the external and internal fields, the grain's total magnetization is diminished, or in other words, the grain partly demagnetizes itself. The strength of the internal demagnetizing (H_D) field is proportional to the applied external field and the demagnetizing factor (N) for uniformly magnetized ellipsoids: $H_D = -N M$.

N is dimensionless-and its magnitude is a function of the relative size of the magnetized/charged grain surface. N depends on the orientation of the specimen in respect to the direction of the applied field and is strongly direction-dependent in largely shape-anisotropic ferromagnetic particles. In contrast, in a uniformly magnetized spherical grain N is equal (⅓ SI) in any direction (Butler, 1992; Dunlop & Özdemir, 1997). This relationship is the cause for the anisotropy in non-isometric grains (de Wall, 2005). The easy axis of magnetization in a grain is the long one. On account of this, for measurements of the magnetization in strongly ferrimagnetic samples, e.g. in basalts, it is crucial to work with nearly spherical specimen in order to avoid introducing "artificial" anisotropy effects. Therefore, the samples should hold a diameter to height ratio of 1: 0.82 (de Wall 2005).

3.5 Magnetic anisotropy and anisotropy energy of particles

Magnetized particles always seek to minimize total energy in order to reach a stable state. The magnetic moment of a particle therefore tends to lie in a direction that minimizes magnetic energy. This direction is termed the "easy" or "spontaneous" direction of magnetization within a grain. Magnetization thus is anisotropic within a crystal, it has one or more preferred directions depending on crystal symmetry. In order to change magnetization direction, energy is required to overcome intervening "hard" directions, which are not favourable to be magnetized. The energy required to move the magnetic moment in the crystal from one easy axis to another one is called ***anisotropy energy***. The magnitude of the magnetic field necessary to overcome hard directions and to switch between the easy ones is termed coercive field H_C.

There are different sources for anisotropy energies, e.g. ***magnetostatic, magnetocrystalline*** or ***magnetostrictive*** energy. ***Magnetostatic energy*** is generated by ***grain shape anisotropy***: A grain or crystal minimizes its magnetic energy when the magnetic charges (positive and negative) at the particle`s surface are located at the opposite ends of the particle`s long axis instead of crosswise. The minimization of magnetic energy is the consequence of an antiparallel internal magnetic field created within the particle as response to the external field (de Wall 2005). ***Magnetocrystalline energy*** is generated by crystal lattice structure, as in non-isotropic crystals such as the platy haematite, goethite or the paramagnetic minerals pyroxene or chlorite. Depending on crystal symmetry, magnetocrystalline anisotropic minerals can have several easy axes. ***Magnetostrictive energy*** is caused by stresses within the crystal. When exposed to an applied field, the magnetic spins move and align within a crystal. These movements cause relative length variations of unit cell axes, termed magnetostriction. The variation of the relative length between the non-magnetized and saturated state is described by the dimensionless magnetostriction constant λ. Mechanical tensile or compressional stresses that deform a crystal, can also crucially change the magnetization direction within a mineral.

Magnetostatic interactions between particles occur, when the intergranular distance falls below a critical value (Grégoire et al., 1998, Cañon-Tapia, 1996) and the magnetic moments interact (Hargraves et al., 1991). In a chain-like alignment of euhedral tmt octahedrons (see chapter 3.7.1), for example, the magnetic moments of all single grains would combine and behave as a bar magnet showing

a strong shape anisotropy (e.g. Cañon-Tapia, 1996). In contrast, if isolated, each of these grains would be almost isotropic because of the very low crystalline anisotropy in the cubic crystals.

3.6 Magnetic hysteresis and hysteresis loop

The magnetic hysteresis is a property of ferromagnetic materials, which refers to the delay of magnetization changes as consequence to changes in direction and strength of the applied magnetic field. Magnetic hysteresis is a consequence of the interaction of neighbouring spin moments and the resulting net magnetic moments attached to distinct orientations (easy axes) within the grains. Anisotropy energies have to be overcome in order to change the internal direction of magnetization.

A hysteresis loop is the record of the magnetization (M) in dependence of the applied field (H), as Figure 3-10 a illustrates. The diagram gives insights into the type (dia-, para, ferromagnetic) of magnetism and into the domain state of the investigated ferromagnetic (s.l.) material. Figure 3-10 c-g shows typical hysteresis loops for materials with the different domain states. The domain state is strongly sensitive to the saturation magnetization (M_S), the grain size and shape and to the state of a minerals mechanical stress (Soffel 1991).

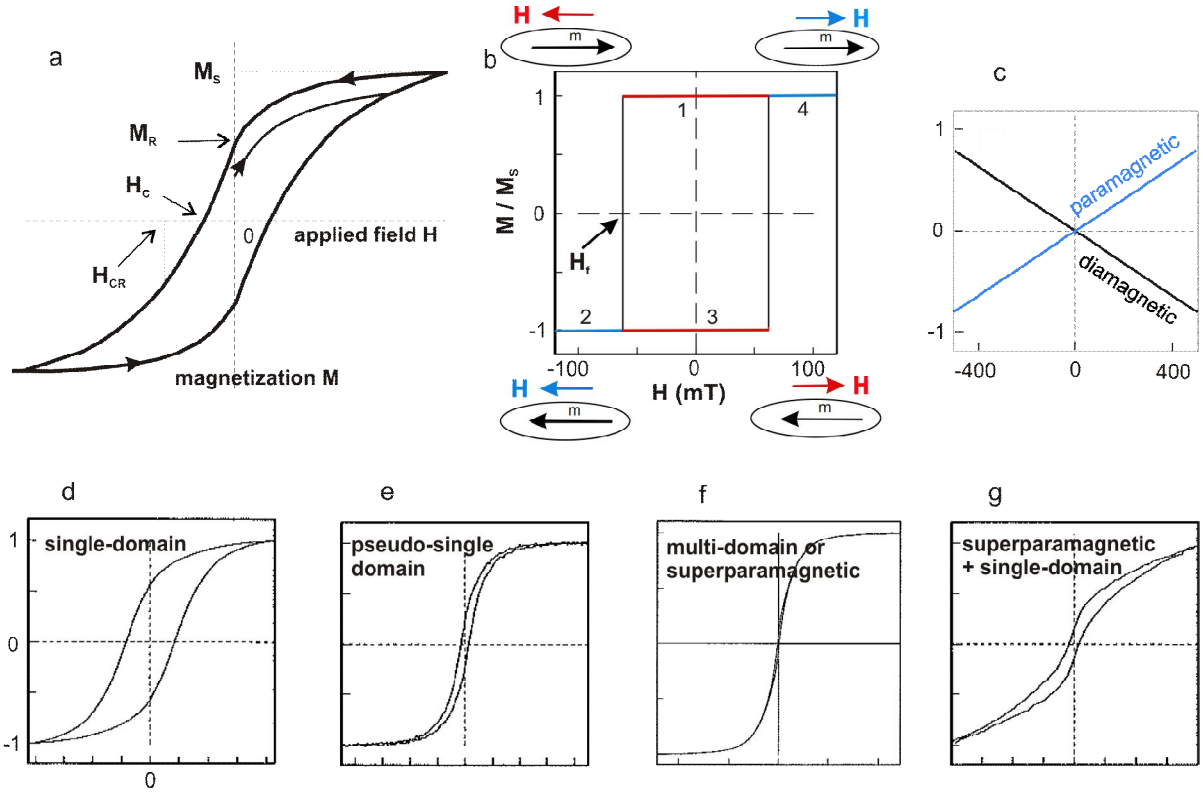

Figure 3-10. Hysteresis loops of ferromagnetic materials; a) Schematic loop of a ferromagnetic (s.l.) multi-grain rock sample; M_S = saturation magnetization, M_R = M_{RS} remanent magnetization, H_C = coercivity, H_{CR} = coercivity of remanence b) Loop of a single-domain SD grain with uniaxial anisotropy; modified from Tauxe 2002; m = magnetic moment of SD particle. Loop starts at point 0, with magnetic saturation, because it is SD. During track 1 the magnetic field is applied in the opposite direction and continuously increases. When reaching the field magnitude H_f, the magnetization flips for 180° in the direction of the applied field. Following track 2 with a growing applied field magnetization will not increase further because the domain is already aligned with the field. Then the field decays to zero and is reversed, but magnetization direction does not flip until H_f is reached again. c-g) Typical loops of different grain populations, modified from Tauxe 2002.

Hysteresis loop measurements of a ferromagnetic (s.l.) material start by subjecting the sample to an increasing magnetic field (H). A schematic hysteresis loop of a ferromagnetic (s.l.) material is depicted in Figure 3-10 a and described in the following. Loops of materials, which already carry a remanent magnetization, start at a point on the ordinate different from zero. In response to the field, magnetiza-

tion of the sample initially increases nearly proportionally. With increasing field force the slope diminishes and the curve flattens gradually until, at a certain field force (H_{max}), the ***saturation magnetization*** (M_S) is achieved. All magnetic moments then are aligned parallel with the field. After saturation, the magnetic field force decays with the same rate as it was increased before. But instead of exactly reversing the magnetization curve, the path of demagnetization M(H) is found above, that is to say with a higher magnetization. On the contrary to ferromagnetic substances, both for para- and diamagnetic materials hysteresis slopes are reversible. When intersecting the y-axis (H = 0), the material`s magnetization has been reduced, but not completely, as expected for para- and diamagnetic substances. A magnetic moment with the initial polarity, termed ***remanent magnetization*** (M_R or M_{RS}), still remains in the direction of the former field. From this point of the descending loop, the magnetic field switches polarity and increases again. At the ***coercive force*** (H_C), finally the remanent magnetization vanishes completely and all magnetic moments become randomized again. After further increase of H, the material again saturates in the antiparallel direction $-M_S$, followed by a field decrease to zero, where a remanence $-M_R$ in the same direction remains. Finally the hysteresis loop completes with the again rising field force.

The hysteresis parameters remanent magnetization (M_R), saturation magnetization (M_S), coercive force (H_C) and remanent coercive force/coercivity of remanence (H_{CR}) are obtained. Their ratios M_R/M_S and H_{CR}/H_C are specific for distinct domain states (SD, PSD, MD) and they serve as classification criterion in the Day plot (Day et al., 1977). High coercivities (H_C) and a high M_R/M_S ratio represent SD particles, also termed magnetically hard, low H_C and M_R/M_S ratios are due to MD particles, termed magnetically soft. PSD grain behaviour ranges in between SD and MD (Figure 3-9). M_S is solely material-specific while H_C both depends on grain size and material (Soffel 1991). The ratio of remanence to saturation magnetization M_R/M_S and coercivity of remanence to coercive force H_{CR}/H_C are primarily dependent on the grain size and domain states of the ferromagnetic component (Soffel 1991). Dunlop (2002) later refined the Day Plot (Figure 3-11 a). He first calculated theoretical mixing curves of

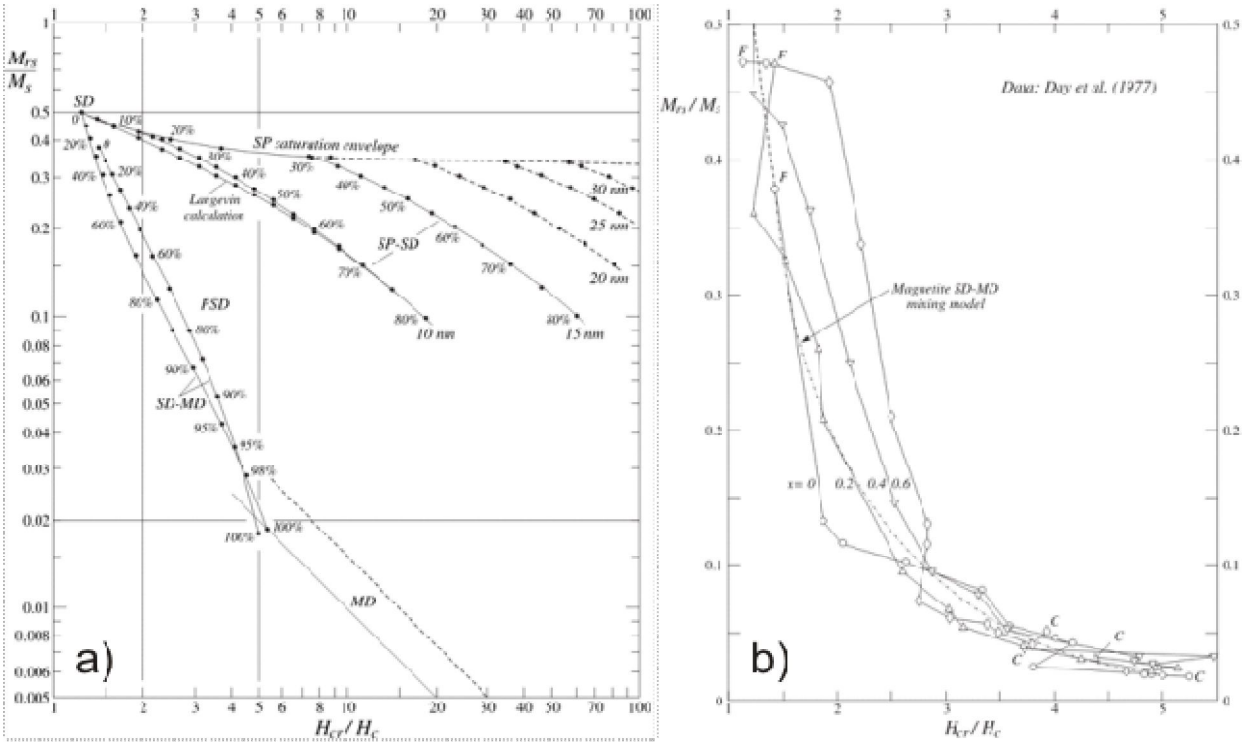

Figure 3-11. a) Day Plot modified after Dunlop (2002) containing theoretical curves calculated for magnetite. Curves with percentage labels are mixing curves of two volumes with different grain sizes. Numbers refer to the volume fraction of the soft component (SP or MD). SP particle sizes are labeled. SD-MD mixing curves are calculated with SD and MD endpoint values based on two different data sets. b) Subparallel curves of sized titanomagnetite from Day et al. (1977) with different titanium contents x. F and C indicate fine and coarse grained endmembers (Dunlop 2002).

single and multi domain grains and then matched the curves with different data-sets of sized tmts. The author proved fine-grained samples to plot in the upper part of the diagram and that grain size gradually grows towards lower M_R/M_S ratios. Dunlop also found the tmt mixture with sorted ulvospinel contents x = 0, 0.2, 0.4, 0.6 to lie on subparallel hyperbolas in a non-logarithmic diagram (Figure 3-11 b).

3.7 Magnetic mineralogy in basalts

All the constituent minerals of basalts are dia- or paramagnetic, except a small percentage of about 5 volume percent of opaque iron-titanium oxides and iron sulphides, which are ferromagnetic (s.l.). Their magnetic properties are several times stronger than those of the para- and diamagnetic phases and, therefore, dominate the magnetic behaviour of the rock.
For magnetic studies in relatively fresh basalts, the most important opaque minerals are iron-titanium oxides, which constitute about three to seven volume per cent of the rocks studied here. The composition of the iron-tita-nium oxides can be displayed in a ternary diagram (Figure 3-12) with titanium oxide (TiO_2), wüstite with divalent iron (FeO), and haematite with trivalent iron (Fe_2O_3). Members of the two solid solution series titanomagnetite/-maghemites and titanohaematite/haemoilmenite represent the dominant carriers of the magnetism of basalts. The oxygen fugacity of a magma strongly influences the type of primary iron oxide being formed during crystallization (titanomagnetite, haematite or/and ilmenite etc; Lattard et al 2006).

Iron sulphides like pyrite, chalcopyrite, greigite, pyrrhotite etc. are often secondary (some also primary) and much less abundant in fresh rocks (<<1 wt%), and rarely contribute significantly to a basalt's magnetic properties. Since titanomagnetite (and its oxidation product titanomaghemite) is ferrimagnetic, its magnetic properties dominate over paramagnetic ilmenite and antiferromagnetic haematite, if the tmt/tmgh contents exceed one weight percent in the bulk rock.

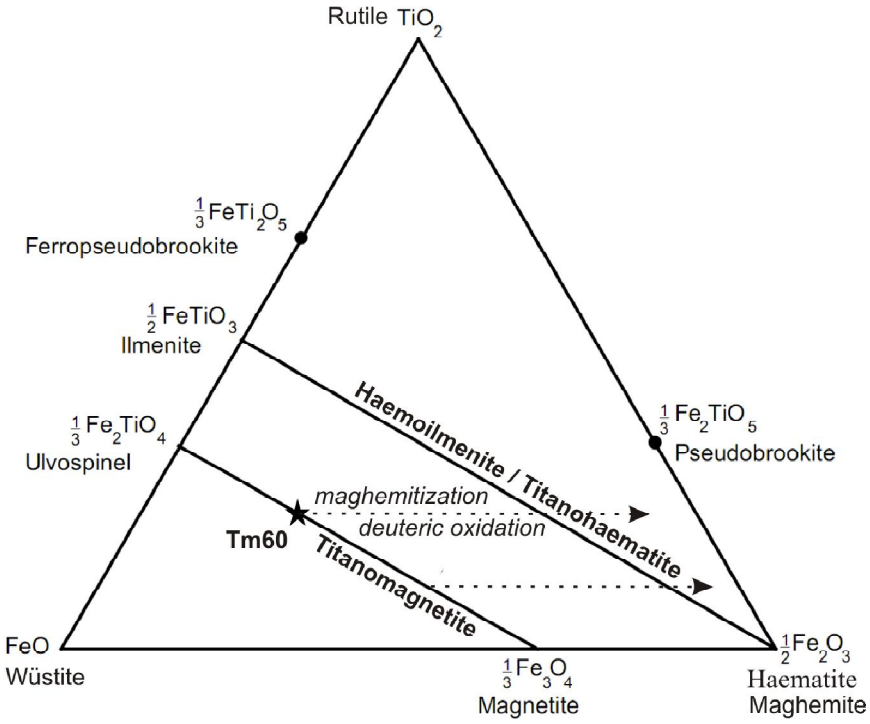

Figure 3-12. Iron-titanium oxide ternary diagram. The star indicates the composition of titanomagnetite with x = 0.6 (TM60; most common primary composition of titanomagnetite in basalts); dashed arrows mark the compositional path of increasing oxidation (both maghemitization and deuteric oxidation); modified after Tauxe 2002.

3.7.1 Magnetite and titanomagnetite

Titanomagnetite (tmt) occurs in cubic face centred, opaque crystals of a solid solution series with the end members magnetite (mt) Fe_3O_4 and ulvospinel Fe_2TiO_4. The general chemical formula of titanomagnetite is $Fe_{3-x}Ti_xO_4$ with x ranging from 0.0 for magnetite to 1.0 for ulvospinel. A unit cell of tmt or mt is a framework of 32 oxygen ions (O^{2-}) arranged in octahedral and tetrahedral symmetry and 24 cations occupying the positions within these octa-and tetrahedrons. A network of two sublattices is formed by the cations: The sublattice A contains 8 sites per unit cell in tetrahedral coordination, surrounded by four O^{2-}, and sublattice B is made up of 16 sites in octahedral coordination, surrounded by six O^{2-} (Figure 3-13). Pure magnetite is a construct of 16 trivalent iron ions (Fe^{3+}) and 8 divalent iron ions (Fe^{2+}) per unit cell, which distribute in an inverse spinel structure between the sublattices A and B. In contrast to normal spinels, the two B sites per formula unit are occupied by different cations, one Fe^{3+} and one Fe^{2+}. A-sites are exclusively occupied by Fe^{3+}, which have five unpaired spins compared to Fe^{2+} with four unpaired spins. This difference leads to unequally strong magnetic moments in the two lattices, which are coupled with antiparallel spins resulting in ferrimagnetic behaviour of magnetite. Pure magnetite is characterized by a Curie-Temperature (T_C) of 570 to 590 °C, depending on crystal impurities and lattice defects. Above this temperature magnetite behaves paramagnetically. Another diagnostic transformation, the Verwey-transition (T_V), takes place in mt when temperature falls below -153 °C (120 Kelvin). At this temperature, the cation ordering is accompanied by a transformation in crystal symmetry from cubic to monoclinic. These modifications lead to a drastic drop in magnetic susceptibility, electrical conductivity and heat capacity. Minor cation substitution may suppress the T_V. Slightly above the T_V at the isotropic point (T_i) at -143 °C, the magnetocrystalline anisotropy constant becomes zero and changes sign such that the easy directions of magnetization change their orientation from [111] above T_i to [100] below (Moscowitz et al., 1998). Thus, in euhedral magnetite octahedrons the easy axes are along the body diagonal above T_i. Below T_i the easy axes are along one of the cube edge orientations (Jackson et al. 2011). If the magnetite grain is anhedral and anisomorphic, shape anisotropy will dominate over crystalline anisotropy abobe T_i and will dictate the direction of the easy axis. The easy axis then will be along the long grain axis.

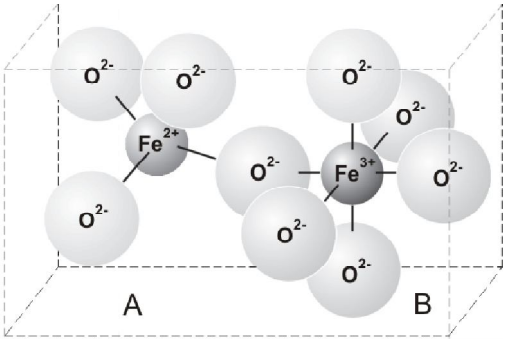

Figure 3-13. Coordinations of iron and oxygen ions in magnetite. A-sublattice divalent cations are in tetrahedral coordination and B-sublattice trivalent cations in octahedral coordination; modified after Butler (1992).

In titanomagnetites, Fe^{3+} is substituted by Ti^{4+}, and in order to maintain charge balance, one Fe^{3+} is replaced by Fe^{2+} ($2Fe^{3+} \rightarrow Fe^{2+} + Ti^{4+}$). Other cations in tmt, such as Al^{3+}, Cr^{3+}, Mg^{2+}, Mn^{2+} and Ni^{2+}, are present at a much lesser extent than Ti^{4+} and they are rather considered as impurities. The most common primary composition of titanomagnetite in basalt is TM60, which indicates a mole fraction of the ulvospinel component in magnetite of 0.6. Compared to pure magnetite, the substitution of Fe^{3+} by Ti^{4+} has a large impact on the structure, magnetic properties and behaviour of the minerals. Pure magnetite is ferrimagnetic with a Curie-Temperature (T_C) of 570 to 590 °C, depending on crystal impurities and lattice defects. M_S reduction by 25% and a T_C decrease of some 50 °C is caused by Al^{3+}-substitution (Tauxe, 2002, lecture 8). T_V, T_C and M_S (saturation magnetization) decrease strongly with increasing Ti-content. The magnetic susceptibility (MS) decreases with increasing Ti-content, which culminates with the antiferromagnetic ulvospinel. Moreover, the MS of tmt is strongly dependent on the magnitude of the applied field. Further effects of Ti-substitution are a slight increase in coercivity (H_C) and in the cell dimension.

The solid solution between magnetite and ulvöspinel is complete at temperatures around 1300 °C, but below 600 °C there is a broad compositional gap. Below this temperature, tmt unmixes or exsolves by solid-state diffusion of Fe and Ti cations producing composite grains made up of ferrimagnetic Ti-poor parts and parts of paramagnetic (Ti-rich) ilmenite. Intermediate tmt compositions are preserved in fast cooling magmas, but in slowly cooling ones, such as plutons, exsolution commonly occurs. This subdivision of tmt grains diminishes their effective size, which alters the magnetic properties.

Since (titano-)magnetite forms cubic crystals, it has a very low crystalline anisotropy. However, it can develop a strong shape anisotropy in non-isometric grains (see chapter 3.5). This is of particular interest when studying the low field magnetic susceptibility of tmt-containing rocks, i.e. in basalts. Furthermore, both the magnetic remanence and susceptibility are influenced to a large extent by the grain size of mt/tmt. Particularly, when measuring the anisotropy of the magnetic susceptibility in basalts with a large portion of SD magnetite/tmt, the interpretation of magnetic fabric orientation becomes complex (see chapter 4.1.2).

3.7.2 Haematite and ilmenohaematite solid solutions

Haematite (αFe_2O_3) is one of the end members of the titanohaematite/ilmenohaematite solid solution series with the generalized formula $Fe_{2-x}Ti_xO_3$. The parameter x ranges from 0 for haematite to 1 for ilmenite. After Soffel (1991), the end members of this series have limited miscibility when crystallizing from a melt. Consequently, natural solid solutions show compositions near one of the end members. Haematite forms rhombohedral, opaque crystals with a corundum structure: O^{2-} ions form close-packed hexagonal layers parallel with the basal plane (0001) and Fe^{3+}ions occupy 2/3 of the octahedral sites. Fe^{3+} layers in trigonal coordination alternate with the O^{2-} layers. The crystal structure is complicated by the fact that the O^{2-} layers deviate slightly from the close-packed arrangement (Ketteler, 2002). In contrast to mt/tmt, haematite has a strong crystalline anisotropy rather than shape anisotropy. Above the Morin temperature of -11°C (~262 K) atomic moments are coupled within the basal plane, perpendicular to the hexagonal c-axis (Bowles et al. 2010), and addidionally, nearly antiparallel between the layers. This slight deviation from 180° results in a net magnetization and, therefore, haematite`s magnetism is termed as canted antiferromagnetism or parasitic ferromagnetism. In places, haematite gains additional magnetization by a "defect moment" caused by lattice defects or crystal impurities such as non-magnetic cations. At the Morin temperature T_M, however, magnetocrystalline anisotropy changes sign and the spins then arrange parallel with the c-axis. Spin canting disappears since the spins in the sublattices are perfectly antiparallel below T_M, and haematite thus becomes antiferromagnetic (Bowles et al. 2010). Above the high Néel temperature T_N of about 675 or 680 °C haematite looses its magnetic ordering and becomes paramagnetic. Haematite is known to have a very high coercivity up to several 10^2 mT and a low saturation magnetization.

A primary titanohaematite/ilmenohaematite ($Fe_{2-x}Ti_xO_3$) solid solution series member in basalts is almost pure ***ilmenite*** $FeTiO_3$ with $0.8 < x < 0.95$. Beside titanomagnetite, ilmenite is the second most abundant primary oxide in basalts with Ti^{4+} layers alternating with Fe^{2+} layers. It forms trigonal-rhomboedric crystals with a rhomboedric to thick-tabular habit. Like haematite, ilmenite is dominated by crystalline rather than shape anisotropy. Within the basal plane (0001), magnetic moments are coupled parallel along (0001). Between the Fe-Layers coupling is antiparallel, which makes up the antiferromagnetic behaviour of ilmenite below its Neel-temperature of -218°C. Above this temperature ilmenite is paramagnetic.

Ti^{4+} substitution in titanohaematites follows the same mechanism as in titanomagnetites. Curie-temperatures are linearly dependent on composition. For $0.0 < x < 0.45$, titanohaematites show canted antiferromagnetism of haematite, but for $0.45< x < 1.0$ the magnetic behaviour changes and becomes ferrimagnetic (Butler, 1997). Soffel (1991) states that ferro(i)magnetic haemoilmenites only form in nature in conditions of rapid cooling. At these high Ti-compositions with $x > 0.45$, Ti-cations start to occupy alternate layers. Instead of occupying a separate Ti-layer they mix into the Fe-layer, thus, deregulating the cation ordering. As a consequence of the missing atomic moment of Ti^{4+}, the parallel coupling between the sublattices flips into an antiparallel coupling. Similar as with tmt, absolute miscibility is only given at high temperatures. Below about 800°C solid solutions become unstable and unmix into haematite with ilmenite lamellaes, yielding a tiger-striped grain.

3.7.3 Iron oxyhydroxides and iron sulfides

Oxyhydroxides such as goethite (αFeOOH) and lepidocrocite (γFeOOH) can occur as weathering product of pyrite (FeS_2) in minor quantities in igneous rocks. Goethite forms orthorhombic, antiferromagnetic crystals with a Néel temperature of 120°C, but natural goethite is commonly weakly ferromagnetic. Lepidocrocite forms cubic crystals and is paramagnetic at room temperature, but antiferromagnetic at very low temperatures with a T_N of -196°C (Butler, 1997) or after Hirt and others (2002) at 52 Kelvin.

As in the oxyhydroxides, iron sulphides play a subordinate role in basaltic rocks. A general chemical formula is given by FeS_{1+x} with $0 \leq x \leq 1$. The most common of these are the cubic, paramagnetic pyrite (FeS_2) and the monoclinic, ferromagnetic pyrrhotite (Fe_7S_8 to Fe_9S_{10}). After Dunlop and Özdemir (1997) natural pyrrhotite is a mixture of monoclinic ferromagnetic Fe_7S_8 and the hexagonal antiferromagnetic phases, such as Fe_9S_{10} and $Fe_{11}S_{12}$. They ascribe the ferrimagnetism of monoclinic pyrrhotite to cation deficiencies (Fe^{2+}) and vacancy ordering. The T_C of pyrrhotite is 320°C. During heating in argon atmosphere, pyrite can alter to magnetite plus pyrrhotite, while in air pyrite turns into haematite (Wang et al. 2008).

3.7.4 High temperature oxidation/ deuteric oxidation of Fe-Ti-oxides

High temperature or deuteric oxidation occurs in primary titanomagnetite and ilmenohaematite (ilmhm) during the original cooling of the igneous rock, when the FeTi-oxides are out of equilibrium with decreasing temperature and oxygen conditions. It is a typical solid state reaction, which occurs commonly above the Curie temperature (T_C) around 750°C (Butler, 1998) and is only avoided by rapid cooling and/or under pressure. During deuteric oxidation the Fe^{3+}/Fe^{2+} ratio increases at a constant Fe/Ti ratio, which shifts the composition to the right in the ternary diagram (Figure 3-12), parallel with the base line. Deuteric oxidation leads to a subdivision of the tmt grains by ilmenite lamellae along the [111] crystallographic planes of the host mineral. Simultaneously, an enrichment of the host tmt in Fe occurs, ending up with a near-mt composition, recognized for example by higher T_C in κ-T curves and for higher M_S. Intermediate tmt oxidation stages result in an intense intergrowth of ilmenite and Ti-poor titanomagnetite (e.g. Tucker & O'Reilly, 1980). This oxide grain diminution is followed by changes in magnetic properties, such as T_C, H_C and M_S. If grain diminution produces SD-magnetite, then the Verwey transition may be suppressed in temperature-dependent susceptibility (κ-T) curves. During advanced stages of deuteric oxidation haematite and rutile are produced from titanomagnetite. Advanced deuteric oxidation of ilmenohaematite yields rutile, haematite and sometimes pseudobrookite (Figure 3-12).

3.7.5 Low temperature oxidation/ maghemitization of titanomagnetite

Continued oxidation of titanomagnetite during cooling below 350°C (Özdemir, 1987) and at ambient surface conditions, or hydrothermal alteration can produce cation deficient spinels, termed titanomaghemite. These non-stoichiometric products of incomplete oxidation evolve by simultaneous diffusion of original Fe^{2+} out of the B sublattice, thereby creating octahedron site vacancies. In completely maghemized magnetite the valence of two thirds of the Fe^{2+} changed to Fe^{3+} and simultaneously one third of the original Fe^{2+} is removed. Chemically, the result of completely maghemized magnetite yields γFe_2O_3, which is compositionally equivalent to haematite, but retains the spinel structure. Compared to magnetite, maghemitized grains have a slightly lower susceptibility and a slightly lower M_S resulting from the Fe^{2+} removal, a lower saturation remanence and NRM, but a higher coercive force and coercivity of remanence (Cui et al., 1994 and references therein). Maghemitization is accompanied by a volume loss, which may result in grain-internal tension and shrinkage cracks. Maghemite (mgh) and titanomaghemite (tmgh) are metastable and can be identified upon heating by measuring the temperature-dependent susceptibility. At temperatures of 300 to 500°C the crystal structure of maghemite transforms irreversibly to a hexagonal array, equal to that of haematite (αFe_2O_3). This transformation is marked by a significant drop of susceptibility in the cooling run and by the irreversibility of the curve itself. Furthermore, the Verwey transition is suppressed in maghemite. Only minor surface maghemization (oxidation) of mt is sufficient to lower and/or suppress the transition (Stacey and Banerjee, 1974; Özdemir et al. 1993). During heating titanomaghemite becomes unstable at

around 250-300°C. Before reaching its T_C the titanomaghemite inversion forms a multiphase intergrowth with a phase assemblage depending on composition (Ti- and Al-content) and the degree of oxidation of the parent tmgh, according to Özdemir (1987). Özdemir (1987) found that for low oxidation states ($0.25 < z < 0.43$; where z is an oxidation parameter varying between 0 and 1, for no or complete oxidation, respectively) near stoichiometric tmt and a rhombohedral phase near ilmenite is produced, while for moderate to stronger oxidation ($0.5 < z < 0.8$) a magnetite near spinel, and rhombohedral phases haemoilmenite and anatase are produced. In contrast, highly oxidised TM60 with $z = 0.9$ inverts to haematite and anatase, with no spinel phase produced (Özdemir, 1987).

4 Methods

Magma flow directions within the dyke rocks were investigated in this study mainly by employing three different methods: the anisotropy of magnetic susceptibility, the anisotropy of magnetic remanence, and image analysis of mineral grains in thin sections. The first two methods concern the magnetic fabric of the basalts and mainly examine the distribution of orientation of strongly magnetic minerals such as iron-titanium oxides and –hydroxides. In contrast, with the image analysis the fabric of the early crystallizing silicate minerals plagioclase and pyroxene was studied. For an accurate interpretation of the magnetic data, attendant investigations of the mineralogy were performed, including temperature-dependent susceptibility, alternating field demagnetization, hysteresis measurements, reflected- and transmitted-light microscopy. Because of the large number of samples, these complementing measurements have been performed on selected ones. The sample selection was on one hand driven by the intention to 1.) investigate all subgroups of HOD samples which were classified during the study on the base of magnetic or other properties, and on the other hand 2.) to compare the results of different attendant investigations for the same sample. In particular, alternating field demagnetization and hysteresis measurements were done complementary and comparatively, as both yield on the domain-size information and coercivity ranges. In individual cases, detailed examination of one sample was undertaken, at places also counterchecking.

4.1 Anisotropy of low-field magnetic susceptibility

The anisotropy of the low-field magnetic susceptibility (AMS) method is a very sensitive tool for determining the magnetic fabric orientation of a rock.

The magnetic susceptibility (MS) of a rock reflects the three-dimensional spatial distribution (Hargraves et al., 1991) of magnetic mineral grains. The recorded susceptibility is an average of all rock components, depending on their intrinsic susceptibility and volumetric abundance in the rock. In many rocks the low field anisotropy of magnetic susceptibility (AMS) results from a mixture of several superimposed effects related to the variety of minerals and their preferred orientation. Anisotropy can arise from oriented minerals with specific crystalline anisotropy (chapter 3.5; predominantly in paramagnetic minerals; e.g. Soffel, 1991, de Wall, 2005), from grain shape anisotropy of minerals with strong self-demagnetization (chapters 3.4 & 3.5; predominantly ferrimagnetic minerals, e.g. Soffel, 1991, de Wall, 2005) and from magnetostatic interactions between anisotropically distributed ferrimagnetic minerals (Stephenson, 1994; Cañon-Tapia, 1996; Borradaile, 2001). Due to large differences in magnitude of the magnetic susceptibility of the various mineral species, a rock's bulk susceptibility can be, and commonly is, dominated by only one strongly magnetic phase. This is commonly the case in igneous rocks, where the ferrimagnetic titanomagnetite (tmt) dominates if its volume exceeds 0.1 percent of the bulk rock content (Tarling & Hrouda, 1993). Other ferromagnetics such as titanomaghemite and pyrrhotite, and/or the antiferromagnetic minerals haematite and goethite, if abundant enough, may also play a role, while the contribution of para- and diamagnetic minerals such as ilmenite, pyroxene or plagioclase to the overall MS signal is typically minor to negligible (Tarling & Hrouda, 1993).
Titanomagnetite has cubic symmetry and is crystallographically isotropic, but nevertheless, it has been shown to cause susceptibility anisotropies in natural basalts (see chapter 4.1.1 for references). As described in chapter 3.7.1, titanomagnetite's preferred (easy) axis of spontaneous magnetization is the long axis in elongate grains, or the body diagonal in euhedral cubic crystals (which is identical with the crystal's long axis). Therefore, the principal susceptibility directions in tmt are controlled by shape anisotropy in non-isometric grains. The preferred orientation of elongate multi-domain ferromagnetic minerals (tmt) in rocks is the most obvious source of magnetic anisotropy and was the first to be discovered. Since Khan (1962), the AMS of igneous rocks has been attributed almost exclusively to this effect for as long as 18 years.

But how do titanomagnetite grains in a rock acquire a preferred orientation or get distributed anisotropically? Many studies of anisotropy of magnetic susceptibility (AMS) in lavas, dykes and sills are based on a deterministic approach (Cañon-Tapia, 2004), which assumes that during magma flow, suspended elongate early crystals become aligned with their long axes parallel with the flow direction. In

basaltic rocks (but not in subduction zone basalts, pers. com. K.-H. Stosch), titanomagnetite is commonly a late crystallizing phase, occupying the interstices between earlier crystallised phases (plagioclase and pyroxene) or their edges and thus mimics the silicate fabric. In particular in dykes, tabular minerals like plagioclase are assumed to be oriented with the two long axes in the dyke plane and the short one perpendicular to the dyke walls. A more detailed consideration of magma flow in dykes, including the effects of magma viscosity and the velocity gradient of flow between the dyke margins and the centre, predicts a shear deformation which may produce an opposed imbrication of the long axes pointing in the flow direction (Cañon-Tapia & Chávez-Álvarez; 2004).

4.1.1 Historical account of AMS application to magma flow in dykes

According to the review of Martín-Hernández and others (2004), the use of AMS has a nearly 70 year-old history up to the present date. In 1954, Graham published a paper advocating the method as a rapid and sensitive petrofabric tool and the technique became standardized as the first measuring instruments, the susceptibility/kappa bridges, of Fuller (1960), Girdler (1961), Graham (1964) and Jelínek (1973) appeared (Martín-Hernández, 2004).

The following brief history of AMS applications to lava flows and dykes has been compiled by Cañón-Tapia (2004) and references are given therein:

Stacey (1960) established some fundamental principles for magma flow in dykes. He remarked that flow in partially solidified magma and deformation in solid rocks normally produces mineral alignments, which can be obvious as lineation or foliation. He also pointed out that even if magnetic minerals formed after the alignment process (flow, deformation), their shape and distribution may be controlled by the alignment of other, already crystallized minerals.

Khan (1962) found a direct correlation of the AMS with the preferred orientation of long axes of magnetite grains. He suspected that variation in anisotropy resulted from the degree of preferred orientation. But he misinterpreted the magma flow direction as being parallel with the intermediate principal susceptibility axis (κ_{int}), a long period of confusion in AMS studies followed. There was no consensus about which of the principal susceptibility axes actually represents the magma flow direction and how this can be proven (see Cañón-Tapia, 2004 for references).

Knight and ***Walker (1988)*** succeeded in breaking through this general controversy with their AMS results from Hawaian dykes. Additional magma flow indicators, in particular lineations on the dyke walls, but also elongated vesicles and imbricated sheet joints allowed them to determine magma flow directions independently and to compare these with the AMS results. These comparisons proved the consistency of flow directions with the magnetic lineation/long fabric axis (κ_{max} or κ_1). Almost all AMS studies after this publication (see Cañón-Tapia, 2004 for references) adopted the assumption that κ_{max} lies within the dyke plane (horizontal, vertical or inclined) and κ_{min} normal to it.
Knight and Walker (1988) also recognized a paired clustering of ***symmetrical κ_{max} imbrications*** (symmetry plane in the dyke centre parallel with dyke plane) ***near to the dyke walls*** (Figure 4-14 b). Each of the two κ_{max} clusters is consistent with the orientation of the dyke wall surface lineation. Departures of the κ_{max} orientation from the dyke plane are in the range of 5 to 30° (Figure 4-14 b) and attributed to shear within the magma caused by the velocity gradient between the dyke margins and the centre. The authors attributed the opposed κ_{max} imbrication to an aligned clustering of platy or prolate magnetic minerals near the dyke walls during laminar magma flow. The sense of imbrication relative to the dyke walls is inferred to be a unique relation, dipping back towards the magma source, giving the absolute flow azimuth (sense of flow; Figure 4-14 b).

In some cases, as for example in very oblate fabrics where κ_{max} and κ_{int} readily exchange, it has been suggested that flow directions can be determined with the help of the κ_{min} axis (Halvorsen, 1974; Geoffroy et al., 2002) being normal to the flow plane. Geoffroy et al. (2002) suggest the flow vector of oblate fabric samples to be normal to the axis of intersection between the magnetic foliation determined near or at each dyke wall and the dyke wall itself (Figure 4-14 c).

Wolff et al. (1989) and Hargraves et al. (1991) raised doubts that the shape anisotropy of magnetite is reflected in the AMS results because almost all titanomagnetite grains in their studies were equant/isometric. Both studies proposed that magnetic interaction between close neighbouring crystals

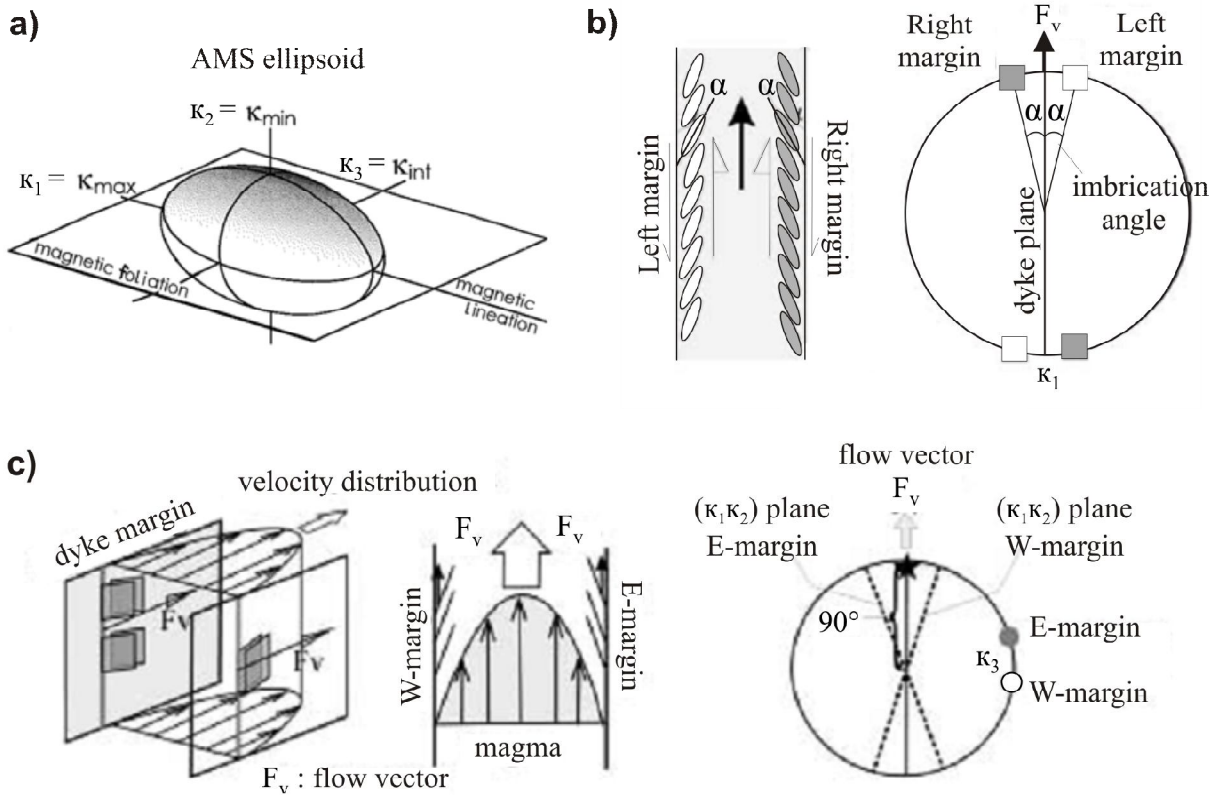

Figure 4-14. a) Magnetic fabric or AMS ellipsoid after De Wall (2005) and determination of magma flow direction in basaltic dykes from AMS data: b) for prolate fabrics from the imbrications of κ_{max} at the dyke walls after Knight and Walker (1988) and c) for oblate fabrics after Geoffroy et al. (2002): flow vector is normal to the axis of intersection between the dyke wall and the magnetic foliation determined near or at each dyke wall. Upper & lower right: equal area projections of AMS data.

accounts for the measured susceptibility anisotropies. A few years later, it was confirmed by Stephenson (1994) that large degrees of anisotropy can be produced by ***magnetic interaction of isometric grains***. It was shown that AMS reflects the shape of grain clusters if the separation between individuals is less than about twice the grain diameter (Cañón-Tapia, 1995). Numerical modelling results of Gaillot et al. (2006) show that magnetic interactions are at maximum, when the particles are touching and become insignificant, as soon as the grain separation distance falls below one quarter of the particle size. Also, magnetic interaction in grain clusters or between close grains can override shape anisotropy of aligned individual particles (Cañón-Tapia, 1995; (Cañón-Tapia, 1995). Hargraves et al. (1991) suggested that the AMS of basalts rather reflects magnetically interacting late crystallized equant tmt grown along the edges of previously flow-oriented phenocrysts. Summing up, AMS controlled by ferromagnetic minerals in igneous rocks can be explained by shape anisotropy of individual magnetite grains or of grain clusters formed by magnetostatic interaction between isometric grains.

However, in many AMS studies (e.g., Raposo & Ernesto, 1995 and more references in Cañón-Tapia, 2004), there is a variable percentage of samples, even in the Hawaiian dykes, where the orientation of principal susceptibility axes departs from the expected 'normal' pattern. A complex relation between the magnetite long and short axes and the maximum and minimum principal susceptibility axes was recognized by Potter and Stephenson (1988). They discovered that the correspondence between long

grain axis and maximum susceptibility axis is only valid for multi-domain (MD) magnetite grains, whereas the reverse relation applies to single-domain (SD) grains, where the long grain axis corresponds to the minimum principal susceptibility axis (***SD***-or ***single domain effect***; see also chapter 4.1.2.). Later studies often attributed AMS fabrics with κ_{min} parallel and κ_{max} normal to dyke walls to the SD-effect (see chapter 5.1.4; Rochette 1988, 1991, 1992). Rochette et al. (1992) term this reverse axial arrangement ***'inverse' fabric*** because of the switched axes. Samples, which are neither normal nor inverse, but with κ_{int} being normal to the dyke plane are described as having '***intermediate'fabrics***. Another type, occasionally referred to as ***'oblique' fabric*** with no or only one principal axis in the dyke plane, is interpreted to be transitional between the inverse and intermediate type (Hrouda, 2002). Finally, cases of magnetic fabric have been described, where none of the principal susceptibility axes lies within the dyke plane, also termed 'oblique' in the present study, or where the axes of several specimens drilled from one block sample or at a single locality scatter ramdomly. Axial scatter is commonly attributed to turbulences during flow.

Inverse, intermediate and oblique fabrics are often summarized by the term '***anomalous' fabrics***. Explanations for the development of 'anomalous' magnetic fabrics other than the SD-effect have mainly been sought for in factors unrelated to magma flow, including the superposition of secondary fabrics acquired during post-emplacement processes, such as hydrothermal alteration (Rochette et al., 1991), metamorphism or tectonic overprints. Park et al. (1988) invoked tectonically- induced changes in the domain structure of magnetite grains for an observed κ_{int} - κ_{min} shift. Tectonics have also been invoked to rotate the whole rock body and consequently also AMS directions (Perroud et al., 1991). Post-emplacement processes in a still-liquid magma intrusion, such as melt convection, bubble rise crystal settling, and growth of minerals normal to the dyke walls have been interpreted to have changed the fabric before final solidification (e.g. Raposo & Ernesto, 1995). As cited previously, in the case of inverse (and also for some intermediate and oblique) fabrics, the SD-effect has been invoked (Rochette et al. 1991, 1992), although in many tests for SD tmt, this hypothesis could not be confirmed or at best gave hints for a mixture of SD and MD (titano-)magnetite (for references see Cañón-Tapia, 2004). Alternatively, anomalous fabrics can also develop when the particle concentration is high, such as the transitional between solid state and suspension flow (Nicolas, 1992).

Instead of analyzing dyke samples individually, another approach to explain anomalous fabrics considers fabric symmetry in profiles across the dyke thickness. The recognition of ***dykes with asymmetric magmatic and magnetic fabrics*** by Tauxe (1998) motivated Correa-Gomes et al. (2001) to develop 2 D models for vertical magma emplacement in dykes with synchronous wall-rock displacement influencing the flow fabric depending on the rate and direction of tectonic shear and of magma flow (Figure 4-15). Asymmetric AMS fabrics in dykes are further reported from Aubourg et al. (2002), Clemente et al. (2007), Féménias et al. (2004) and Poland et al. (2004), who support the suggestion of Correa-Gomes et al. (2001) to relate them with ***tectonic shearing of the dyke walls*** synchronously with magma intrusion.

In and after the mid- 1990s the interpretation of varying susceptibility axes became more advanced in two ways. First, post-solidification processes were given less importance for the reoriention of AMS fabric unless there was evidence for fabric changes. Second, along with AMS, other petrofabric indicators were analysed and compared with the magnetic data. In general, two different approaches were applied: the deterministic and the systematic-variation approach (Cañón-Tapia, 2004). The deterministic approach makes the assumption that the orientation of principal susceptibility axes remains constant during flow and that a certain susceptibility axis points along the flow direction. All studies cited previously in this chapter follow this idea. The other approach includes all aspects of Jefferey's equations (Jefferey, 1922), who derived equations for the motion of a suspended elliptical particle in a steady-state, slow moving viscous fluid. Jefferey's model predicts a cyclic movement of the symmetry axis of any particle represented by a rotational ellipsoid (Cañon-Tapia & Chávez-Álvarez; 2004; Cañon-Tapia 2004). Consequently, systematic variations of the principle susceptibility axes and the degree of clustering occur, which bear a close relationship with the three-dimensional deformation the magma experiences during flow. These variations depend on the particle's position within the flow and on its movements introduced by the flow geometry. Jefferey's equations are valid for mechanically non-interacting particles suspended in a viscous Newtonian fluid.

The cyclic particle movement predicted by Jeffery (1922) leads to a systematic and periodic change in the directions of the principal susceptibility axes. Experiments clearly show, in contrast to the assumption made in many AMS studies (see introduction to this chapter), that κ_{max}, κ_{int} and κ_{min} have no unique relation to the direction of magma flow and all magnetic fabrics, including the "anomalous" ones, can theoretically be explained by cyclic movement of elliptical particles during flow.

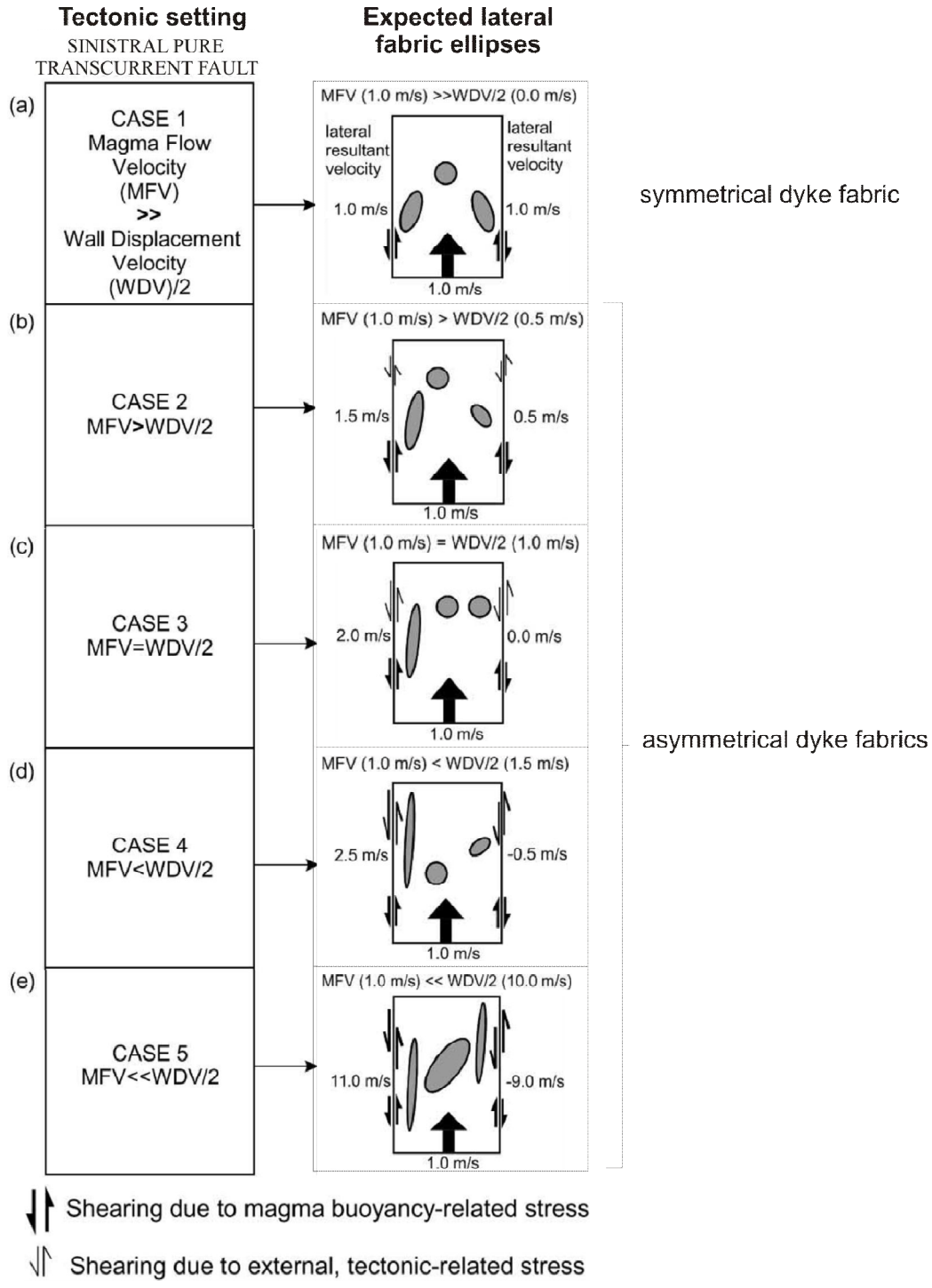

Figure 4-15. 2 D models for symmetrical and asymmetrical dyke fabrics after Correa-Gomes et al. (2001) with magma emplacement during synchronous wall-rock displacement (shear). Flow fabric depending on rate of external shear or wall displacement (WDV = half of the wall displacement velocity) versus rate of magma flow (MFV 0 Magma Flow Velocity). WDV increases from a) to e) while MFV is constant.

In 1997, Jefferey's equations were applied by Dragoni et al. (1997) to the AMS technique. They modelled a sill-like geometry in 2-D assuming steady-state laminar flow of a Bingham fluid (i.e., constant viscosity and increasing shear rate), driven by a pressure gradient. Suspended titanomagnetite crystals considered to produce magnetic anisotropies by grain shape anisotropy, were modelled as three-dimensional prolate ellipsoids. The ellipsoids determine the three-dimensional anisotropy of the susceptibility with the principal axes κ_{max}, κ_{int}, κ_{min} or κ_1, κ_2, κ_3 (Figure 4-14 a; see chapter 4.1.2). For these conditions, the authors determined the orientation of a large number (197) of rigid ellipsoidal particles with a uniform distribution of initial orientations immersed in fluid as functions of time and strain. It was shown that the spatial orientation of prolate ellipsoidal grains depends on (1) the initial particle orientation, (2) the amount of strain and, therefore, of its position relative to the sill walls, and (3) the duration of strain (cooling time), all of which can vary throughout a tabular magma body. It was found that all three principal susceptibility axes systematically change their positions with respect to the magma flow direction. Magnetic lineation was found to oscillate periodically in the vertical plane around the flow vector with an angular difference of 45°. Although the horizontal orientation prevails over time, magnetic foliation flips from the vertical to the horizontal plane as a function of the particles' shape ratio. The more equant the particles are, the more frequently does the foliation end up in the vertical plane, because minimum and intermediate susceptibility axes exchange. Dragoni et al. (1997) compared the modelling results with the magnetic fabric of the Ferrar dolerite sills in East Antarctica, and found good agreement. They concluded that the magnetic lineation is a good flow marker in contrast to the foliation, which can be parallel or perpendicular to the laminar flow plane.

Cañon-Tapia and Chávez-Àlvarez (2004) extended the study of Dragoni et al. (1997) to a wider range of particle shapes and to variable initial distribution and orientation of particles. Integrating these results, they derived a model of magma flow which includes the unequal distribution of shear deformation in a tabular intrusion such as a dyke. The model of predicted elliptic particle movements were run in full cycles of particle rotation and the degree of clustering susceptibility axes was analysed after various steps during the cycle. The authors showed that particle shape as well as the amount of shear influence the quality of AMS results. The models were run with prolate and oblate particles separately, and almost the same axial distributions were generated by both. However, the axial ratios of the particles play an important role. Strong contrasts in fabric were created when changing the axial ratio and/or the degree of grain clustering. For example, a closer grouping of κ_{max} axes was achieved with more elongated particles compared to equant ones, and the "correct" sense of κ_{max} imbrication relative to dyke geometry crucially depends on the axial ratio. Only cases of very elongate grains (axial ratio 1:10) of "perfectly prolate/oblate ellipsoids of revolution" consistently achieved the correct sense of imbrications (incorrect sense: 180° opposite to flow direction). With less elongate particles (e.g. ratio 3:10) the wrong imbrication is produced for half the time that it takes to complete one full cycle of particle rotation. Furthermore, because shear deformation in viscous magma is a function of the position within the magma body and the duration of exerted shear, large dispersion of susceptibility axes is possible independent of the particles' axial ratio.

Cañon-Tapia & Pinkerton (2000) used experiments to obtain a more detailed relationship between the flow regime and the AMS. They showed, for example, that when high-temperature lava stops flowing, the magnetic fabric is lost because the low magma viscosity prevents the fixing of microlite orientation acquired during flow. If lava cools more rapidly, fabrics can be preserved, and the degree of anisotropy relates to flow deformation. The experiments also demonstrated that samples with switched susceptibility axes can coexist within only a few centimetres.
However, Ildefonse et al (1992) and Arabet et al. (1996, 1997) pointed out that all these models only apply when particles do not interact mechanically. Otherwise their interactions may control the fabric development, where tiling structures may evolve and imbrications along the direction of deformation can result. If particles of different shape interact, subfabrics can develop.

During the past decades of AMS studies, a transition from a simple deterministic model to a more complicated model has occurred. The basis for interpretation of flow direction varies from the magnetic lineation (κ_{max}) to the imbrications of the lineation to the magnetic foliation (κ_{max} - κ_{int}) and its imbrications.
Potential influences on primary magmatic fabrics producing anomalous fabrics are diverse ranging from primary geological processes over secondary overprints to grain size effects (SD-effect). Alterna-

tively, models have been developped to explain all fabric types by cyclic variations of particle orientation during magma flow as a function of the flow regime without need for any further post-emplacement process. This introduces an uncertainty to AMS interpretation because it shows that there is a non-uniqueness of orientation of the principal susceptibility axes along flow and a careful analysis is necessary.

4.1.2 Measuring procedure

The anisotropy of the low-field magnetic susceptibility, measured on each specimen before any other of the magnetic treatments is done, is referred to as ***(initial) AMS*** or $\boldsymbol{AMS_{INITIAL}}$.
The AMS can be assessed by exposing a rotating rock sample to an external magnetic field while measuring the magnitude of induced MS in different directions. From the MS data recorded in all directions, a three-dimensional MS-magnitude ellipsoid (Figure 4-14 a) is computed, reflecting the AMS of the bulk material.

For the AMS measurements, an average of 6 to 12 oriented standard rock cylinders with 2.5 cm in diameter and 2.1 cm in height were drilled and cut in the laboratory. These dimensions result in a width-to-height ratio of about 1.2, which reduces the influence of sample shape on the orientation-dependent variation of the sample's Demagnetizing Factor (N). With this shape ratio, the cylindrical specimens geometrically approach the ideal case of a sphere, wherein N is equal in all directions. Thus, anistropies induced by the sample shape are avoided.

Both the drilling machine and the rock saw are water-cooled in order to avoid heating of the samples and an unwanted overprint of secondary remanences. The devices work with special non-ferrous diamond bits and saw blade in order to avoid contamination of the samples with magnetic material.

The anisotropy of magnetic susceptibility κ (Kappa) is measured at room temperature in a low magnetic field (H) of 300 A/m and at a frequency of 875 Hz with a KLY-4 Kappabridge from AGICO, Brno (Jelinek, 1980; Hrouda, 1994). The instrument works as a fully automatic inductivity bridge with a sensitivity of 2×10^{-8} SI. Before inserting the specimen into the measuring coil, the instrument is zeroed. During the measurement the sample is spinning slowly and the magnetization M is measured various times in each plane perpendicular to the axis of specimen rotation (Hrouda, 2009). Since in low fields < 1 mT, the magnetization as a function of the applied field is linear, the bulk (volume) susceptibility κ_{bulk} is calculated by: $M = \kappa_{bulk} H$.
However, for titanomagnetite, Jackson et al. (1998) and de Wall (2004) found that the transition to non-linearity is already reached at 100 A/m. Thus, for titanomagnetite, the magnetic susceptibility depends on the field`s magnitude.

For AMS measurements, the specimen is adjusted into the automatic holder of the Kappabridge and measured in three perpendicular positions. At the end of the ca. two minutes of measuring time, additionally κ_{bulk} is determined. Finally the measuring software calculates the second rank susceptibility tensor for the specimen with a known volume. Geometrically, this tensor can be visualized as an AMS ellipsoid with the three orthogonal principal axes: κ_{max} or κ_1, κ_{int} or κ_2, κ_{min} or κ_3. The orientation and relative length of these axes is given referred to both geographic coordinates and separately to the specimen. κ_{max}, the long axis of the AMS ellipsoid, represents the magnetic lineation and together with κ_{int} spans the plane of the magnetic foliation. κ_{min} as the short axis corresponds to the pole of the magnetic foliation plane. Additionally, the mean susceptibility value is calculated by:

$\kappa_{mean} = (\kappa_1+\kappa_2+\kappa_3)/3$ (e.g. Tarling and Hrouda, 1993, de Wall 2005)

in SI units. Furthermore, the instrument software (SURFAR) creates a variety of parameters to describe the shape of the AMS ellipsoid. Its degree of eccentricity, for instance, is expressed by the parameter P_j or also P' (Jelinek, 1981), the corrected anisotropy degree, defined as:

$$P_j = \exp\left[2(\ln \kappa_1 - \ln \kappa_{mean})^2 + (\ln \kappa_2 - \ln \kappa_{mean})^2 (\ln \kappa_3 - \ln \kappa_{mean})^2\right]^{1/2}.$$

This equation expresses the deviation of the ellipsoid axes from a perfect sphere in all 3 spatial dimensions while $P = \kappa_3/\kappa_1$ (Nagata, 1961) only considers the axial ratios of two of them (de Wall 2005). In

this study, P_j or P' is utilised synonymously for "degree of anisotropy". T is the shape parameter, varying from +1 for a perfectly oblate (disk-shaped) ellipsoid to –1 for a perfectly prolate (rod-shaped) one (Jelinek, 1981). The shape parameter T is calculated by:

$T = (2\ln \kappa_2 - \ln \kappa_3)/(\ln \kappa_1 - \ln \kappa_3)$.

Axial ratios of the AMS ellipsoid axes are the lineation factor L with $L = \kappa_1/\kappa_3$, and the foliation factor F expressed by $F = \kappa_2/\kappa_3$

The geographical orientations of the 3 principal susceptibility directions of the AMS tensor κ_1, κ_2, κ_3 within one sample's specimens are displayed as lower hemisphere projections in a stereonet together with their Jelinek(1978) tensor means (calculated by the programmes Anisoft 4.2, AGICO Company or StereoNett Version 2.46; J. Duyster, Univ. Bochum), the mean confidence angles and the great circle of the particular dyke. The confidence angles define the statistical accuracy of the determination of the individual principal susceptibilities directions using the Jelinek (1978) tensorial mean method on the (block) sample level on the 95% level of significance (AGICO 2009, MFK1-man, User's Guide). The direction determined on a cylindrical specimen (drilled from the block sample) is weighted by the corresponding anisotropy ratio: nearly isotropic data do not influence the statistics (Rochette et al., 1999). If the susceptibility is large, reliable axial orientations can be obtained down to an anisotropy of 1.001 (0.1%; Rochette et al., 1999).

AMS_{AFD}

After demagnetization in an alternating field (AF) the AMS has been measured for a second time, then referred to as AMS_{AFD}, on 152 specimens selected from 48 samples. 2 to 5 specimens have been measured per sample. This partial demagnetization is called "magnetic cleaning", because it erases secondary remanences, such as the viscous remanence. Secondary remanences may be acquired long after rock formation (e.g. magma cooling) in magnetic fields oriented differently from the field existing during rock formation and may overprint or deflect the primary thermoremanence (acquired during magma emplacement/cooling). Also, secondary remanences can be much stronger than the original NRM (e.g. a lightning-imprinted isothermal remanence).
The measurement of AMS_{AFD} was considered necessary in order to exclude NRM influences on AMS vector after recognizing explanation difficulties when comparing the orientation of $AMS_{INITIAL}$ and AARM fabrics. Since this was at the end of the study, not all samples could be remeasured. Since the potential NRM vector influence is not considered in most AMS studies it was not planned for in the early stage of this study, and only later was the effect tested on selected samples having particular properties: high NRM, high Koenigsberger ratio, anomalous AMS fabric or anomalous AARM fabric. The results are presented and discussed in chapters 8 and 9 because the relevance is mainly on the vector orientation and its comparison with the $AMS_{INITIAL}$ vector.
Most of the AMS_{AFD} measurements have been done after the AARM measurements, where the specimens were demagnetized by tumbling in a field of 100 mT (rarely 200 mT) in the LDA5 AF Demagnetizer (AGICO, Brno). The few specimens, that have been demagnetized stepwise in order to determine the medium destructive field (MDF), and that have not been measured for AARM afterwards, were demagnetized statically in three directions in peak alternating fields of 160 mT (see chapter 4.5). The effect of the demagnetization is an orientational randomization of the magnetic domains within the multi-domain and pseudo-single domain particles. All magnetic particles with coercivities below the applied peak alternating fields are affected by the cleaning.

SD- or Single-domain- effect

In samples with mt/tmt as the carriers of the magnetic susceptibility, the grain size, or more precisely, the domain state, is of importance for the interpretation of the directional AMS data. As mentioned previously in this chapter, the magnetic behaviour of ferromagnetic (s.l.) minerals, in particular (titano-)magnetite, is domain state-dependent. The AMS of a magnetite multi-domain (MD) grain would perfectly reflect the grain shape or crystalline anisotropy, but the signal of an elongate single-domain (SD) grain is inverse. The easy axis of magnetization in mt is always the long grain axis and the hard direction is the shortest axis. Thus, the magnetic moment in a SD mt grain will be directed along the long grain axis. Consequently, in an uniaxial prolate SD grain the long (easy) axis is already magneti-

cally saturated. Applying a magnetic field in this direction will not have any effect and measured susceptibility along this axis will be zero (Daly 1970, O'Reilly 1984, Stephenson et al. 1986). As a consequence, in the AMS data the grain's long axis κ_{max} or κ_1 will be defined as κ_{min} or κ_3 (Hrouda, 1982; Potter and Stephenson, 1988), an effect that Rochette (1992) termed *inversion*. Fabrics with this phenomenon are termed *inverse*. In samples with large portions of SD magnetites/tmts, therefore, κ_1 and κ_3 can be inverted. For this reason accompanying grain size investigations of titanomagnetite are performed. Even 20 vol% of SD-tmt particles is sufficient to change a normal AMS fabric by exchange of κ_2 and κ_3 into an *intermediate* fabric, as model calculations of Ferré (2002) demonstrate.

4.2 AARM – Anisotropy of anhysteretic remanent magnetization

The anhysteretic remanence (ARM) is an artificial magnetization. It affects exclusively hysteretic trace minerals such as ferrimagnetic titanomagnetite, -maghemite, pyrrhotite and antiferromagnetic haematite and goethite. Remanence susceptibility is much higher for ferri- than for antiferrimagnets and depends on the grain size: it is much higher in single-domain magnetite than in multi-domain grains, by up to two orders in magnitude (Jackson, 1991).
In the present study, the AARM has mainly been applied in order to investigate the origin of the anomalous AMS fabric types (II to IV, see chapter 7.5). The method allows to separate the ferromagnetic (s.l.) rock fabric component from the paramagnetic one (e.g. Hrouda, 2002), since only ferromagnetic particles are able to store a remanent magnetization. Further, it allows to test, whether prolate SD-titanomagnetite influences the AMS fabric of some samples, since the AARM is insensitive to single-domain (SD) effects, unlike the AMS. A comparison of AARM and AMS ellipsoids (directional results) can reveal the single-domain mt/tmt component (e.g. Borradaile and Gauthier, 2003; Potter, 2004). AMS fabric type III samples are expected to reveal fabric type I in AARM analysis when dominated by elongate SD grains oriented with the long axes along the MD longest axes.

An AARM is imparted by exposing the samples simultaneously to an alternating field (AC) and a steady magnetic field (DC) of lower intensity. The acquired ARM is usually parallel to the steady field and its intensity depends on the magnitude of both applied fields (Stacey & Banerjee, 1974). For small DC fields, the ARM is linearly related to the field and the ARM susceptibility is independent upon the applied field, but not for the DC fields of 50 μT and more (Tauxe, 2013), such as the ones applied here (100 or 500 μT).

For the AARM method, cylindrical samples are magnetized in distinct directions by the Anhysteretic/Pulse Magnetizer PAM1 and then tumblingly demagnetized in steps with the LDA5 AF Demagnetizer, both instruments from AGICO, Brno. After every magnetizing step, the imparted magnetization is measured and recorded with a JR5A spinner magnetometer. The entire measurement procedure starts with the demagnetization of the rotating and tumbling sample inside a shielded coil in a smoothly decaying peak alternating field of 100 (rarely 200) mT. In this way, the stored natural or earlier imparted remanent magnetization is removed (at least to a large extent). That means, the magnetic moments of all particles with coercivities below 100 (200) mT are randomized and do not contribute to the net remanent magnetization anymore. Afterwards, the specimen is remagnetized in the first position in a weak AC field of 20, 30, 40 or 50 mT, superposed by a DC bias field of 100 or 500 μT. The remanent magnetization vector thus acquired is measured and recorded with the spinner magnetometer. For the next step, the cycle restarts with the sample`s demagnetization in AF fields slightly higher than the magnetizing AF fields, that is 30, 50 or 80 mT. A remagnetization in the second position then follows.
After magnetizing in 6 positions, the three-dimensional vector of anhysteretic remanence is computed from the 6 partial measurements. Since this calculation is based on small differences in the remanence magnitude for the 6 directions, the complete cancellation of RM before measurements and before every step of remagnetization is required. If an initial cancellation is not achieved with the applied field (100 or 200 mT) because of a distinct content of magnetically "hard" (highly coercive) components, a residual vector R remains. If R is large with respect to the range of directional remanence differences, it will influence the direction of the ARM tensor.
Ideally, the magnetization is imparted in six directional pairs, giving 12 directions of antiparallel components. Applying this measurement design, opposite directions are subtracted from each other and the residual vector R is eliminated when calculating the final 3d-AARM ellipsoid.

The 12-direction measurement scheme (mode A) takes twice as long (40 min per specimen) as the 6-position measurement mode B. Therefore, mode B was used for most specimens, but with the disadvantage of potentially uncompensated residual RM vectors. In order to overcome this problem, it was reasonable to keep the difference between magnetized state and demagnetized RM-vector (M-D) at least 10 times larger than the residual vector by adjusting the AC/DC fields for individual specimens. However, in order to save time, this was not tested for every specimen and every sample before the measurement. Later, during data processing, large residual vectors were recognized for some specimens/samples (marked in the results table and in the stereonets) suggesting that the orientation of their ARM vector may be influenced by R.

The appropriate field strengths were determined by pilot tests before the measurements, in order to check the range of their coercivity spectra. For that purpose one low- and one high-coercive specimen were magnetized in a DC-field of 500µT and superposed AC-fields increasing stepwise from 0 to 100 mT. Afterwards they were demagnetized in precisely the same descending steps, in order to recognize at which fields the specimens reach a high level of magnetization and at which level it disappears. It turned out that low coercive specimens are magnetized in relatively low AC fields of about 20 to 30 mT and are easily demagnetized in only slightly higher fields of about 40 to 50 mT. High coercive specimens need AC fields of 50 mT or much more (>100mT) to be magnetized and, consequently, even higher fields to be demagnetized.
It was concluded that specimens with higher coercivities and small differences in remanence magnitude (3 to20 times) between magnetized and demagnetized state were measured in 12 instead of 6 different positions.

Normally, AARM measurement of at least 5 cylindric specimens is necessary for statistical significance of the directional results in the software ANISOFT 4.2 (AGICO, Brno). However, in order to test as many samples as possible for their AARM, the specimen number was reduced during the measurement campaign to only 2 or 3 cylinders per sample.

Two specimens were also tested for their magnetic viscosity and its possible influences on the measurements. This was found to be sufficiently small to be neglected.

4.3 Image analysis

Image analysis was performed in order to investigate the orientation of silicate minerals and to compare the silicate fabric orientation with the magnetic fabric orientation. Because this method is very time-consuming, analysis of the silicate fabric was limited to three samples. The objective was to quantify the shape-preferred orientation (SPO) of inequant silicate minerals such as plagioclase and in some cases also pyroxene. In contrast to the AMS and AARM methods, image analysis was done on two-dimensional oriented images (thin sections). For each sample, 3 mutually orthogonal thin sections were cut from block or cylindrical specimens. Based on the 2D results, a 3D ellipsoid was calculated for comparison with the AMS and AARM fabric ellipsoids (see Figure 4-16). The thin sections are oriented horizontally and vertically relative to the earth`s surface and vertically parallel with the dyke`s attitude (strike and dip angle). Samples were chosen according to the following criteria: (1) Only fresh dyke samples at or near the direct contact to the country rocks were considered. The outer part of the dyke is assumed to represent the material from the first magma pulse that entered the dyke fissure. (2) Analyses were preferentially performed on samples with vitrophyric and porphyric rather than intergranular textures, because a free movement of crystals or phenocrysts is expected when they are in a fine-grained matrix. Furthermore, image analysis is complicated when crystals touch each other or even interpenetrate each other.

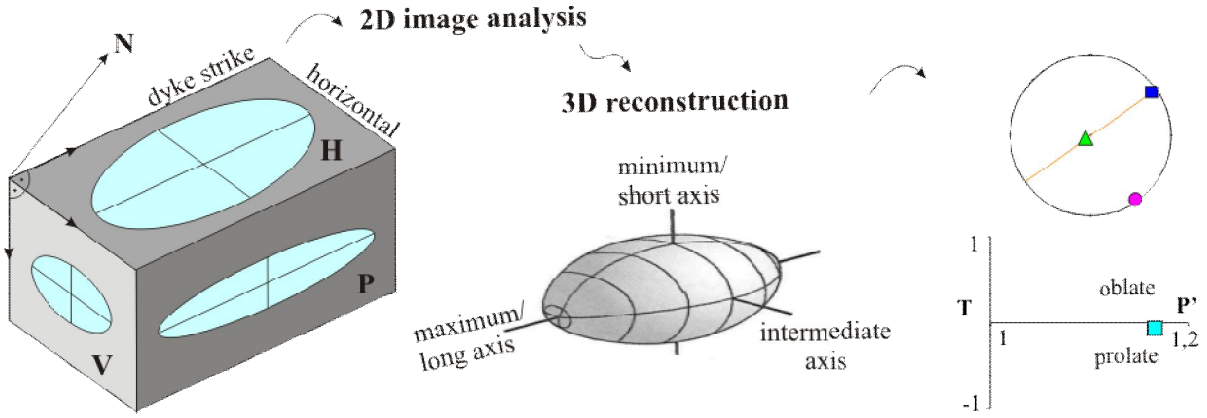

Figure 4-16. Procedure from 2D-Image Analyis of 3 perpendicular planes to 3D-ellipsoid determination and stereographic projection.

Analyses of samples 52 and 77 were performed on oriented micro photographs (crossed-nicols) and of sample 21 on scanned thin sections. For a better contrast, the scans or images were edited and transformed into an 8-bit grayscale tif-file using the Corel Photopaint software. These files were then imported into the software ImageJ 1.42q (Wayne Rasband, 1997-2012), which automatically detects and counts particles and determines their shape parameters. In order to reduce artefacts, further editing/processing was done in ImageJ before analysis, including the separation of contiguous crystals, the joining up of parts of separated crystals, and erasure of rock fractures or surface disturbances. After the user determines a threshold level of contrast, the image analysis programme marks the corresponding dark or colour-saturated pixels and pixel aggregations, which constitute the objects to be analysed. After this pre-editing, the measuring mode "fit ellipse" is applied to each coherent group of pixels, corresponding to a crystal grain. The programme determines the "shape descriptors" of the individual ellipses including the maximum and minimum axis lengths, shape ratio and total area, as well as the angle of the maximum axes with the horizontal image axis. Artifacts were minimized by excluding the smallest grains. Pixel size is adapted to the micrograph's magnification and to the size of the analysed particles. By keeping the circularity well below 1, nearly circular particles are excluded. Where possible, one thousand measured particles per sample were analysed to obtain significant statistics. The 1000 particles are also the upper limit of data that can be handled in the software programme Fabric8 (Wallbrecher, www.geolsoft.com), which displays the orientation distribution of particles in a rose diagram and provides statistical parameters including the arithmetic vector mean of crystal orientation (mean angle) and the degree of mineral orientation. Since ImageJ measures ellipsoid angles from the horizontal counterclockwise, all Fabric8 output orientations were converted by rotating 90 degrees counterclockwise and inverted by a vertical mirror plane (compare Appendix 15, "angle of long axis of mean shape ellipse", where the first angle is the original output angle of ImageJ; the second angle is the converted one).

Finally, to combine the orientation results of all three thin sections into a three-dimensional ellipsoid, the freeware Visual Basic programme "Ellipsoid 2003" (Robin, 2002; Launeau & Robin, 2005) was employed. This programme was input with the orientation data of the 3 thin sections, including strike and dip angles, the shape ratios and orientations/rake (rakes, see Figure 4-17 a) of the mean ellipse long axis. For comparison the best-fit 3D ellipsoid was determined based on the particle orientation data (rake) of the three different sources: 1) means and data of ImageJ, 2) means generated by Fabric8, based on ImageJ data, 3) rose diagram maxima based on displayed ImageJ data. As thin section 21H was prepared at a small-scale irregularity in dyke trend of about 30°, all three ellipsoid determinations of sample 21 were additionally run with a 30°-corrected rake of plane 21H (ellipsoid determinations 2, 4 and 6; Appendix 16).

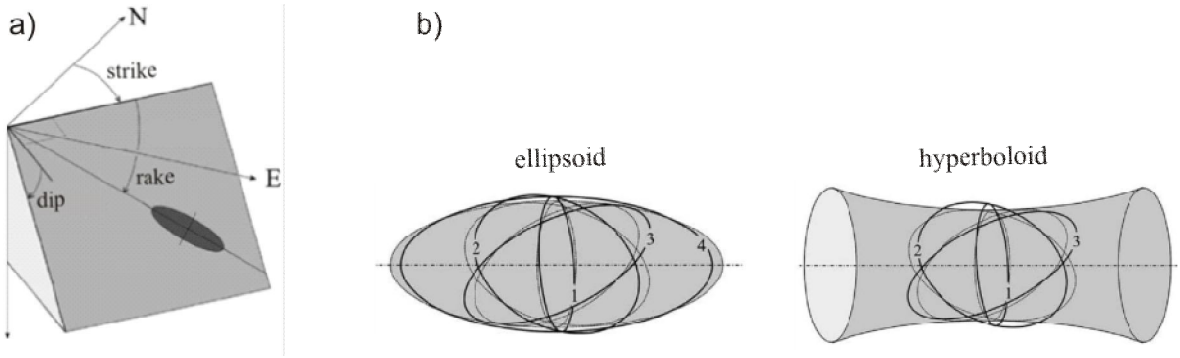

Figure 4-17. a) Convention for the description of planes/thin sections for the programme Ellipsoid (Launeau & Robin, 2005). b) Ellipsoid versus hyperboloid; best fits of the program Ellipsoid (Launeau & Robin, 2005)

The computation gives the orientations of the three principal axes, the orientation of the foliation plane and shape parameters of the calculated ellipsoid, such as P´and T. An evaluation of the ellipsoid`s conformity with the sectional ellipses is given by the global Incompatibility Index ($\sqrt{F}$) and by the individual Incompatibility Indices for each section. By assigning a weight to the individual sections between 0 and 1, the confidence of results can be assessed for the individual sections and the influence of outliers on the resulting ellipse can be minimized. This provides a means to decrease the global Incompatibility Index, which is sometimes necessary as the programme always yields a result, regardless of whether the input data are compatible or not (Launeau & Robin, 2005).

For comparison, a second ellipsoid was determined with the rakes derived from the vector means from Fabric8 (which are almost identical with the ImageJ means) and a third with the rakes derived from rose diagram orientation maxima. However, the orientation maxima derived from the rose diagrams do not represent mean orientations, but maxima. Calculating fabric ellipses based on these maxima would imply to disregard all particles with different orientation. Therefore, maxima are not appropriate for a comparison with the AMS and AARM fabric ellipsoids.

4.4 Methods for analysing the magnetic mineralogy

4.4.1 Temperature-dependent magnetic susceptibility

The temperature dependence of the magnetic susceptibility, κ(T)-curves/κ-T curves (Hrouda, 1994), is a crucial diagnostic tool for identifying ferromagnetic minerals, which carry the susceptibility and remanence in rocks. Therefore, this method complements AMS studies (e.g. Hrouda, 1994, 1997).

About 0.5 cm^3 powdered rock material of a representative piece of sample is measured in theAGICO KLY-4 Kappabridge, fitted with the temperature control apparatus CS-3/CS-L of AGICO. Measurements ran from a temperature range of -192 °C up to 700 °C in two separate cycles. Before the start of the heating run, liquid nitrogen cools down the sample holder to -192°C and then the susceptibility is recorded every few seconds while the sample gradually warms up to room temperature. Then the same sample material is used for the high-temperature run up to 700 °C with a heating rate of 3 – 4 °C/min. Subsequently, temperature is reduced gradually to 15 °C in rates of 10 to 14 °C/min. In order to minimize mineral reactions with atmospheric oxygen during heating, the experiment is performed in argon atmosphere (50 ml/min). After the measurements the raw data were corrected with the software programme "Cureval" (Hrouda, 1994) for the susceptibility of the empty furnace and were normalized to the susceptibility magnitude at 15°C (low-temp. run) and to the initial susceptibility at room temperature (high-temp. run). Susceptibility curves are then plotted against the temperature and interpreted in terms of reversibility and mineral-specific transition temperatures. Diagnostic temperatures from Curie, Néel, Verwey and Morin transitions were taken from the point where susceptibility begins to drop significantly. As a measure for the degree of reversibility between the cooling and the heating run an alteration index was introduced by Just & Kontny (2011). Here, the difference between $\kappa_{normalized}$ at 40 °C during the cooling and $\kappa_{normalized}$ at 40°C during the heating run (Al-index = κC_{room}-κH_{room}) is calcu-

lated. Elevated susceptibilities in the cooling run as compared to the preceding heating run result in a positive Al-index and reduced susceptibilities during cooling result in a negative index.

4.4.2 Transmitted- and reflected-light microscopy

53 samples were investigated optically in polished rock thin sections of an approximate thickness of 30 µm. All samples were examined in transmitted light and 38 in reflected light also. Except for a few individual cases, two or even three oriented thin sections per sample were prepared from perpendicular planes, respectively. About one third of them were cut from AMS cylinders after the measurements. They are parallel with the $\kappa_{max} - \kappa_{int}$ (x-y) and the κ_{max}-κ_{min} (x-z) planes of the calculated susceptibility ellipsoid and were named accordingly.

Microscopy of the dyke rocks was aimed at variable goals. Transmitted-light observations concentrated on the following features: fabric/texture of the silicate rock, obvious mineral alignment and possible magma flow texture, mineral alterations and secondary minerals, and signs of a secondary tectonic fabric overprint. Reflected-light studies focused on identifying iron-titanium-oxide minerals as potential main carriers of the magnetic susceptibility and assessing their volumetric abundance; their shape and the order of their grain size, particularly in the case of titanomagnetite; their possible alignment; their state of alteration and the degree of tmt-exsolution. Observations in reflected light were intended for verifying and complementing the results given by the temperature-dependent susceptibility measurements.

Two thirds of the thin sections were especially prepared for the image analysis of plagioclase orientations described above. Therefore, slices were prepared from samples taken near or at the dyke margins. These sections are orthogonal to one another and were cut from the block samples or from extra drill cores. The sections are oriented vertically (V) and horizontally (H) to the dyke plane, and after examining all the sections, for three suitable samples also a third section has been prepared parallel (P) with the dyke plane. The P-slice was needed for the image analysis and the programmeme “Ellipsoid”, which requires the input of results of three perpendicular rock planes.

For discriminating ferrimagnetic (mt, tmt, pyrrhotite) from antiferro- or paramagnetic iron minerals (ilmenite, haematite) in reflected light, thin sections were covered with diluted ferrofluid (EMG 807) from Ferrofluidics GmbH and covered by a glass slide. Dilution ratio was 1:10 ferrofluid to distilled water. The fluid disperses on the thin section and is attracted by strong magnetic minerals which can then be observed with a reddish-brown dye.

4.4.3 Alternating field demagnetization and median destructive field

The Alternating Field Demagnetization (AFD) of the natural remanent magnetization (NRM) serves to identify samples whose AMS directions are influenced or disturbed by single-domain (titano-)-magnetite or other ferromagnetic minerals than mt/tmt. Since the demagnetization behaviour depends on the coercivity spectrum of a specimen’s remanent minerals, information about their domain states are given. AFD curves further provide hints on the presence of other highly coercive minerals, such as haematite and iron hydroxides.

During the AFD in a demagnetizer from AGICO, a sample is exposed to a static alternating field in 3 orthogonal directions consecutively in a zero magnetic field environment. The field strength is augmented incrementally, reducing the sample`s natural remanent magnetization stepwise. After every one of the 12 steps the remaining remanence vector is measured with a spinner magnetometer. Its directional and magnitude changes give information on the grain size/domain state dependent coercivity spectra of the remanence and AMS carrying titanomagnetites/-maghemites. Thus the method helps to unravel single domain and/or pseudo-single domain tmt/tmgh contributions to AMS.

Before starting the demagnetization the vector of natural remanent magnetization (NRM) was measured with a spinner magnetometer. Since not all of the samples were demagnetized effectively, the NRM value provides a reference.

Demagnetization starts after having measured the NRM with a JR5A spinner magnetometer from AGICO. In the first demagnetizing step samples are exposed to a smoothly decaying alternating field of 2.5 mT. Magnetic moments of all particles with coercivities below 2.5 mT that have components parallel with the applied field will get unlocked (Tauxe 2002). The magnetic moments track the oscillating field and are fixed as soon as the field decreases below each grain's individual coercivity (Tauxe 2002). By this procedure, magnetic moments become randomized and have zero net contribution to the sample's remanence. Thereafter, the sample`s remanence vector is determined again. In the second demagnetization step the peak alternating field is set to 5 mT and the procedure is repeated such that now all particles with coercive forces ≤ 5 mT get randomized. The maximum peak field during the last cycle of that incremental demagnetization is 160 mT .

Finally, the absolute values of the remanence vectors are normalized to the highest one and then plotted against the applied field, respectively. Samples with dominantly MD tmts/tmghs as AMS carriers, for example, show a rapidly decaying remanence within the first demagnetizing steps with the firstly measured remanence value, the NRM, being the highest one. From this curve then the median destructive field (MDF), which is the value of alternating field, where half of the sample`s original remanence has been erased, is determined graphically. The magnitude of MDF gives information about the coercive force (H_C) of the dominant carrier minerals of magnetic remanence (which are partly the same carriers as for AMS). High MDF values account for a high fraction of hard magnetic minerals (with a high coercive force) and/or magnetic minerals in the single-domain state, and low values point to softer magnetic carrier minerals in the pseudo-single or multi-domain state with low coercivities.

4.4.4 Hysteresis measurements

The manner by which materials change their directions of remanent magnetization can be described by hysteresis curves/loops and is influenced by the material's domain structure. In this study the samples' hysteretic behaviour was investigated in order to unravel the bulk domain state of ferromagnetic (s.l.) minerals, mainly titanomagnetite/-maghemite and possibly also haematite and iron (hydr-)oxides.

Hysteresis loops and back field demagnetizations were performed and the parameters magnetization remanence M_{RC}, saturation magnetization M_S, coercive force H_C, and remanent coercive force/ coercivity of remanence H_{CR} were determined for a subset of 36 selected specimens from 33 samples. The magnetization M is recorded as a function of H. Measurements were performed at ambient temperature with a Micromag 2900 Alternating Gradient Force Magnetometer (AGFM) from PRINCETON MEASUREMENT CORPORATION at the University of Tübingen. Rock material was taken from drill cores. It was pestled and a very small amount (≤ 1g) thereof was attached to a 0.25 cm^2 piece of adhesive foil. This foil was attached to the sample holder with grease paste, and the holder fixed in between the two coils of the AGFM instrument that generate the field gradient. The hysteresis loops were measured at magnetic field forces ranging from -500 mT to 500 mT, which impart an isothermal remanent magnetisation on the rock powder. For one of the samples (no. 19) the field had to be raised up to 800 mT (and -800 mT) to achieve magnetic saturation.

The coercivity of remanence (H_{CR}) is acquired with the help of a separate "backfield curve" measurement, where the sample is demagnetized and subsequently acquires an isothermal remanent magnetization (IRM).

In the presence of additional paramagnetic components, such as in the studied basalts, magnetization would still continue to rise after saturation of the ferromagnetic component. For the determination of H_{CR}, M_R, M_S and H_C it is essential to saturate the ferromagnetic components during hysteresis measurements and to subtract the paramagnetic (and diamagnetic) components afterwards. This step is done directly in the Micromag software that asks to "enter the percent of H_{Max} at which saturation is assumed". Experiences of the Tübingen Paleomagnetic working group showed that at 70 % a good fit is achieved. Thus, for the "paramagnetic correction" a linear slope above 70 % of H_{Max} was subtracted from each sample which results in a compression of the loop along the vertical axis.

4.5 Other measurements

4.5.1 Natural remanent magnetization and Koenigsberger ratio

The natural remanent magnetization (NRM) was measured with a JR5A spinner magnetometer (AGICO, Brno) in almost every sample. The precision of these measurements is 2.4 µA/m. For the samples 5 and 71 to 114, only 4 to 6 standard specimens were measured in order to save time. According to the user manual of the JR5A apparatus, the magnitude and orientation of the NRM-vector is measured by rotating the cylindric specimen at a constant angular speed in the pick-up unit inside a pair of coils. An AC voltage is induced in the coils whose amplitude and phase depend on the magnitude and direction of the RM vector of the specimen. After amplifying, filtering and digitizing the voltage, the computer calculates two rectangular components of the projection of the RM vector by Fourier analysis into the plane perpendicular to the axis of rotation.
On the basis of the NRM-magnitude, the bulk susceptibility and the total intensity of the magnetic field in September in Namibia (at -22°S, 15°E, altitude: 100 m) of the year 2010 taken from the International Geomagnetic Reference Field IGRF2010 (H_{Earth} = 28826.7 nT = 22.9460532 A/m), the Koenigsberger ratio (Q; see chapter 3.1 for equation) and its mean (Q_{mean}) have been calculated.
Highly NRM- and Q-bearing specimens are suspected to be magnetized by lightning strikes. The magnitude of the NRM can give a hint for the type of remanence that the rock is carrying and was utilized as an indicator for possible influences of the remanence on the magnetic susceptibility.

4.5.2 Geochemical analysis

All chemical analyses were performed at the GFZ German Research Centre for Geosciences in Potsdam. Lab access and help with analyses were kindly provided by R. Naumann, A. Gottsche, H. Rothe and S. Tonn. Rock samples were jaw-crushed and ground in a disc mill (agate) to a grain size of < 62 µm. Sample homogeneity was assured by sieving, regrinding of oversize and homogenization. The major elements Si, Ti, Al, Fe, Ca, Mn, Mg, Na, K and P, and the trace elements Cr, Ni, Zn, Zr, Y, Rb, Sr, Ba and Nb were determined by X-ray fluorescence (XRF) using a PANalytical AXIOS Advanced instrument with a Rh tube.
The determination of major elements was performed on fused disks prepared with lithium tetraborate flux. Analyses of H_2O and CO_2 were made by infrared spectrometry (Leco RC-412) and FeO by titration.

5 Field studies of dykes

Field work focused on the acquisition of oriented dyke samples and on determining and documenting geometric, magnetic and orientation properties of the dykes. Furthermore, relations between different dyke segments of the same dyke, between intersecting dykes (relative ages), and, where possible, between dykes and host rocks were studied.

Dyke selection, distribution and sampling

The two field campaigns in September 2009 and September/October 2010 were prepared on the basis of satellite images (Landsat and GoogleEarth). Generally, sampling areas were preselected according to apparently good outcrop and access conditions and to provide samples over large parts of the dyke swarm, especially with respect to varying distances from and along the coastline.

For the present study 42 dykes and one sill, have been sampled. Most of them crop out in the Erongo region between the rivers Ugab and Khan and a few, which are the northeasternmost ones, belong to the western part of the Otjozondjupa region. A set of 112 rock samples were collected from localities distributed over seven sampling areas (Figure 5-18): The three areas Horingbaai-Bocock's Bay, Omdel dam and Rossing Mountains are located less than 45 km from the present coastline, the Gross Spitzkoppe and Okombahe areas are at intermediate distances and the Kalkfeld and Mt. Klein Etjo areas are farthest from the coast with a distance of 230 and 250 km. Most of the sample localities are in the Central Zone of the Damara Belt, except those west of Messum crater at Horingbaai- Bocock`s Bay, which occur in the Southern Kaoko Zone of the Kaoko Belt (Figure 2-4). Outcrops of dykes further inland are rare and of poor quality. An attempt was made to sample dykes identified on aeromagnetic maps from a previous study (Hahne 2004), but the "outcrops" consisted of loose, basalt boulders

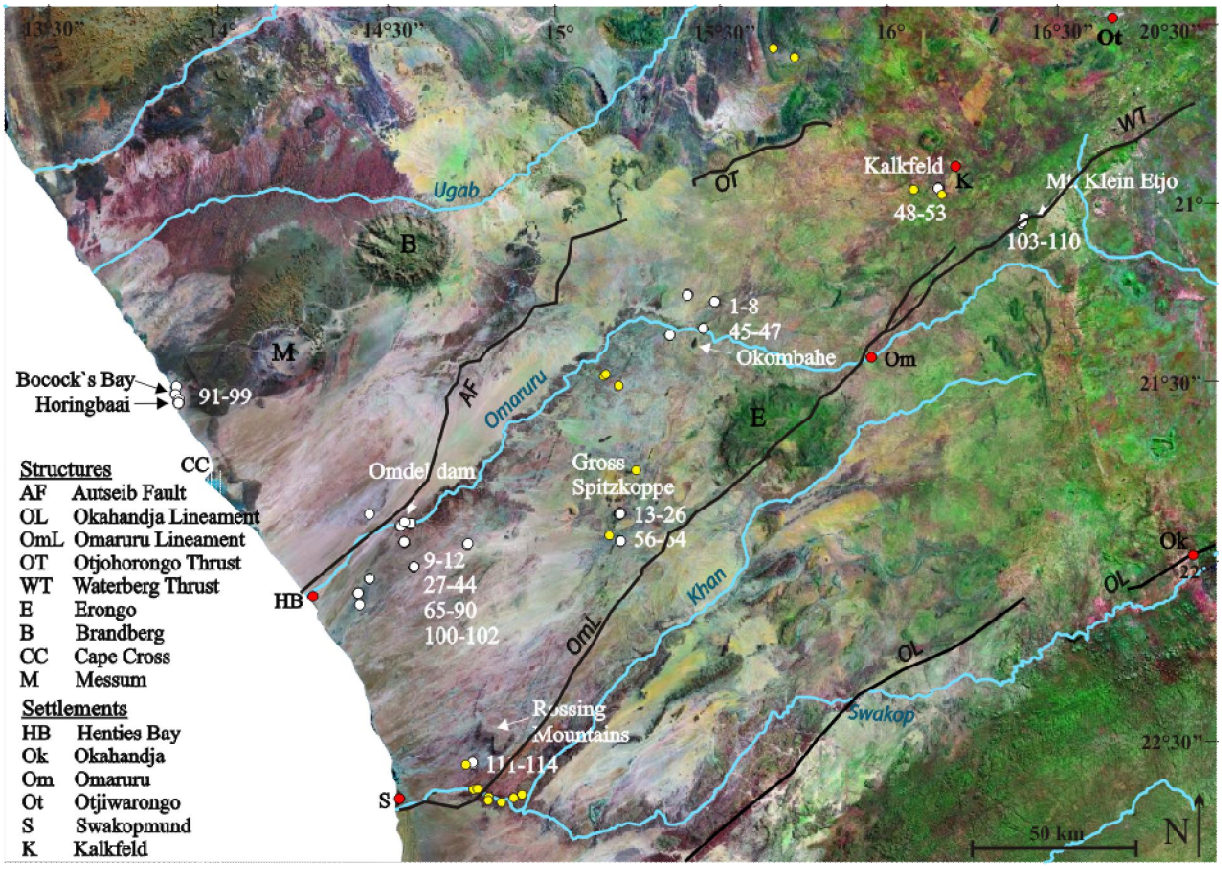

Figure 5-18. Satellite image of NW Namibia outlining the sample locations, marked with white circles. Yellow circles denote sample locations from a previous AMS study of Wiegand et al. (2011).

from which the dyke orientation cannot be measured. Because of this, all sampling in the Kalkfeld area was restricted to road cuts near the settlement Kalkfeld.

Prior to the sampling, the rock`s magnetic susceptibility was measured with a hand kappameter six to eight times at various rock planes as an indicator for the amount of magnetite in the rocks. Susceptibility values were used to characterize dykes as mafic and helped to distinguish them from felsic or other dykes that were not sampled. Sample 48 was taken in spite of the dyke's very low susceptibility.
Most dykes were sampled twice; once for geochemical analyses at the GFZ (German Research Centre for Geosciences) in Potsdam, and once for magnetic measurements at the KIT. The geochemical samples were taken with the aim of minimal alteration and influence of wallrock contamination, so they are generally from the dyke centres. By contrast, the oriented samples were mostly taken at or close to both dyke margins, where the likelihood of flow-related orientation is maximized. Ten of the dykes having a thickness of at least three metres have been sampled on both margins and in the central part. In some cases of thin dykes (< 0.5 m), samples comprise the entire dyke width (samples 16, 17, 22, 24, 25, 27, 28 and 106).

The following seven NE-striking dykes have been sampled twice or three times along strike, as described below, in order to test for fabric variations:

- samples 65 to 67 (both dyke margins and centre) are located 387 m to the NE than sample 12;
- samples 16 and 17 (Figures 5-23, 5-24, 7-49; complete-width samples) are separated by about 50 m along strike;
- samples 18 and 19 (both margins, N), separated by 10 to 15 m from samples 20 and 21 (both margins, S; Figure 7-50)
- samples 71 and 72 (both margins, SW), are separated by 1500 m from samples 86 to 88 (both margins and centre, NE)
- samples 103 and 104 (Figure 5-25; both margins, SW), are separated by about 300 m from the complete-dyke sample 106 (NE).
- sample 27 (complete width) is from a SW segment of a dyke (Figure 5-28 G), sample 28 (complete width) is from 14 meters to the NE (Figure 5-29 K), and samples 29-30 (both margins) is about 160 m NE of sample 27.
- Finally, samples 39 to 43 represent a composite dyke, which was formed by a set of dyke-in-dyke intrusions (see Figures 5-19, 5-30 L, M). Its individual dykes, were formed by consecutive magma pulses (from older to younger: G_1, G_2, G_3 etc.), indicated by dyke-internal chilled dyke margins (Figure 5-30 L). The samples were taken alongstrike and mostly comprise one or two internal chilled margins, which means that they are composed of material from at least two magma pulses. Samples 39 and sample 40 are separated alongstrike by only 0.3 m, similar with samples 41 and 42. The arrangement of individual dykes changes within a few metres from dyke-in-dyke-intrusions to a set of parallel, 15-25 cm thick individual dykes, which are separated by thin lenses of schistous country rock.

The only sill within the sample set was sampled at its top and again 115 m more to the NNW at 0.6 m below its top. The sill thickness is unclear (at least 0.6 m) because its base is covered. Rarely, only one sample per dyke was taken (numbers 10, 44, 48, 57).
Except for individual exceptions (no. 27; Figure 5-28 G), it was avoided to sample the (thinning) end of dyke segments or points of lateral dyke displacement (no. 47, 62-64, 13-15). Appendix 1 list all the samples with their field properties and location.

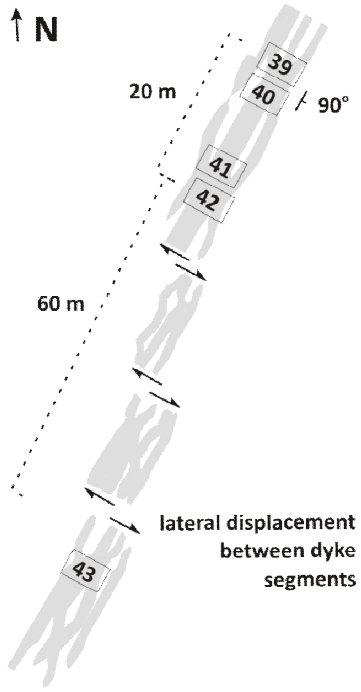

Figure 5-19. Sketch of the composite dyke represented by the sample numbers 39-43. Grey: dyke rock; white: country rock. Note segmentation and lateral displacement of the individual segments.

Similar to the dyke set described above (samples 39 to 43), but on larger scale, another set of parallel dykes is observed at Omdel dam area. These dykes run parallel over several tens of kilometers, at places bifurcating/braiding and/or rejoining (Figure 5-20). They are segmented and, at places, show lateral displacements or steps. Samples 79-81 and 82-85 represent two of these dykes directly east of Omdel dam and samples 33-34 and 37-38 another two from the same dyke set, but about 6 km SW of the others.

Dyke and sample orientations were measured with a magnetic compass. In order to avoid possible influence of the rock`s magnetic field, the compass was first oriented at the rock surface to be measured, then moved vertically away from the outcrop while maintaining its orientation and observing the compass needle for changes. Where necessary, corrections of plane azimuths were made. The measuring error introduced by this practice is estimated to be less than five percent.

Outcrop conditions

Most sampling areas are flat wide plains, at places with unconsolidated or poorly consolidated Quaternary deposits obliterating outcrops. Only some coarse-grained, several metres thick dykes emerge as more competent ridges from these plains with a few to several tens of metres in height. Outcrop conditions are best in the Omdel dam area at the Omaruru river. In contrast to wide parts of other areas, the landscape at Omdel dam is not leveled to a plain but is dissected by a large number of valleys, some meters up to tens of meters deep. Dykes in that place form morphological ridges flanked by country rock (Figure 5-20) or, rarely, they are exposed vertically for a few metres. Most of the dyke rocks there are in relatively fresh condition, which is also true for the other areas.

Figure 5-20. Landscape at Omdel dam area: Morphological ridges with dark dykes being the backbones flanked by light gneiss and migmatite country rocks. View to the SW. Note bifurcations of dykes in upper left.

Orientation, dip and thickness of the sampled dykes

Figure 5-21 compiles the strike, dip and thickness of all the 42 sampled HOD dykes. Dykes have variable strikes, but there is a clear majority of NNE to NE strikes (26 in total), which agrees with earlier studies based on satellite and aeromagnetic mapping (Hahne, 2004; Trumbull et al., 2004). Further, 8 WNW striking dykes, orthogonal to the others, and another 8 with variable orientations were sampled. Figure 5-22, which depicts the Horingbaai-Bocock's Bay area in the southern Kaoko Zone is dominated by NW-striking dykes. In the Gross Spitzkoppe and Okombahe areas, exclusively NE-striking dykes have been sampled because of the lack of others. In the remaining areas, NE-dykes prevail, but others were also sampled. Intersecting dykes have been sampled at the Omdel dam area and near the Rossing Mountains.

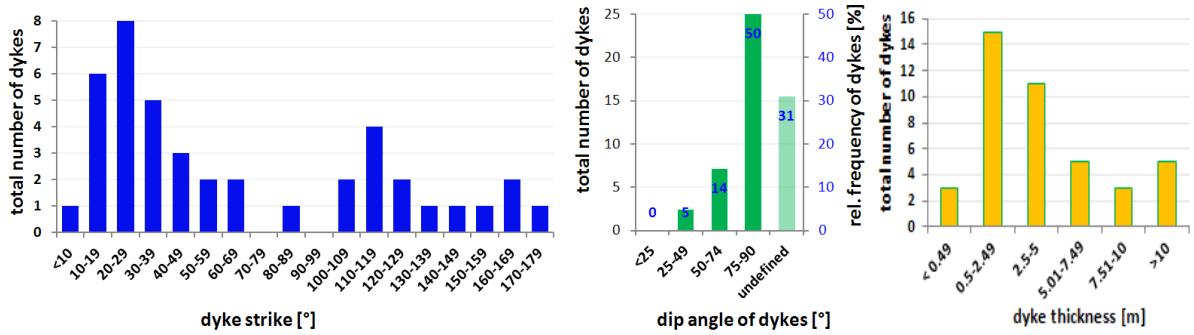

Figure 5-21. Frequency of strike, dip and thickness of all 42 sampled HOD dykes.

The strike within single dykes can alternate by as much as several tens of degrees, locally - for example between two dyke segments. Locally, the dyke strike can differ crucially from the regional strike orientation. For example, samples 93 to 95 were taken from a NE-striking dyke segment of 20 m length, which is a transfer zone of lateral displacement. The regional strike of that dyke is N-S. Similar conditions account for samples 13 to 15 and 62 to 64, which are from a place, where the NE-striking

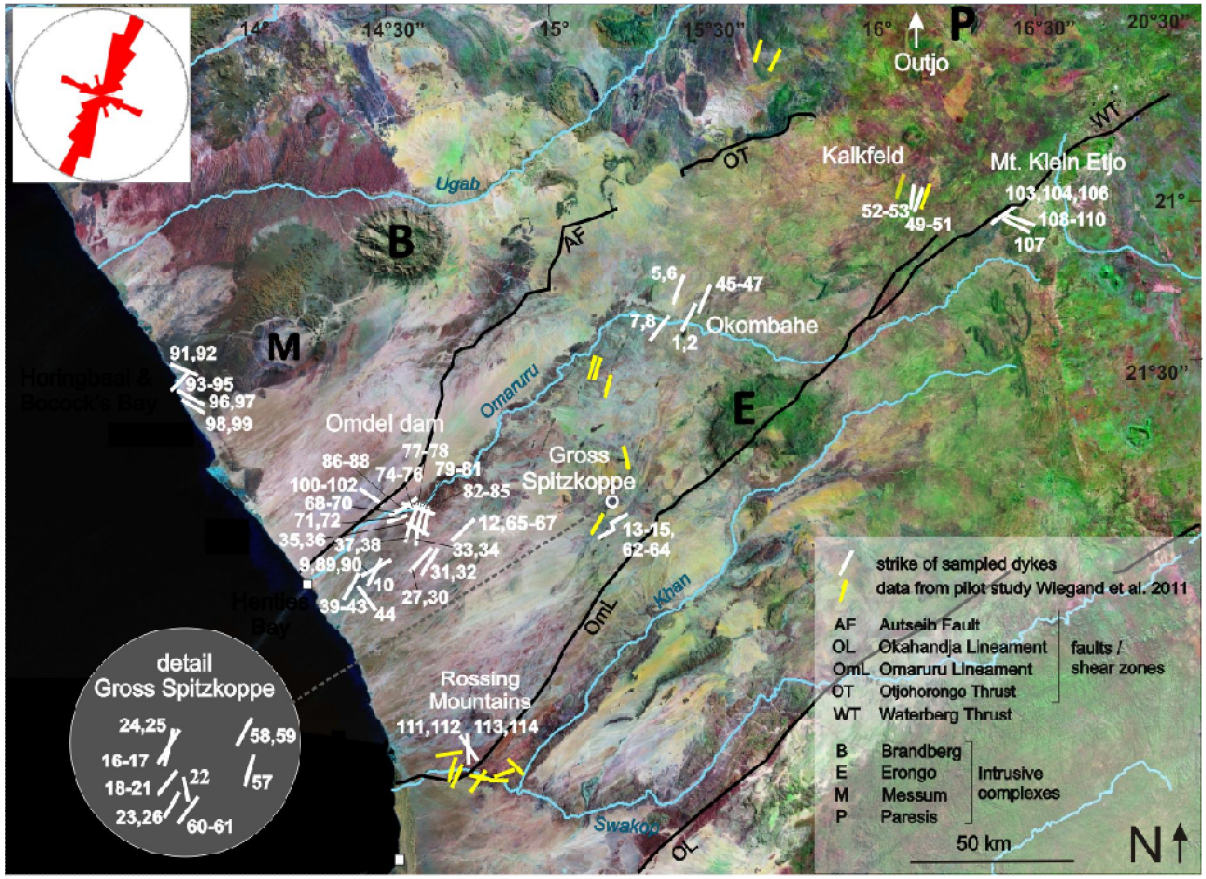

Figure 5-22. Satellite image of NW Namibia showing the strike of the sampled HOD dykes (white bars) and sample numbers affiliated with the respective sample site. Yellow bars refer to dykes from the previous AMS study of Wiegand et al. (2011). Inset: Rose diagram showing the strike of all 42 sampled HOD dykes.

dyke performs a left-lateral step. The two displaced segments are tied with a NW-striking dyke segment, where samples 14, 15 and 63 are taken from. Also, dyke dips have been observed to be variable within short distances alongstrike, as is shown, for example, by the change of dip between samples 103/104 (321/49) in the SW and 106 (144/64) 270 m more to the NW.

Steep to vertical dip angles prevail among the dykes (Figure 5-21). Dip information could not be acquired for 13 dykes, since their margins were eroded or the dykes are leveled to the ground with only some in-situ boulders left (dykes 10, 33-34, 35-36, 37-38, 44, 57, 91-92, 93-95, 96-97 and 107), or the country rock contact was obliterated by blocky slope debris, such as the dykes represented by the samples 1-2, 5-6 and 57. In these cases, dips had been assumed to be vertical (marked in Appendix 1). Six out of eight non-vertical NE trending dykes dip steeply to the SE, the remaining two dip towards the NW. Dyke thicknesses range from 0.1 to about 30 m with the majority between 0.5 and 5 m (see Figure 5-21). Thickness of dykes that are flanked with blocky debris covering the country rock contacts, such as 1-2, 5-6 and 7-8, could only be approximated. Because of the debris slopes, these thick dykes often appear thicker on satellite images than they really are.

Dyke morphology and geometry

Despite the preselection on satellite images and Google Earth, the aspect and weathering condition of the dykes is very variable. In general, HOD dykes produce a positive to neutral morphology. Thin dykes (< 0.5 m) barely influence the morphology. They are completely leveled to the ground (Figures 5-23 to 5-28) or stick out for some centi- or decimetres (Figure 5-29 I-K).

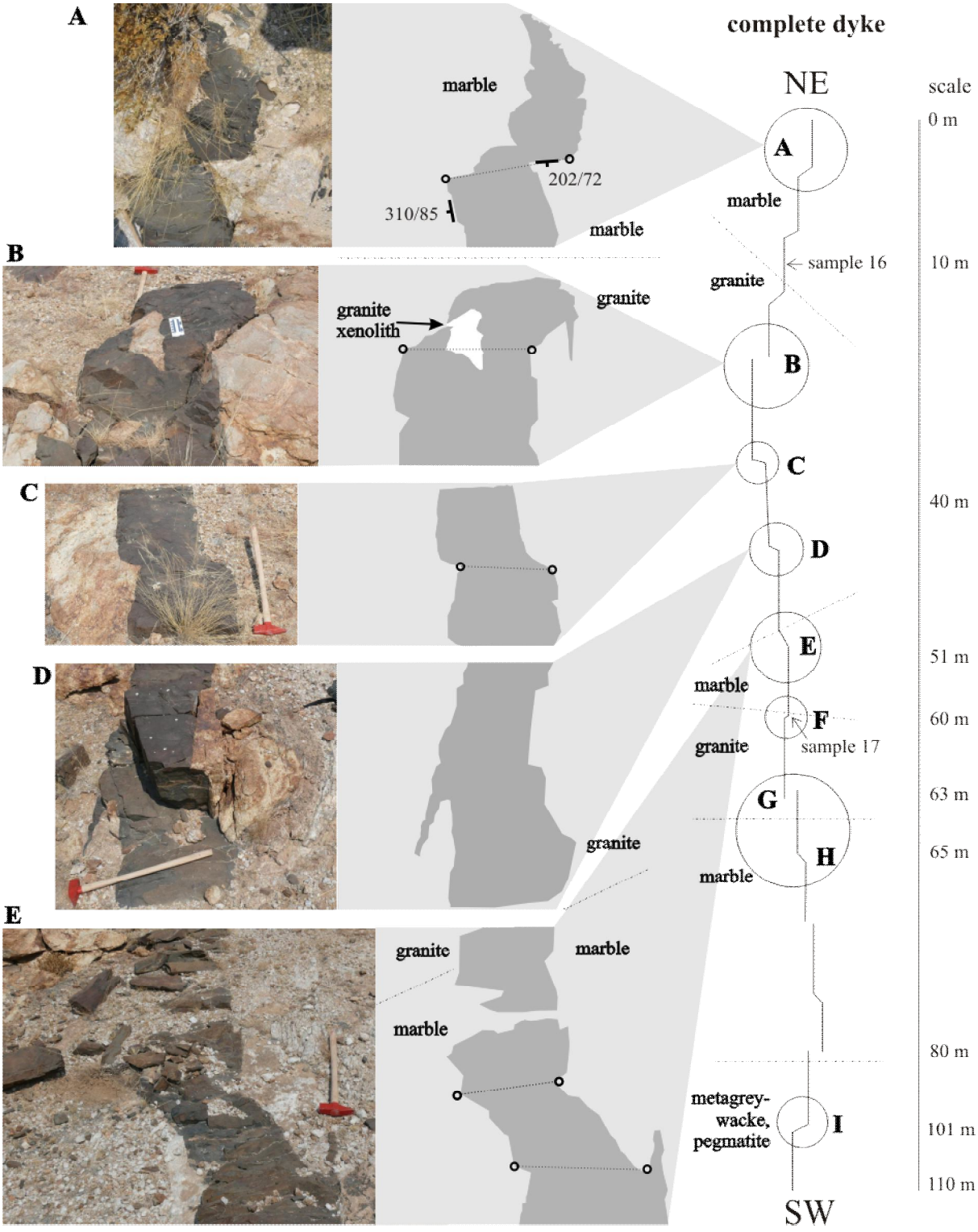

Figure 5-23. Field details of NE dyke near Grosse Spitzkoppe. Sample nos. 16-17 Right: schematic outline of dyke with varying host rocks and main features, e.g. segments, displacements, length. approximate distances of features from the NE dyke end are estimated on the scale. Open circles at grey photograph sketches relate points of identical coordinates before crustal extension and dyke emplacement. Dotted line between the circles delineates dislocation path of these points. A. NE thinning end of dyke with right-lateral step. B. Xenolith of granite host rock and dyke offshoot in granite. C. Left-lateral step. D & E. Left-lateral step and dyke offshoot in granite (D) and marble (E). F. Right-lateral step in granite at the contact with marble. Position of sample 17. G. Left-lateral step of dyke strike in granite. H. Transfer zone of crustal extension in marble: dyke segments thin out towards their ends, bend and overlap; records interaction of local stress fields during fracture propagation**;** extension is transferred laterally from one segment to the other; I. Right-lateral step. Note: Photographs are not taken perpendicular to the ground and azimuths of view vary.

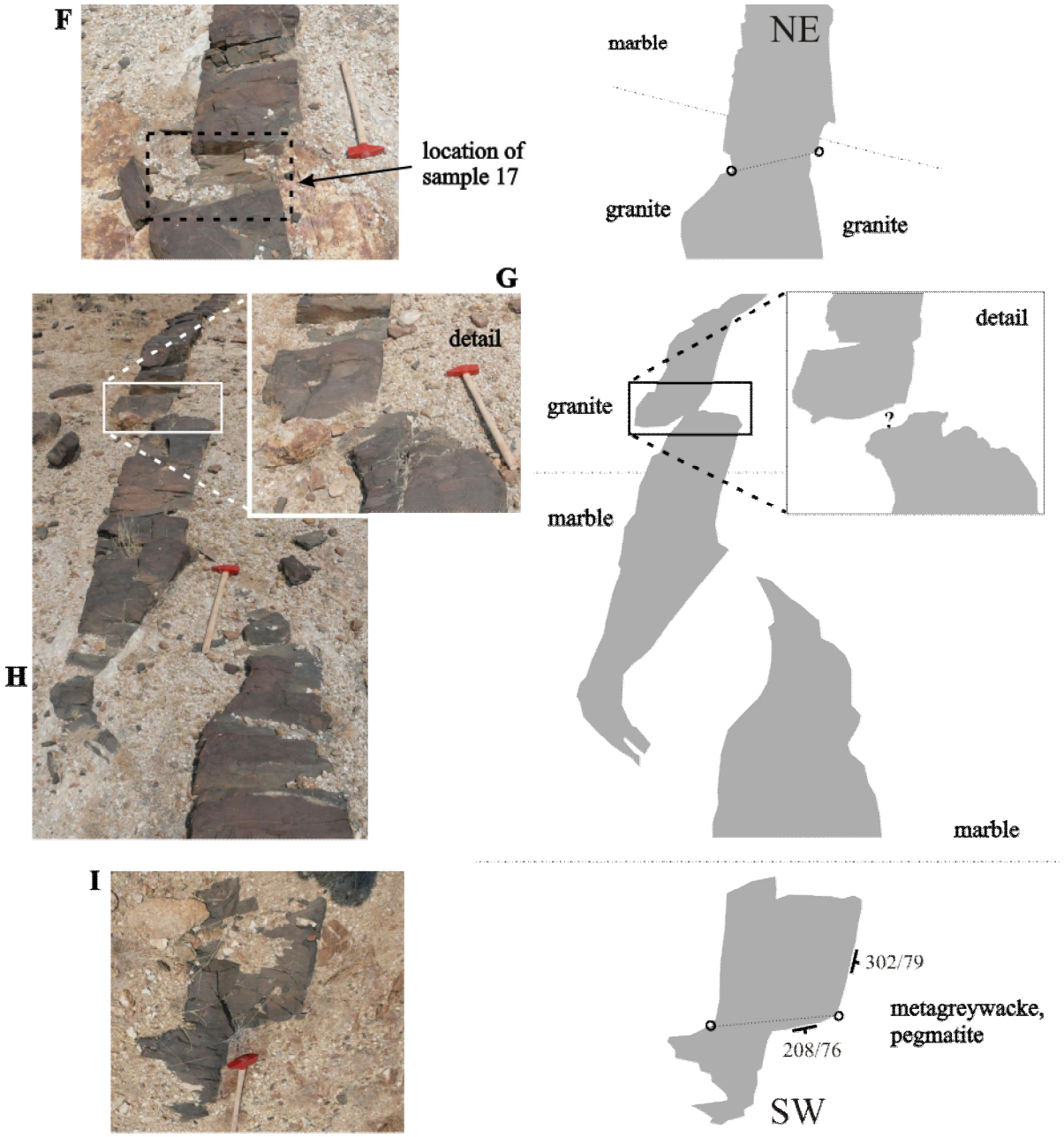

Figure 5-24. Field details of NE dyke near Grosse Spitzkoppe, continued. F. Right-lateral step in granite at the contact with marble. Position of sample 17. G. Left-lateral step of dyke strike in granite. H. Transfer zone of crustal extension in marble: dyke segments thin out towards their ends, bend and overlap; records interaction of local stress fields during fracture propagation**;** extension is transferred laterally from one segment to the other; I. Right-lateral step. Note: Photographs are not taken perpendicular to the ground and azimuths of view vary.

But thicker dykes (> 0.5 m), at places, are the backbones of gentle swells (Figures 5-20 & 5-30 M) or steep ridges in the range of about 1 metre up to several tens of metres in height.

Dykes in the HOD are continuous at a large scale, but satellite images and field observations often reveal segmentation at a scale of some metres to hundreds of metres or tens of kilometers (Figures 5-24 H, 5-26 A & 5-28 G). The segments commonly thin out towards the ends. At places, they are laterally displaced, often both left and right stepping within the same dyke, seldom purely en echelon. Overlapping segments can often be observed (Figures 5-24 H, 5-26 A & 5-28 G) and sometimes their thinned ends bend towards each other (Figure 5-24 H).

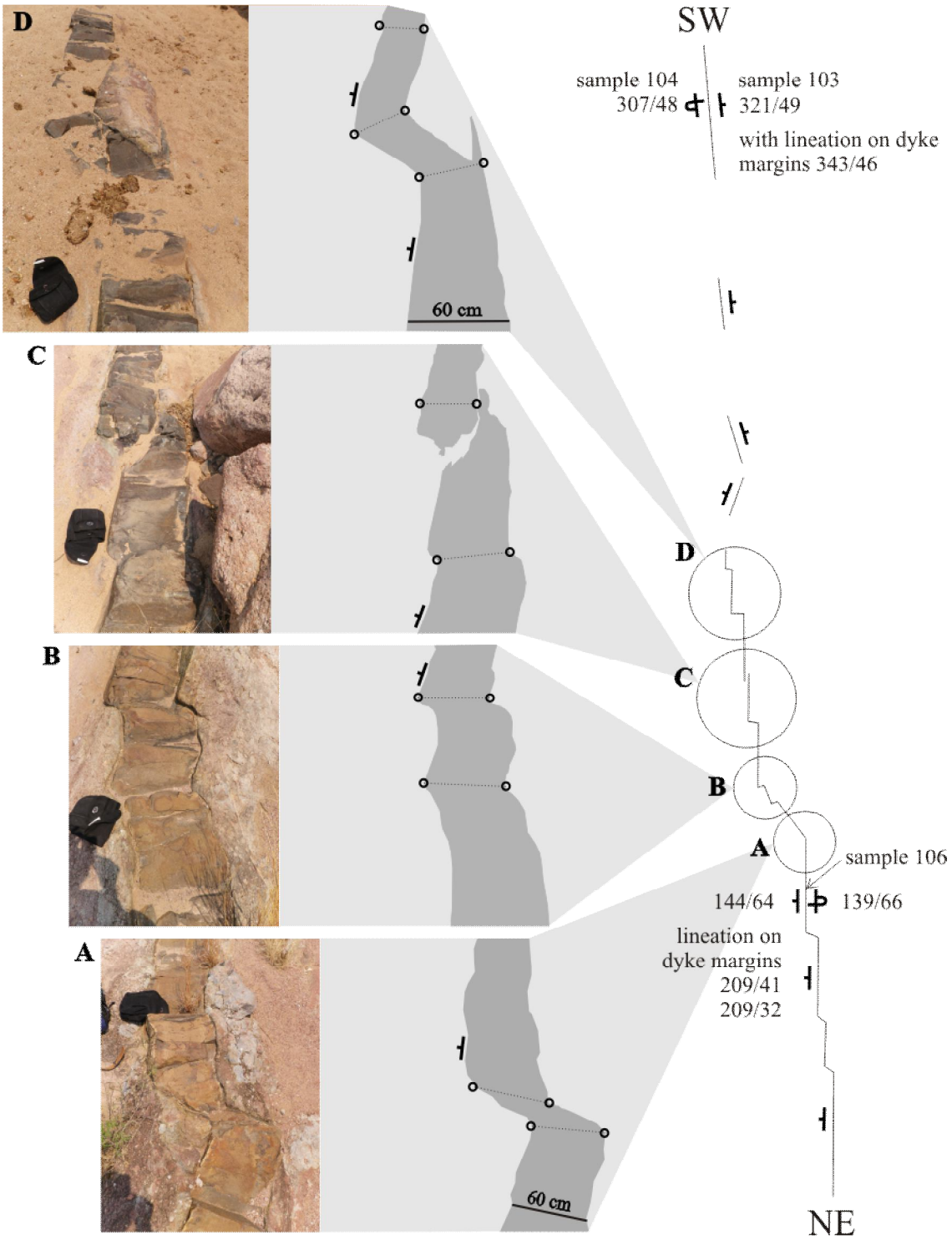

Figure 5-25. Field details of NE dyke at Mt. Klein Etjo. Sample nos. 103-106; host rock: Karoo sandstone. Right: schematic outline of dyke (not to scale) with main features and location of field photographs A to D; Open circles at interpretation sketches relate points of identical position before extension and dyke emplacement. Dotted lines between the circles connect these points. Field observations and images A to D show exclusively left-lateral dyke steps, C. two overlapping left-lateral dyke steps; D. offshoot placed exactly at the dyke bend. Note: dyke attitude changes from subparallel with a moderately NW dip in the SW to discordant with a moderate SE dip. Both dyke margins exhibit numerous lineations. Some parts of the dyke are covered with Quarternary deposits.

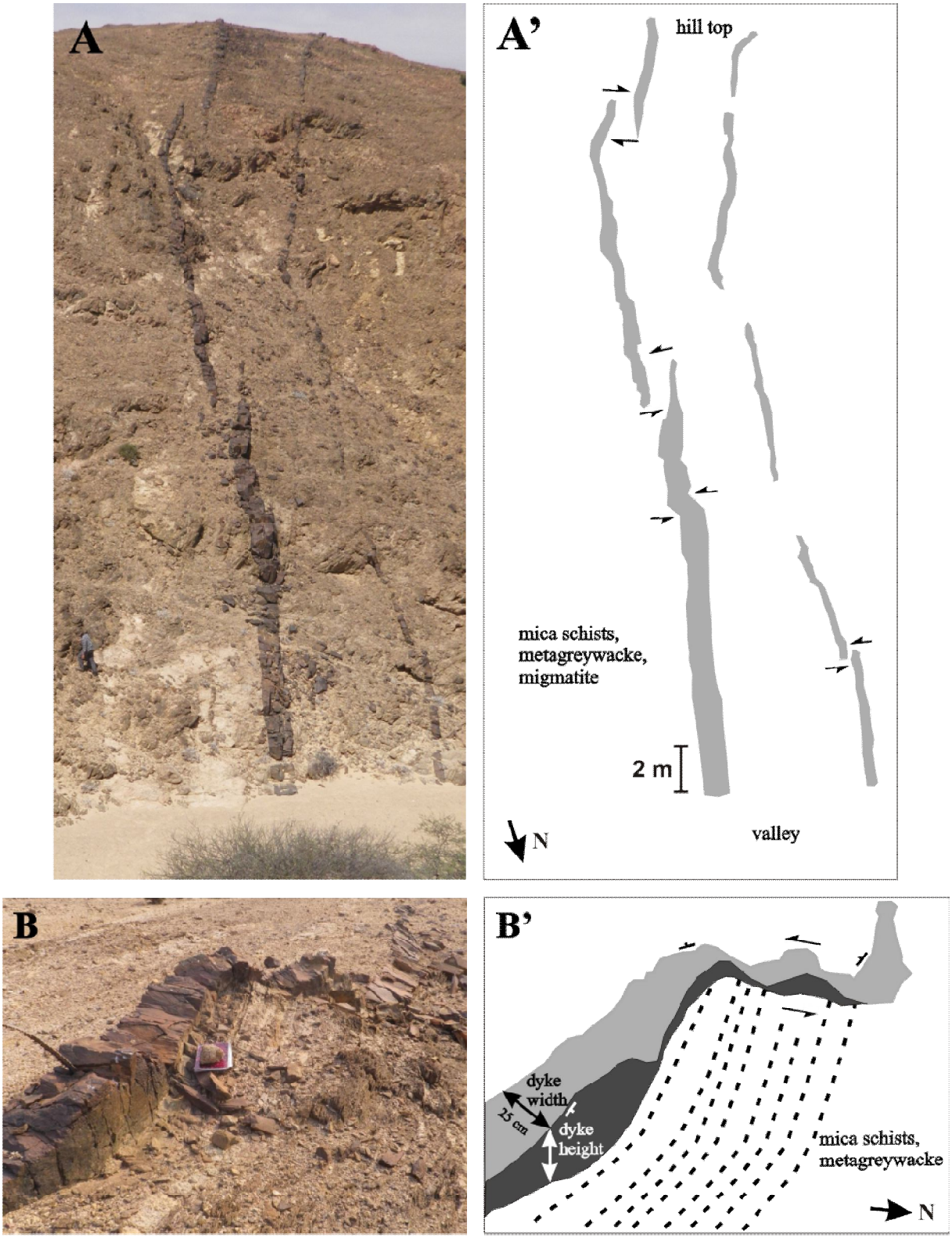

Figure 5-26. Field observations. Sketch at the right highlights and interprets important features. Here: dyke outcrops in the Omdel dam area. A. NE trending segmented dykes at the flank of a hill with both left- and right-laterally displaced sections, intruded into metasediments. B. Nearly vertical dyke that intruded into metasediments. Suddenly, it cuts through the beds, then, it turns again to the former strike direction. Change of dip direction indicated by symbols.

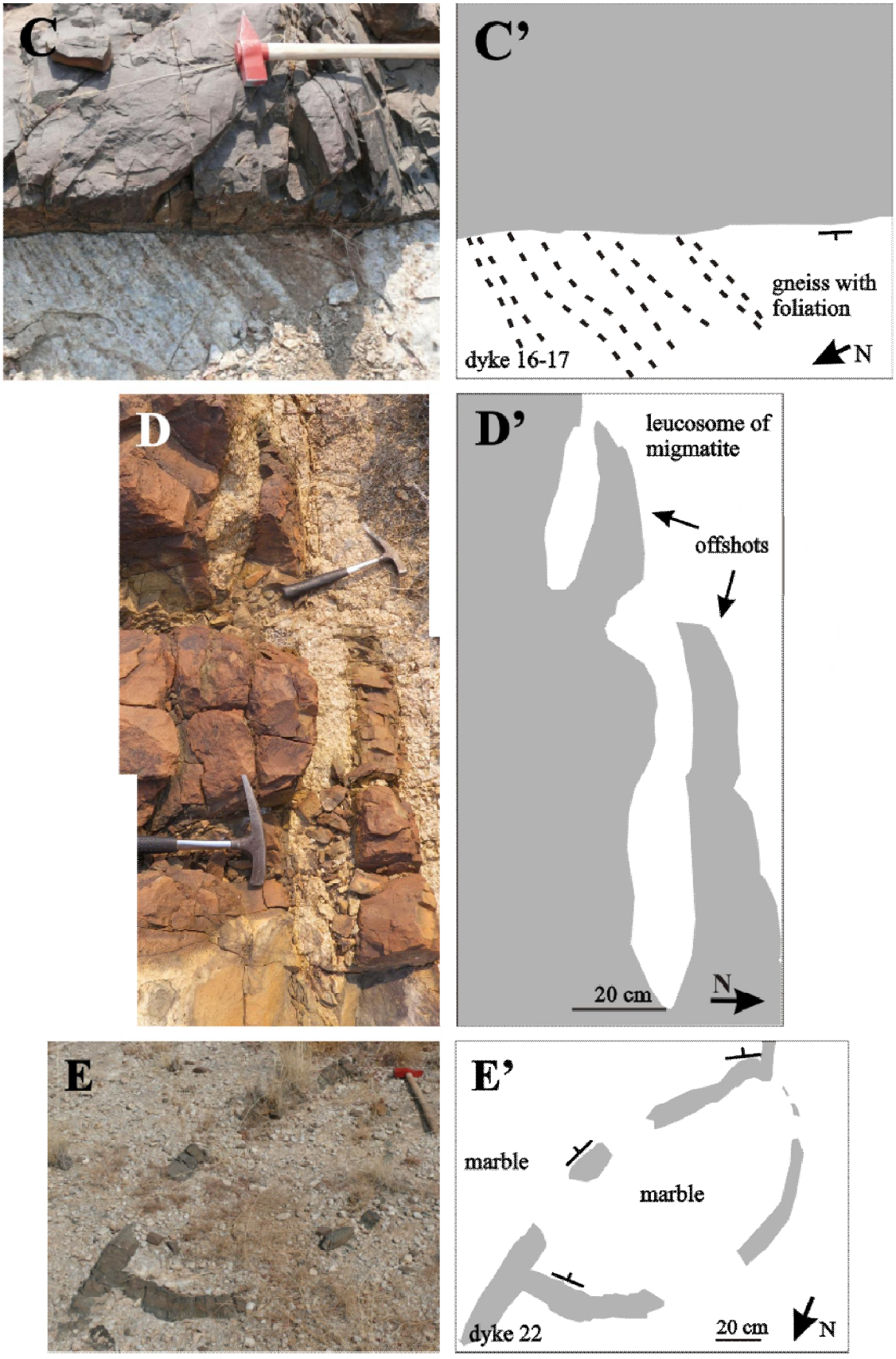

Figure 5-27 C-E. Field observations, continued. C. Gneiss with foliation at the contact with the NE trending dyke 16-17; foliation is almost perpendicular to dyke strike, near Grosse Spitzkoppe. D. Segmented 1.5 m thick dyke in the Omdel area with several offshoots. E. Thin dyke bifurcating and reuniting in marble rocks near Grosse Spitzkoppe.

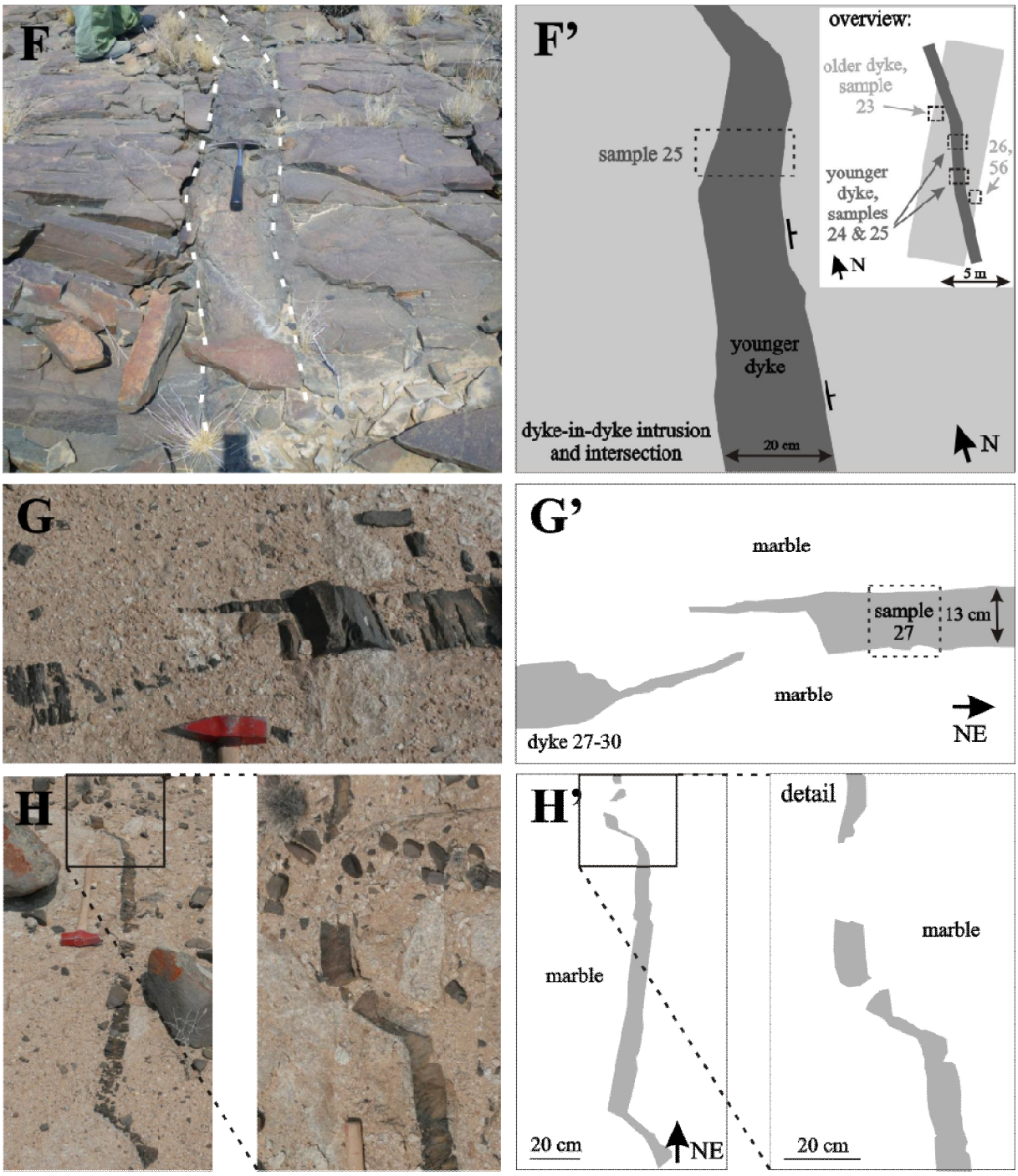

Figure 5-28 F-H. Field observations, continued. Geometrical dyke features, continued. F. Thin younger N trending dyke intersects an older NE trending thicker one; note the two kinks performed by the young dyke within the older one. G. Two segments of a dyke within marble rocks thin abruptly towards each other, ending each in fingers that overlap; the finger of the SW part points directly to the abrupt end of the NE segment; the finger of the NE part does not meet the SW segment in its prolongation. H. Straight thin NE striking dyke within marble rocks kinks and bends at both ends for about 40 degrees: the NE end to the left and the SW end to the right.

Occasionally, offshoots/apophyses of dyke rocks into the country rocks are observed, for example in dykes 16-17, 103-106, 39-43 and 73-76. These geometrical features are developed regardless of country rock type, in gneiss, migmatite, marble (Figures 5-27 D & 5-28 G), granite (Figures 5-26 B & 5-27 D), and also in sandstone (Figure 5-25 D).

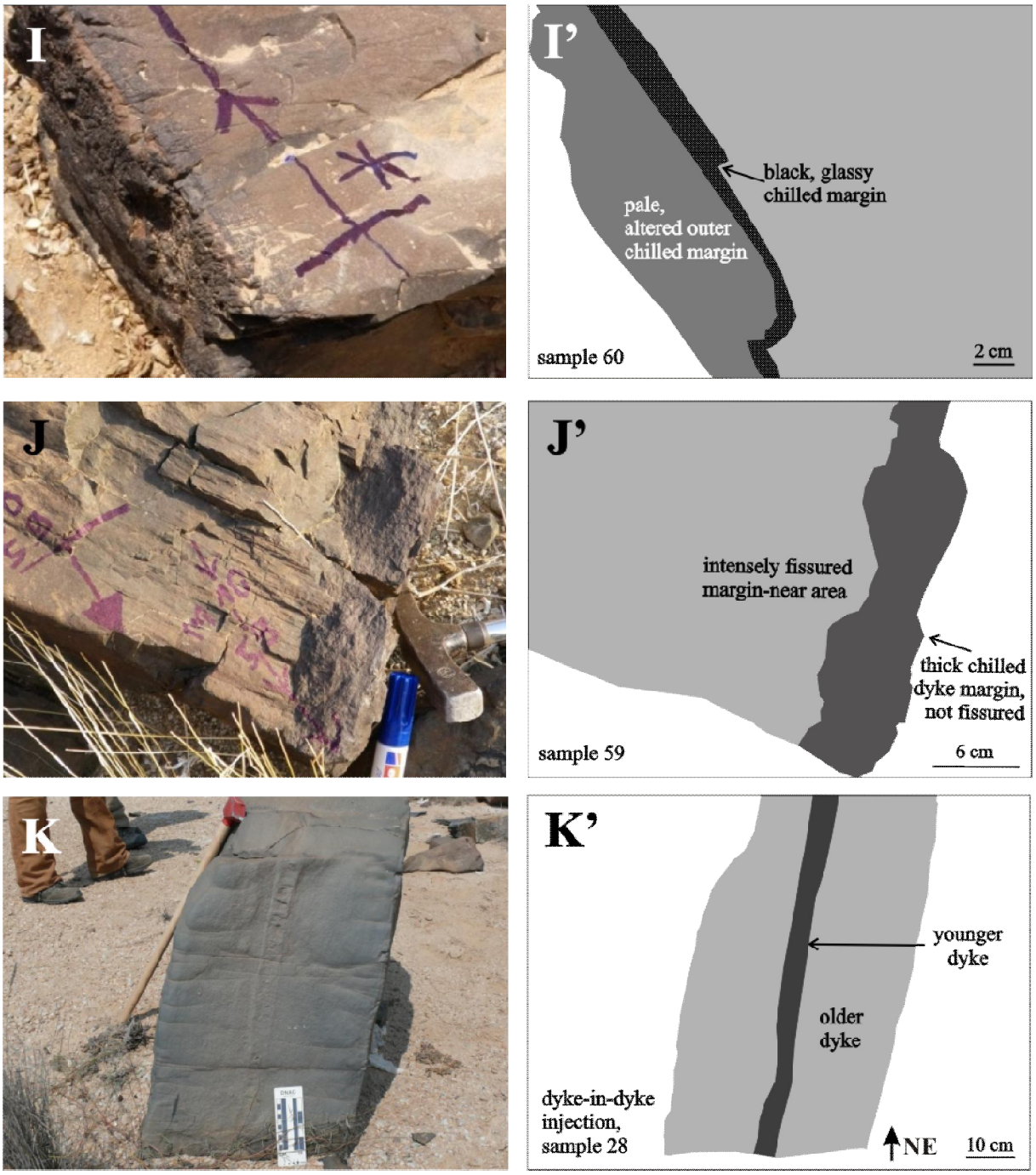

Figure 5-29 I-K. Field observations, continued. Chilled margins of dykes. I. Sharp boundary between the weathered pale brown outer part of the dyke's chilled margin and the inner part with black fresh glass. J. Relatively thick and rarely fissured chilled margin nonlinearly but sharply abuts against a closely fissured margin-near dyke part. K. Dyke showing finer-grained strike-parallel stripe in its centre; Stripe is interpreted as younger dyke intruded into the older one.

Satellite images and field observations prove that dyke strike is continuous at a large scale, but it can differ at a local scale or change by up to several tens of degrees between adjacent dyke segments. In places, dykes anastomose or bifurcate, which is obvious from aereal photographs and on GoogleEarth satellite images (see also Figure 5-20). At Gross Spitzkoppe area, one 15 cm thin dyke intruded in an elliptical shape, into marble country rocks (Figure 5-27 E).

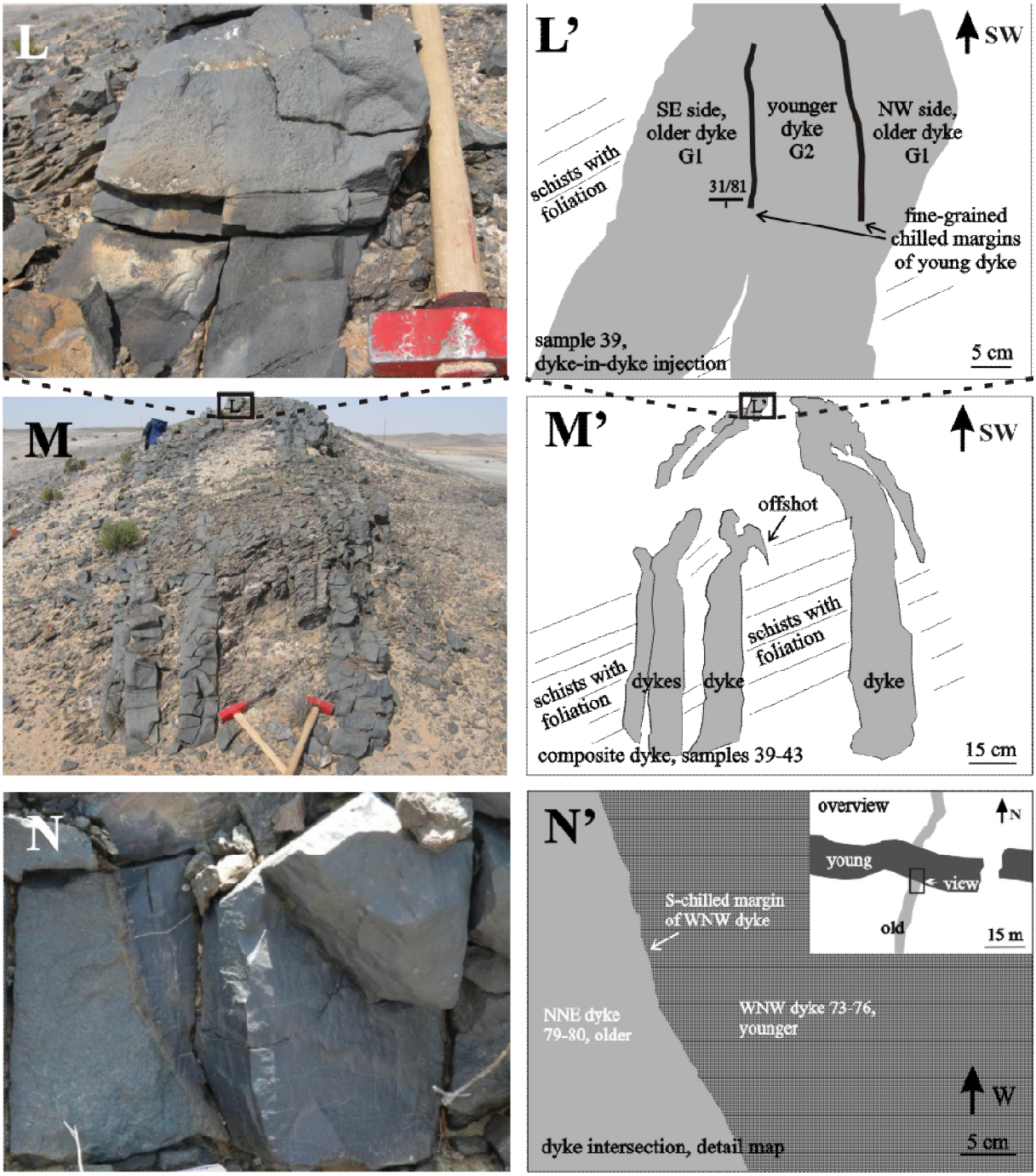

Figure 5-30 L-N. Field observations, continued. L & M. Composed dyke with varying aspect. In places, several thin dykes are separated by slim stripes of schist host rock, elsewhere, one thicker dyke is encountered with strike-parallel chilled margins in its centre, interpreted as dyke-in-dyke injection. Occasionally offshots occur. N. Dyke intersection of an older NNE striking dyke cut by a younger W trending one, see small overview map top right; foto shows a sharp boundary between the older dyke on the left and the darker younger dyke plus pale chilled margin on the right.

Dyke weathering seems to depend strongly on the grain size. Fine-grained dykes, where merely some plagioclase laths can be seen in an aphanitic matrix, are often more narrowly fissured. Coarse grained dykes with minerals of several millimetres to centimetres in size form boulder-sized debris, such as the dykes of samples 1-2, 5-6, 7-8 and 107.

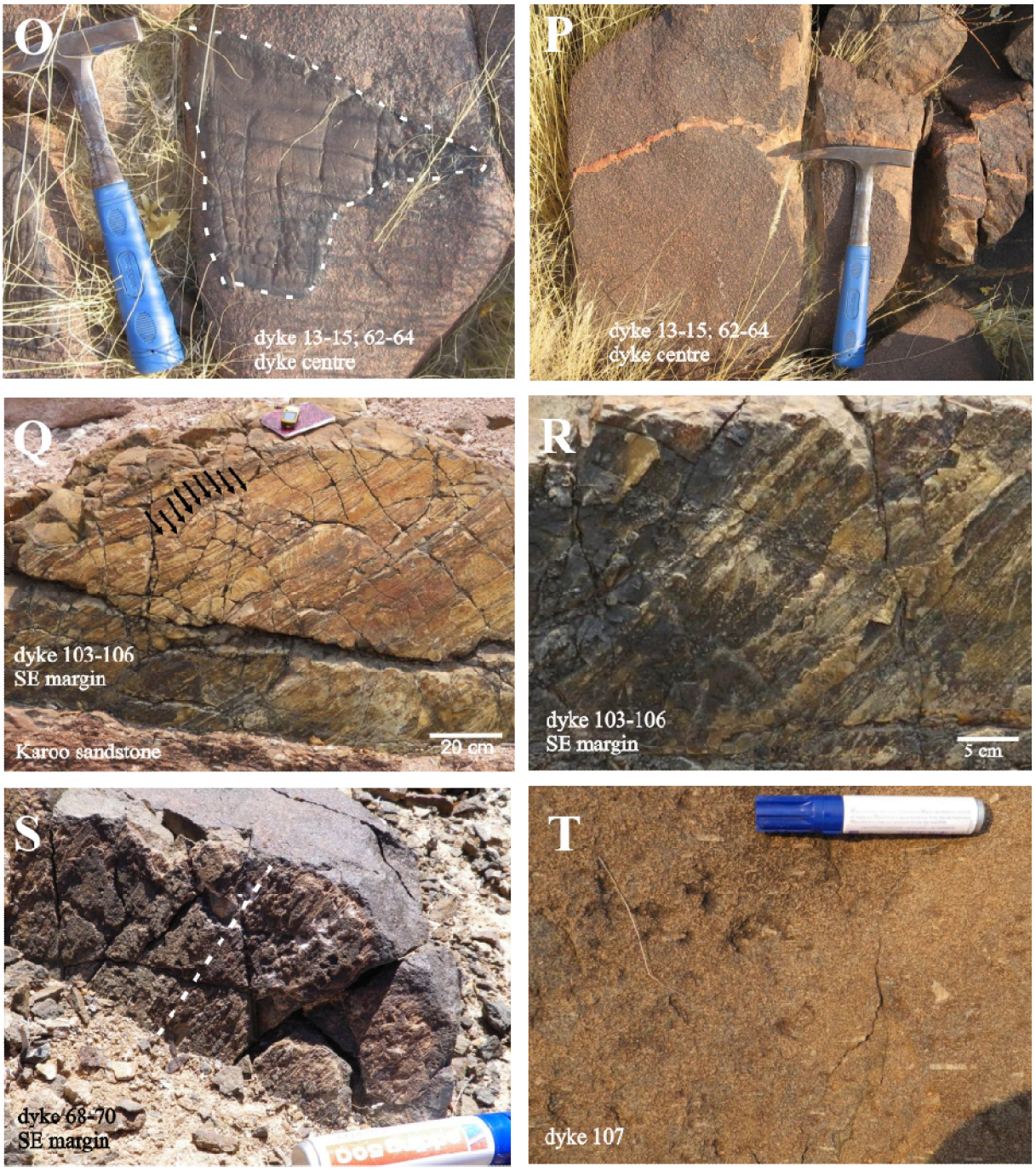

Figure 5-31 O-T. Field observations, continued. O & P. Magma mingling in a kink area of a 30 m thick dyke, near Grosse Spitzkoppe. O. Fine-grained dark material (marked with white dashes) surrounded by brighter coarser grained rock. P. Felsic magma vein in mafic dyke rock. Q-S. Surface lineation on dyke walls. Both curved (black arrows in C) and straight dyke wall surface lineation on pale-brown altered outer dyke margin. Dykes in Q &R intruded into Karoo sandstones at Mt. Klein Etjo, S in metasediments at the Omdel dam. T. Dyke-parallel oriented bright plagioclase phenocrysts in a WNW striking dyke situated in the NE striking Waterberg Fault zone. Topview.

Dyke margins, dyke-in-dyke intrusions and intersections

Dyke margins are variable in scale with a thickness of about one up to eight centimetres. Commonly, the margins are more closely fissured and finer grained than the rock in the dyke centre or even glassy, due to rapid cooling ("chilled margins"). Sometimes, they can be distinguished from the inner dyke parts by colour, such as pale yellow-brownish alteration colours or, for example, they are darker (Figures 5-29 I, J & 5-31 Q-S). At places, dyke margins are eroded at the contact with the country rock. However, chilled or fine-grained dyke margins are not only found at the contacts, but also inside the dykes (dyke no. 28, 39-43). They are about 1 cm thick and run parallel with the dyke strike, allowing recognition of dyke-in-dyke intrusions (Figures 5-29 K, 5-30 L). Variations of these composite dykes are observed along strike of dyke 39-43: This dyke is composed of several individual dykes, each one not thicker than 15 to 20 cm, at places separated by flakes or strips of host rock ,and sometimes, as dyke-in-dyke-intrusion with chilled margins of each inside of the earlier one (Figure 5-30 L, M). Another example crops out at the Gross Spitzkoppe area, where a a NNE striking 25 cm thin dyke (samples 24+25) intruded into the NE-striking, 5 m thick older one (dyke no. 23/26/56). The thin and younger dyke runs for a few metres nearly parallel within the older one before it bends when meeting the margins of the older dyke and continues at an increased angle in the country rocks (Figure 5-28 F).

Outcrops of dyke intersections are often covered by Quaternary deposits, or dyke rocks are intensely jointed and eroded at this point, which complicates the examination of the contact and the determination of relative dyke ages. Unfortunately, the intersection of dykes 111-112 and 113-114 is such a case. But, two dyke intersections at Omdel dam were found to be well exposed: The 10 m thick WNW-striking dyke represented by sample numbers 73-76 is younger and cuts a swarm of parallel NE-striking older and thinner dykes (dyke 79-81; intersection at -21°53'49.45''S, 14°34'14.26''E; and dyke 82-85). The chilled margin of the WNW dyke 73-76 was found in contact with the NE striking dyke 79-80 (Figure 5-30 N). About 13 km WNW of these intersections, again a NW-striking dyke (no. 100-102) is observed to cut two older dykes (intersection coordinates -21°52'12.72''S, 14°26'42.24'' E and -21°52'20.74''S, 14°26'59,60''E) with northeastern strike directions.

Lineations on dyke walls

On the wall of the SW-NE striking (50-54°) dyke 103-106 (0.6 m thick) in contact with Jurassic sandstone country rocks west of Mt. Klein Etjo, a pronounced lineation with continuous inclined plunge is noticeable (Figure 5-31 Q, R) on both dyke walls. This lineation can be described as uniformly oriented grooves and ridges all over the dyke`s surface that has already been altered to a yellowish-brown, probably clay-rich material in the about 1 cm thick outer margin range. At the site of the more southerly samples 103 and 104 dyke dip is inclined to the NW (321/49) and lineation plunges 343/46. Especially at the site of sample 106 the steeply SE dipping dyke wall (144/80) at this location is largely exposed over a few metres and a varying depth up to 1 m. There, the plunge of lineation (209/41) is observed to vary weakly up to 15°. An inclined lineation on the southern dyke margin is encountered at a second dyke: the 2.5 m thick dyke 68-70, directly SW of the Omdel dam, but this lineation on a hand-sized dyke surface area rather looks like elongate vesicles in the porous rock margin (Figure 5-31 S). Lineations are displayed together with the AMS and AARM fabric ellipsoids in the lower hemisphere projections, Appendices 12 & 14. For all these sites, lineation is either interpreted to record the magma flow direction at the contact with the country rock in the initial state of dyke emplacement or, alternatively, to record tectonic shear at the dyke walls contemporaneous with magma injection. This latter interpretation is supported by the angular discrepancy of about 20 to 30° between the maximum/long principal susceptibility axis (κ_{max}) and macroscopic dyke wall lineation.

Oriented feldspar phenocrysts

1-2 cm sized tabular feldspar phenocrysts, which are clearly aligned with their long axes parallel with the dyke strike were observed in the coarse grained, 5 m thick dyke (sample 107, Figure 5-31 T) at Mt. Klein Etjo. The phenocrysts are interpreted as magma flow indicators. The alignment has been observed on a horizontal rock plane, suggesting that magma flow was horizontal, but a vertical alignment cannot completely be excluded. As the dyke is strongly eroded, with only a few huge in situ boulders

of 1-2 m in diameter remaining, the dip angle of the dyke could not be measured and is assumed to be nearly vertical like most other dykes where dips were determined.

Country rocks and their interaction with dykes

Field observations show that the dykes intruded into folded, sometimes migmatized crystalline rocks, such as mica schists, calc-silicate rocks and marbles, and also into granites and sandstones. Neoproterozoic Swakop Group gneisses, mica schists or migmatites of the Namibian aged Damara Sequence can be found in the Omdel dam, northern Okombahe and Gr. Spitzkoppe areas and marble or calc-silicate rocks (nos. 16-17, 62-64, 27-32, 52-53) at Gross Spitzkoppe, Omdel dam and Kalkfeld areas. The Bocock's Bay dykes (nos. 91-99) and Okombahe dykes (nos. 1-2; 7-8) intruded into Cambrian and syntectonic granites. Jurassic Karoo sandstones host dyke 103-106 and mudstones host dyke no. 108-110 at Mount Klein Etjo area (Figure 5-25).

To a degree, dyke strike is influenced by the host-rock structures. At the Omdel dam area in gneiss or schist host-rocks, a dyke is observed parallel with the foliation for a certain length and then cuts across it (Figure 5-26 B). The same can be seen on a regional scale from satellite images. Non-parallelity of dykes with the host-rock foliation is often observed in the field (Figure 5-27 C & 5-30 M).

The 30 m thick dyke near Gross Spitzkoppe (samples 13-15 and 62-64) was sampled in the place where two laterally displaced segments combine via a segment deviating from the regional strike of that dyke. In this part of the dyke, felsic material is noticed to interfinger with the mafic dyke rock and, vice versa, dyke rock-fingers are found in felsic country rock (Figure 5-31 O, P) within the dyke's interior. Also, in the thin dyke 16/17 a head-sized part of the host granite is found (Figure 5-23 B). The felsic partly molten rock within the dykes is interpreted as a former bridge of country rock between two previously separated and now merged dyke segments.

6 Geochemical classification of the dyke rocks

36 out of 42 dykes have been analysed geochemically for major and trace elements (Appendix 2). The total volatile contents in the samples (sum of $H_2O + CO_2$, or loss on ignition, LOI) varies from about 1 to 6 wt% because of variable presence of alteration minerals like sericite and chlorite and carbonate-filled round vugs and veinlets. To avoid influences of these secondary effects on comparisons of dyke rock compositions, the descriptions and diagrams are based on data recalculated to total 100 wt.% on a volatile-free basis, and with total Fe expressed as FeO. Appendix 2 reports the measured, uncorrected compositions and Fe as FeO and Fe_2O_3.

After the Total Alkali vs. Silica (TAS) classification diagram (Figure 6-32) most of the 42 dyke rocks can be classified as subalkaline basalts and some are basaltic andesites. As described earlier by Frei (2011) and Trumbull et al. (2004) the rocks follow a tholeiitic trend. A few samples have higher alkali contents and plot in the fields of alkaline basalts, basanite and trachybasalt. SiO_2 contents vary from 44.5 to 54.6 wt%. Dyke 58-59 is a more evolved trachyandesitic outlier with 59 wt% SiO_2. The alkali contents ($Na_2O + K_2O$) range from 1.9 to 6.6 wt%. One exception is the phonolitic dyke 48 containing 16.9 wt% alkalis.

Figure 6-33 shows the magnesium (MgO), iron (FeO) and titanium oxide (TiO) contents of the rocks. MgO contents range from 4.21 to 11.89 wt%, with two exceptions (no. 48 and 59) having contents of 0.12 and 1.52 wt%. Iron oxide contents vary from 8.5 to 13.9 wt% with a minimum and maximum outlier of 6.3 and 15.6 wt%, respectively. After Ewart and others (1998), all but three samples belong to the low-titanium type with Ti-contents < 2.5 wt%. Samples no. 36 and 44 hold slightly higher Ti contents of 2.7 and 2.6 wt% while sample no. 50 stands out with a Ti-content of 3.3 wt% and belongs to the high-Ti-type volcanics.

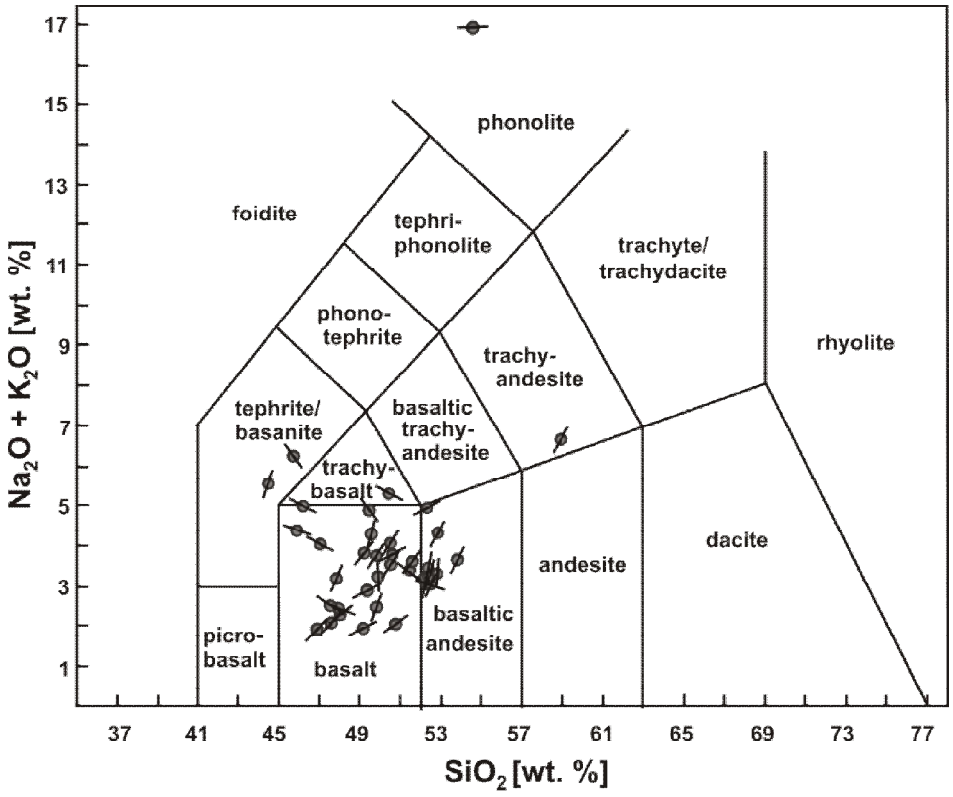

Figure 6-32. Total Alkali vs. Silica (TAS) diagram classifying the HOD samples geochemically as dominantly basaltic**;** data from R. B. Trumbull, GFZ Potsdam. Dyke strikes given by the bars (vertical = 0°; horizontal = 90°) at the sample points show that there is no relation between dyke strike and geochemistry.

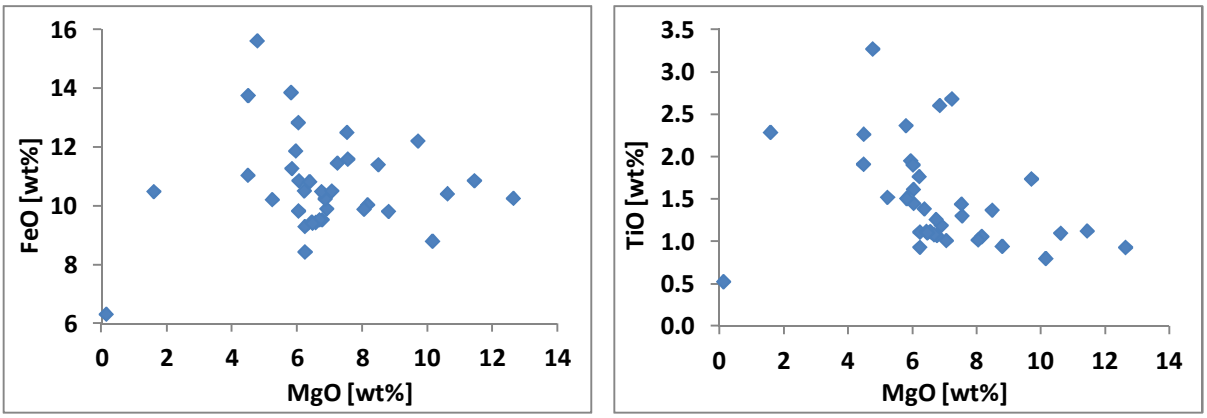

Figure 6-33. Harker diagrams showing the dyke rock`s iron and titanium oxide contents vs. the content of magnesium oxide; data from R. B. Trumbull, GFZ Potsdam.

7 Results

7.1 Petrography of the samples

The grain size of the dyke rocks ranges from aphanitic or very fine grained up to a few millimetres, with sizes increasing as a function of dyke thickness. Plagioclase-phyric rocks are very common, but the thicker dykes with a more gabbroic texture also show olivine and pyroxene phenocrysts (e.g. Figure 7-34 D). Most of the mafic dyke rocks appear relatively fresh in the field with grey to dark grey colours on fresh surfaces. An exception was dyke 103 to 106 in the sandstones, which appeared yellow-brown altered (Figures 5-25 A, B & 5-31 Q, R). Towards the dyke margins, alteration commonly increases with yellow-brownish secondary mineralization. Unaltered dyke margins commonly show or black-brown colours from glassy or devitrified quench texture due to rapid cooling. Moreover, margin rocks are often narrowly fissured with open fissures or alteration advancing from there into the rock.

Transmitted-light microscopy

53 samples (56 thin sections) have been investigated microscopically in transmitted light. Appendix 3 provides a detailed summary of the observations. Mineral contents are given in volume percent (vol%) from visual estimates, where grain sizes were coarse enough and alteration sufficiently weak to allow mineral recognition. Some thin sections were not examined in detail, since they were especially prepared for image analysis of plagioclase orientation. In these cases, the presence of minerals is acknowledged by the symbol "x", but without volumetric abundance. Microscopy revealed that the samples typically consist of abundant plagioclase (40-70 vol.%), common (clino-) pyroxene and 3 to 5 vol.% titanium-iron oxides, such as titanomagnetite and ilmenite. Olivine and orthopyroxene are locally present in minor amounts. Plagioclase often has a seriate grain-size distribution, occurring in the matrix as microphenocrysts, as phenocrysts, and locally also as oscillatory zoned, large xenocrysts, wich are sometimes broken (samples 76 and 77). Plagioclase crystals are mostly lath-shaped or thin-tabular, often with lamellar twins (e.g. samples 8, 16, 71; Figure 7-34 A-G). Occasionally, clinopyroxene and olivine occur as phenocrysts in the basalts. Reddish-brown titanium-(Ti-) augite occurs in (at least) 7 dykes (36, 40, 41, 43, 44, 51, 62) with alkaline compositions. Brown hornblende is present as a minor phase in samples 37, 40 and 62, and is more abundant in samples 31, 44 and 80 with 15 to 25 vol.%. In samples 36 and 44, hornblende grows around Ti-augite cores at the expense of the latter. Accessory apatite is found in samples 13 and 28, and chrome spinel in no. 28.

Microscopic textures are often intergranular to ophitic or subophitic, with intergrown plagioclase and clinopyroxene. Titanium-iron oxides are usually found in the interstices, together with groundmass minerals. Thin sections from the outer dyke margins commonly show chilled glassy or devitrified fabrics, sometimes strongly replaced by very fine brown material, presumably clay minerals. Thin sections from close to the margins are often vitro-or porphyric with individual feldspar-phenocrysts and rarely phenocryst-agglomerates. Others from thin dykes (16, 17, 103-106) show an intersertal texture, where glass occupies the interstices between microphenocrysts. Sometimes the latter show quench textures, with skeletal crystals of plagioclase in the form of fibrous sheaves and needles (samples 60, 52-53, 103-106). The rock samples from the very close and parallel dykes 33 and 73 to 85 are very similar in texture and composition (see also Appendix 2). Samples 22 and 24 are from very thin dykes and show an almost complete alteration of almost all the primary minerals. They have been replaced by yellow-brown, very fine-grained phyllosilicates.

25 of the samples display weakly to distinctly oriented fabric with aligned plagioclase phenocrysts. Locally, pyroxene and rarely olivine phenocrysts also contribute to the alignment. The degree of alignment is evaluated and documented in Appendix 3. Not only phyric or vitrophyric sections at the direct dyke margins (for example samples 21, 16, 86, 87) have a distinctly oriented silicate fabric, but also rock sections 20 up to 50 cm away from the margins, such as samples 16, 19, 28, 31, 36 or 93-95, with intersertal and intergranular to (sub-)ophitic textures. Thin sections 41 and 43 clearly expose a flow fabric: elongate crystals are aligned (Figure 7-34 H) and the opaque phases are anhedrally elongate and even curved (Figure 7-36 B). In thin section 64 two different rock types (basalt and

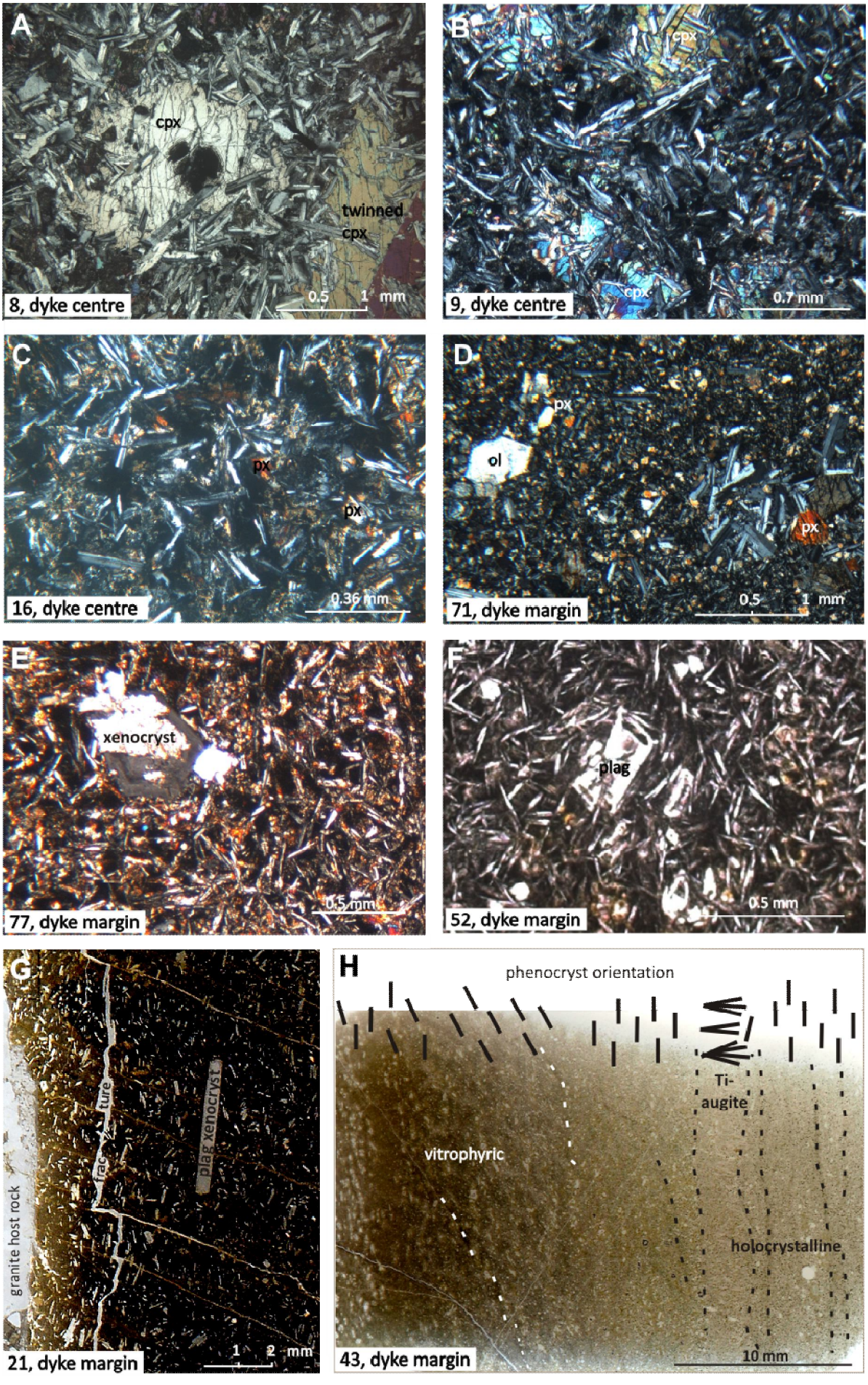
A
cpx
twinned cpx
0.5 1 mm
8, dyke centre
B
cpx
cpx
cpx
0.7 mm
9, dyke centre
C
px
px
0.36 mm
16, dyke centre
D
px
ol
px
0.5 1 mm
71, dyke margin
E
xenocryst
0.5 mm
77, dyke margin
F
plag
0.5 mm
52, dyke margin
G
granite host rock
fracture
plag xenocryst
1 2 mm
21, dyke margin
H
phenocryst orientation
Ti-augite
vitrophyric
holocrystalline
10 mm
43, dyke margin

Figure 7-34. (previous page). Textures of the HOD rocks. A to F show transmitted-light micrographs of polished thin sections (TS) in cross-polarized light. G & H present parts of scanned polished thin sections. Sample numbers in the lower left. A) ophitic intergrowth of large clinopyroxene (cpx) and smaller grey-white plagioclase (plag) crystals; B. subophitic intergrowth of cpx and plagioclase laths; C & E. intergrowth of plagioclase laths and pyroxene (px), intersertal; D) porpyritic to glomerophyric texture with px, plagioclase and olivine microphenocrysts in a hypocrystalline matrix composed of px, plagioclase and glass; F. vitrophyric to intersertal fabric with plag (white) laths. a few tabular skeletal crystals and roundish px (yellow-orange);G. vitrophyric flow fabric at the dyke margin (left): dyke-parallel oriented plagioclase xeno-and microphenocrysts in a dark glassy matrix; H. vitrophyric to holocrystalline flow fabric at the dyke margin (left edge of TS) with phenocryst long axes parallel or with low angle (max. 45°) to the dyke margin; dashed lines accentuate dyke-internal planes, black bars in the upper part symbolize the preferred orientation of elongate crystals in the according part of the thin section. Note the domain with fanning Ti-augite arrangement with crystals long axes perpendicular to the dyke plane.

calc-silicate rock) can clearly be distinguished next to one another: a finger of calc-silicate rock is surrounded by basaltic dyke rock. The calc-silicate rock is most probably derived from the adjacent country rocks and contains distinctly aligned feldspar laths and a finer grained fabric than the basaltic part. This microscopic study confirms the macroscopic field observations (compare Figure 5-31 O, P).

Locally, voids are observed macroscopically (samples 73-76, 58-59) and they seem to originate from alteration of minerals (samples 73-76) rather than vesicles, since their shape is most often angular. Microscopically, voids are seldom and only observed in thin sections 24, 28, 31, 58-59 and 70 where they are rounded (indicating magma degassing) and secondarily mineralized with chlorite, other phyllosilicates, quartz and carbonate. Microjoints or veinlets are frequent in the margin sections and sometimes filled with secondary minerals like calcite and quartz. Their density and frequency decreases distinctly with increasing distance from the dyke margin. Sample 19 is intensely jointed although it is 0.5 m away from the dyke margin.

Common alteration minerals identified in transmitted-light include calcite, sericite, chlorite, biotite, serpentine and epidote/clinozoisite. Calcite and chalcedony occur in voids; sericite and chlorite partly replace plagioclase to variable degrees. Olivine and Ti-augite rims are often opacitised, and in rare cases, complete crystals are affected (samples 13-15, 62-64, 40, 41, 43). Further, olivine is locally replaced by serpentine or iddingsite (mixture of fine-grained goethite, chlorite, clay minerals among others). Saussuritisation of plagioclase (replacement by more albitic plagioclase and epidote) is observed in sample 80.
Strong alteration of the entire rock is observed in only 13 samples (see Appendix 3) distributed over the dyke swarm: 13, 19, 28, 31, 36, 40, 64, 70, 76, 77, 80, 96 and 97. In these cases, mostly a strong carbonatization was recognized, accompanied by abundant sericitisation of plagioclase and chloritization of plagioclase and pyroxene. Most of these strong and less strong alterations can be ascribed to hydrothermal activities by meteoric fluids.
Only very locally, bent or broken pyroxene and plagioclase crystals are observed or their undulatory extinction (e.g. samples 2, 9, 13, 57, 76, 80). These features may point to cooling stresses within the solidifying magma.

7.2 Magnetic mineralogy

7.2.1 Reflected-light microscopy

The reflected-light microscopic observations are summarized in Appendix 3. Iron-titanium-oxides are accessory with estimated 3 to 5 vol.%. Thereof, titanomagnetite (tmt) is the most abundant opaque phase with more than 50 vol.% in 21 of the 35 evaluated thin sections, as Figure 7-35 shows. Four thin sections show 5 or less vol.% of titanomagnetite and instead contain abundant (haemo-)ilmenite. There are two exceptions: sample 58-3 from inside of the 6 cm thick chilled margin, where 80 vol.% of the opaque phases is made up by sulphides (pyrite, pyrrhotite and other undefined ones); and sample 28 has about 30 vol.%. sulphides among the opaque phases. Apart from these, sulphides are present in minor amounts in most of the dyke rocks. Occasionally, also haematite occurs as product of tmt

oxidation. Haematite and probably also iron hydroxides, in places, are finely dispersed, replacing the primary iron-titanium oxides tmt and ilmhm. Increased amounts of haematite are found in sample 76, where haematite (martite) pseudomorphically replaces about 50 vol.% of tmt.

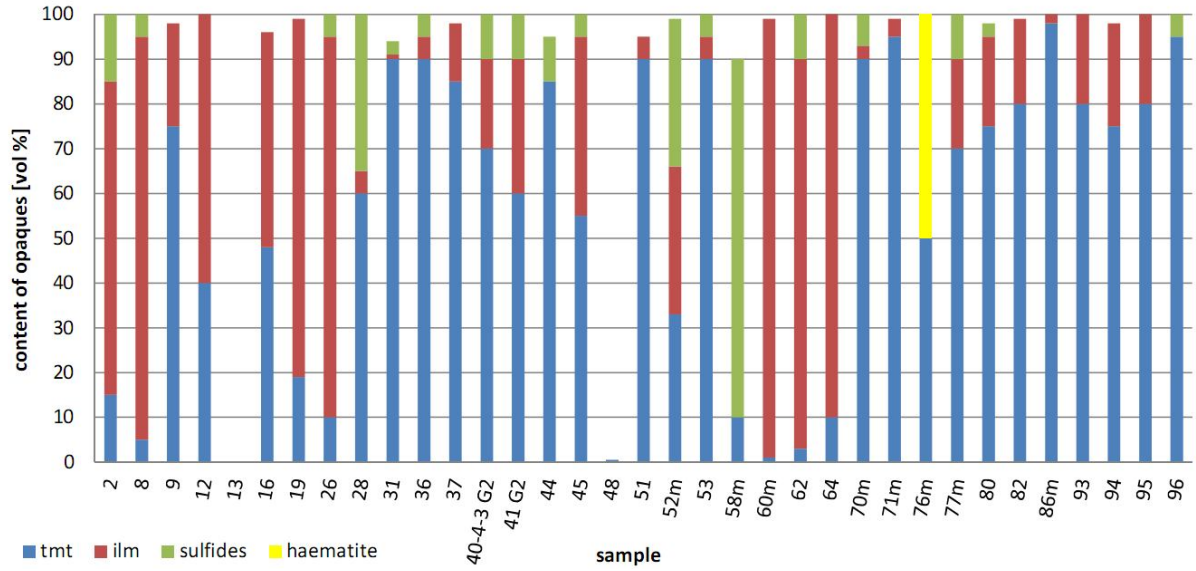

Figure 7-35. Diagram summing the contents of major opaque minerals in the studies thin sections; percentages estimated on the basis of 100% opaque phases; minor amounts of iron oxides and hydroxides not included

Opaque phases are distributed in the interstitial matrix and sometimes directly border pyroxene crystals and plagioclase (Figure 7-36 A-C). Titanomagnetite and (haemo-) ilmenite/ ilmenohaematite crystals are mostly found in euhedral or subhedral crystal shapes. Strongly aligned elongate, but anhedral tmt together with ilmenohaematite occurs in the flow fabric of sample 41. In about 35 % of the thin sections, octahedral-shaped or elongate or cruciform dendrite (skeletal) titanium-iron oxides are found. In another 30% of the thin sections titanomagnetite and ilmenohaematite are, in places, complexly intergrown. Euhedral tmt occurs in octahedrons. If not intergrown, ilmenite is observed as elongate shapes or bars. Dendrital shapes of ilmenohaematite are needles or fish bones. Tmt-dendrites are cruciform or with a main branch forming an elongate shape (sample 57), branching perpendicular (Figure 7-36 D) and, in places, terminate with a more or less euhedral octahedral crystal. Cruciform dendrites often share one branch, which creates an elongate overall shape, as can also be seen from Figure 7-36 D. Crystals with melt inclusions are observed occasionally (samples 37, 96). Pyrite and pyrrhotite most often form isometrical crystals much more fine-grained (5-20 µm) than, and frequently associated with, tmt (Figure 7-36 E-G) and ilm crystals. Grain sizes of tmt vary on average between 1 and 200 µm, or even larger in a few samples. A few thin sections are generally very fine grained and reveal very small Fe-Ti-oxide grains between 1 and 10 µm or even below 1 µm. Grains smaller than1 µm belong to the single- or pseudo-single domain range and are beyond the microscope resolution, but are expected to be present in some samples, such as in sections 52, 76 and 85, where crystal sizes are generally small.

Exsolution of thin ilmenite lamellae is a very common phenomenon in the tmts of the sample set (Figures 7-36 F & 7-37 C, D.). About half of all the examined samples (14 out of the 34) with abundant tmt display a variable amount and density of exsolution lamellae (Appendix 3). The subsolvus exsolution/decomposition of tmt is the product of magma cooling, but may also occur during deuteric/high-temperature oxidation (see chapter 3.7).

Fresh tmt was encountered in only a few samples. Frequently tmt, and occasionally also ilmenite, shows a certain degree of alteration. The use of ferrofluid to make alteration on tmt more visible was partially successful. Normally, the colloid is attracted by the ferrimagnetic tmt (and also by ferromag-

netic pyrrhotite), marking them with a reddish-brown coating. In many of the examined thin sections, however, tmt does not dye uniformly, but irregularly or blotchy/patchy with more or less intense dye.

Blotches are rounded, ellipsoidal or irregular in shape, as depicted in Figure 7-36 C. Borders of patches are either relatively sharp (e.g. samples 45 & 51, Figure 7-37 A & B), ascribed to ilmenite

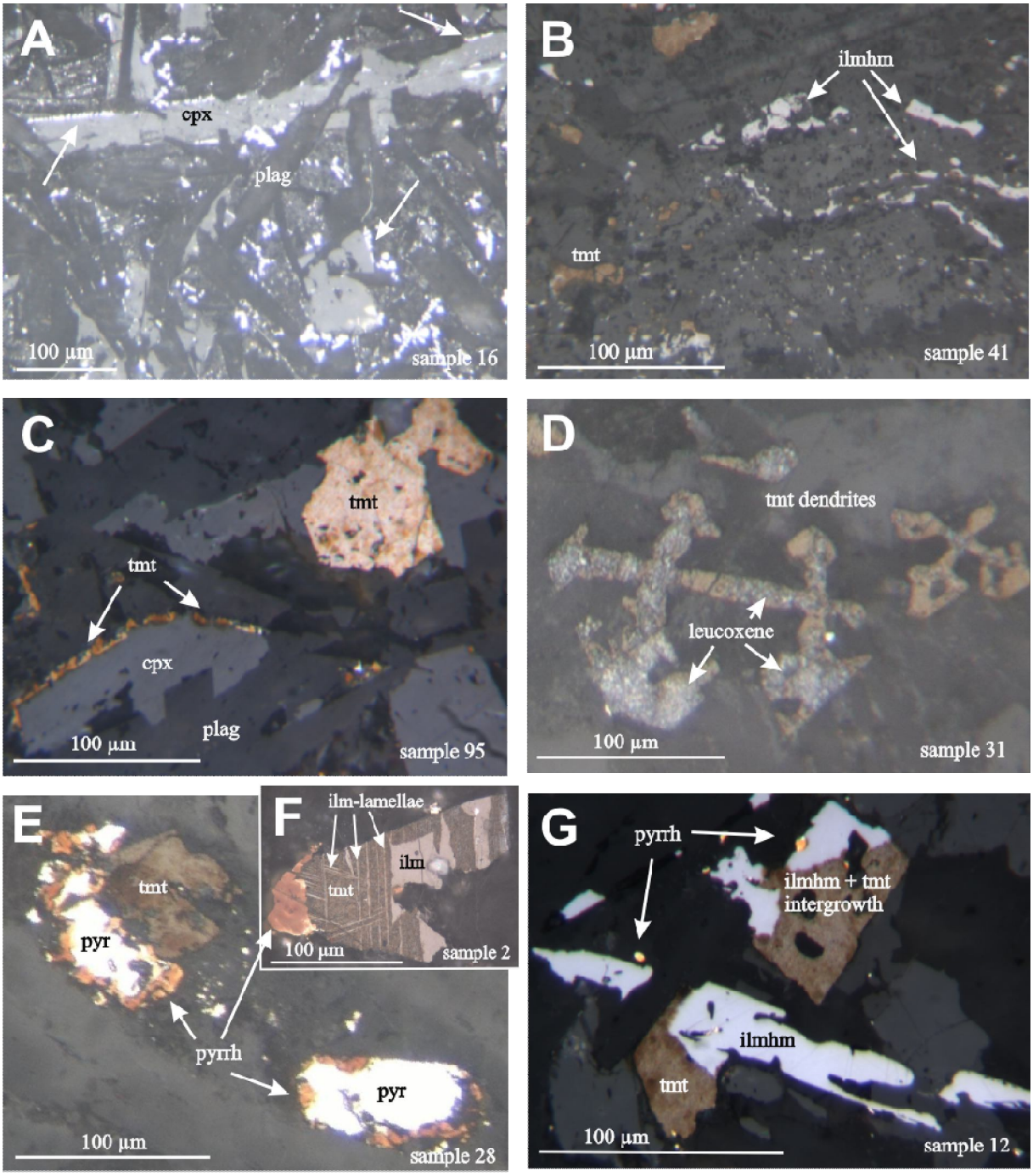

Figure 7-36. Reflected-light microscopy; A-C. Preferred orientation of opaque phases; D-G. Variety of opaque phases, shapes and intergrowths: A. Arrows point to titanomagnetite (tmt) and ilmenohaematite (ilmhm) dendrites aligned alongside of clinopyroxene crystals. B. Flow fabric with anhedral elongate ilmhm-and tmt-phases. C. Tiny aligned tmt-crystals rimming clinopyroxene next to a larger euhedral tmt. D. Tmt-dendrites with leucoxene (greyish parts). E & F. Association of tmt with pyrrhotite and pyrite. Note exsolution lamellae of ilm in tmt of a tmt-ilm intergrowth. G. Common intergrowth of tmt and ilmhm in eu- to subhedral crystals. Note tiny pyrrhotite in association with tmt-ilmhm. Thin sections B to G were treated with ferrofluid.

exsolution, or patches gradually fade to weaker dyed parts (Figure 7-36 C), ascribed to a variably strong alteration, or maghemitization (chapter 3.7.5), which may reduce the magnetic susceptibility. Normally, stronger maghemitization is accompanied by Fe^{2+}- and volume loss, but shrinkage cracks are rarely found, such as in sample 51 (Figure 7-37 B), where strong maghemitization is also indicated by the κ-T curve (see chapter 7.2.2). Consequently, from the scarcity of cracks in other HOD samples, it is concluded that, in general, maghemitization is rather weak.

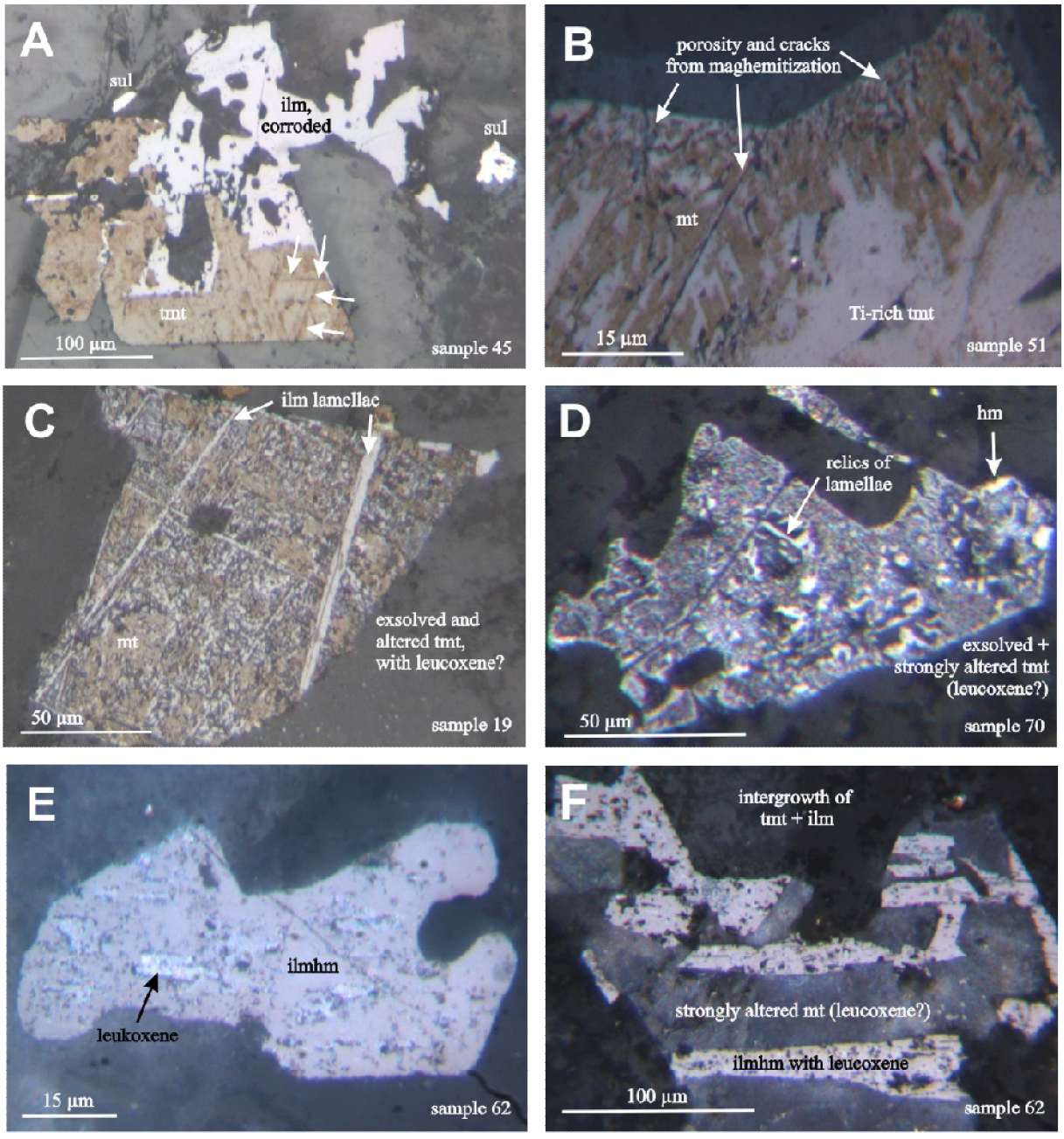

Figure 7-37. Reflected-light micrographs showing alterations of titanomagnetite (tmt) and ilmenohaematite (ilmhm). All fotos taken in plane-polarised light. Thin sections have been treated with ferrofluid. A. Tmt-ilmhm intergrowth. Ilmhm is corroded while tmt reveals signs of beginning exsolution into Ti-poor tmt or magnetite (deeply red-brown) and ilm (pale red-brown). Exsolution lamellae are oriented parallel to crystal lattice (see arrows). B. Partially exsolved tmt with Ti-rich (pink) and Ti-poor tmt/magnetite (red-brown) with fractures and secondary porosity indicating volume loss during maghemitization (compare κ-T curve 51-4). C & D. Exsolved tmt with alteration, presumably leucoxene, and secondary porosity. E. Subhedral ilmhm with leucoxene. F. Tmt-ilmhm intergrowth with porous ilmhm and strongly altered tmt.

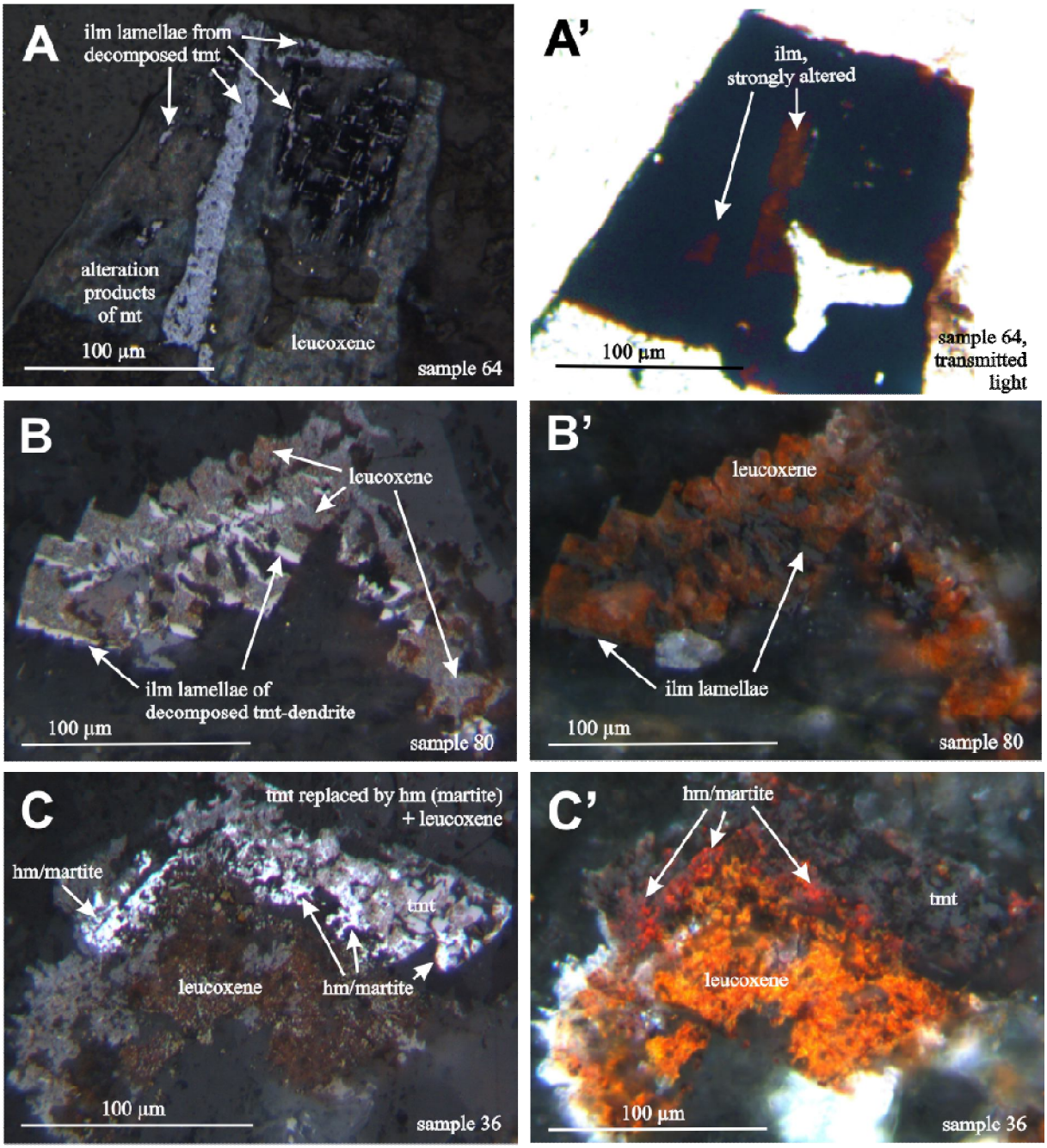

Figure 7-38. Examples of strong alteration of tmt and ilmhm in reflected light micrographs. A, B, C in plane-polarised light, B' and C' with crossed polarizers, B' in plane-polarized transmitted light. A & B. Euhedral tmt, strongly altered with leucoxene,with two thick ilmenite (ilm) lamellae and relics of thin exsolution trellis of ilm. Note that the thick ilm lamella in A' and also parts of the remaining tmt are transparent. B & B'. Exsolved tmt-dendrite; Ti-poor tmt between the ilm lamellae is strongly replaced by leucoxene. C & C'. Strong alteration: leucoxene and haematite (martite) replacing primary tmt.

In sample 51 ferrofluid attraction of tmt is barely noticeable in sharply defined parts (Figure 7-37 B), probably because of the high titanium content (compare with κ-T curve, chapter 7.2.2, Appendix 4). Only a few intensely dyed spots or areas occur, probably where pure magnetite is bound by ilmenite lamellae.

Some parts of tmt or even entire grains do not attract the ferrofluid at all (Figure 7-38 A-C). They are interpreted as being strongly altered. Often, leucoxene is recognized (Figures 7-36 D, 7-37 E-F, 7-38 A-C), which is described as a non-resolvable fine- or coarser grained mineral mixture of haematite (white in reflected, red halos in transmitted light), rutile (dark brown in transmitted light, Figure 7-38 A', B', C'), anatase and titanite (Pichler & Schmitt-Riegraf, 1993) in varying fractions. Strongly altered and unmixed Fe-Ti-oxides with leucoxene (red halos, white reflexions, brown mineral phases) are observed in samples 13-15, 36, 64, 80 (e.g. Figures 7-37 D, E, 7-38 A-C) and are interpreted as product of hydrothermal alteration. Strongly altered crystals are observed to become porous (13, 19, 70, 36, 62, see Figure 7-37 B-D). Furthermore, moderate to completely opacitised olivine is encountered in samples 13-15 and 62-64, which are all from the same dyke. Opacitisation produces tiny secondary magnetite grains among other minerals, which pseudomorphously replaces olivine.
In some thin sections, tmt and/or ilmhm crystals are strongly corroded, most often with worm-shaped texture. While in some samples ilmhm corrodes and tmt remains intact (Figure 7-37 A), it is the opposite in others, where ilmhm or Ti-rich tmt is more stable and Ti-poor tmt is strongly replaced by leucoxene or oxidised to martite, Figure 7-38 C, C'). The corrosion is probably primary magmatic and not secondary.

7.2.2 Temperature-dependence of the magnetic susceptibility

The temperature dependence of the magnetic susceptibility (κ-T) of 56 samples from 35 dykes was determined in order to identify their dominant magnetic phases. An overview of the κ-T samples with characteristic features of the curves and/or their interpretation are summarized in Appendix 5 and all the κ-T curves are displayed in Appendix 4. Generally, one measurement per sample was performed, but from selected samples several κ-T curves were produced to test variations within the dyke between dyke margins and dyke centres and also to test data reproducibility. Consequently, a total of 65 κ-T curves were produced. Additionally, four of the samples (33, 45, 49, 50) were exposed to a second measuring cycle of heating and cooling on the same rock powder that has already been used during a first cycle.

The measurements produced mostly irreversible curves when comparing heating and cooling runs. It is inferred, therefore, that mineralogy changed during the measurement at higher temperatures. Also, the four repeatedly measured κ-T curves are irreversible, indicating mineral reactions during the measurments. Most often, both the magnitude of susceptibility, as well as the Curie Temperature (T_C), differ in the associated heating and cooling curves. Only six of the measurements (samples 16_{-7-5}, 26_{-10a}, 39_{-4}, 40_{-1-3}, 41_{-1-2}, 58_{-5}) show reversible heating and cooling curves. The κ-T curves are grouped according to the magnitude of their mean bulk susceptibility (κ_m) into "low-κ" (29 curves) and "high-κ" (36 curves). All curves of samples with κ_m below $10*10^{-3}$SI, plus two exceptions with 11 and $13*10^{-3}$SI, belong to the low-κ group, the others to the high-κ group. According to the characteristic low-temperature behaviour of some samples, this group is again subdivided into low-κ_F (F = "ferrimagnetic") and low-κ_M (M = "mixture of ferri- and paramagnetic minerals"), which are 12 and 17 curves, respectively. High-κ and low-κ_F curves are not distinguishable. Only low-κ_M curves are different concerning the low-temperature range of -192°C to -160°C. Figure 7-39 shows that low-κ curves are marked by a hyperbolic course starting at the lowest temperature range (c. -192°C), also decribed as "concave" following the Curie law ($\kappa_{para} = C/T$, Soffel, 1991). This decay of magnetic susceptibility is interpreted to indicate an (paramagnetic) ilmenohaematite with a composition close to ilmenite with a Néel temperature just below -192°C, beyond the monitored temperature range. The other types of κ-T curve lack the incipient decrease of susceptibility. Most often, they start with an increase of the susceptibility up to a more or less sharply defined peak at around -160 to -145°C. In agreement with microscopic observations of abundant titanomagnetite, this peak is interpreted as the Verwey-Transition (T_V) or isotropic point of magnetite (see e.g. Dunlop & Özdemir, 1997; Moskowitz et al., 1998) from a low-susceptibility magnetite with monoclinic to a highly susceptible crystal of cubic symmetry. All curves show a drop in susceptibility at a temperature interval between 480 and 580°C. In some cases, a sharp peak, known as the-Hopkinson peak, appeared before this drop (see also Just & Kontny, 2012; Vahle et al. 2007), such as in samples 2_{-6} in the cooling run and in the heating run of samples 29_{-2-2}, 33, 36_{-3-4}, 37_{-2-4}, 108 and 109. The Hopkinson peak is generally interpreted to be due to small single-domain grains of magnetite (Dunlop & Özdemir, 1993). The temperature of the peak just before the drop is interpreted as the Curie temperature (T_C). This method to determine T_C is called the "peak

method" (Lattard et al. 2006). A T_C of around 560-580°C indicates pure magnetite. If the T_C is shifted towards lower temperatures down to ca. 480 °C a magnetite-near Ti-magnetite/-maghemite with partial titanium or other cation substitution is indicated (see chapter 3.7.1). In some cases, the drop is first gradual over some tens of degrees Celsius and then steep, such as in examples 5_{-1} and 6_{-2} in Appendix 4. Two possible scenarios may explain this gradual transition: either a variable degree of tmt-maghemitisation, or the presence of tmts/tmghs with a varying Ti-content. In low-κ curves the background noise is relatively strong compared to the sample's susceptibility, which is documented by an increased curve oscillation, such as in samples 8_{-1-2}, 23, 48_{-2-5}, 58_{-2}, 60V, 61_{-2-1}, 80_{-2-1} or 100_{-1}.

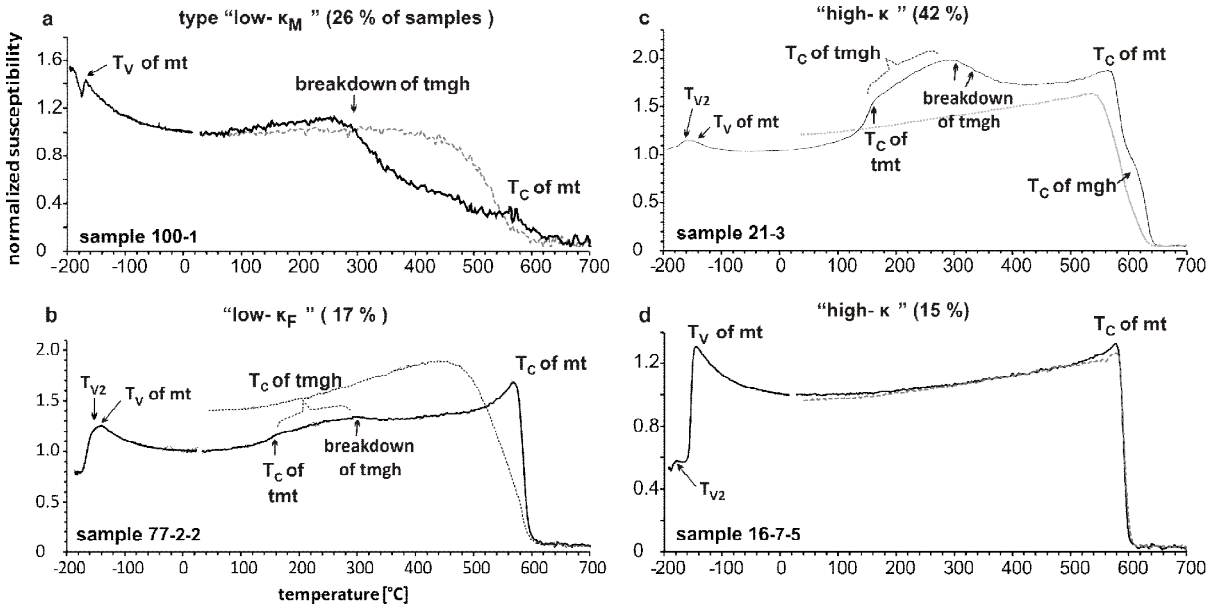

Figure 7-39. Types of temperature dependence of magnetic susceptibility (κ-T) curves and their frequency among the HOD samples. solid curves were recorded during heating, dashed ones during cooling (for explanation see text).

A common feature in low- and high- κ types is the normally irreversible "two-peak hump" at intermediate temperatures (Figure 7-39 a and c). This characteristic hump is variable in magnitude: in places pronounced, e.g. in samples 37, 76, 80_{-2-1}, and in others faint or almost not apparent (e.g. samples 77_{-1}, 95_{-1-3}). Normally, this hump disappears in the cooling curve, except for a very few cases, such as in sample 37_{-2-4}. The hump typically starts with a sharp increase of susceptibility up to the first peak at around 150-160°C, and is followed by a less steep increase up to the second peak at around 260-300°C. These two peaks are not sharply defined and sometimes shifted by some tens of degrees Celsius. On the basis of microscopic observations, relevant quantities of strongly magnetic minerals other than ilmenite and Ti-magnetite/-maghemite are not probable. Consequently, the "two-peak hump" is interpreted as a partly oxidised/maghemized intermediate Ti-magnetite, where the first peak (at T_C = 150-160°C) is the original titanomagnetite with an ulvospinel (Ti) component (X_{Usp}) of about 0.6 (TM60) and the rest of the hump including the second peak (around 260-300°C) are titanomaghemites with a variable degree of maghemitization and decreasing X_{Usp}.down to 0.4. The ulvospinel content is calculated from the T_C with an equation given in Lattard et al. (2006). This ulvospinel content also coincides with the T_C – temperature graph of Akimoto et al. (1957; referenced in Soffel, 1991). Depending on the state of maghemitisation, X_{Usp} content is slightly higher, as T_C shifts to higher temperatures with increasing maghemitisation. Rarely, such an intermediate tmt-composition peak only appears in the cooling curve, e.g. 45_{-2}, indicating that these compositions are no longer stoichiometric.

The Curie-Temperature of titanomaghemite (tmgh) is often lower in the cooling path than in the heating path. This heating-caused shift or irreversibility is ascribed to a stoichiometric reordering of non-stoichiometric, metastable phases during the measurements. Maghemitization leads to non-stoichiom-

etry, which is compensated successively during heating by an annealing process creating Fe-poorer tmt (Oliva-Urcia et al., 2011). The T_C-shift in curves 49, 50, 51_{-4}, 53_{-6}, 104 and 110 between heating and cooling cycle is very strong. Low T_Cs in the heating cycle between -50 and 100°C suggest titanomagnetites with an ulvospinel component of around 0.8 – 0.9 (Akimoto et al. 1957 in Soffel, 1991), which have been partly maghemized. Otherwise, tmt with such a high ulvospinel content would be paramagnetic (Butler, 1992), which can be ruled out for these samples because of their high bulk susceptibility. The suggested maghemitization also matches with a poorly defined heating T_C of samples 50, 51 and 53 arguing for different maghemitization stages within the tmgh grains. On the contrary, the sharply defined heating T_C in sample 49, from the same dyke as samples 50/51, is interpreted as advanced and uniform maghemitization of the entire tmt grains from the rims to the grain centres. The cooling curves of all the three samples are nearly identical.

Generally, samples from different locations within the same dyke yield similar curves and, therefore, show similar magnetic mineralogy. Stronger variations may occur due to different alteration stages related to the position of samples within dykes and/or different cooling rates. For example, in dyke margin samples intermediate tmts may be preserved (slight humps) owing to rapid cooling against the cold country rock walls, while magma in dyke centres cools more slowly and tmt crystals may decompose to ilmenite and Ti-poor tmt or even magnetite**.** The three samples of dyke 58 perfectly illustrate this example: the chilled margin sample 58_{-4} and the near-margin sample 58_{-5} have relatively high κ_m and their ilmenohaematite content is only faintly indicated by a decreasing curve between -200 and -180 °. Sample 58_{-2}, which is the most distant from the margin, shows a hyperbolic or paramagnetic decrease of magnetic susceptibility with two low tmt/tmgh T_Cs at 440 and 560°C.

In the four samples that were measured repeatedly, the second-run curves differ from the first-run curves. In samples 33 and 45, both in the first and in the second run, the temperature ranges of heating and cooling cycle peaks do not coincide, indicating an ongoing reequilibration over various measuring cycles. In samples 49 and 50 the near mt-peak between 400 and 500°C coincides in temperature, but not in magnitude.

The Verwey transition or isotropic point peak is not always sharp, but sometimes broadened across 10 to 20°C (for example, samples 70SE, 77_{-2-2}, 77-1, 86_{-2}, 95_{-1-3}HV, 107, 110); in other samples two Verwey transitions occur. The second T_V is at slightly lower temperature, than the "regular" one described above. It forms a peak (16_{-7-5}, 20_{-6}, 23, 26_{-10a}) or a shoulder (samples 19_{-3-3}, 58_{-4}, 58_{-5}, 78_{-4}) left of the main T_V. Both the broadening and the doubling of the transition can be a consequence of minor substitution by Ti or other elements, or of a varying degree of tmt-maghemitization (Dunlop & Özdemir, 1997), possibly combined with a grain size effect – smaller grains being more strongly maghemized than larger ones (Mang & Kontny 2013). In places, this peak is suppressed in magnitude, such as in samples 34_{-1-1} or 20_{-6}, or completely missing, such as in samples 33, 37_{-2-4} and 108, which may result either from maghemitization, or from a higher portion of SD magnetite (e.g. Muxworthy, 1999; Moskowitz et al. 1998 and references therein) or because there is no magnetite in the sample. The latter may occur, when the mt, which is indicated by the T_C peak around 580°C, is formed during the κ -T measurement. In some curves, such as 49, 50 and 51_{-4}, the T_V likely is masked by a tmt/tmgh Curie temperature nearby, since a magnetite-near T_C is evident and, therefore, a respective T_V peak is expected.

The comparison of κ magnitude changes between cooling and heating runs, which is a consequence of mineral reactions during measurements, is expressed by an alteration index (Al-index; Just & Kontny, 2011; Hrouda, 2002). This index gives the difference between the normed susceptibility of both runs at room temperature, (Al-index = $\kappa_C$room - $\kappa_H$room). Elevated susceptibility in the cooling run produces a positive alteration index from >0 to 2.45 (mean = 0.6), indicating the formation of minerals with a higher susceptibility than their reactants, such as mt or tmt. This applies to 45 of the 65 κ-T curves in this study. An increased susceptibility in the cooling cycle may be acribed to the formation of Ti-poor tmt at the expense of tmgh, which is supported by the disappearance of the tmt/tmgh-T_C peak in the cooling curve. The Al-index of 4 samples is zero and negative values between -0.1 and -0.75 (mean = -0.4) were found in the remaining 12 samples. A negative Al-index implies a loss in susceptibility, which in this study is probably due to the breakdown of ferromagnetic mgh, and formation of antiferromagnetic haematite.

Finally, in 28 κ-T curves (43%), the susceptibility change is relatively low with Al-indices below ± 0.3 indicating minor mineralogical changes.

In some samples, such as 5_{-1}, 6_{-2}, 8_{-1-2}, 60V, 78_{-4} or 100_{-1}, where bulk susceptibility is low, a measuring artefact of unknown origin has been introduced at the beginning of the low-temperature run between -195 and -185°C, below the T_V temperature(s). A remarkable artefact, extending over the range of -192 to -160°C, is obvious in curve 80HV Appendix 4.

In summary, the κ-T curves reveal the presence of high-, intermediate- and low-Ti-titanomagnetites as evidenced by the varying Curie temperatures. Intermediate titanomagnetites/-maghemites (T_c = 150 - 310 °C, "hump-samples") and low-Ti titanomagnetites compositionally near magnetite (T_c = 400 to 580°C; e. g. samples 16_{-7-5}, 39_{-1-2}, 40_{-1-3}, 26_{-10}) are present in almost every sample. Near-ulvospinel compositions with T_Cs between -50 and 100°C, such as in samples 49, 50, 53_{-6} and 104, are rare.
Tmt/tmgh is interpreted to occur exclusively in primary titanomagnetite. Although the titanomaghemite formation is secondary, it reflects a primary Ti-rich composition of the originally titanomagnetite. In contrast, magnetite may be both primary, as a product of exsolution during cooling or deuteric oxidation, or secondary, formed during hydrothermal alteration or from tmgh-inversion during the heating cycle of the κ -T measurment.

7.2.3 Hysteresis measurements

The hysteretic behaviour was investigated in order to reveal the domain states of the ferromagnetic (s.l.) minerals, especially (titano-)magnetite. Hysteresis measurements of 36 samples have been done at the Magnetic Laboratory, University of Tübingen. The individual hysteresis loops are shown in Appendix 6. Samples 56 and 58 attracted attention for their heterogeneity in previous measurements, such as AMS and AFD. Hence, material from several cylindric specimens of varying distances from the dyke margin was taken for hysteresis examination.

Within the sample set, three different hysteresis loop types can be distinguished, which are depicted in Figure 7-40. Two of the types have s-shaped curves, characteristic for ferromagnetic (s.l.) materials (Figure 7-40 a & b). The third type is almost linear, but with a very weak s-shape and very narrow waist (Figure 7-40 c). In accordance with microscopic observations and low bulk susceptibility, the linearity is ascribed to paramagnetic minerals, which strongly contribute to the magnetization in these samples. While most loops are s-shaped, only 3 of them are almost linear or dominantly paramagnetic (samples 23, 26, 100_{-3}).

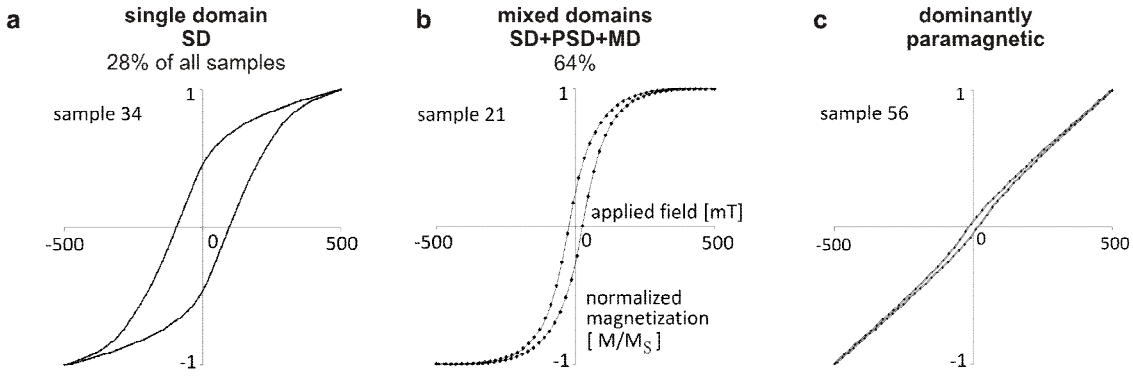

Figure 7-40. Different types of hysteresis loops after paramagnetic slope correction.

Narrow-waisted s-shaped curves such as of sample 21, are the most abundant ones (Figure 7-40 b, 23 samples), resembling the pseudo-single domain (PSD) curve type (Figure 3-10), as shown by Tauxe (2002). Nevertheless, they are interpreted to represent samples with ***mixed domain states of SD, PSD and MD*** tmt, in accordance with microscopic observations. The remaining s-shaped loops, such as of

sample 34 (Figure 7-40 a) are broader-waisted than the latter type. Their width is variable with extremes that resemble the ***single-domain (SD)-type*** in Figure 3-10 e. They represent the second-most abundant loop type among the investigated samples. The transition from broad loops indicating SD, to thinner PSD-like loops is gradual. The hysteresis loops of samples such as 19, 20, 75 and 94, are transitional, pointing to higher coercive, SD-like grains. The three almost linear (***dominantly paramagnetic***) curves also reveal a very faint s-shape, interpreted as a ferromagnetic (s.l.) component. Its waist is narrow and ranges from fields of -200 to 200 mT. Similar to the dominantly paramagnetic ones, the PSD and SD type curves are also not purely ferromagnetic (s.l.), but they have a more or less strong paramagnetic component.

Hysteresis parameters saturation magnetization, remanent magnetization, coercivity, coercivity of remanence (M_S, M_R or M_{RS}, H_C and H_{CR}) and their ratios of all measured samples are listed in Appendix 7. After paramagnetic slope correction 4 of the samples (33, 34, 76, 108) exhibit M_{RS}/M_S ratios above 0.5 and plot in the single domain field within the Day Plot (Day et al, 1977; Figure 7-41).

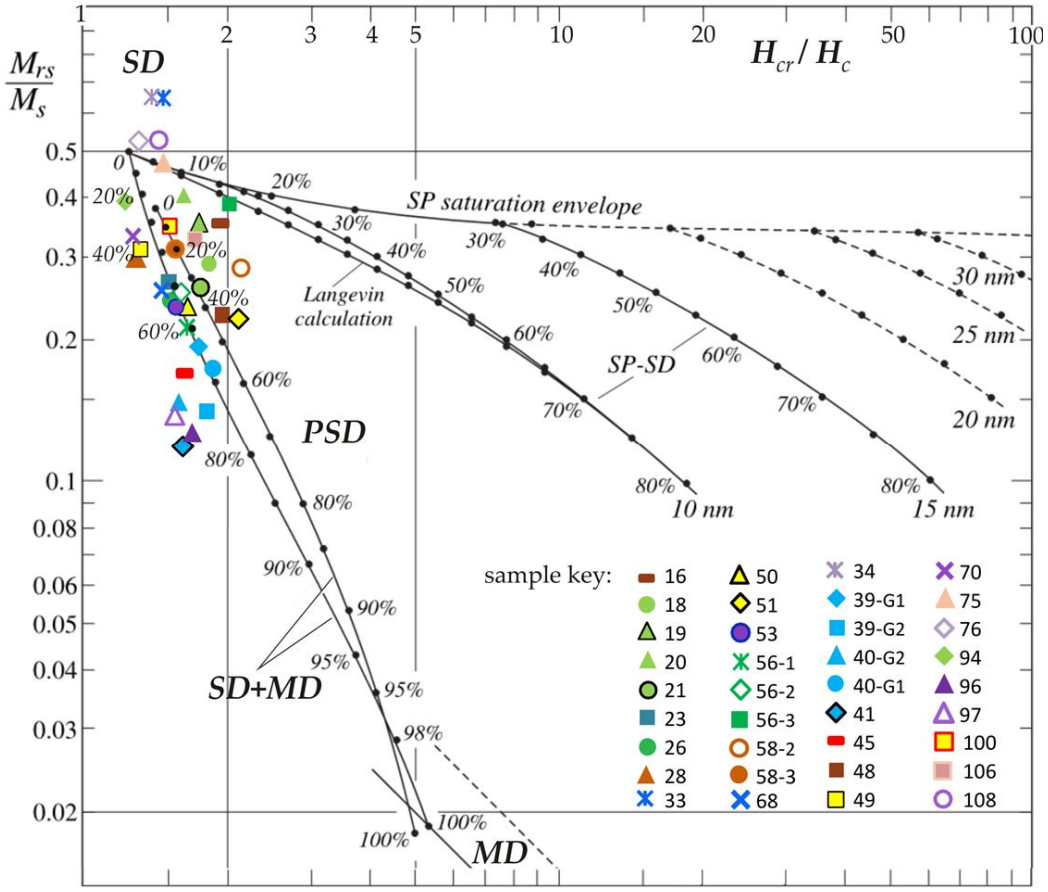

Figure 7-41. Day plot with theoretical curves after Dunlop (2002, modified) and the paramagnetically corrected HOD hysteresis data. Diagram outlines the hysteresis ratios Mrs / Mr versus Hcr/Hc plotted on a log-log scale. Most of the samples plot along the magnetite SD+MD (single-domain & multi-domain) mixed curves, left of the PSD (pseudo-single domain) area. The percentages along the curves represent volume fractions of the soft component (MD or SP).

From this it is concluded that tmt in the SD state predominates in these samples, which is also indicated by the suppressed Verwey-transitions in their κ-T curves (this can also point to non-stoichiometry by maghemitization; Muxworthy, 1999; Moskowitz et al. 1998 and references therein). M_{RS}/M_S ratios of all the other samples are between 0.1 and 0.5, and almost all H_{CR}/H_C ratios range between 1 and 2. Consequently, samples occupy the upper left part of the PSD field (H_{CR}/H_C = 1.5 to 5) and the adjacent area further left. After Dunlop's (2002) modification, the minimum PSD area limit is

shifted to 2 and the majority of HOD samples then are located on the left, outside of the PSD area (Figure 7-41). Nearly all the samples plot on or very close to Dunlop`s (2002) two mixing curves (different ulvospinel contents) of SD with MD magnetite/titanomagnetites, with different SD portions between 20 and 100 % and variable H_{CR}/H_C ratios. Samples 75_{-3} and 56_{-3-1} lie on or close to the 10 nm-grain-size mixing curve of superparamagnetic and single domain particles (Dunlop, 2002) with SD-contents of more than 80%, and a few samples between this curve and the before described SD-MD curve. The PSD field sample 51 may be part of the high titanium tmt-hyperbola (Figure 3-11 b), which fits the Curie Temperature of its κ-T curve.

Coervivities (H_C) are highest in samples with the highest M_{RS}/M_S ratios and gradually decline toward low ratios. Maximum paramagnetically corrected coercivities are 91 and 108 mT (samples 33 & 34), which agrees with the broadest ferromagnetic (s.l.) hysteresis loops. Minimum coercivities between 10 to 12 mT (samples 96 & 97 and 40 & 41) are found in two different dykes, both of which have the highest mean susceptibilities within the sample set.

Samples 56 and 58 show hysteretic heterogeneity within the sample: one of the hysteresis loops is paramagnetic and the other ferromagnetic (s.l.). Sample 58 shows ferromagnetic (s.l.) behaviour within the 8 cm thick dyke margin and dominating paramagnetism 16 cm away from the margin. The opposite is found in sample 56, where the dyke margin is dominantly paramagnetic and two other samples from 17 and 22 cm away from the margin show ferromagnetic behaviour. Similar differences have been observed with the help of the κ-T measurements.

In summary, the hysteresis loops of most of the measured samples are typical for ferromagnetic (s.l.) PSD tmt grains. No sample yields an ideal MD hysteresis curve, not even the ones where microscopy proved abundant coarse mt/tmt grains of >40 µm, which are expected to behave as multi-domain grains (PSD-MD threshold of mt: ≥ 15 µm; of TM60 ≥ 30-40 µm; Dunlop, 1983). In the Day plot more than half of the HOD data points are arranged on and along the theoretical SD-MD mixing curves of Dunlop (2002), in the PSD field. From this it is inferred that the HOD samples also contain SD grains in variable proportions, which in combination with PSD and MD grains give a bulk PSD signature in the hysteresis loops. This is plausible because of the coarse tmt grains observed in microscopy. Dominantly highly coercive SD-grains are indicated for samples 33, 34, 76 and 108.

7.3 Natural remanent magnetization and Koenigsberger ratio

The natural remanent magnetization (NRM) has been measured at almost all samples, except nos. 6 and 9 to 15. Because these measurements are time consuming, the NRM was not measured for all specimens, but at least for 4 of each sample. The results are summarized in Appendix 8, where the magnitude of the mean NRM (NRM_{mean}) of every sample is given, and in cases where the NRM is very heterogeneous, its range is bracketed. The NRM_{mean} values of the samples range from one outlier at 0.006 up to 475 A/m (Ampere per metre). As the left histograms in Figure 7-42 show, 67 samples have NRM values between 0.1 and 10 A/m (in accordance with the magma cooling ages of the HOD rocks of 130 Ma) and a further 12 samples between 10 and 20 A/m. Twenty samples show NRM values above 20 A/m, 8 of which even exceed 100 A/m, which is anomalously high and suggest magnetization by lightning strikes. Within a single sample, the values are mostly homogeneous within a few percentage of the mean value. Only in a small number of samples, are the variations remarkably high, such as 5 (49 ± 112 A/m), 40G2 (60 ± 30 A/m), 46 (98 ± 63 A/m), 62 (78 ± 70 A/m), 64 (15 ± 8 A/m), 71 (12 ± 9 A/m) and 107 (88 ± 30 A/m), which are most probably also attributed to lightning strikes.

On the basis of the NRM and magnetic susceptibility, the ***Koenigsberger ratio (Q)*** and its mean (Q_{mean}) have been calculated. The results for the individual samples are tabulated in Appendix 8 and summarized in the histogram in Figure 7-42 (right). In summary, 68 of the samples have mean Q values below 20, which is within the range considered normal for basalts. In 20 samples Q is anomalously high (above 50), which again points to a magnetization by lightning strike (Soffel, 1991). Similar to the NRM_{mean} values, Q_{mean} varies little within most of the samples, except for a few very heterogeneous cases, such as samples 16, 40, 46, 59, 64 and 97. In these cases, the range is given in brackets in addition to the mean value Q_{mean}. From the calculated Koenigsberger ratio it is concluded, that the

magnetization of most samples is dominated by the remanence rather than by induced magnetization (Q > 1; Soffel, 1991). The exceptions are 7 samples with Q values below 1.

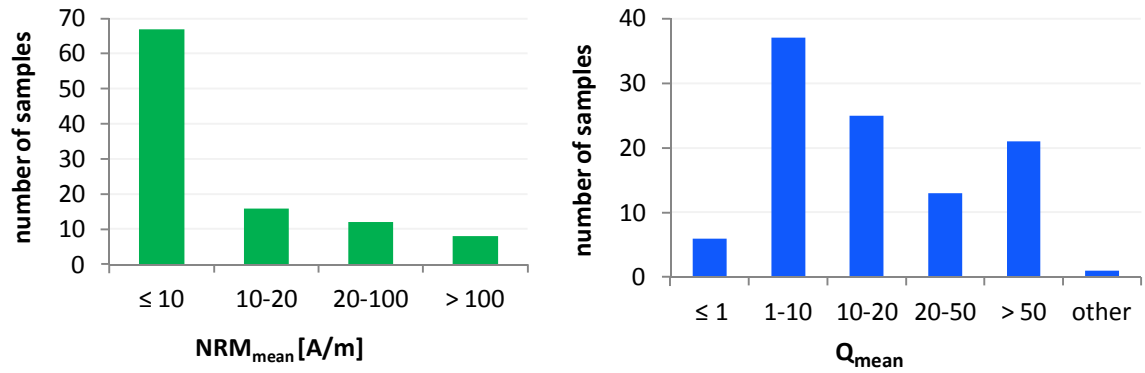

Figure 7-42. Histograms of magnitude frequency distribution of natural remanent magnetization (NRM) and Koenigsberger ratio (Q).

According to Soffel (1991), a Koenigsberger ratio between 1 and 20 indicates SD-grains (with long relaxation times), which applies to 64 of the HOD samples. The possibility that these Q-values result from young volcanics (Soffel, 1991) can be ruled out as there is no activity younger than about 80 Ma known in this area. Further, there is also support for the presence of SD-tmt in the HOD samples from AFD, hysteresis and AARM measurements. Q-values below 1 are encountered in 5 samples and point to multi-domain mt/tmt grains (Soffel, 1991), marked by shorter relaxation times.

7.4 Alternating field demagnetization

Stepwise demagnetization in an alternating field (AFD) provides further insights on the domain state of magnetite and titanomagnetite in the HOD rocks. Care has to be taken in interpreting AFD data, if mt or tmt is maghemized. Moskowitz (1980) showed experimentally that the pseudo-single domain (PSD)- multi-domain (MD) threshold in TM60 can be as high as 42 -150 µm (unoxidized ≥ 30-40 µm; Dunlop, 1983) depending upon the degree of oxidation. As documented by Dunlop (1983) and later confirmed by Cui et al. (1994), the oxidation state of mt/tmt is of crucial importance. Already partial oxidation can strongly increase the particles' anisotropy and coercivity (Cui et al., 1994). Consequently, the median destructive field (MDF; field strength, where half of the sample's magnetization is erased; $M/M_{max} = 0.5$) values, a measure for the strength or stability of the magnetization, also extend to higher values for all particle sizes. Dunlop (1983) distinguishes between exponentially falling AFD curves with MDFs below 5 mT of unoxidized multi-domain magnetite and their oxidized counterparts with MDFs above 5 mT and an initial plateau in the AFD curve. Cui et al. (1994) found that partly oxidized magnetite with grain sizes above 53, 106 or 250 µm behaved as PSD grains during AFD and hysteresis. The threshold, where mt/tmt-SD grain coercivities begin, may be transitional in nature and also depends on partial oxidation and crystal impurities. MDFs above 20 mT may already be due to a small fraction of SD grains, since the realistic threshold value of the coercive force for cubic (isotropic) mt-grains is given as about 20 mT (Dunlop & Özdemir, 1997; Butler, 1998).

47 specimens from 45 samples were stepwise demagnetized in increasing fields. Samples with AMS fabrics other than type I have been selected preferentially for AFD. Therefore, 27 of the specimens have AMS type II-IV fabrics and the other 20 represent type I samples for comparison (see chapter 7.5 for classification of AMS fabric types). Results are shown as curves of the NRM (normalized to the maximum NRM value M/M_{max}) as a function of the applied alternating field (Appendix 9) and data is summarized in Appendix 10. Three main curve types are distinguished (Figure 7-43) on the basis of the median destructive field value according to Dunlop & Özdemir (1997), which is between 3 and 60 mT in the HOD sample set.

The three curve types are:

- ***magnetically soft***: This curve type is represented by 13 specimens with relatively low coercivities, that is their remanent magnetization is easily erased with very low alternating magnetic fields. The curves are characterized by a rapid, exponential decay of the NRM resulting in a steep slope, mostly flattening in ranges of 20 percent (0.2) of remaining magnetization. The MDF is below 10 Millitesla. In agreement with the literature previously cited, this curve type is related to dominantly multi-domain (MD) titanomagnetite as the main carrier of the magnetic remanence.
- ***magnetically medium:*** This type includes 16 specimens with MDF values ranging from 10 to 25 mT. Curve slopes here are somewhat less steep and the decay of magnetization is mostly a little delayed which is evidenced by a narrow plateau at the curve start. Compared to the magnetically soft specimens, coercivities are higher, which is illustrated by a curve that flattens at distinctly higher magnetic fields. This magnetical behaviour may be due to a large fraction of pseudo-single domain tmt and/or partially maghemized MD tmt (compare chapters 3.7.5 & 7.2.2) along with minor MD and single-domain (SD) tmt grains.
- ***magnetically hard*****:** 14 specimens yield curves with high coercivities and MDFs above 25 Millitesla, interpreted to be due to a higher fraction of single-domain tmt and/or to a stronger degree of maghemitization along with minor MD and PSD grains. The slopes of the curves are much less steep. Strong alternating fields are necessary to clear their magnetization. Curves mostly start with a more pronounced plateau before declining and they flatten at higher applied fields than the magnetically intermediate specimens.

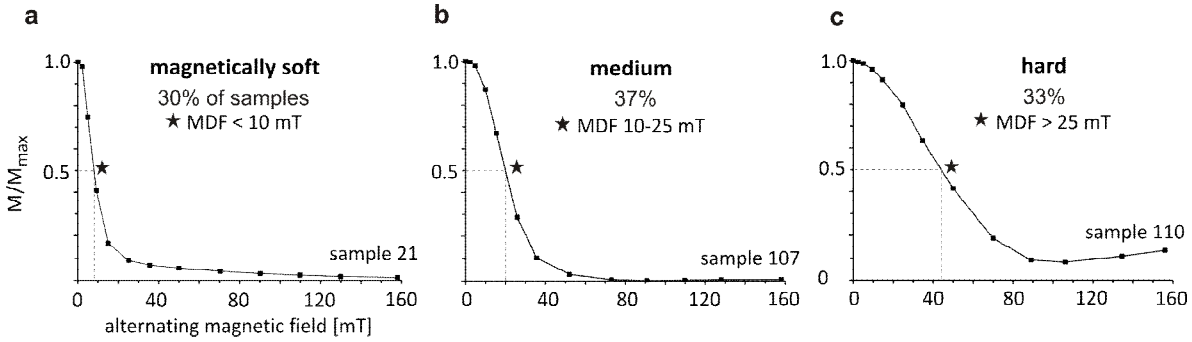

Figure 7-43. Curve types of the alternating field demagnetization), classified by the range of the median destructive field (MDF, black star) and the shape of curve. The normalized NRM (M/M_{max}) is plotted versus the applied alternating field.

All curves except for one start with a slight initial plateau preceding the drop, probably resulting from partially oxidised MD mt/tmt particles (Cui et al., 1994). Most curves decline uniformly, but some of them reveal weak or pronounced kinks in their trends (specimens 94_{-2-1}, 86_{-2-2}, 72_{-2-1}, Appendix 9). Although the curves of magnetically soft specimens drop rapidly, many of them are initially convex upward and then convex downward, similarly with the initial plateau shown by the magnetically intermediate types (e.g. samples 16, 71, 79, 87). The transition between the three curve types is gradual. A common feature, especially of magnetically hard but also intermediate curves, is a degree of non-demagnetizability in the applied maximum field of 160 mT. Instead of decreasing to nearly zero magnetization, the curve flattens at a higher level and a more or less strong remanent magnetization of up to 30 percent of the initial value remains (e.g., specimen 110, Figure 7-43). This points to a certain portion of NRM carrier minerals with coercive forces above 160 mT, possibly haematite or goethite. In 5 specimens, a resurgence of the magnetization after a major drop is observed (compare Appendix 9). Among these, specimens 77_{-1-4} and 78_{-3-2}, both from the same dyke, show only a minor second rise of about one tenth of the original NRM. In contrast, specimen 58_{-4-2} from the inside of the 8 cm thick chilled dyke margin, shows a strong resurgence of magnetization as high as the initial value. A zig-zag trend is observed in specimen 86_{-2-2} (Appendix 9) with a short resurgence of the NRM after a magnetization decrease during the first two demagnetizing steps. Finally, specimens 60_{-4-2} and 23_{-2-2}, which are

shown to have a paramagnetic susceptibility, can barely be demagnetized (Appendix 9), probably related to stronger coercive phases. The latter appear to be distributed heterogeneously within some samples, since a second specimen of sample 23 (23_{-1-3}) shows a significantly lower coercivity and can be readily demagnetized (similarly with sample 58).

Most AFD curves show that the NRM drops over a broad range of alternating fields, which is evidence for a broader spectrum of coercivities and, consequently, for a mix of tmt with different domain states. Samples with dominantly MD, others with dominantly PSD or maghemized tmt and others with dominantly SD states occur. Increased coercivities due to maghemitization are probable in some cases. Temperature-dependent susceptibility curves indicate maghemitization in many HOD samples, although this may also be heat-induced during the measurement itself. Microscopic observations in most samples show weak signs of maghemitization (compare chapter 7.2.1). A few samples maintain a residual remanent magnetization after AFD, which is interpreted as a certain content of highly coercive minerals, such as haematite or goethite (although oxidised SD mt/tmt/tmgh cannot be excluded).

7.5 Magnetic susceptibility and its anisotropy

Appendix 11 lists the mean values of the sample's magnetic susceptibility and its anisotropy data. Among the 1181 cylindric specimens from 111 samples measured, the mean bulk magnetic susceptibility (κ_m) varies from 0.4 to 151 $*10^{-3}$ SI, as demonstrated in Figure 7-44. The majority of samples shows κ_m between 5 and $35*10^{-3}$ SI. After Tarling & Hrouda (1993), $\kappa_m$values in basalts above $5*10^{-3}$ SI point to ferrimagnetic minerals controlling the rock magnetic fabric. In accordance with thin

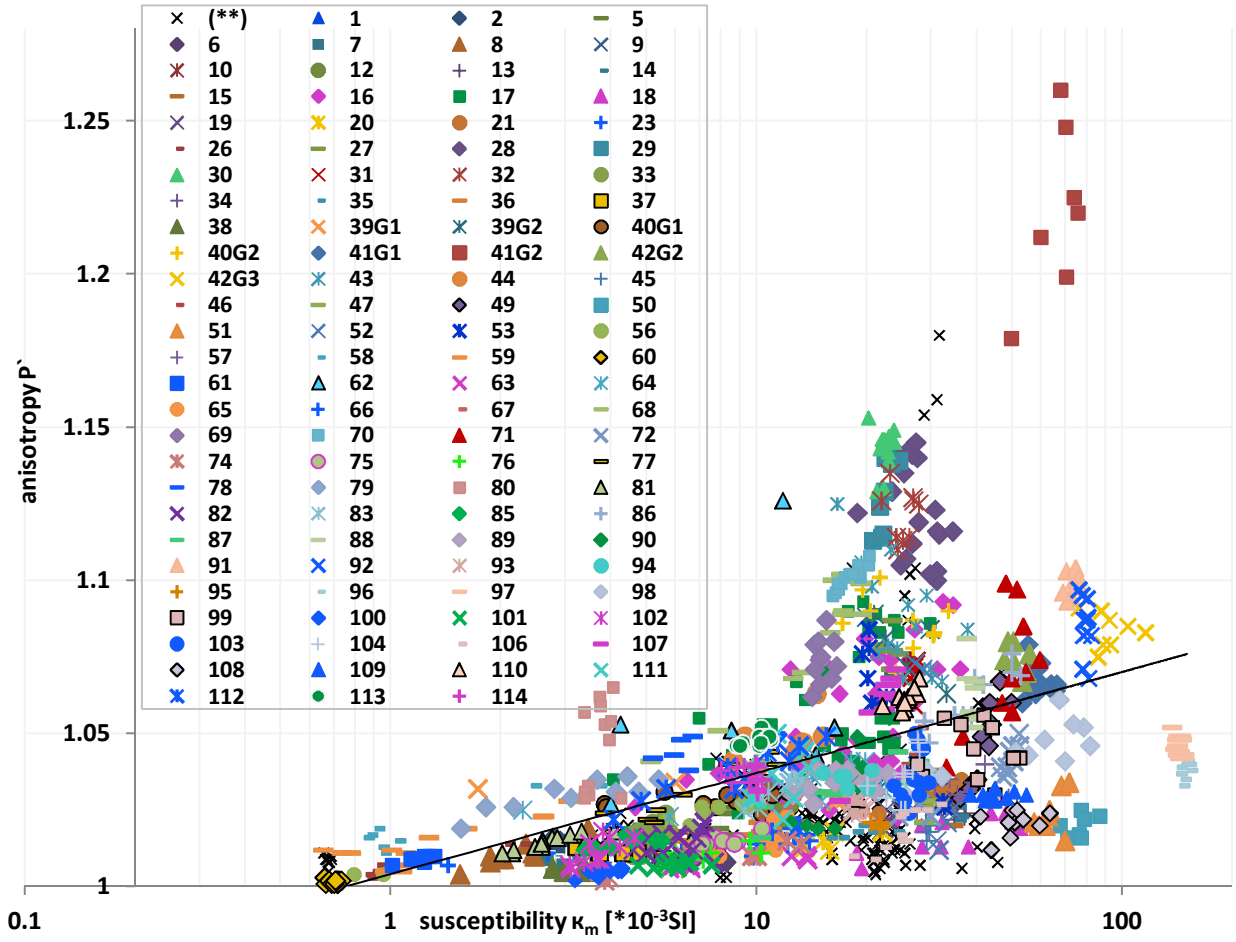

Figure 7-44. Relation of the mean bulk susceptibility (κ_m) of all 1181 specimens with the corrected susceptibility anisotropy (P'). Correlation coefficient for the trendline from this study is R = 0.5. Symbol X(**) refers to data from Wiegand et al. 2011.

section analyses in reflected light and the κ-T curves, these minerals are interpreted to be titanomagnetite/-maghemite (tmt/tmgh) of mostly intermediate (x ≈ 0.6) to zero titanium (Ti)-content. From the graph in Figure 7-45 it is obvious that the magnitude of κ_m is a function of the iron (and tmt) content in the rocks. The peak values of $151*10^{-3}$ SI refer to one tmt-rich dyke (no. 96-97; Figure 7-44). 23 samples yielded a κ_m less than $5*10^{-3}$ SI, but above $5*10^{-4}$ SI (except sample 48), which Tarling & Hrouda (1993) interpret as a mixed magnetic fabric control of para- and ferrimagnetic components. Microscopy and κ-T curves reveal that low κ_m samples contain glass or less tmt compared to paramagnetic ilmenohaematite.

Most samples plot in the lower part of the κ_m vs P' diagram (Figure 7-44; P' = corrected degree of anisotropy of the magnetic susceptibility), revealing low anisotropies and no correlation with κ_m. About 75% of the specimens have P' values below 1.05 (5%), the remainder yield values up to 1.27 (27%). Of the latter group, the majority plot in the oblate field of the Jelinek diagram (Jelinek, 1981; Figure 7-7-46). Samples 28, 29, 30, 32, 41, 43 and 70 exceed P' = 1.1 (10 %), which Tarling and Hrouda (1993) and de Wall (2005) consider as a rough boundary in ferrimagnetic- dominated rocks between primary magmatic flow fabrics (P'< 1.1) and secondary fabrics (P'> 1.1). These higher anisotropic samples are those with stronger flow fabrics recognized in the thin sections. Commonly, these samples, such as numbers 16, 28-30, 31-32, 39-43, 53, 68,70, 71, show dominantly pure magnetite in their κ-T curves (Appendix 4) and no or only a weak T_C indicating intermediate tmt/tmgh. Weakly magnetic anisotropic samples with P' ≤ 1.01, such as samples 7, 22, 24, 25, 26, 34, 38, 48, 59, 60, 61, 63, 74, 76, 100, 101 and 102 also have low bulk magnetic susceptibilities (κ_m< $10*10^{-3}$ SI). There is no general correlation of P' values and bulk magnetic susceptibility in the samples which argues against a frequent influence of field dependency on AMS fabrics (De Wall, 2000).

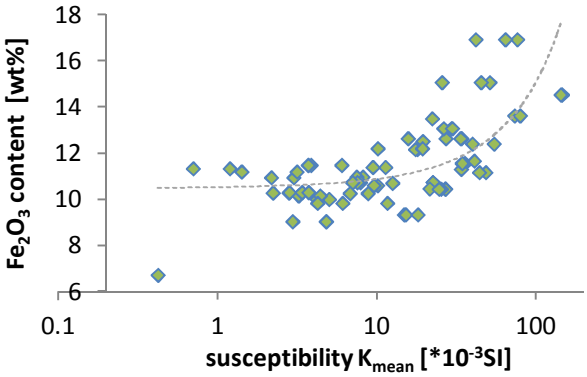

Figure 7-45. Dependency of magnetic susceptibility on the iron oxide content in the HOD samples.

In the ***Jelinek-Plot***, Figure 7-46) the axial ratios of the anisotropy ellipsoid are evaluated by plotting the degree of anisotropy against the shape factor T. Within one (block) sample the degree of anisotropy is commonly homogeneous, and only varies stronger in a few ones (such as samples 16, 17, 28, 41_{G2}, 71 and 80). Specimens plot throughout the entire T-range from prolate to oblate shapes, but there is a distinct majority of oblate fabrics. T may occasionally differ within one block sample from strongly oblate to strongly prolate shapes, but nearly homogeneous T values are common as well.

Within a sample the magnetic susceptibility of individual specimens occasionally varies over one (for example samples 18 to 21) or even two orders of magnitude (samples 39 to 43, Appendix 11), but more commonly, κ varies little even in thicker dykes (for example samples 100 to 102 or 45 to 47). The degree of magnetic anisotropy within a dyke can both be relatively constant (samples 96 and 97: 1.03 > P' > 1.05), or may vary highly (sample 17: 1.025 > P' > 1.10). No uniform systematic variation has been found in the distribution of P' across the dyke width, regardless of whether dykes are thin or thick. From 14 locations where dykes were sampled across the total width, 7 show higher anisotropies in the dyke centre compared to the margin (e.g. samples 88, 110), 5 show the contrary behaviour (e.g. samples 16 & 17) and in 2 of the dykes there is no difference between margin and centre. An example for the second case is illustrated in Figure 7-49: the dyke with the samples 16 and 17 reveals higher P' at the margins and lower P' in the centre. Its shape factor T is also symmetrical across the dyke width:

moderately oblate at the dyke walls and becoming triaxial and even weakly prolate towards and in the dyke centre. However, generally, there is no uniform variation of the T-factor across the dyke width: in 7 of the 14 locations both dyke margins have similar T-factors; in the others T does differ. 4 of the 7 examples of this latter group have prolate centres but oblate dyke margins, while 2 of the 7 show the reverse pattern. Variations of T, even within the same sample, are occasionally large (samples 18, 26, 58, 60, 65), and can be even larger across the dyke width. Similar T-factors in all samples and specimens of the same dyke are rare (e.g. dyke 91, 92 or 96, 97).

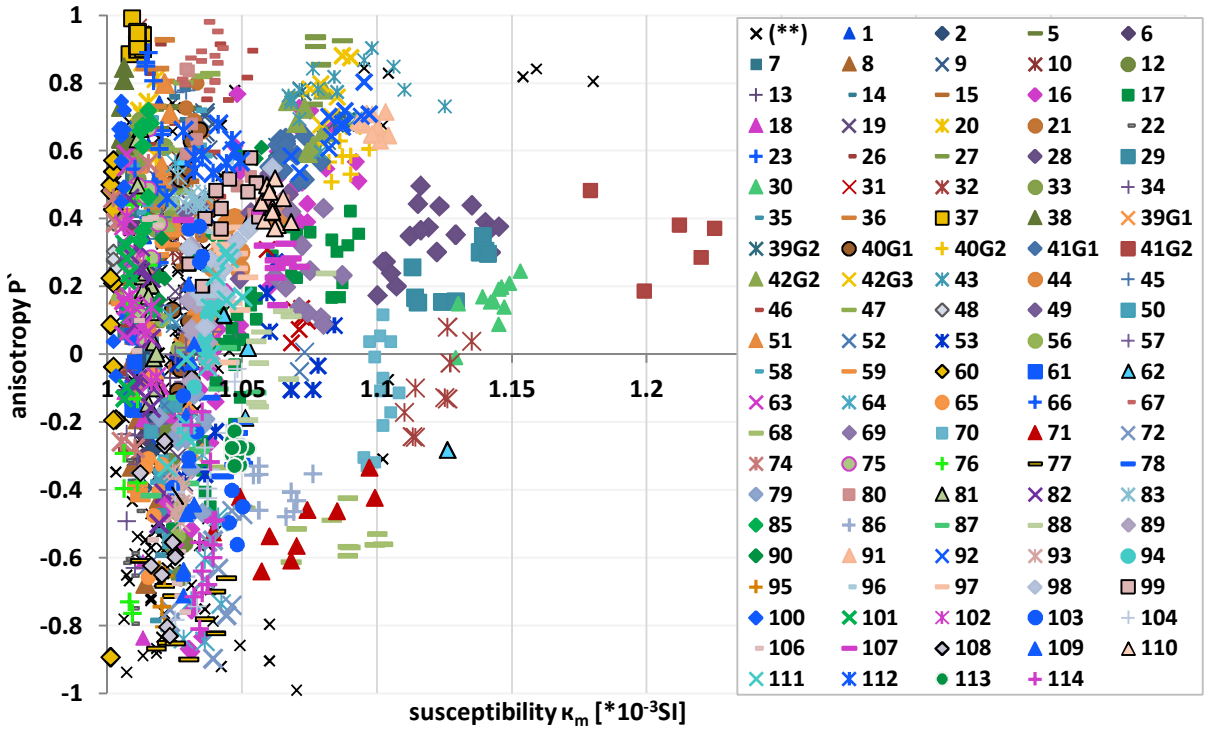

Figure 7-46. Jelinek diagram (Jelinek, 1981) with shape factor (T) versus corrected degree of anisotropy (P'). N = 1181 (this study). Symbol X(**) refers to data from Wiegand et al. (2011).

Orientation of AMS ellipsoids

A summary of the initial AMS orientation is shown in stereographic projections in Figure 7-47. The maximum principal susceptibility axes (κ_{max}) are mostly in the dyke plane with vertical to subvertical inclination in NE-striking dykes. The minimum principal susceptibility axes (κ_{min}) are horizontal and normal to the dyke plane in most cases, but a weak girdle configuration in some cases have κ_{min} axes within or close to the dyke plane (but still horizontally oriented). In the NW-striking dykes most κ_{max} axes are within the dyke plane, while their inclination varies between horizontal over moderately to steeply inclined. Similarly to the NE dykes, horizontal κ_{min} axes prevail, but a group of samples with steep axes close to the dyke plane is also present.

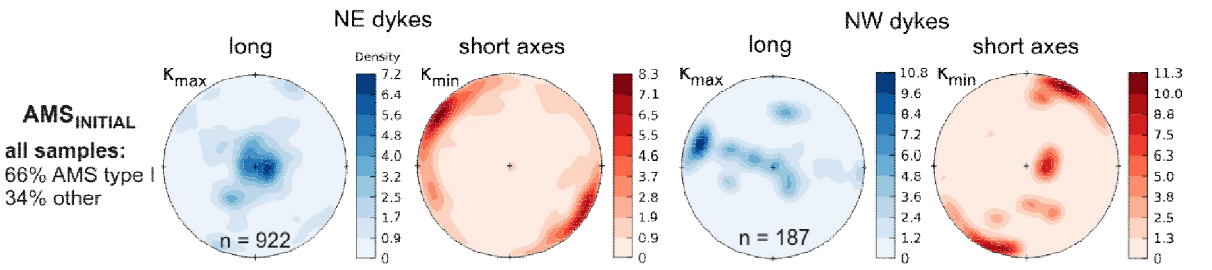

Figure 7-47. Density plots (lower hemisphere, equal area projection; Fisher distribution) of maximum and minimum susceptibility (κ_{max} and κ_{min}) in NE and NW-striking dykes in the HOD.

An overview of the initial AMS orientation for each sample before demagnetization is given in lower hemisphere (stereonet) projections in Appendix 12. The stereonets reveal that in most of the samples there is a good or very good clustering of the specimens' principal susceptibility axes κ_{max}, κ_{int}, κ_{min} (e.g. samples 16, 18, 19, 21, Figures 7-49 & 7-50. An elongate or girdle distribution of two of the axes may occur in the case of strongly prolate (lengths of κ_{int} and κ_{min}-axes are almost equal, e.g. samples 65, 72, 77 in Appendix 12) or oblate fabric ellipsoids (lengths of κ_{max}- and κ_{int}-axes are almost equal, e.g. sample 14, 20, 21, 38, 46, 66, 85 in Appendix 12). In these cases, confidence areas principal susceptibility axes are elongate and overlap in places (e.g. samples 20, 26, 58, 59 or 66).

The samples have been grouped based on their mean κ_{max}, κ_{int}, κ_{min}-directions in relation to the dyke plane, following the example of many authors (see chapter 4.1.1). As Figure 7-48 demonstrates, four different magnetic fabric types (I to IV), have been distinguished by this method.

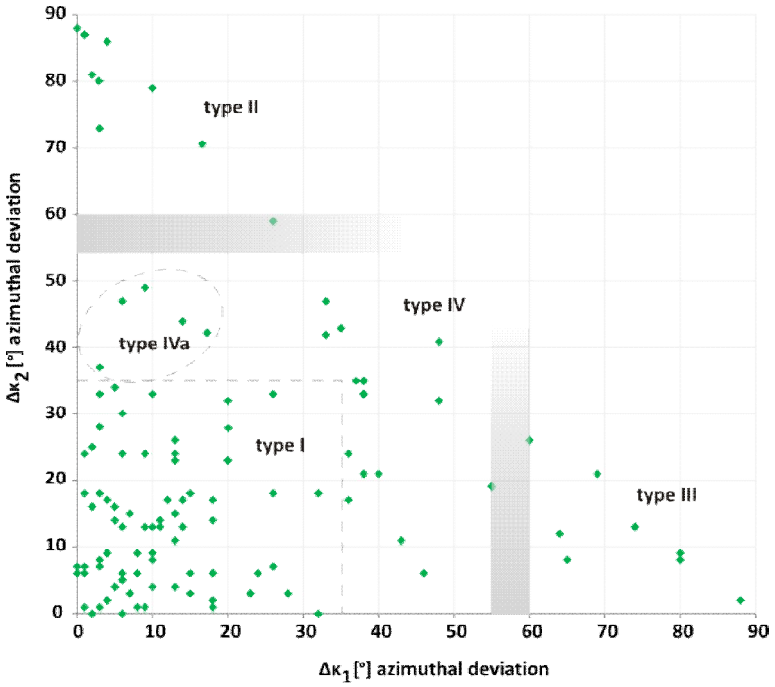

Figure 7-48. Classification of AMS fabric types according to the orientation of the long and intermediate susceptibility fabric axis (κ_{max} and κ_{int}) in relation to the dyke plane. Shown are the angular/azimuthal deviations of κ_{max} and κ_{int} axes from the dyke plane.

Transitions between the individual fabrics are fluent, marked by the shaded areas. Types I to III have also been found in other studies (e.g. Rochette, 1991, 1992; Borradaile and Gauthier, 2001) and correspond to the types that Raposo & Ernesto (1995) found in the Ponta Grossa Dyke swarm at the Brazilian side of the South Atlantic Ocean, which is approximately synchronous with the HOD. The following fabric types are distinguished:

- ***Fabric type I*** is the fabric type generally termed as "normal" after Rochette et al. (1991, 1992) and is characterized by the mean maximum and intermediate susceptibility axes κ_{max} and κ_{int} lying within the dyke plane, while κ_{min} is perpendicular to it (Figure 7-49). The term "normal" refers to the fact that dykes generated by laminar magma flows in planar bodies, are expected to have the magnetic lineation and foliation parallel with the dyke plane. Rocks are considered to have normal magnetic fabrics when the magnetic and the rock fabrics coincide, mean that the structural and magnetic axes are parallel (Rochette et al. 1992). This is the most abundant type in this study and is shown by 73 samples (66%). In strongly oblate fabrics, κ_{max} and κ_{int} axes of all the specimens from the same sample do not cluster, but are often exchanged and/or form a girdle parallel with the dyke plane (e.g. samples 27, Figure 7-52). Owing to repeated (re-)orientation steps during sampling and specimen preparation, 35° of azimuthal deviation of

κ_{max} and κ_{int} axes from the dyke plane are considered insignificant or uninterpretable, similar to the cut-off of 30° in the study of Raposo & Ernesto (1995).

- ***Fabric type II*** or the ***intermediate fabric type*** (Rochette et al., 1992, 1999) has mean κ_{max} and κ_{min} axes within or very close to the dyke plane, resulting in the κ_{int} axes being (nearly) perpendicular to it (Figure 7-50, sample 20). Azimuthal deviations of the κ_{max} axis from the dyke plane are up to 30°. Fabric type II is represented by 8 samples (7%).

- ***Fabric type III***, also termed **inverse** (Rochette et al. 1992), has the magnetic lineation (κ_{max}) normal to the dyke plane, while the intermediate and minimum axes κ_{int} and κ_{min} are within or close to it (Figure 7-50, samples 18 & 19) within deviations of up to 30°. This fabric type was recognized in 8 samples (7%).

- ***Fabric type IV***, the second-most frequent type with 22 samples (20%), contains all the transitional fabric patterns between the other three types. These fabrics are termed ***oblique***, because they are not coaxial with the dyke plane. While in fabrics I to III two of the principal AMS axes are parallel with the dyke plane, the oblique samples reveal none or at most one of the principal susceptibility axes within the dyke plane (Figure 7-50, sample 21). A particular configuration is represented by ***subtype IVa***, where κ_{max} is situated within or near the dyke plane. 5 samples out of the 22 show this fabric.

All AMS fabric types other than I are referred to as anomalous by Rochette et al. (1992). Three of the samples (58, 59, 62) are heterogeneous and show an internal division referring to their κ_{max}, κ_{int}, κ_{min} directions. In these cases, axes κ_{max} and κ_{int} of the individual specimens are interchanged. Therefore, calculation of the mean makes no sense. The individual specimens of samples 58 and 59 form two κ_{max} clusters. One cluster contains all specimens from near the dyke margins and the second cluster comprises those most distant from the margins. Splitting the two samples into these subgroups results in types IV, II (margin specimens of no. 59) and IVa (centre-specimens of no. 58). Sample 62 is a special case, because at its location, the dyke is laterally displaced and the dyke rock contains light schlieren, presumably from assimilation of molten wallrock (see chapter 5). This sample is heterogenous with respect to several magnetic properties, such as the bulk susceptibility, the NRM and AARM.

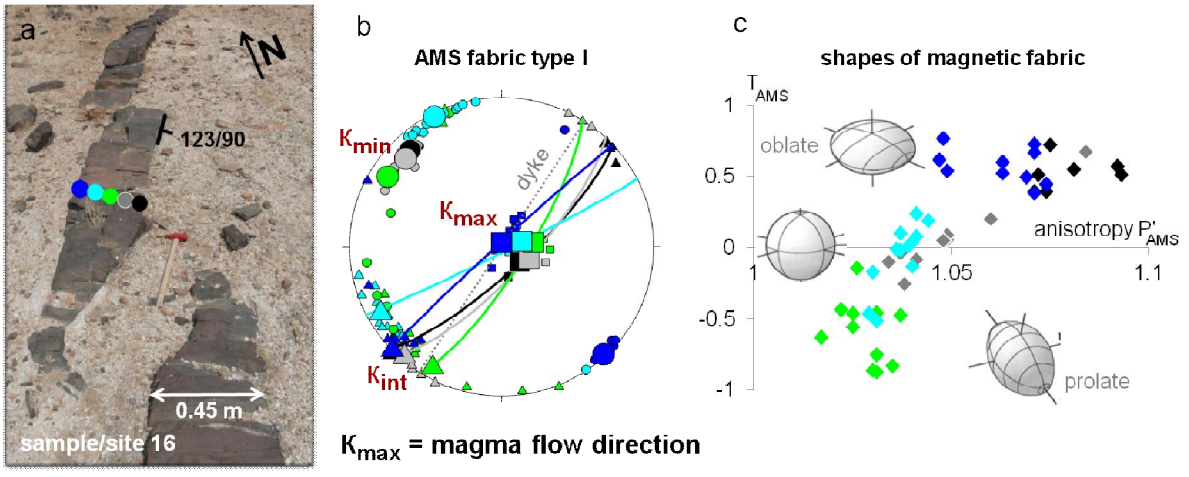

Figure 7-49. Example of AMS type I (normal), sample site 16. a: Segmented and laterally displaced thin dyke, showing specimen distribution. b: AMS data in lower hemisphere stereonet projection; steep κ_{max} is interpreted as vertical magma flow. Large symbols represent means of κ_{max}, κ_{int}, κ_{min}. Great circles represent planes of magnetic foliation; c: the shape of magnetic fabric ellipsoid varies across dyke thickness, oblate near dyke margin and prolate in the center.

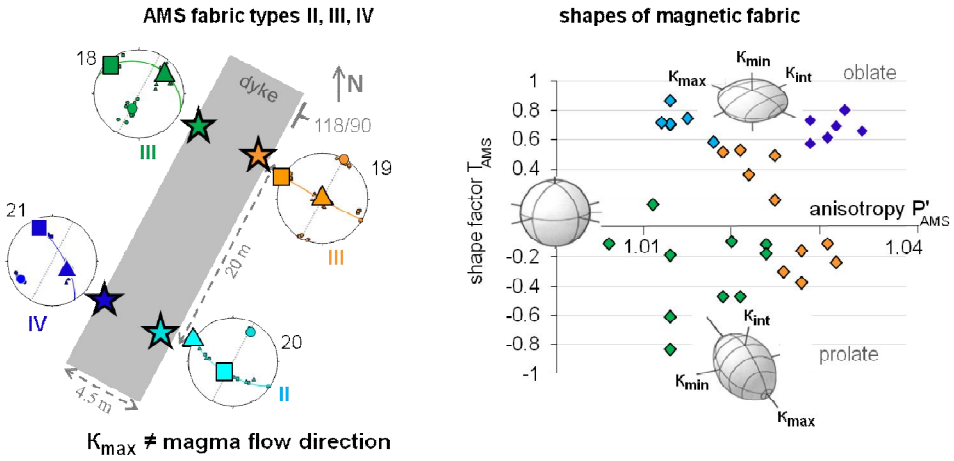

Figure 7-50. Examples of anomalous AMS fabric types within one dyke (gray, idealized) with margin samples 18-21 (stars). Left: Sample distribution of fabric types II, III, IV shown in lower hemisphere projection (square: κ_{max}, triangle: κ_{int}, circle: κ_{min}). The magnetic foliation is perpendicular to the dyke plane or at a steep angle to it. Right: shapes of magnetic fabric ellipsoids vary along dyke strike and locally even within one sample (no. 19).

The distribution of the different fabric types across the HOD is random as shown in Figure 7-51. Fabric type I samples occur in each of the sampled areas and are generally the dominant type. Anomalous fabrics are also found in every area, but not each of the anomalous types is present everywhere.

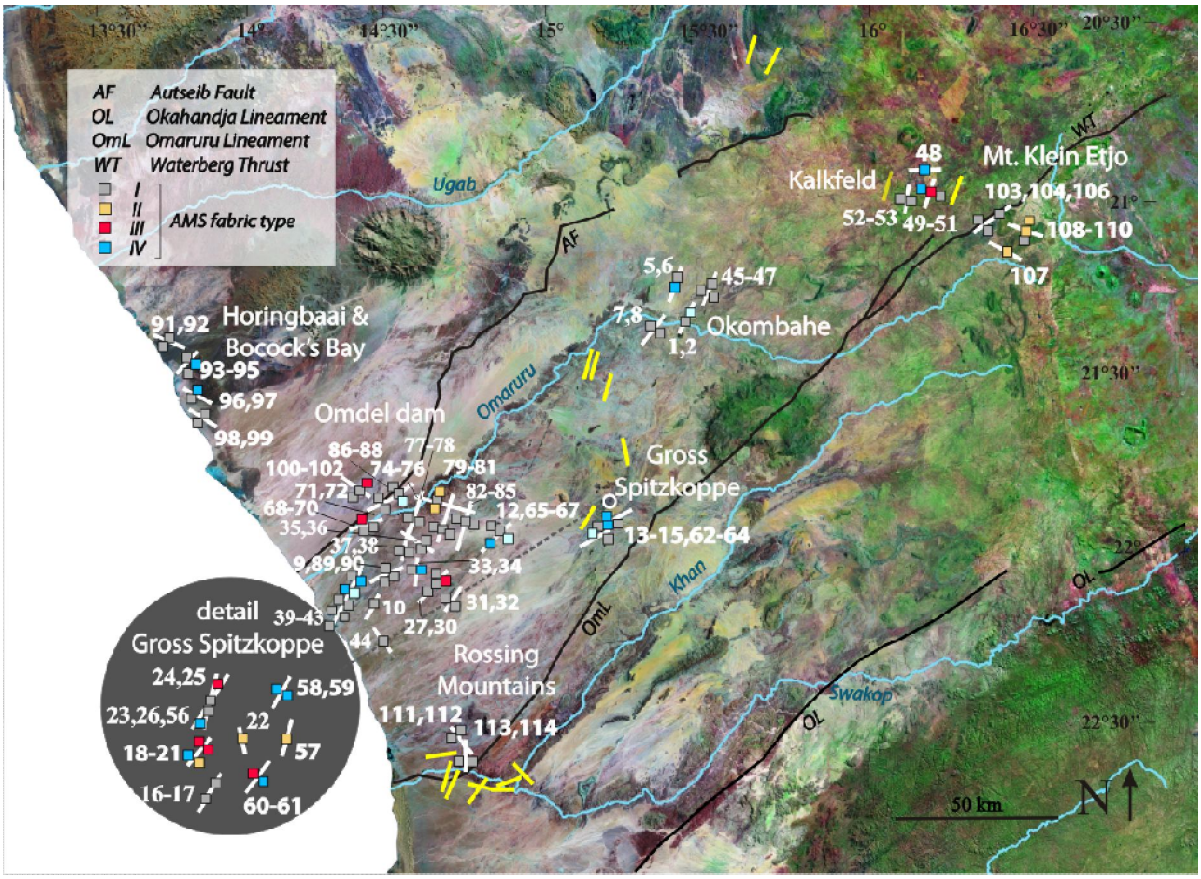

Figure 7-51. Distribution of different $AMS_{INITIAL}$ fabric types across the HOD dyke swarm shown on a satellite image. White and yellow bars show strike of dykes. Yellow bars denote dyke locations from the previous AMS study of Wiegand et al. (2011). Sample numbers in white.

When comparing the results dyke by dyke, 11 dykes (e.g. dykes 31-32, 71-72, 77-78, 111-112,113-114) reveal nearly the same AMS fabric (commonly type I) and same orientation in both margin samples, regardless of the dyke thickness. Commonly, however, different fabric types occur within one dyke; both normal and anomalous types are distributed unsystematically across the dyke width and along strike (e.g. dykes 39-43, 49-51, 12/65-67, 27-30, 18-21 in Figures 7-51, 7-52 and 7-53). For the 8 thicker dykes, except of one (dyke 82-85), the two margin samples and the sample of the centre are not identical, at least one of the three samples differs in AMS type or axes orientation from the other two. However, comparing κ_{max} orientation within the same dyke and site, differences are minimal in 5 of them (74-76, 79-81, 82-85, 86-88, 108-110). A variety of two or more types of anomalous fabrics within the same dyke is observed in 4 dykes (60-61, 18-21, 23-26-56, 49-51). It can be generalized, that although fabric types may be different within a dyke, in places the mean κ_{max} orientation is the same (e.g. dyke 18-21, 93-95).

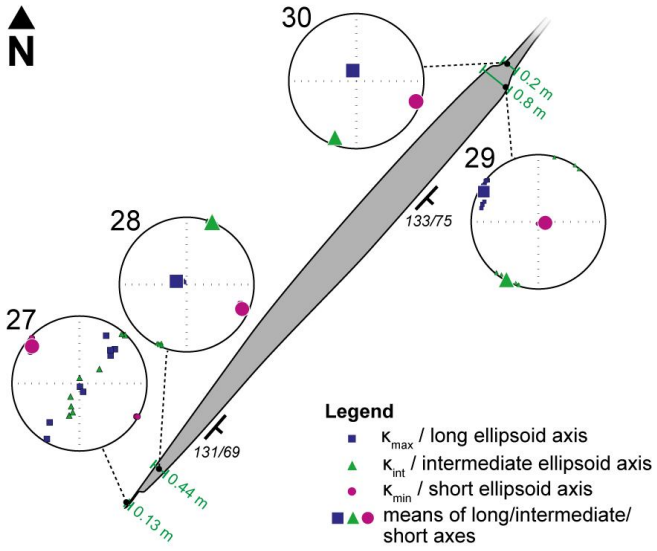

Figure 7-52. Dyke segment with different AMS fabric types (sample 27, 28, 30: normal, type I; sample 29: inverse, type III) and asymmetric κ_{max} orientation at both dyke margins (samples 29 and 30). Note the change in orientiation of maximum ellipsoid axes (blue squares) leading to an oblate fabric towards the thinning segment tip, sample 27 (length of dyke segment 160 m).

For the interpretation of magma flow directions in the dykes, the fabric orientation across the dyke width is important, especially the orientation of κ_{max} or magnetic foliation near the dyke margins, where the flow direction of the initial magma intrusion is best recorded. From the imbrication of the magnetic lineation/foliation against the opposing dyke walls an asymmetry or symmetry of the magnetic fabric within a dyke is distinguished (Figure 7-53). This aspect of the fabric could be assessed in 23 HOD dykes that were sampled very close to the dyke margins (within 0.2 m; Appendix 11, "sample position within dyke"). Sixteen of them, where the magnetic lineation is imbricated, show fabric asymmetry on the opposing margins, and only 3 dykes yielded a strictly symmetrical imbrication according to the model of Knight and Walker (1988) (e.g. 79/80, Figure 7-53). In a broader sense, dykes at 8 sites are symmetrically imbricated (nos. 17, 23/26/56, 31/32, 33/34, 62/64, 65/66, 79/80, 89/90), although not with exactly the same angle. As demonstrated by Clemente et al. (2007) asymmetry can be important (chapters 4.1.1, 9.2.4 and 10 for details). After Clemente et al. (2007) 3 cases are distinguished according to how the κ_{max} axes are rotated compared to the symmetrical case and these cases are also recognized in the HOD dykes. In case (a), which is most common (6 dykes), the κ_{max} clusters on opposite dyke margins within or close to the dyke plane (as in fabric type I). But, instead of being mirror-symmetrically opposed, they are displaced along a great circle (in the stereonet) parallel with the dyke plane. In case (b), shown for example in Figure 7-50, the displacement of κ_{max} axes is within a plane normal to (or at high angle with the dyke plane (samples 18, 19, 21). Finally, case (c) shows a

displacement of κ_{max} along great circles (planes) that cut the dyke plane in an oblique angle less than 90°. Interestingly, unequal absolute displacements in all 3 cases are also observed at the dyke margins. No imbrication and no asymmetry is shown by 5 thinner dykes (e.g. Figure 7-49).

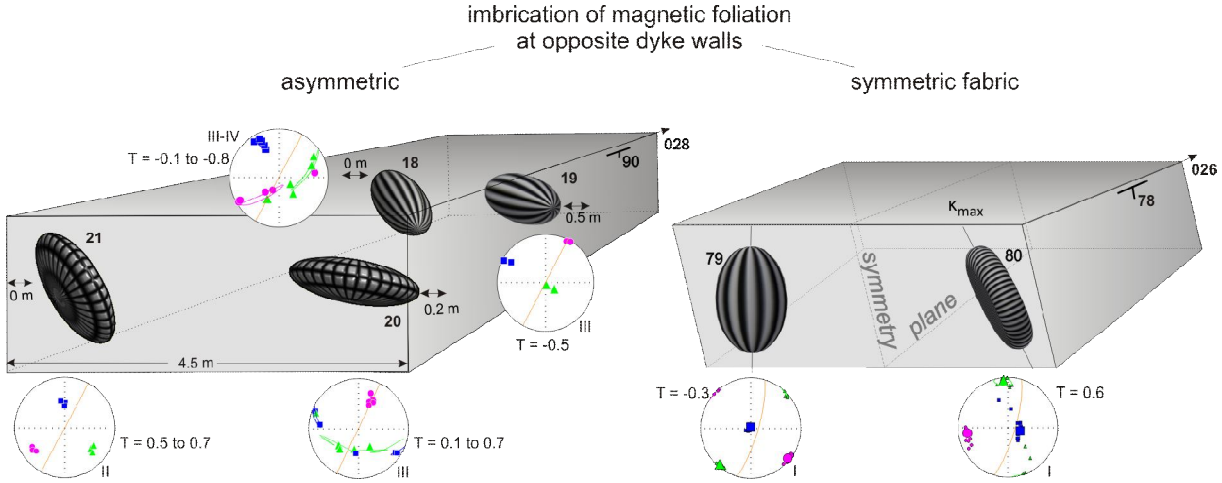

Figure 7-53. Examples for the symmetry and asymmetry of AMS fabrics within the dykes (dykes with sample nos. 18-21 & 79-80). Asymmetric configurations of the magnetic lineation/foliation are common in the HOD swarm. Roman numerals refer to AMS fabric types. Note: AMS_{AFD} fabrics are shown for dyke 18-21 and $AMS_{INITIAL}$ fabrics for dyke 79-81. Colour key: blue = κ_{max}, green = κ_{int}, pink = κ_{min} axes.

In summary, the AMS measurements indicate that ferrimagnetic minerals dominate the rock magnetic fabric of most HOD samples. Microscopy and κ-T curves identify these phases as titanomagnetite/-maghemite. In 23 samples (21 %) the fabric is interpreted to be controlled by a mix of para- and ferrimagnetic components, i.e., titanomagnetite/-maghemite and commonly ilmenohaematite. Anisotropies of the magnetic susceptibility are below 10% in most samples, which argues for primary magmatic flow fabrics. No uniform, systematic variation of P' or T across the dyke width was found. The long and intermediate axes of the AMS fabric ellipsoids are within the dyke plane (normal/type I fabrics) in 73 samples (66%) with mostly vertical to subvertical orientation of the long axis, which is interpreted to record magma flow. The remainder samples have anomalous AMS fabrics (types II to IV) with a non-dyke parallel orientation of magnetic foliation. The distribution of the AMS fabric types is random throughout the HOD swarm as well as across the width and along the strike of individual dykes. The sense of imbrication of the magnetic foliation/lineation on opposing dyke walls is asymmetric in most cases.

7.6 Anhysteretic remanent magnetization and its anisotropy

The anisotropy of the anhysteretic remanent magnetization (AARM) has been determined from 159 cylindric specimens derived from 54 samples, that is 2 to 6 specimens per sample. A compilation of the data set including the measurement settings is given in Appendix 13.
Since this method was aimed at the analysis of the remanent magnetic fabric within the rock, directional results are the focus of interest rather than quantitative ones. Therefore, the magnetic fields were varied in magnitude when imparting the anhysteretic remanence on the rock cylinders (see Appendix 13), which makes comparisons of the resulting bulk remanences among the samples difficult. Still, it is obvious from Appendix 13a, that the samples have mean bulk remanent magnetization values (M_{AARM}) which do not correlate with the applied AC field strength. M_{AARM} values range from 0.9 x 10^{-4} up to 0.42 A/m, which is a scatter of 4 orders in magnitude. Most samples have M_{AARM} below 0.1 A/m, except 5 samples or 2 dykes, respectively.

In the Jelinek plot (Jelinek, 1981) of Figure 7-54 the specimens' AARM ellipsoid shapes are described with respect to the corrected degree of anisotropy P' and the shape factor T. In contrast with the AMS,

there are slightly more specimens with prolate than with oblate fabrics. Specimens plot more or less equally distributed between the T-interval -0.9 and 0.8. ARM anisotropies mostly range from 1.02 to 1.2 in the oblate and to 1.25 in the prolate field. A few specimens are even more anisotropic with P' values up to 1.66 and with T-values in the range between -0.2 and 0.4.

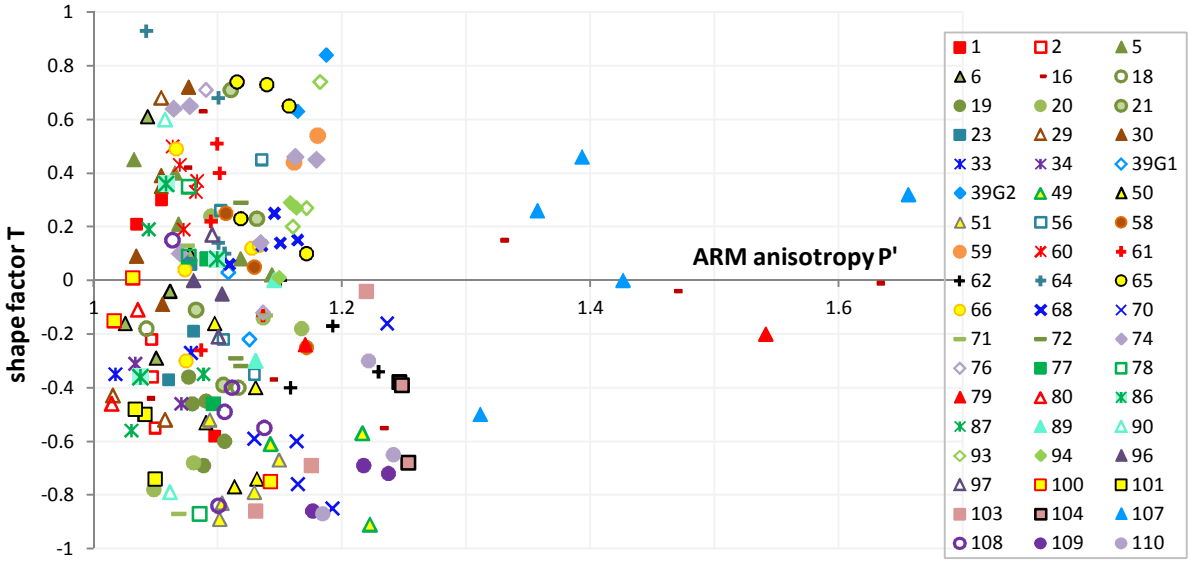

Figure 7-54. Shape parameters T and P' of the anhysteretic remanent magnetization (ARM) ellipsoids of the cylindric specimens. T and P' have qualitative, but not quantitative character, since applied field strength varies. Consequently the specimens cannot be compared regarding the magnitudes of T and P'. Samples numbers are specified by a specific symbol (see legend). Symbols correspond to the ΔM_1-ΔM_2 plot in Figure 7-57.

Orientation of AARM ellipsoids

In contrast with the AMS results, where type I fabrics predominate, type IV fabrics are by far the most abundant ones shown by AARM, with 23 samples (43%), followed by type III (22%) and I (19%). In Figure 7-55 (left) this difference becomes obvious in particular for the NE dykes, where the long axis of remanent magnetization (M_{max}) is mostly horizontal, oriented NW-SE, at high angles or even perpendicular to the dyke plane while the short axis M_{min} is mostly within the dyke plane. However, steep M_{max} axes within or close to the dyke plane also occur. Compared with the relatively clear cluster of vertical κ_{max} of the AMS in NE dykes, the M_{max} axes of the AARM are more scattered in NE dykes. For the NW dykes AARM fabrics are of type I (Figure 7-55, right) but data are too few for a statistical significance.

Most of the samples have specimens with clusters of M_1, M_2 and M_3 (M_{max}, M_{int}, M_{min}) axes or with a girdle arrangement of two of them. Where only 2 or 3 specimens have been measured and the respective principal axes do not cluster, the pattern is difficult to interpret. For the statistical calculation of mean directional data $M_{1,2,3\ mean}$ in ANISOFT4.2. (AGICO, Brno), the results of at least 5 measured specimens are required, but 5 cylinders have been examined only from 18 samples. From the other 36 measured samples, only 2 to 4 specimens have been analysed. In these cases, $M_{1,2,3\ mean}$ had to be calculated alternatively with the programme STEREONETT (Version 2.46; J. Duyster, Univ. Bochum), which calculates means also from two values. In a comparison, the means from the two programmes of the same specimen set differ significantly. While the STEREONETT means of $M_{1,2,3}$ appear rather arithmetical, the ANISOFT means apparently are weighted in favour of clusters. Means calculated from 2 or 3 specimens are less statistical representative. The ANISOFT means are considered to be more robust, but STEREONETT means are accepted for the samples with less than 5 specimens measured for AARM.

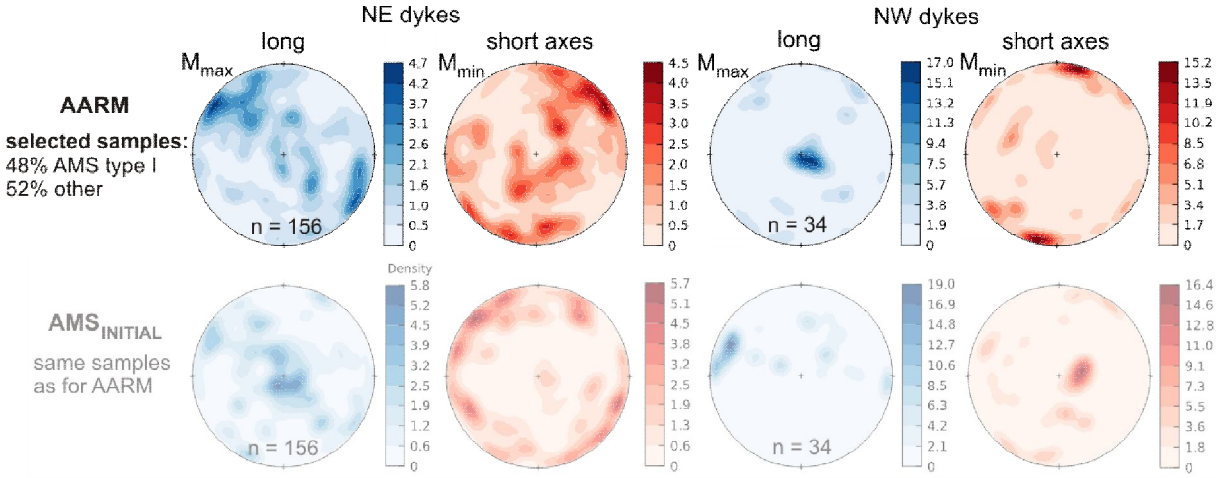

Figure 7-55. Density plots of AARM fabrics (lower hemisphere, equal area projection; Fisher distribution) with maximum and minimum remanent magnetization axes (M_{max} and M_{min}) in selected NE and NW-striking dykes in the HOD. For comparison with the AMS fabrics see the lower row.

For the presentation of the three principal axes of magnetization $M_{1,2,3}$ in stereonets (Appendix 14) together with the dyke plane only the ANISOFT means are shown. Samples with a potential influence of the residual vector (see chapter 5.2) on the ARM vector in some/all specimens are marked with a black/grey star. Stereonet patterns have been classified into 4 main fabric types (Figure 7-56) as with the AMS results: The azimuthal deviations ΔM_1 and ΔM_2 between the means of M_1 or M_2 and the dyke plane were determined and serve as criteria for the typification (Figure 7-57). Samples with less than 5 specimens have been grouped according to their STEREONETT means. The resulting grouping into four types is described as follows:

- AARM fabric ***type I*** is characterized by the two principal magnetization axes M_1 and M_2 being parallel/within the dyke plane. Deviations up to 35° are allowed for M_1 and M_2 (ΔM_1, ΔM_2) 10 out of 54 samples belong to this type (e.g. sample 107, Figure 7-56).

- In AARM ***type II*** samples, M_1 and M_3 axes are within the dyke plane and M_2 is the pole to that plane. ΔM_2 equals or exceeds 60°. Type II comprises 5 samples (e.g. sample 6, Figure 7-56).

- AARM ***type III*** samples show M_2 and M_3 axes within the dyke plane and the axis of maximum magnetization M_1 normal to it. ΔM_1 exceeds 59° and is represented by 12 samples (e.g. sample 19, Figure 7-56).

- Fabric ***type IV*** is the most frequent AARM fabric type in this study with 19 samples (e.g. sample 65, Figure 7-56). It contains all the transitions between the first three fabric types with at least ΔM_1 or ΔM_2 or both of them ranging between 36 and 59°. Samples with only M_1 within the dyke plane (± 20°) and ΔM_2 ranging between 36 and 59° are grouped into ***subtype IVa***, which contains 3 samples (e.g. sample 66, Figure 7-56).

There are 5 samples with only two or three measured specimens, where the principal magnetization axes are exchanged or broadly scattered. Since reliable axial means can not be calculated from this sparse data, these samples are not interpreted and declared as undefined (Appendix 14).

Stereonet patterns of samples 58, 59 and 62 strongly resemble the ones from AMS measurements. They show an internal fabric subdivision between the individual specimens because their M_1 and M_2

directions are exchanged. Calculations of their means are not reasonable in that case. Therefore, means have been calculated for individual pairs and not for the whole specimen set. Their directions resemble the ones of the corresponding AMS means.

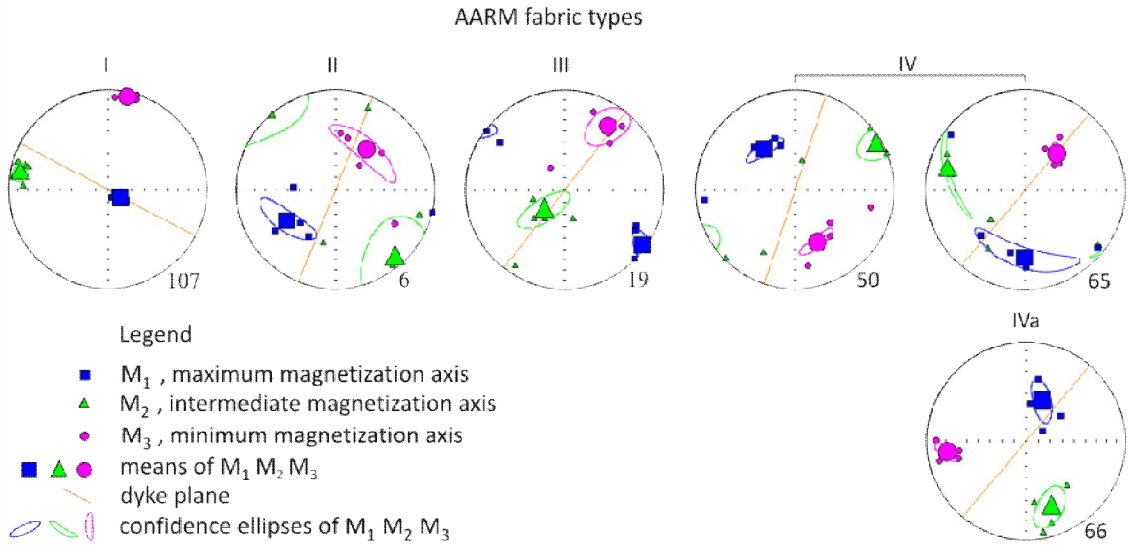

Figure 7-56. Stereograms (lower hemisphere) presenting an example of the 4 AARM fabric types

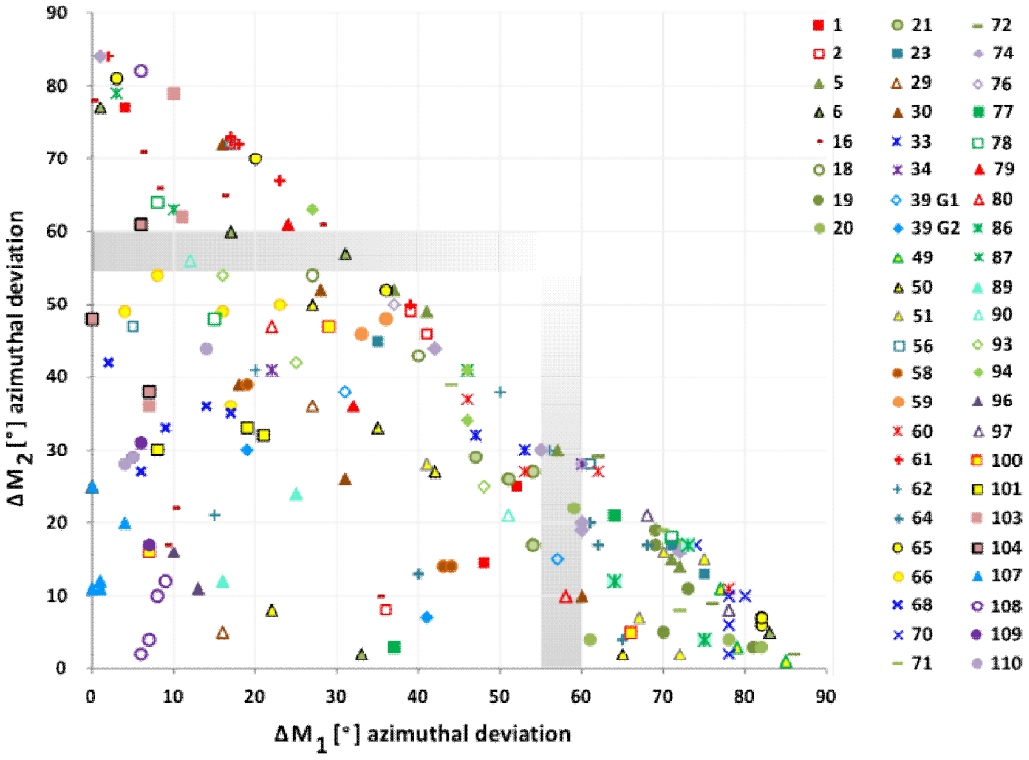

Figure 7-57. Deviation of the specimens principal (M_1) and intermediate (M_2) AARM axes from the dyke plane; plot is used for classifying AARM fabric types of single specimens.

In summary, type IV AARM fabrics are the most abundant ones with 23 samples (43%), followed by type III (22%) and I (19%). Compared with mostly vertical and subvertical long principal AMS fabric axes in NE dykes, the long axis of ARM is mostly horizontal, oriented NW-SE, at high angles to the dyke plane while the short axis is mostly within the dyke plane. Compared with the relatively clear cluster of vertical κ_{max} of the AMS in NE dykes, the M_{max} axes of the AARM fabric are more scattered.

7.7 The silicate rock fabric

The shape preferred orientation of plagioclase in sample 21, and of plagioclase as well as pyroxene phenocrysts in samples 52 and 77, have been investigated by image analysis of three perpendicular thin sections oriented horizontally (H), vertically (V) and vertically parallel (P) with the dyke strike. The samples are from 3 different dykes at their NW margins and show the following textures:

- ***Sample 21*** is vitrophyric and contains mostly isolated plagioclase phenocrysts embedded in a glassy matrix. The average size of plagioclase is between several hundred micrometers to 1.5 mm with rare examples of up to 4 mm.

- ***Sample 52*** reveals a vitrophyric to intersertal fabric with tabular pyroxene and acicular plagioclase.

- ***Sample 77*** is porphyritic at the dyke margin with large plagioclase grains in a matrix of small plagioclase laths and thin-tabular pyroxene with interstitial glass.

Silicate mineral orientation

Shape preferred orientation of phenocrysts is already obvious from microscopy in most thin sections, also subdominant directions are apparent. Alignment of crystals parallel with the dyke margin is most distinct in sample 21. The analyses of the individual micrographs and scans are summarized in Appendix 15 and mineral orientations of analysis with less than 1000 particles (the data limit in Fabric8) are displayed in rose diagrams (Figure 7-58). From the rose diagrams shape preferred orientation (SPO) of silicate phenocrysts in each thin section is inferred from the shape of the roses. Mineral alignment is suggested parallel with the main maximum direction (dashed black line, Figure 7-58) within the analysed plane. Clear secondary maxima are rare, such as in roses 21H and 52H. In some roses the main maximum is distributed over a wider range of angles (40 to 50°, e.g. 21V, 52V, 77P). A poor preferred orientation is indicated by only poorly developed maxima of plane 52V and 77P. The mean particle orientation calculated by ImageJ is given by the angle of the long axis of the mean shape ellipse (solid black line, Figure 7-58) with the horizontal reference line of the image. The orientation of mean shape ellipse commonly deviates from the main maximum between 10° to 55°.

Appendix 15 also documents analysis parameters such as the angle of vector mean (comparable with ImageJ's angle of long axis of mean shape ellipse- parenthesized) and the degree of preferred orientation calculated by Fabric8. On the right side, Appendix 15 displays the rake (orientation; see Figure 4-17; Launeau and Robin, 2005) of the mean ellipses long axes derived from three different origins: Fabric8, ImageJ and the estimated maximum of the rose diagram (Figure 7-58). For some sections (21V, 52P,77V), two different micrographs of the same thin section have been analysed independently to test if there are SPO differences at the thin section scale. These are found to be insignificant (Figure 7-58Figure 7-; compare rose diagrams of the right column with the respective analogue). Also, analyses have been done repeatedly on the same image (21H, 52H-1, 77P-7) including different ranges of the particle (pixel) size and/or permitting an increased circularity of particles to test the effects of these factors on the derived SPO. The results of these comparisons show no major differences between the angles of mean ellipses long axes (differences of 1 to 3°), and a slightly larger effect on the axial ratios of the mean ellipsoids. The mean ellipse angles derived from ImageJ and the vector mean of Fabric8 from the same section are nearly the same, both deviating distinctly from the mean maximum orientation of the rose diagrams. The three rakes behave accordingly. Thin section 21V is an exception, where both SPO means coincide with the rose maximum, resulting in equal rakes. Further angular deviation between the rakes of mean orientation calculated by ImageJ and the orientation maximum es-

timated from the rose diagram is given on the right of Appendix 15. Apart from section 21V, where the rakes are in perfect agreement, the differences are typically between 14 and 55 degrees. Also, the angular deviation of the crystal orientation maxima (from rose diagrams) from the direction of dyke strike in sections H and V are tabulated. Except for section 21V, where the majority of the particles are oriented parallel with the dyke strike (deviation of 2.6°), the inclination of particle long axes in the other thin sections is between 20 and 30 degrees referred to the dyke margin.

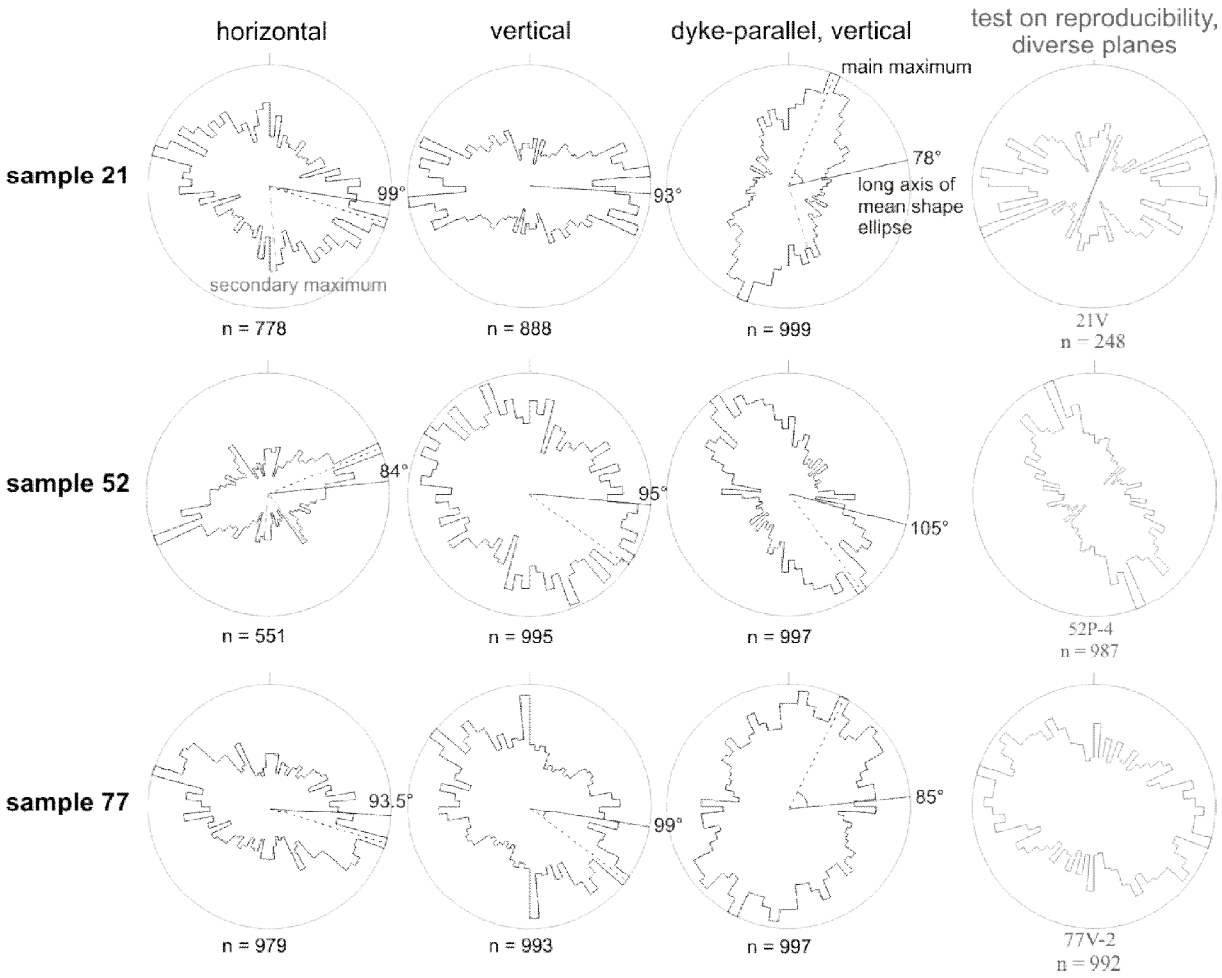

Figure 7-58. Orientation distribution of plagioclase and pyroxene phenocrysts at the dyke walls in 3 samples, obtained from the software programme ImageJ (Rasband, 2012). The long axis of silicate mean shape ellipse is shown by a black line. n = number of analysed particles.

In order to test if a micrograph image can be considered representative for the entire thin section, all three thin sections of sample 21 have been analysed sectionwise within strips parallel with the dyke margin. Particle orientation of the individual strips has been compared for changes depending on the distance from the dyke margin. The thin sections were subdivided into 3 (21V, P) or 4 (21H) strips with approximately the same width. Angular variations of the mean ellipse's long axis orientation within one thin section are small, between 1.2 and 7.8° in planes P and V. Surprisingly, the angles do not change with distance from the dyke margin at this scale, and the greatest differences were found between the direct margin strip and the adjacent one. Section H shows a larger difference of 12° between the strip closest and the strip farthest from the dyke margin, but this is an exception and it can be concluded that the results within a single thin section are consistent.

Silicate fabric ellipsoids

For each of the three samples, a 3-D ellipsoid was derived from orientation data (rake) of three different sources (ImageJ, Fabric8, rose diagram). Appendices 15 &16 present the in- and output data of the multiple ellipsoid determinations. Individual ellipsoid determinations are numbered and the origin of the utilized rakes is given, as well as the ellipsoid's shape parameters "degree of anisotropy" P' and the parameter T.

The results based on rose diagram-derived rakes for all three samples yield a hyperboloid and not an ellipsoid. According to Launeau and Robin (1995), a hyperboloid is not a mathematically valid solution and consequently, these runs are regarded as unsuccessful and are not considered further. All determinations with rakes derived from ImageJ and Fabric8 (including determinations 2, 4 and 6 of sample 21, which were corrected for 30° in the H-planes, see remark in chapter 5.3) result in ellipsoids. As expected from the similarity of their rakes, the ImageJ and Fabric8-derived ellipsoids of the same samples strongly resemble each other in terms of orientation as well as the shape parameters anisotropy and T. The 30° correction of plane 21H influences the dip direction of all three ellipsoid axes with a clockwise shift by 30°.

The misfit between sectional ellipses and the calculated ellipsoid is expressed by the "global" and "individual" incompatibility indices (I-indices; see chapter 5.3). Generally, the individual I-indices in this study are lower than the global I-index, because each of the three planes has been fully weighted (with 1) for the ellipsoid determination. The ellipsoids derived from ImageJ and Fabric8 are similar (see axial orientation, Appendix 15).

Sample 21 shows the highest global I-index of 10.9 or 10.7 %, followed by sample 77 with 7.3 or 7.1% and sample 52 with a very low I-index of 3.7 or 2.8. The ellipsoids with the corrected H-ellipse determinations 2, 4 and 6 of sample 21 have significantly higher I- indices with 17.2 and 15.2 compared to their uncorrected equivalents. Therefore, and also because of the very limited effect of this irregularity to the results of the whole thin section, it is considered negligible and the correction as irrelevant.

ImageJ - derived ellipsoids have been chosen as representatives for the SPO analysis of silicate minerals by image analysis since they yield the lowest global and individual Incompatibility indices in the programme Ellipsoid. The stereographic projections of all three samples' ellipsoids against the dyke plane suggest a normal, or type I silicate fabric with the long and intermediate crystal axes parallel with the dyke walls (Figure 7-59). For sample 77 the deviations of maximum and intermediate axes are within about 25° from the dyke plane, while for samples 21 and 52 the deviations are within 10°. The degree of anisotropy for the ellipsoids is relatively high (between 4.4 and 7.5) due to the anisotropic lath shape of the analysed crystals (Appendix 16, Figure 7-34 F, G). According to their positive shape parameters of 0.4, 0.6 and 0.35 the ellipsoids are moderately oblate.

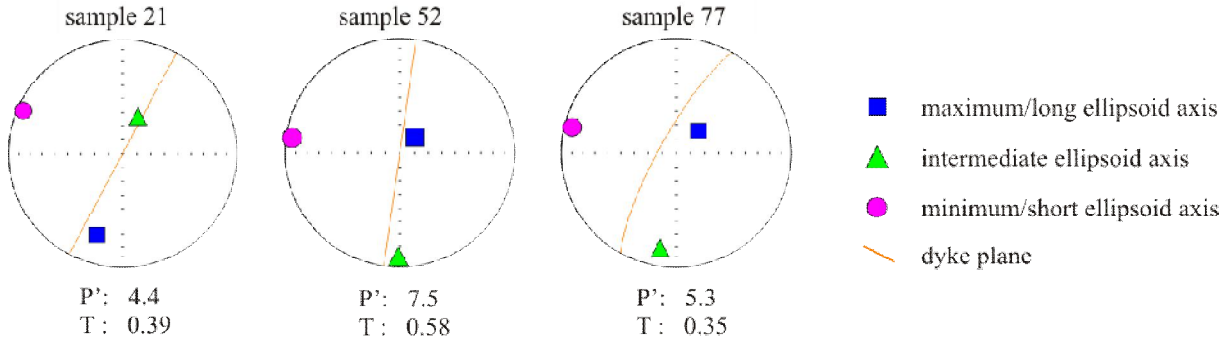

Figure 7-59. Silicate fabric ellipsoids, each calculated by the programme Ellipsoid with microphenocryst orientation data from three perpendicular thin sections; lower hemisphere projections.

In summary, in all 3 samples the thin sections show a shape preferred orientation (SPO) of phenocrysts in the dykes at the contact with the country rock. SPO is parallel with the dyke margin and occasional secondary orientation directions occur. The calculated silicate fabric ellipsoids are all of type I, that is the long and intermediate fabric axes are parallel with the dyke plane. Therefore, the silicate fabrics are interpreted to record the magma flow direction of the first magma pulses during dyke opening. Vertical magma flow is inferred from the long axes in samples 52 and 77 from the Kalkfeld and Omdel dam area and nearly horizontal, NE-SW-oriented flow in sample 21 from the Spitzkoppe area.

8 Comparison of rock fabrics

8.1 Magnetic fabrics: AMS versus AARM

A comparison of the Anisotropy of Anhysteretic Remanent Magnetization (AARM) fabrics with the AMS fabrics is useful to identify anomalous, SD-influenced AMS fabrics. The following comparison refers to the $AMS_{INITIAL}$.

Of the investigated samples, 26 are of AMS type I, and 28 of other types. The orientation of the principal AMS and AARM ellipsoid axes mostly does not coincide: the AARM fabrics of most samples show a change or reorientation of their axial configuration compared with their AMS fabric, and in these cases the fabric type may also change. Thus, the AARM fabric of 41 samples is reoriented compared to AMS, whereas in 13 samples there is minor or insignificant change (departures of the principal ellipsoid/tensor axes orientations of 20-30° in average, max. 40°), referred to as "stable" axial configuration (e.g. sample 19, Figure 8-60). The reorientation is expressed either as an exchange of two or all three principal ellipsoid axes (in 30 and 7 samples, e.g. nos. 16 and 107, Figure 8-60) or in an undefined change of all axes (samples 19, Figure 8-60), or both.

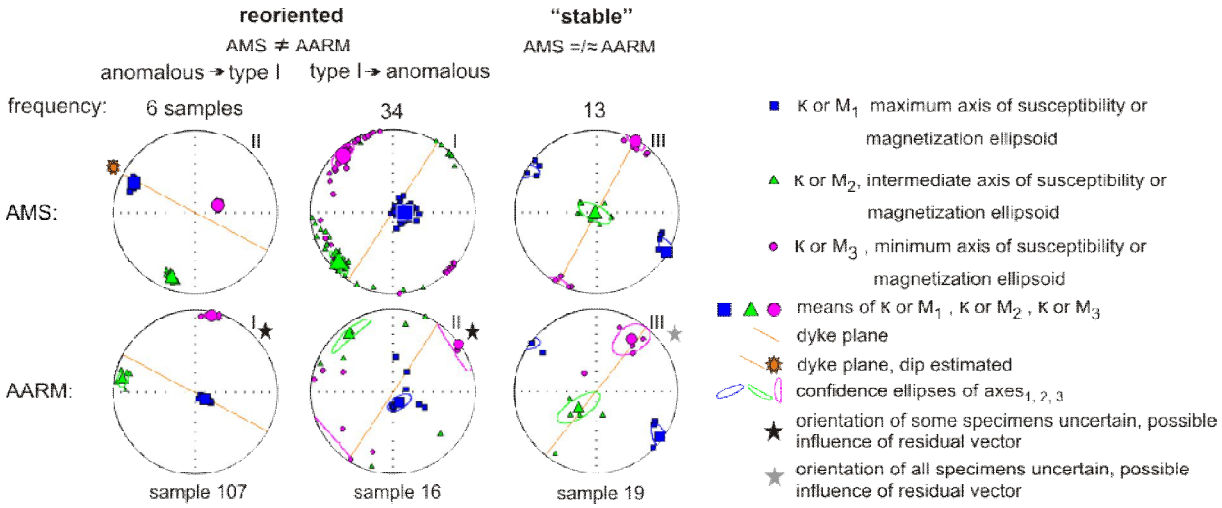

Figure 8-60. Comparison of AMS and AARM fabrics. For explanation see text.

Figure 8-61 illustrates the difference between the orientation of the long and short fabric axes of all AMS (upper row) and all AARM (central row) fabrics in density plots in lower hemisphere stereonets. For a direct and better comparison the AMS fabrics of only the AARM samples are shown in the lower row. Steep κ_{max} axes of the normal fabric type samples prevail in NE striking dykes (upper left), but there are also shallow and inclined ones perpendicular to dyke strike from the anomalous types, which becomes more clear in the lower left stereonet. In contrast with the AMS, anomalous fabrics with rather shallow to inclined dipping M_{max} axes (normal or oblique to the dyke plane) prevail in the respective samples for the AARM. κ_{min} axes are horizontal with a maximum roughly perpendicular to the dyke plane and a secondary maximum within this plane. In contrast, M_{min} axes are frequently within the dyke plane with a variable dip angle ranging from horizontal to steeply inclined. The small data base from the NW striking dykes reveal dyke-parallel shallow to steep κ_{max} and both shallow and steep κ_{min} axes compared with steep M_{max} axes and shallow M_{min} axes perpendicular to the dyke plane (normal AARM fabric).

The reorientation of AARM fabrics compared to AMS is ascribed to a variably strong SD-effect (see chapter 4.1.2). In terms of the magnetic fabric changes, three cases are recorded: 1. normal type (I) changes to anomalous (II-IV; e.g. sample 16, Figure 8-60), 2. anomalous turns normal (e.g. sample

107, Figure 8-60), and 3. anomalous changes to anomalous (not shown). Only 6 of 28 AMS-anomalous samples (Table 8-1, nos. 29, 68, 96, 107, 109, 110) become AARM normal, type I, which is the expected reorientation based upon the classical SD-effect for samples with a high proportion of primary magma flow-oriented SD grains. Twelve samples showed a change from one anomalous to another anomalous fabric type, in contrast to the expectation from the SD-effect. Most AMS-normal fabrics, however, become AARM-anomalous, which is even less consistent with the SD theory.

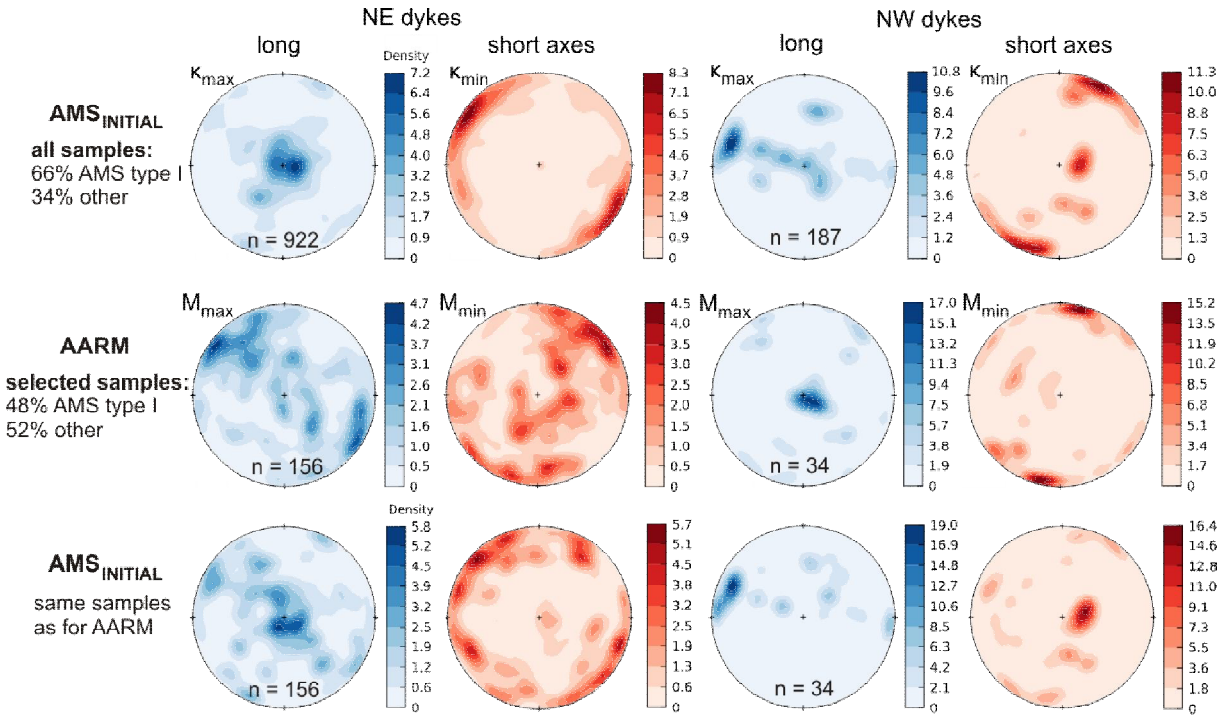

Figure 8-61. Density plots (lower hemisphere, equal area projection; Fisher distribution) of maximum and minimum susceptibility (κ_{max} and κ_{min}) and remanent magnetization axes (M_{max} and M_{min}) in NE and NW-striking dykes in the HOD.

The changes in fabric type for the individual samples are given by the matrix in Table 8-1 only 15 samples hold the same fabric type in both methods (but not necessarily the same orientation of long and intermediate axes). All others change their fabric types. The fabric type changes are not as expected from the SD-theory (i.e. a change from $AMS_{INITIAL}$ type II or III to AARM type I by exchange of κ_{int} and κ_{min} axes or κ_{max} and κ_{min} axes, respectively) except in 6 samples mentioned previously, but are rather unsystematic. Compared with only 10 type IV (oblique) AMS fabrics of 101 samples, the percentage of oblique AARM fabrics is much higher, with 25 of 54.

Remarkably, most of the stable fabric samples are of type III or IV (bold numbers in Table 8-1), and 3 of the 4 unstable type IVsamples keep the same type of fabric despite changes in ellipsoid orientation. The AARM fabric type of 4 samples remains unclear due to a statistically insufficient number of measured specimens and due to a scatter of their ellipsoid axes. These samples are excluded from the comparison.

The Jelinek plots of both the $AMS_{INITIAL}$ and AARM methods show that all types of fabrics occur from extremely oblate to extremely prolate ellipsoid shapes. While oblate fabrics ($T > 0$) predominate among the $AMS_{INITIAL}$ ellipsoids (Figure 7-46), prolate shapes ($T < 0$) are slightly more common among the AARM ellipsoids (Figure 7-54). Of the most important magnetic fabric parameters from both methods, the ellipsoid shape parameter T_{AARM} and T_{AMS} often differ strongly comparing the samples one by one. The means of the corrected anisotropies of AARM (P'_{AARM}) are mostly higher than the corresponding mean P' of the $AMS_{INITIAL}$ (P'_{AMS}; Appendix 18). Generally, P'_{AMS} of most samples

is below 1.05, while P'_{AARM} is higher, mostly below 1.2. Jackson (1991) explains this difference by the fact that the remanence is measured in a zero-field and the susceptibility is not. He argues that inducing a reversible magnetization in an energetically unfavourable orientation is easier than imparting a remanent magnetization.

Table 8-1. Comparison of fabric $AMS_{INITIAL}$ and AARM types; black samples are unstable and reorient, fabrics of bold samples differ minimally or are stable

Anisotropy of Anhysteretic Remanence (AARM)

Anisotropy of Magnetic Susceptibility ($AMS_{INITIAL}$)

fabric type	I	II	III	IV	IVa	AARM undefined
I	39G2 **89** 101 108	6 16 87 103	49 64 70 71 72 97	1 5 30 33 **93** 94	66 78 **104**	79, 80, 90
II	107 109 110	-	20	74 76	-	-
III	29 68	-	**19** 23 **51** **60**	18		100
IV	96	**61**		**21** 34 **39G1** **50** 56 **58** 59	-	77
IVa	-	-	86	2 **62** 65	-	-

AARM versus AMS_{AFD}

In a late stage of this HOD study, the AMS of some specimens from 48 samples was measured again after a partial demagnetization in alternating magnetic fields ("magnetic cleaning") in order to exclude the influence of the NRM vector on the AMS orientation. In fact, in 27 of these samples the AMS fabric after AFD (AMS_{AFD}) changed weakly to moderately compared to the $AMS_{INITIAL}$. However, since these remeasurements were performed as a test at the end of this study, not all samples and not enough specimens from each sample were remeasured to provide a statistically sound reference.
In principle, the sense of differences between the AARM and the AMS_{AFD} fabrics is similar to those between AARM and $AMS_{INITIAL}$. In 30 of the 48 samples the fabric ellipsoids differ moderately to strongly and for 13 samples the ellipsoids have similar orientations, with weak changes of 20 to 45 degrees (see Appendix 17 for comparison). The ellipsoid orientation in 5 samples cannot be evaluated because of a heterogeneous orientation of the principal AARM axes. The differences in the 30 other samples consist of an exchange of 2 (18 samples) or all 3 principal ellipsoid axes (11 samples), often combined with a minor to moderate rotation (20 to 40° on average) of 2 or all 3 axes. Maximum and minimum principal axes exchanged in 13 samples and intermediate and minimum axes in 6 samples.

Compared with the AMS axes the AARM ellipsoid axes of a number of samples cluster less well, such as in samples 21 and 77, Figure 8-62.

In summary, 41 of 54 samples investigated yield AARM fabrics which differ in orientation from their respective AMS fabric. They are reoriented, which is expressed either as an exchange of two or all three principal ellipsoid axes or/and in an undefined change of all axes. In 13 samples there is minor or insignificant change, referred to as "stable" axial configuration. The reorientation of AARM fabrics compared to AMS is ascribed to a variably strong SD-effect due to a variable proportion of single-domain (SD) tmt in the dyke rocks. Only 6 of 28 AMS-anomalous samples become AARM normal (type I), which is the expected reorientation based upon the SD-effect for samples with a high proportion of primary magma flow-oriented SD grains. All other fabric reorientations are not as expected and most AMS-normal fabrics even become AARM-anomalous, which is even less consistent with the SD theory. From this it is concluded that the long axes of SD tmt grains are not oriented parallel with the dyke plane.

8.2 AMS fabrics before and after alternating field demagnetization

The AMS, measured after the alternating field demagnetization (AMS_{AFD}) on 48 selected samples, is compared with the AMS measured before AFD ($AMS_{INITIAL}$) in order to test, if the orientation of (type II-IV) AMS fabrics is influenced by the natural remanent magnetization (NRM) of the rocks.
In the few cases, where specimens of the same sample were demagnetized in different peak alternating fields (AF), their AMS_{AFD} fabric ellipsoids are almost equally oriented, demonstrating that the difference in peak AF is negligible, here. In the few cases, where they are not oriented similarly, no mean fabric orientation has been calculated.
Appendix 17 shows the $AMS_{INITIAL}$ and AMS_{AFD} (and AARM) in stereographic projections of the lower hemisphere. 22 samples yield no or only minor changes in the fabric orientation between $AMS_{INITIAL}$ and the AMS_{AFD} ellipsoid (max. about 10°), they have stable fabrics. The remainder of 26 samples show reorientation of the principal susceptibility axes after demagnetization (e.g. κ_{max} of sample 77, Figure 8-62). The reorientation is not always obvious at the sample scale, but when comparing the AMS ellipsoid of the individual cylindric specimens one by one, it becomes apparent. Slight to moderately strong reorientations between 20 and 45° are shown by 18 samples. An exchange of κ_{max} and κ_{min} occurs in one sample, of κ_{max} and κ_{int} axes in 4 samples and in one sample all three axes are exchanged. Occasional girdle configurations in the $AMS_{INITIAL}$ become clusters in the AMS_{AFD} (see samples 21 and 77 in Figure 8-62).

There are more reorienting samples among the AMS-normal (type I) than among samples of other fabric types. While among the 26 normal-type samples 10 show moderate and 7 show minor axial changes, among the 22 anomalous-type samples there are only 5/4 with major/minor changes.
Concerning the fabric types, the matrix in Table 8-2 compares the AMS fabric types before ($AMS_{INITIAL}$) and after AFD (AMS_{AFD}). Though 27 samples are reoriented after AFD, it is remarkable that most of them do not change their type of fabric, except of 6 samples.
Apart from directional changes, there is a five to eightfold increase in the bulk susceptibility after AFD. Basically, all scalar AMS parameters (P', T etc.) change, but, since the focus in this work is not on these details, these results are not displayed here.

From minor to strong reorientations between $AMS_{INITIAL}$ and AMS_{AFD} fabrics in 26 of 48 samples it is concluded, that the natural remanent magnetization vector influences the orientation of the AMS fabric ellipsoid, but rarely influences the type of fabric. If so, then fabrics do not necessarily become the normal type (I) after demagnetization, which proves that the NRM vector is not responsible for anomalous AMS fabrics.

Table 8-2. Matrix with comparison of fabrics: $AMS_{INITIAL}$ versus AMS_{AFD}; Bold: not reoriented/stable (22 samples), normal: weakly reoriented (13 samples), grey italic: strongly reoriented fabrics (13 samples)

Anisotropy of Magnetic Susceptibility ($AMS_{INITIAL}$) \ AMS after demagnetization (AMS_{AFD})	fabric type	I	II	III	IV	IVa
	I	*1* 5 *6 (+ IVa)* **16** **30** *33* **49** *64 (+ II)* *66* **70** **71** **72** **78** *79* **87** **89** 90 *93* 94 **97** 101 103 104	*108*	-	*80*	-
	II	-	**74** 76 107 **109** 110	*20*	-	-
	III	-	-	18 **19** *23* **29** **60** **68** 100	-	-
	IV	77	21	-	**50** **56** **58** **61** **96**	-
	IVa	-	*2* 65	-		**86**

8.3 Magnetic versus silicate fabrics

This section compares the orientation of induced (AMS) and spontaneous/remanent magnetization (AARM) fabric ellipsoids with the bulk silicate fabric ellipsoid orientation (calculated on the base of ImageJ mean ellipses orientations) on the example of 3 selected samples nos. 21, 52 and 77. The respective fabric ellipsoids are shown in lower hemisphere projections in Figure 8-62 and Appendix 18 tabulates the respective orientation of the principal fabric axes and shape parameters. For comparison, both the NRM influenced $AMS_{INITIAL}$ and the cleaned AMS_{AFD} fabric ellipsoids are displayed.
All three samples have one property in common: an average orientation of the phenocryst long axes parallel with the dyke plane, that is their silicate fabric ellipsoids are all of normal type (I).

Sample 77:
The silicate fabric ellipsoid of sample 77 corresponds quite well with the AMS_{AFD} (and also with the $AMS_{INITIAL}$) ellipsoid, both revealing normal fabric types with the long and intermediate axes parallel with the dyke plane. The long axis is very steep with 70 to 75°. The mean AARM fabric ellipsoid is difficult to interpret and statistically not sound, because it is based on data of only 2 specimens, whose long axes scatter and the other two axes interchange. It is speculated that these differences in fabric orientation may be due to an increased single-domain tmt content in the non-type I specimen supported by a higher MDF value of 48 mT and by a residual remanent magnetization of 15% after demagnetization (H= 100 mT), both pointing to a fraction of highly coercive grains. The exact orientation of the mean AARM ellipsoid remains speculative, but either an oblique fabric with moderately steep long axis dipping E, similar to that shown by the $AMS_{INITIAL}$, or an inverse fabric type with a flat long axis nearly normal to the dyke plane are probable. In the latter case the long axis would be oriented nearly parallel with the short axis of the AMS_{AFD} fabric and would deviate moderately from the ImA fabric. The AARM definitely differs in orientation from the AMS_{AFD} and silicate fabric ellipsoid.

Sample 21:
The two magnetic fabric ellipsoids AMS_{AFD} and AARM are similar in orientation for sample 21, although axes scatter more in the AARM than in the AMS_{AFD}. Both ellipsoids show moderately steep long axes. The AMS_{AFD} represents an intermediate fabric type and the AARM fabric is oblique transitional to inverse (type III). A clockwise rotation of about 30° transfers the AARM fabric into the AMS_{AFD} configuration. However, the silicate fabric ellipsoid is normal (type I) and does not match either of the magnetic ellipsoids. Its long axis is flat with 20° inclination. Mean axial AARM ellipsoid orientations have been determined with the statistics in StereoNett 2.46 and in Anisoft 4.2 for comparison. Except for the 12° deviation in dip direction of the intermediate axis, the axial orientation means nearly coincide.

Sample 52:
The orientations of the principal magnetic and silicate fabric ellipsoids of sample 52 correspond very well. Both define normal fabrics with steep long axes. However, no AARM and AMS_{AFD} ellipsoids were determined for sample 52.

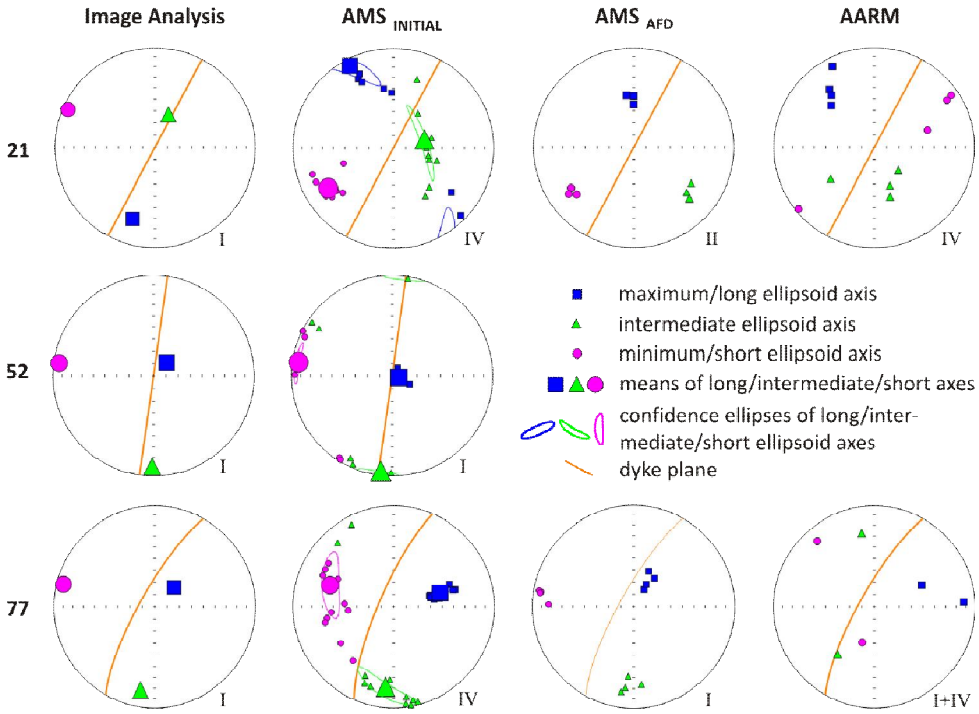

Figure 8-62. Comparison of fabric ellipsoids obtained from the methods Image Analysis, AMS and AARM; orientations of the principal ellipsoid axes are given in a lower hemisphere projection; roman numbers indicate fabric type

The shape parameters of the anisotropy ellipsoids derived from all methods are listed in Appendix 18. Generally, the degree of anisotropy of the image analysis -ellipsoids (P'_{ImA}) of all three samples is more than one order of magnitude higher than P' of the magnetic methods, while the anisotropy of the AARM ellipsoid (P'_{AARM}) is significantly higher than P'_{AMS}. Concerning the shape parameter (T), the magnetic and silicate ellipsoids of sample 21 are both moderately oblate. Also, the AMS_{AFD} and ImA ellipsoids roughly agree in their weak to moderate oblateness, while the AARM ellipsoid is weakly prolate. The shape parameters of magnetic and silicate fabric ellipsoids of sample 52 do not agree, but care has to be taken when evaluating the shape factor, because it has proven very sensitive to slight changes in rake or dip when determining an ellipsoid.

As described in chapter 5, large dyke-parallel oriented feldspar phenocrysts are observed in the dyke with the sample no. 107, Klein Etjo area. Whether the phenocryst's long axis is oriented vertical or horizontal is not clear, but the latter is very probable. If so, then phenocryst orientation coincides with the long axis of the AMS fabric, but disagrees with the steep AARM long axis.

In summary, samples 21, 52, 77 (and 107) have dyke-parallel silicate fabrics (type I), which are consistent with expected magma flow. Steep long fabric axes are recorded for samples 52 and 77 and horizontal ones for nos. 21 and 107. The silicate fabric coincides with the AMS fabric orientation for samples 52 and 77, suggesting the same orientation mechanism. Both magnetic fabrics of samples 21 and 77 agree roughly in orientation, which points to larger tmt grains mainly in the PSD and MD range (inferred from low MDF = 7 mT and lower M_{RS}/M_S ratio = 0.26; slope corrected; see Appendix 7 & Appendix 10). In sample 21, the magnetic fabric orientation does not coincide with silicate fabric orientation at the immediate contact with the country rock.

9 Discussion

9.1 Magnetic mineralogy

Grain shape, distribution and alteration of magnetic phases

Transmitted- and reflected light microscopy and temperature-dependent susceptibility measurements clearly identify titanomagnetite/-maghemite as dominant magnetic phase in most of the HOD samples. It is the main carrier mineral of the AMS and AARM. The temperature-dependent susceptibility (κ-T) curves, S-shaped hysteresis loops and mean bulk susceptibilities (κ_m) above $5*10^{-3}$ SI in 86 out of 111 samples support these results (Tarling and Hrouda, 1993).
Titanomagnetite is a late crystallizing phase, either occurring separately or clustering in the interstices of ophitic/subophitic pyroxene grains, or aligned along narrow spaces between individual pyroxene and plagioclase crystals (e.g. Figure 7-36 A, C). This distribution anisotropy of tmt in the HOD samples with occasional close grain spacings suggests magnetostatic interactions between the tmt grains, which are considered to create magnetic fabric anisotropies (Wolff et al., 1989; Hargraves et al., 1991, Stephenson, 1994; Grégoire et al., 1995; Cañon-Tapia, 1995, 1996; Gaillot et al., 2006). Tmt/-tmgh typically forms either individual octahedral grains, irregularly intergrown with ilmenite or cruciform or elongate dendrites with rectangular side branches**.** Consequently, distribution anisotropy of tmt grains are suggested to be responsible for the bulk of AMS and AARM fabrics except of in the dendrite bearing samples, where grain shape anisotropy may contribute or even dominate. Exsolution of titanomagnetite/-maghemite, indicated by mostly thin ilmenite lamellae within tmt is common. In rare cases with strong flow fabrics (samples 41 and 43) elongate-anhedral tmt/tmgh is distinctly aligned parallel with the silicate components and parallel with the dyke walls. In many other samples, a more or less weak silicate microphenocryst orientation is recognizable (Appendix 3, 'crystal alignment'), including those with ophitic and subophitic fabrics. The long axes of microphenocryst are roughly parallel with the dyke walls, which is attributed to the aligning force of the magma flow.
The κ-T curves reveal details about the Fe-Ti ratio: Except for a few samples, the curves indicate intermediate titanomagnetite and -maghemite with a variable degree of oxidation (ulvospinel content of around 0.4 - 0.6 at T_C = 150°C) and either pure magnetite or a titanium-poor titanomagnetite/-maghemite.
Initial plateaus in the AFD curves can also be interpreted in terms of MD grain maghemitization (not only in terms of smaller grain sizes), according to Dunlop (1983), Cui et al. (1994) and Ryall et al. (1977). However, tmts show rare signs of strong maghemitization, such as shrinkage cracks.

In places, there are considerable variations of the mean bulk susceptibility between samples from the same dyke and, also, between specimens from the same sample (compare Appendix 11), indicating mineralogical heterogeneity at the dyke and also at the sample scale. The reason for these heterogeneities is probably differing degrees of tmt alteration (e.g. formation of leucoxene, maghemitization) and/or in varying fractions of tmt and ilhm.
22 samples show mean susceptibilities between $5*10^{-4}$ and $5*10^{-3}$ SI (Appendix 11). Such relatively low susceptibilities can indicate a potential control of para- and ferromagnetic (s.l.) phases on the magnetic fabric (Tarling & Hrouda, 1993), a lack of tmt, tmt alteration, magnetostatic interaction or coexistence or superposition of differently oriented magnetic subfabrics (Cañon-Tapia, 1996). Because of its high magnetic susceptibility, which is at least 3 orders in magnitude higher than the susceptibility of other ferri- and paramagnetic minerals found in the samples, tmt/tmgh/mt dominate the magnetic properties of a rock if they make up a minimum of 1 volume% (Tarling & Hrouda, 1993; Tauxe 2002). In some of the low-κ samples, microscopy commonly shows that ilmenite/ilmenohaematite is volumetrically more abundant than tmt/tmgh. This is consistent with the samples' temperature-dependent susceptibility (κ-T) curves, which reveal the T_Cs of tmt/tmgh/mt at temperatures between 150 and 590 °C and often start with a hyperbolic decrease in κ at the lowest temperatures pointing to ilmenohaematite compositionally close to ilmenite (see chapter 8.2.2). Hysteresis loops of these samples mostly reveal a less pronounced s-shape (ferrimagnetic response) and stronger linear (paramagnetic) component.

Together with ilm/hm, pyroxene may likely also contribute to the bulk susceptibility in individual low-κ samples. Although ilmenite has a slightly higher intrinsic susceptibility than pyroxene, the latter is in general much more abundant.
Besides a low tmt/ilm-ratio, alteration and pseudomorphous replacement of mt/tmt/tmgh by leucoxene (mixture of goethite, haematite and phyllosilicates), as commonly observed in thin sections (compare Figure 7-35, Appendix 3), may lower the bulk susceptibility to about half of its initial value (pers. comment A. Kontny). Haematite rarely occurs in large quantities, except where it constitutes part of leucoxene, and it may occasionally contribute to AARM, rarely also to AMS. Goethite (except where as constituent of leucoxene), pyrrhotite and pyrite or other iron minerals only occur abundantly in more altered samples, but they are considered negligible for the bulk magnetic susceptibility of the rock because of their low κ and absence in κ-T curves (haematite is absent as well). A contribution of goethite or ferromagnetic pyrrhotite to remanence and its anisotropy can not be excluded for samples with coercivities above 100 or 160 mT.
Low bulk susceptibilities in basalts can originate from the lack of tmt/tmgh, which can also result from rapid cooling/quenching of the magma. Whether other ferromagnetic (s.l.) iron (hydr)oxides or minerals, such as haematite, goethite or pyrrhotite, contribute to the bulk susceptibility (κ_m) can be inferred from the coercivity spectra of the samples obtained from alternating field demagnetization (AFD) or from hysteresis curves and ratios. Ferromagnetic pyrrhotite, haematite or goethite have variable coercivities of tens of teslas (Tauxe, 2002). The AFD curves of some HOD samples indicate a residual remanent magnetization up to 30% of the initial natural remanent magnetization (NRM) after demagnetization (H = 160 mT), which points to the presence of highly coercive (H_C > 160 mT) minerals carrying parts of the remanence. The same is true for individual specimens or samples that are not demagnetizable in an alternating field of 160 mT (see chapter 7.4). According to Soffel (1991) the coercivity of single-domain mt/mgh/tmt is not higher than 150 mT, nevertheless, coercivities may be higher for their dendrites (Shaar & Feinberg, 2013). However, the latter authors report dominantly lower coercivities for SD to PSD dendritic samples with up to 2 µm grain size, a "tail of high coercivity grains" exceeds 100 mT in FORC (first order reversal curves) diagrams.
Microscopic observations only rarely show higher volume percentages of pyrrhotite, while the amount of haematite and goethite is difficult to estimate, in particular within leucoxene or when goethite is dispersed in very fine-grains. However, their contribution to AARM is low because of a low remanence susceptibility compared with tmt/tmgh (Jackson, 1991).
Whether maghemitization increases or decreases the coercivity of SD tmt is discussed controversially (Moskowitz et al., 1980 and reference therein). For larger grains Moskowitz et al.(1980) and Ryall et al. (1977) found that oxidation/maghemitization can increase the coercivity of tmt by as much as a factor of 2 to 3.
Finally, low bulk susceptibilities (and anisotropies) can also be caused by the coexistence and superposition of differently oriented magnetic and silicate subfabrics, which may compensate each other. Secondary maxima of silicate phenocryst orientation of samples 21, 52, and 77 (Figure 7-58) provide hints to this.

Grain size and domain state of titanomagnetite/-maghemite

Microscopic studies of thin sections show that the grain sizes of the titanomagnetites/-maghemites in the HOD samples are variable. Some samples contain mt/tmt ranging continuously from 1 to a few hundreds of micrometres in diameter, others contain only smaller grains with the upper size limit of a few tens of µm, which is the lower grain size limit of samples with coarser grains. Grains smaller than 1 µm are beyond the resolution of the petrographic microscope.
Considerable size reduction of MD grains occurs at least in 18 samples by the decomposition of tmt due to exsolution and/or deuteric oxidation, producing a subdivision of the MD grains into subvolumes separated by paramagnetic ilmenite lamellae (e.g. Butler, 1998). Exsolution is observed to produce small or/and very thin and elongate grains in the HOD samples, possibly also in the SD range.

Domain state information is obtained from ***hysteresis measurements***, the alternating field demagnetization and from the Koenigsberger ratio. The hysteresis loops of the HOD samples (Appendix 6) are of pseudo-single domain (PSD) type and the positions of the data points in the Day plot are along the

theoretical single domain (SD)-multi-domain (MD) mixing curves (Figures 3-11 & 7-41). From this it is inferred that the HOD samples contain between 20 and 100 % SD grains (beyond the resolution of the microscope), which in combination with PSD and MD grains give a bulk PSD signature in the hysteresis loops. Dominantly SD-grains are indicated for 4 samples (nos. 33, 34, 76 and 108), in accordance with the suppressed Verwey-transitions in their κ-T curves (it can also point to maghemitization). No sample yields an ideal MD hysteresis curve, not even the ones where microscopy has revealed abundant coarse mt/tmt grains of >40 µm, which are expected to behave as multi-domain grains.

Similar with the hysteresis measurements, stepwise ***demagnetization in an alternating field (AFD)*** shows a broad spectrum of coercivities attributed to mixtures of different tmt domain states (MD, PSD, SD) in the HOD basalts from dominantly MD, over dominantly PSD or maghemized to dominantly SD states (compare chapter 7.4). Increased coercivities due to maghemitization are probable in some cases as well as rare contributions from highly coercive minerals, such as haematite or goethite.

Finally, the ***Koenigsberger ratio (Q;*** $Q = M_{rem} / (\kappa * H_{Earth})$, see chapter 3.1***)*** between 1 and 20 gives hints for SD tmt grains in 64 of the HOD samples. The possibility that these relatively high Q-values result from young volcanics (with high M_{rem} = NRM values, due to high MD fractions, where self-demagnetization of MD grains has not yet proceeded so far; Soffel, 1991) can be ruled out as there is no activity younger than about 80 Ma known in this area. Q-values below 1 in 5 samples point to MD tmt grains (Soffel, 1991).
Support for the presence of SD grains in the HOD samples also comes from the comparison of the AMS and AARM fabric ellipsoid orientation (see chapter 8.1).

Comparison of domain state results from AFD and hysteresis data

Hysteresis loops and AFD curves reveal strong differences of the coercivity spectrum for some samples. Both the AFD derived, coercivity-related MDF and the hysteresis-derived coercive force (H_C) values represent bulk values. Discrepancies show up when comparing the range of MDF with the H_C value: samples 16, 21, 33, 94, 100 are regarded as magnetically soft according to the MDF value (< 10; Appendix 9), but have high M_R/M_S ratios and plot near, or even within (no. 33) the SD field in the Day Plot (Figure 7-41). Figure 9-63 illustrates this mismatch and demonstrates that in most cases H_C is higher than MDF. However, in a few samples the opposite is true.

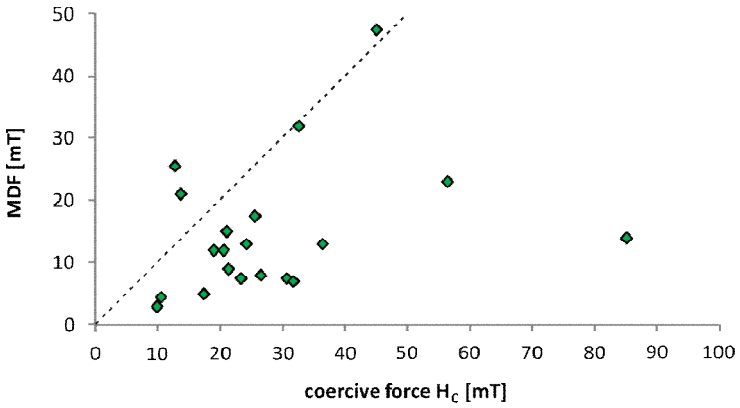

Figure 9-63. Comparison of MDF values from AF demagnetization with coercive force (left) and ratio of saturation remanence to saturation magnetization (right) from hysteresis measurements.

It is concluded that at least some of the samples are heterogeneous in their magnetic properties. Heterogeneities depending on the distance to the country rock are probable. It is noted that the sample material for the hysteresis measurement was not taken from the same cylindrical specimen, where AFD

was measured. Similar heterogeneities within one sample are revealed by bulk susceptibility, AFD curves and hysteresis measurements. Alternatively, discrepancies may be explained by the lapse of time between the sample preparation for hysteresis and its actual measurement, because a few hysteresis samples (ground sample powder) were measured one year after its preparation, possibly allowing oxidation of tmt. When samples are magnetically harder in the hysteresis than during AFD, discrepancies may be explained by mechanical stresses, which may have been induced in tmt by crushing and grinding for hysteresis sample preparation. This may increase the coercivity (H_C) values by induced stress anisotropy.

AFD-derived domain size information sometimes also appears to disagrees with microscopic observations, e.g. MDF values indicate high SD tmt fractions but optical studies reveal coarse tmt grains (e.g. samples 19, 51, 80, 86). On the second glance, ilmenite-exsolution lamellae are found (except in one sample no. 80) to subdivide the tmt-grains into smaller subgrains, which may explain the discrepancies along with the insufficient microscopic resolution for small grains.
In a few samples, very thin-branched dendrites, invisible under the microscope, may be responsible for a SD or PSD signal during demagnetization, although among the named ones only sample 86 contains visible dendrites. Shaar and Feinberg (2013) describe a magnetite dendrite of a few tens of micrometers in size with a branch thickness in the submicrometer scale, which behaves like a PSD grain due to magnetic interaction between branches. Further, they found tmt-dendrites of a few micrometers in total size, built from interlinked octahedral crystallites of a few hundreds of nanometers in size to behave as SD or very small PSD grains, although clearly beyond the SD-MD threshold for simple geometrical crystals.

However, it is necessary to point out that the thin sections and the hysteresis sample material often have been taken from different parts of the block sample. Although the material may only have been separated by a few centimetres (at max. about 20 cm), it may be sufficient for grain size and/or mineral variations due to different magma cooling conditions (e.g. cooling rate, oxygen fugacity etc.) within the dyke.

Summary magnetic mineralogy

Titanomagnetite is the main carrier mineral of the anisotropy of magnetic susceptibility (AMS) and anhysteretic remanent magnetization (AARM) in most of the HOD rocks. Owing to the alignment of tmt along previously crystallized silicate phases and its clustering in their interstices, the origin of magnetic rock anisotropy is basically distributional in nature, most probably with magnetic interactions between close tmt grains. Occasionally, anisotropic tmt grains, such as elongate dendrites, dominate and may add a component of grain shape anisotropy to the AMS. Depending on the orientation of the dendrites, this may enhance the distribution anisotropy or reduce it. From microscopy, κ-T, hysteresis and AFD measurements it is concluded that the titanomagnetite/-maghemite grains within the majority of the HOD samples cover diverse grain sizes and domain states, ranging from single-domain (SD) over pseudo-single domain (PSD) to multi-domain (MD) in variable proportions.

9.2 Rock magnetic fabrics

The predominance of normal (type I) compared to anomalous (intermediate, inverse, oblique) anisotropy of magnetic susceptibility (AMS) fabrics (types II –IV/IVa) found in the Henties Bay-Outjo dyke swarm is roughly comparable with the results of similar studies worldwide (e.g. Park et al. 1988, Rochette et al. 1992, Raposo & Ernesto, 1995, Borradaile and Gauthier, 2001; Herrero-Bervera, 2001; Archanjo et al., 2002; Cañon-Tapia, 2004; Craddock et al. 2008 etc.), which showed that magnetic fabrics can be utilized to derive magma flow directions.
Normal magnetic fabrics, where the κ_{max} and κ_{int} axes are within the dyke plane, and no evidence for a secondary overprint are considered as primary in origin. The studies of Stacey (1960) and of Knight and Walker (1988) brought a consensus among AMS researchers that the orientation of primary mag-

netic fabrics of basalts originate from mineral alignment by magma flow. Conversely, most AMS researchers consider samples with fabrics deviating from the normal type (I), where at least one of the two axes κ_{max} or κ_{int} is not within the dyke plane, as not suitable to infer magma flow directions (i.e. Rochette 1992; Borradaile & Gauthier, 2001).
In the following, magnetic fabric types are discussed in terms of the magnetic and dyke properties, to evaluate the potential origins of the magnetic fabrics. The emphasis is on the anomalous fabric types because the normal type is acknowledged to likely reflect primary magma flow. Attempts are made to identify fabric overprints in order to discriminate secondary from primary, flow-derived fabrics.

Origin of anomalous AMS fabrics in the Henties Bay-Outjo dyke swarm

Anomalous AMS fabrics (types other than I) are frequently regarded as the product of other causes than laminar magma flow, causes which interfere and influence simple flow fabrics. Different approaches have been made to explain the origin of anomalous fabrics (for examples see references in chapter 4.1.1): secondary fabric overprints after magma emplacement (e.g. Borradaile & Gauthier, 2003; Raposo & Berquó, 2008), tectonic stresses during magma emplacement (e.g. Clemente et al. 2007; Féménias et al. 2004), grain/domain size (single-domain or SD-) effect of the magnetite/titanomagnetite (Potter & Stephenson, 1988; Rochette et al., 1992, 1999; Ferré, 2002), distribution anisotropies combined with magnetic interactions between close magnetic grains (Stephenson, 1994; Cañon-Tapia, 1996), influence of remanence (Rochette, 1992; Cañon-Tapia 1996; Schöbel et al. 2013) or vorticity/magma shear due to velocity gradients during flow between magma flowing near to the dyke wall and the centre (Passchier and Trouw, 2005). Alternatively, anomalous fabrics may be the result of the cyclic movement that particles perform during laminar magma flow (Jefferey, 1922; Dragoni et al. 1997; Cañon-Tapia 2004; see chapter 4.1.1). The nature of fabric-influencing processes acting after/during magma emplacement is diverse. Internal cooling stresses of the magma (Rochette, 1992), tectonic movements (Raposo & D'Agrella-Filho, 2000; Borradaile & Gauthier, 2001, Correa-Gomes et al., 2001; Féménias et al. 2004, Clemente et al. 2007) or solid-state deformation, may account for the generation of anomalous fabrics. In the case of fabric overprints, either the entire rock fabric has been modified, or at least parts of the mineral components have been affected, representing competing subfabrics superimposed on the original fabric.
Mineralogical causes for anomalous fabrics may be post-flow mineral alterations, e.g. (re-)crystallization of magnetic oxides or the presence of AMS-inverse minerals. Further, hydrothermalism may lead to the growth of euhedral magnetite aligned along the fluid migration path (Rochette 1991, 1992) or low- and high-temperature oxidation may reduce the grain size and divides the mt/tmt grains into subgrains along crystallographic lattices.

As described above, the nature of the anomalous AMS fabrics found in the HOD may have a number of causes, which will be examined and discussed one by one in the following subchapters.

9.2.1 Anomalous fabrics due to magnetic minerals other than tmt

One hypothesis relates anomalous AMS fabrics to low bulk susceptibilities (κ_m), which, may among other reasons may be due to magnetic phases with a strong crystal anisotropy, such as ilmenite, haematite and/or goethite. As argued in chapter 9.1 higher fractions of these low susceptibility phases relative to tmt are indicated by lower bulk susceptibilities ($< 5 \times 10^{-3}$ SI), if the samples do not contain glass. In order to discriminate this, in Appendix 19 the samples are sorted by colour according to their fabric type, but no clear relation between AMS fabric type and low κ_m is obvious: 45% of the fabrics are anomalous (types II to IV) among the low κ_m samples and 31% among the high κ_m ones (although the number of samples with anomalous fabric types may be insufficient for reliable statistics). If holocrystalline, low bulk susceptibility samples are commonly richer in ilmenite/ilmenohaematite at the expense of tmt, which makes a difference in the trend of the κ-T curve. But, when comparing κ-T curve types with the AMS fabric types (Figure 9-64), again there is no correlation. Consequently, no relation is found between anomalous AMS fabrics and contribution of magnetic minerals other than tmt to the bulk susceptibilities.

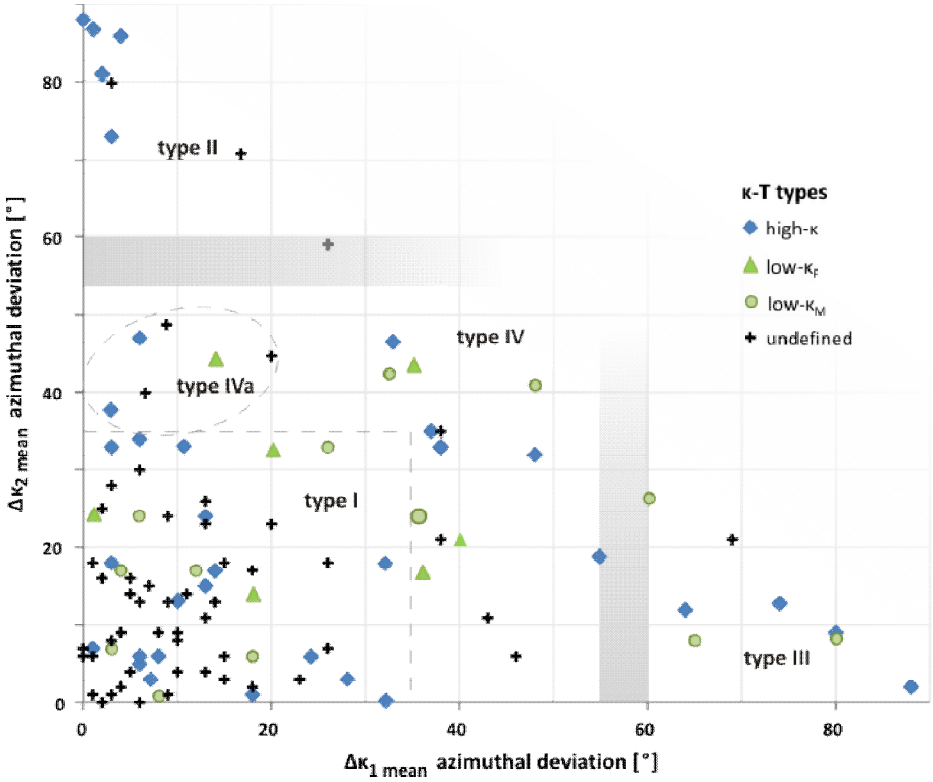

Figure 9-64. Relation between AMS fabric types I to IV and κ-T (temperature dependence of susceptibility curve) types. Angular deviation of the principal and intermediate AMS ellipsoid axes κ_{1mean} and κ_{2mean} from the dyke plane do not correlate with AMS fabric types.

9.2.2 Is there a single-domain effect?

The SD-effect refers to the inversion of easy and hard magnetic axes in a prolate titanomagnetite/-maghemite single-domain (SD) particle when the AMS is measured (see chapter 4.1.2). If a rock's magnetic susceptibility and its anisotropy (AMS) are mainly carried by oriented prolate SD tmt/tmgh particles, then the maximum principal susceptibility should be parallel with the short axes of the SD particles. In contrast to the induced magnetization, the inversion of magnetic axes does not affect the remanent magnetization, so that AARM gives true particle orientations (if no other influences interfere). Anomalous AMS fabrics were attributed to the single-domain effect by, e.g., Rochette et al. (1992), Ferré (2002) and Hastie et al. (2010). In accordance with Rochette et al. (1992), rocks with an inverse AMS fabric contain a higher volume percentage of SD mt/tmt and a fraction of 20% SD-particles is sufficient to generate an intermediate AMS fabric (Ferré, 2002). Oblique fabrics are not mentioned in these studies.
Domain size investigations (AFD, hysteresis loops, AARM, microscopic observations) in many HOD dykes described in chapter 9.1 indeed find evidence for the presence of single-domain grains along with pseudo-single and multi-domain titanomagnetite/-maghemite grains. Therefore, the SD-effect probably plays a role for the AMS fabric type. However, volumetric proportions of the SD, PSD and MD grains are uncertain or only rough estimates.

Influence of titanomagnetite composition, low T/high-T oxidation or degree of anisotropy?

During cooling and solidification of the primary magma, tmt/tmgh with an intermediate composition ($0 > x_{ulvospinel} > 1$) becomes unstable and unmixes into lamellae of Ti-rich and subvolumes of Ti-poor titanomagnetite, often intimately intergrown within one grain, forming trellis structures. These exsolution textures reduce the tmt grain size and may produce pseudo-single- and single-domain (PSD and SD) grains. Already 20 volume percent of SD tmt grains suffice to produce intermediate AMS fabrics (Ferré 2002), more SD grains can generate inverse fabrics. Further, the principal susceptibility axes

within the so-generated Ti-poor tmt subgrains may not be oriented analogous with the axes of the former solid solution crystal, also resulting in anomalous fabrics.

In order to test if the grain size reduction by unmixing/deuteric oxidation influences the AMS fabric type development the MDF values of the HOD samples with exsolution lamellae are examined. Higher SD fractions are expected to result in elevated coercivities and MDF values. Titanomagnetites in 18 of 34 investigated samples (see Appendix 3 for details) contain ilmenite lamellae. 8 of the lamella-bearing samples have been demagnetized in alternating fields and gave a mean MDF value of 22 mT. Of the 13 lamellae-free samples, 5 have been demagnetized and yielded a mean MDF of 18 mT - only minimally lower than the ones with lamellae. Statistically, these data are not sufficient to draw a robust conclusion, but the observed variable MDF values within both lamellae-rich and lamellae-poor sample groups (7 to 45 and 4.5 to 45 mT, respectively) suggests no distinct correlation between lamella-bearing samples and high coercivity. Consequently, this comparison provides no evidence for SD grain formation by grain subdivision. Hysteresis measurements also show heterogeneities within the lamellae-rich and -poor groups, although, among the 5 lamellae-free samples, only one shows a broader hysteresis loop pointing to an elevated SD portion. Both groups are inferred to contain some samples with MD- (low coercive) and others with SD-grain dominance (highly coercive).
A different way to test the effect of exsolution on magnetic properties is to check, whether samples with compositionally intermediate tmt have higher bulk coercivities, since tmt grain-subdivision occurs in Ti-bearing tmt. Samples with intermediate tmt composition (known from κ-T curves), have a wide range of MDF values from soft to hard magnetic (low to high coercivity) behaviour. Good examples are samples 19, 20 and 21, all from the same dyke, but at different distances from the margins. The samples have similar Curie temperatures and thus similar tmt/tmgh composition, but sample 21 has a very low MDF value (7.5 mT) indicating soft magnetization, while the other two have relatively high MDFs (32 and 47.5 mT) pointing to harder magnetization in the SD range. Similarly, samples, whose κ-T curves suggest the presence of nearly pure magnetite, free of titanium, show different AMS fabric types. It is concluded that the HOD data set shows no correlation between AMS fabric types and the Ti-content (T_C) of their carriers.

Finally, a correlation was found between the tmt composition and the degree of anisotropy (P'): samples with higher magnetic anisotropies (P'>1.1) show dominantly magnetite in their κ-T curves with little or no intermediate tmt/tmgh. This suggests that the decomposition of tmt due to magmatic cooling or deuteric oxidation reduces the degree of magnetic anisotropy.

AMS types versus hysteresis ratio and position in the Day Plot

At first, the hysteresis parameter ratios are compared with the HOD samples' $AMS_{INITIAL}$ fabric type. Since the ratios of remanent magnetization to saturation magnetization (M_R/M_S) and coercivity of remanence to coercivity (H_{CR}/H_C) are indicative of the volume percentage of single-domain (SD) tmt/tmgh (e.g. Day, 1977, Dunlop, 2002), the samples' position within the Day Plot should be related to their AMS fabric type, if the fabric types are domain-state specific. A harder magnetization attributed to small grain sizes of tmt/tmgh in the SD/PSD range (see also chapter 9.1) is expressed by higher M_R/M_S and low H_{CR}/H_C ratios. In keeping with the theory of Rochette et al. (1992), inverse AMS fabric samples with a higher SD tmt/tmgh content should plot in the upper part, in or near the SD field and normal type samples should plot in lower part of the diagram, with intermediate type samples in between.

The Day plot of Figure 9-65 contains the HOD samples marked according to their AMS fabric type. It can be seen that the distribution of the HOD samples is more dependent on the M_R/M_S ratio than on the coercivities. The samples are grouped according to their fabric type, but the groups overlap to some extent. Remarkably, the type I samples are split into a high and a low M_R/M_S ratio subgroup, holding the highest and lowest M_R/M_S ratios of the complete sample set. Intermediate or type II samples have comparable high ratios, sharing SD-field or close-to SD field positions with type I high M_R/M_S samples. Inverse (type III) samples hold intermediate M_R/M_S ranges compared with the range given by the sample set. For three of the SD field samples (33, 76, 108), an absolute SD-grain dominance is also confirmed by a suppressed Verwey-transition (T_V) in the κ-T curves.

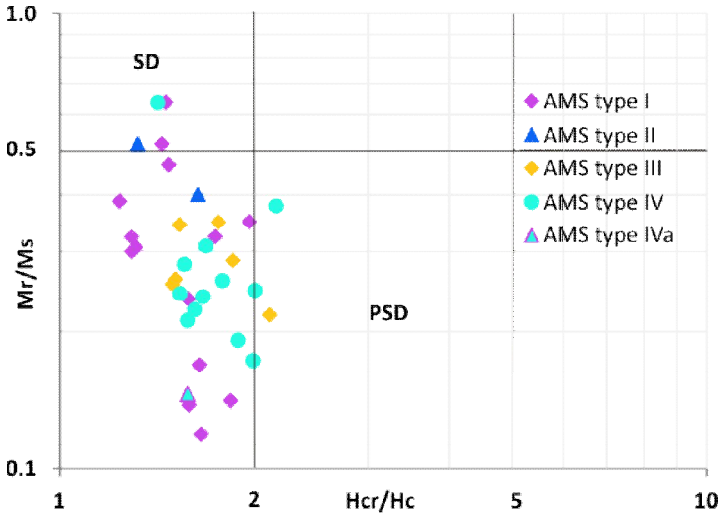

Figure 9-65. Upper left detail of the Day Plot with the paramagnetically corrected HOD samples sorted by AMS fabric type

Table 9-3. Means of remanent magnetization to saturation magnetization ratio (M_R/M_S) calculated for every AMS fabric type

AMS fabric type	M_R/M_S	number of specimens
II	0.46	2
I	0.315	14
III	0.285	6
IV	0.270	13

Summing up, for many HOD samples the hysteresis properties do not correspond with the AMS fabric types as expected from SD theory. More than half of the type I samples have unexpectedly high SD-range M_R/M_S ratios compared to the M_R/M_S ratios of the inverse and intermediate type samples. Therefore, it is assumed that these type I samples also contain high SD grain proportions, either with elongate SD-grains oriented perpendicular to the dyke plane or with isomorphic SD grains. The samples' reoriented AARM fabric further corroborates this idea. Oblique type (IV) samples with intermediate magnetization ratios support the idea that their transitional nature is due to a balance of grain size mixtures.

AMS types versus MDF values

The median destructive field inferred from the alternating field demagnetization gives a rough idea about a sample's coercivity spectrum. The histogram in Figure 9-66 discriminates the samples' MDF value against the AMS fabric types. It is obvious that the individual MDF values can not be correlated with the AMS fabric types. Higher, intermediate and lower MDF values occur in all samples, regardless of the fabric type. However, the mean MDF values of each fabric type reveal a clear difference

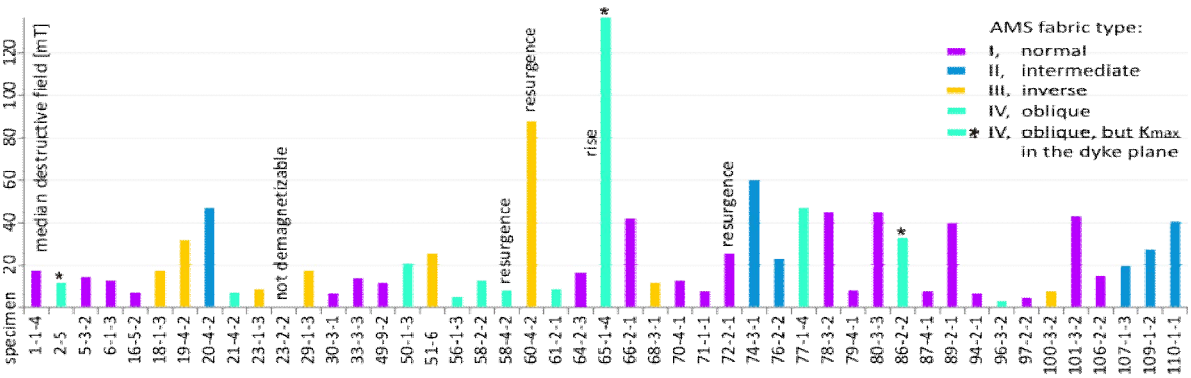

Figure 9-66. Comparison of the specimens' median destructive field (inferred from demagnetization behaviour in an alternating field) and their AMS fabric types.

Table 9-4. Median destructive field (MDF) values calculated for every AMS fabric type

AMS type	mean MDF [mT]	number of specimens
II	37	6
IVa	23	2
I	19	20
III	17	7
IV	15	7

between the group of intermediate type (II) samples with MDFs/coercivities approximately twice as high (37 mT) as the ones of all the other fabric types (see Table 9-4), except a subgroup of 5 type I samples, which also hold very high MDFs above 40 mT. This agrees with the comparison of the hysteresis ratio with the AMS fabric type (Table 9-3), where the intermediate type samples as well as a subgroup of type I samples showed the highest coercivities.

AMS_{AFD} versus AARM fabric orientation

As stated in chapter 9.1 in most of the examined HOD samples magnetite/titanomagnetite/-maghemite is the dominant magnetic phase and the main carrier of AMS and AARM. From this it was expected that the AMS_{AFD} and AARM fabric ellipsoids should be oriented similarly provided that paramagnetic or minerals with an inverse magnetic susceptibility, such as single-domain tmt or goethite, have negligible influence on the bulk magnetic properties. However, it can be seen from Appendix 17 that the AARM fabrics of 30 of 48 measured HOD samples differ (are reoriented) from their AMS_{AFD} fabrics. 13 samples are referred to as stable because they show only minor changes (between 20 and 40° in average). Potential reasons for reorientations are most likely to be sought in the magnetic mineralogy. Either the AMS of the reoriented samples is not dominated by multi-domain (MD) mt/tmt, but also by contributions of paramagnetic and/ or antiferromagnetic minerals, with inverse susceptibility or oblique (not dyke-parallel) shape preferred orientation; or there is a variable content of single-domain magnetite/titanomagnetite/-maghemite, which is responsible for the differences in magnetic fabric orientation.
An influence of paramagnetic minerals can be excluded for the majority of reoriented samples because only 3 of 29 reoriented samples have a low bulk susceptibility ($\kappa_m < 5 \times 10^{-3}$SI). Antiferromagnetic minerals, such as haematite and goethite are rarely abundant enough to exert an influence on the bulk magnetic fabric in the HOD samples, except of samples 23 and 58 (compare AFD or κ-T curves). Further, the remanence susceptibility is much smaller in antiferromagnetic than in ferrimagnetic minerals (Jackson, 1991). As argued in chapters 9.1 and 9.2 the presence of a certain content of SD-mt/tmt/tmgh is indicated for a number of samples. Matching with the idea of SD-influenced fabric changes, in all 29 reoriented samples 2 or all 3 of the AARM fabric ellipsoid axes exchange compared to their AMS_{AFD} fabrics. Therefore, the orientational discrepancies between the AMS and AARM fabric ellipsoids are mainly attributed to a variable SD-mt/tmt/tmgh fraction in many HOD samples. The SD-effect of elongate magnetite/titanomagnetite/-maghemite grains has an impact on the induced magnetization and its anisotropy (AMS), but not on the anisotropy of remanence. Therefore, the AARM should give true particle orientations.

In accordance with the SD-effect theory (Rochette, 1992; see chapter 4.1.2), 4 AMS-intermediate and 3 inverse samples yield normal (type I) AARM fabrics (chapter 8.1). Only 5 of these 7 samples have higher median destructive fields (MDF 17.5 - 43mT), ascribed to a higher SD tmt content, and one sample shows 25% residual magnetization (after treatment of 100 mT in AF) pointing to a grain fraction of harder magnetization (SD tmt or/and other phases). However, other samples change their fabrics and often also the fabric type, but do not become normal. In addition, and interestingly, the fabric in almost all of the 20 AMS-normal samples also reorients and changes type in the AARM (compare Appendix 17); nearly stable samples 66, 103 and 104 change their fabric but reorient minimally).

Thus, the phenomena that need to be explained are:

a) Why do AMS-normal fabric samples become anomalous in the AARM?

b) Why do AMS-anomalous samples not have normal AARM fabrics (as expected from SD theory)**?**

c) The origin of the anomalous stable AMS/AARM fabrics.

Question a) can be answered by the probable presence of a varying volume percentage of elongate SD-mt/tmt/tmgh grains in these samples, whose long axes are oriented oblique to the dyke plane. Their obliquity is attributed to their formation by unmixing, deuteric oxidation or hydrothermal alteration. These SD grains exert stronger influence on the AARM than on the AMS fabric, because, according to Jackson (1991), the remanence susceptibility of SD particles is much stronger than the remanence susceptibility of MD-particles. For pure magnetite the remanence susceptibility of particles < 0.5 µm is on average one order of magnitude higher than for particles > 100 µm. A similar trend is shown for tmt (Jackson, 1991 and references therein). For this reason, normal AMS fabrics may become anomalous in the AARM and the fabric type then depends on the SD-content. Further differences between the two magnetic anisotropies (induced and remanent) on the particle level arise from the fact that AMS is measured in an applied field, but remanence in the absence of a field (Jackson, 1991 and references therein). Jackson (1991) emphasizes that in the absence of a field, major magnetic domains in uniaxial/prolate grains are arranged parallel with the particle's long axis and the magnetization of small closure domains (see chapter 3.3) is parallel with the surface at the grain end, thus minimizing magnetostatic energy. SD particles are only able to aquire a remanence parallel with their long axis, while remanence susceptibility is zero perpendicular to the long particle axis. Because of this strong single-grain anisotropy effect, the degree of anisotropy is much stronger for ARM than for MS.
Hence, SD particles contribute to AARM to a much larger extent than to AMS. The SD volume percentage may be too small to substantially affect the AMS, resulting in mainly normal AMS fabrics, in contrast to the AARM. Jackson (1991) showed that the discrepancies between AMS and AARM fabrics in his samples reflect sensitivity differences between the two methods. He demonstrates that the AMS is much less sensitive than the AARM to gradational and progressive rock deformation and changes only after a larger degree of deformation is accumulated. Thus, weak shear or vorticity (rotation of a flowing liquid) in the HOD samples may be recorded by AARM, but not by AMS fabrics.
Consequently, it is assumed that in the HOD samples the primary magma flow-oriented magnetic fabrics are superposed by SD subfabrics from deuteric oxidation and/or alteration subfabric. The superposition mostly only affects the AARM fabric, but is too weak to be recorded by AMS because of a sensitivity contrast between both methods.

In principle, **question b)** may be discussed with the same arguments as question a): In the sense of Jackson (1991) small amounts of elongate (dyke-non-parallel) SD tmt/mt grains may contribute more to AARM than to AMS in relation to MD grains and may be responsible for anomalous AMS fabrics that change, but do not become normal in the AARM.

It was tested whether artefacts from the AARM measurement may also be relevant to problems a) and b). A few individual samples could not be demagnetized and/or remagnetized properly due to their high coercivity. Nevertheless, they have been measured in Mode B, which resulted in a residual vector larger than about 10 % of the vector length difference between κ_{max} and κ_{min}. Such a residual vector may influence the orientation of the ARM anisotropy tensor (Jackson 1991, see chapter 4.2), and even more so, if the residual vector is formed by minerals which were not aligned or oriented by magma flow, but are oblique due to their formation from deuteric oxidation or hydrothermal alteration. However, since this applies to only 7 samples at most (of the instable ones with defined AARM fabric type), it is not a valid solution to problems a) and/or b) for the bulk of the samples.

Another measurement artefact may account for problem b): The remagnetizing field (between 20 and 50 mT) applied for the AARM measurements was too low in half of the samples to affect all SD

grains. Magnetite/tmt/tmgh grains with coercivities above the applied fields were not affected. The AFD curves demonstrate that the residual magnetization at 30 or 50 mT is still high in many samples, pointing to a certain volume percentage of minerals with higher coercivities: 27 samples show a residual magnetization (M_{resid}) higher than 20% (average 45%) of the initial value at applied fields of 30 or 50 mT, and also 8 samples exceed 50% (max. 85%). Followingly, only MD, PSD and lower-coercive SD particles would be remagnetized and contribute to the AARM ellipsoid, but not particles with coercivities higher than the remagnetizing field (20, 30, 40 or 50 mT). SD grains with a higher coercivity (but < 100 mT) would remain in their random magnetization state. Thus, the AARM ellipsoid is a record of an incomplete set of particles in many samples compared with the complete set measured for AMS. Additionally, particles with higher coercivities than the initial demagnetizing field (100 or 200 mT) would contribute to the AARM introducing a residual vector. However, these higher coercive particles influence the AARM only, if their orientation deviates from the lower coercive ones.

Finally, some comments to address **point c):**
Among the ***13 relatively stable samples*** **(**reorientation max. 45°) 4 samples have type IV/oblique AMS fabrics and 2 of these 4 reveal a low bulk susceptibility below $5*10^{-3}$ SI, pointing to a potential contribution of other minerals to the AMS than only tmt. AFD curves corroborate this in these two cases revealing higher coercive phases in these samples. The mean median destructive field (MDF) value should indicate the presence of a higher content of harder magnetic single-domain particles and samples with higher MDFs were expected to be the instable, reoriented ones. However, the MDF value is similar for stable (23.5 mT) and for instable samples (20 mT) and is therefore no indicator for one or the other.

Further, it was checked, if the residual vector or highly coercive minerals act as a "fabric stabilizer". The term "highly coercive minerals" comprises all ferromagnetic (s.l.) minerals with coercivities (H_C) > 100 mT, including very hard magnetic SD tmt grains. - Theoretically, higher contents of highly coercive (> 100 mT) minerals may stabilize the fabric, since they are not affected by demagnetizing fields of 100 mT or below. But, this idea may apply to only 2 of the 13 stable samples (no. 58, 60), which remain with a residual remanent magnetization of more than 20 % (around 60%) of the initial NRM after AFD of 100 mT.

In summary, the reorientation of AARM fabric compared to the AMS fabric is ascribed to a variable SD-mt/tmt content, but consistent correlations with rock or sample parameters are not found for all samples with reoriented AARM fabrics. Some of the normal fabric samples are more single-domain (SD)-indicative than the inverse samples. MFD values and hysteresis data ascribe the highest SD contents to intermediate and some normal AMS fabric type samples and not, as expected, to the ones of inverse type. The relative fabric stability of the 13 samples suggests little or no SD-effect and rather a dominance of multi-domain or larger pseudo-single-domain grains with an anomalous orientation in 8 and normal orientation in5 cases. However, as an alternative fabric stabilizer, magnetic interactions between close grains can not be excluded.

Reliability of AARM results for the deduction of magma flow orientation

The comparison of AMS and AARM fabrics reveals some single-domain tmt/tmgh content in most HOD samples. Instead of just cancelling out the SD-effect from anomalous AMS fabrics and making them normal/type I AARM fabric, there are even more anomalous AARM fabrics. Also, samples with normal AMS fabrics have anomalous AARM ones. The main reason for this is probably the importance of SD tmt/tmgh grains for AARM fabrics. If there are abundant secondary, non- flow-oriented SD grains compared to the volumetrically dominant (because larger) MD grains, a strong component of anomalously orientated grains may effect the bulk AARM. Because of this unproportional weighting of the secondary, weak subfabric in competition with the flow-oriented primary rock fabric, anomalous ellipsoid orientation results, which does not relate to magma flow.
Support for this theory comes at least from sample 70 with dyke-wall lineation, which is interpreted to record the first pulses and orientation of magma flow into the opening dyke fissures. The magnetic fabrics and dyke wall lineation roughly agree in the case of samples 103 and 104, but not for sample 70. Here, the AMS long axis (κ_{max}) coincides with the lineation orientation, but not the AARM long axis (see Appendix 17), which may be due to the unproportional effect of a non-oriented SD sub-

fabric as described. The macroscopic flow markers (lineation) are more reliable. This example illustrates the problem of using AARM for the deduction of magma flow orientation for HOD samples.

Summary single-domain-effect

It is already stated in the previous chapter 9.1 that alternating field demagnetization (AFD), hysteresis and anisotropy of anhysteretic remanent magnetization measurements indicate the presence of elongate or non-equant single-domain (SD) titanomagnetite in many HOD samples in variable proportions between 20 and 100 % of the total tmt content. However, the SD indications are not confined to the anomalous AMS fabric type samples, as expected.
No consistent correlation between the AMS_{INI} fabric types and tmt composition or coercivities (MDF or hysteresis ratios) has been found. MFD values and hysteresis data ascribe the highest SD contents to intermediate and some normal AMS fabric type samples and not, as expected, to the ones of inverse type.

A significant SD-mt/tmt content for about 73% of the samples is inferred from the difference in orientation between AARM and AMS_{AFD} fabrics. However, the high fraction of 66% normal AMS_{INI} type samples with primary magmatic fabrics suggests that its volumetric content is too low to influence the AMS fabric (type). The AMS fabrics of only 7 samples of intermediate and inverse types (II and III) appear to be exclusively due to the classical SD-effect because their fabrics become normal (type I) during AARM measurement. The other anomalous AMS fabric samples appear to have other or additional influences, as well as weakly differing/reorienting or stable samples with anomalous AMS fabrics, as discussed in the following subchapters.

9.2.3 Influence of Natural Remanent Magnetization on AMS - NRM, Q and AMS_{AFD}

Motivated by difficulties to explain anomalous AMS and AARM fabrics and by the works of Park et al (1988), Rochette et al. (1992) and Schoebel et al. (2013; 2014) the influence of the NRM vector on the AMS orientation was investigated. The named authors found the AMS axes to reorient after alternating field demagnetization (AFD) and explained this with the influence of the NRM vector.
Cañon-Tapia (1996) studied magnetic interactions between close magnetic particles in varying arrays in an externally applied magnetic field and examined the resulting AMS directions. He argued that when the ratio of induced to remanent magnetization in the particles is near or less than one, the enhancing field experienced by the particles will be due to the remanent magnetization of their nearest neighbours and not to the externally applied field, as is the case when the ratio of induced to remanent magnetization is much larger than one. Since the magnetization of most of the HOD samples is dominated by the remanence ($Q > 1$; Soffel, 1991), except in 7 samples ($Q < 1$), and anomalously high NRM and Q values in 20 samples have been obtained, an influence of the NRM on the AMS directions was considered probable in the HOD study.
In the studied sample set, the NRM of about one third of the samples is relatively or anomalously high. About two thirds (67 out of 103) of the samples show an NRM below 10 A/m, which is within the range found in natural basalts of other studies (Oliva-Urcia et al., 2011; Schoebel et al., 2013 and references therein). Since the HOD dykes are assumed to have Cretaceous ages, their NRM is expected to be lower than 10 A/m, because of the relaxation-related decrease of NRM with time. 16 samples have NRM values between 10 and 20 A/m, which exceeds commonly found values, but is occasionally ascribed to inhomogeneous magnetization (Oliva-Urcia et al., 2011). However, 20 samples exceed these values by far, which can not be explained by regular acquisition of remanence during magma cooling in the Earth's magnetic field. Since many of those samples were taken from topographically exposed sites, it is possible or even likely that they have been struck by lightning since lightning strikes can impart a strong isothermal remanent magnetization (Soffel, 1991; Dunlop and Özdemir, 1997). Koenigsberger ratios (Q) of 50 or higher in the named samples and in some others (with a lower NRM value) support this suspicion (Soffel, 1991). It was hypothesized that the domain structure of multi-

domain mt/tmt can be changed in this way, contributing to a deflection of the principal AMS directions in lightning-affected samples.

Anisotropy of Magnetic Susceptibility after Alternating Field Demagnetization (AMS_{AFD})

In order to check the hypothesis of an NRM-vector influence on AMS fabrics, the $AMS_{(AFD)}$ has been measured again after specimen's remanence has been minimized by partial demagnetization in peak alternating fields of 100 mT (magnetic cleaning) and then compared to the $AMS_{INITIAL}$ fabric. Indeed, after AFD the parameters of the magnetic susceptibility (bulk susceptibility, degree of anisotropy, shape factor) differ and for 27 of 48 samples also the orientation of principle axes differs. Slight to substantial reorientations occur somewhat more frequently in AMS-normal samples (16 of 26 samples; compare chapter 8.2, Appendix 17) than in the anomalous types (10 of 22). Similar correlations were found in Schoebel et al. (2013) and Schoebel and De Wall (2014), who discriminate reorienting normal and inverse from stable inverse fabrics in the Deccan basalts. The reorientation clearly proves an influence of the NRM-vector on the AMS directions in these samples. As Schoebel et al. (2013) reason, demagnetization in an alternating field leads to a partial rearrangement of the magnetic domains and their orientation in multi-domain magnetite and titanomagnetite grains with coercivities below 100 mT.
AMS reorientations after AFD have already been reported much earlier by Park et al. (1988) and Rochette et al. (1992). Remarkably, in the HOD sample set there is a kind of systematic in the reorientations: although reorienting, the fabric types (I to IV/IVa) mostly remain the same. Systematic changes of the principal AMS axes are also described by Park et al. (1988), who observed the AMS axes to move along great circles during stepwise alternating field demagnetization (AFD). In contrast, Rochette et al. (1992) report a scatter in AMS axes, which is removed by AFD.

No properties have been found which allow the discrimination of AMS_{AFD}-stable from reoriented fabric in the HOD sample set. A lightning-produced strong IRM can not be excluded as AMS-influence, but there is no proof that lightning-struck rocks (high NRM and/or Q) are less appropriate for AMS studies or should be demagnetized before.
SD-indicated samples (judging from MDF values and position in Day Plot) are among both the stable and reoriented ones with similar frequency. Thus, in contrast with Schoebel et al. (2013), no clear correlation of stable AMS-inverse samples and a high SD content has been found.

Causes for AMS reorientation after AFD

Schoebel and De Wall (2013) showed that the AMS tensor is deflected into the NRM vector direction and demonstrated a decoupling of the induced from the remanent magnetization direction after tumbling alternating field demagnetization in MD and PSD grains. They argue in the sense of Stacey and Banerjee (1974) that the intrinsic susceptibility is much higher parallel with the domain walls than perpendicular to them. Consequently, the direction of the lowest self-demagnetization is deflected from the grain's long axis to the NRM vector direction as well. After AFD cleaning, the orientation of the magnetic domains will better reflect the grain or crystallographic anisotropy in MD/PSD particles (Schoebel and De Wall, 2013). Depending on the volume percentage of MD and PSD magnetite/titanomagnetite grains in the sample and on the strength and direction of the initial remanence vector, the AMS_{AFD} will reorient compared to the $AMS_{INITIAL}$. SD particles, however, unaffected by AFD, are considered to keep their TRM, further exerting influence on close neighbouring magnetite/titanomagnetite grains and on the bulk NRM and AMS of the sample. According to Schoebel and De Wall (2013) this may explain the stability of the SD-dominated stable inverse AMS fabrics. Coercivity values in the literature vary from 20 mT (Dunlop & Özdemir, 1997) for (cubic) crystallographic up to 150 mT (Soffel, 1991; Butler, 1998) for shape anisotropic SD-magnetite grains. As referred to in chapter 9.1, particles with larger grain sizes may also to consist of only one single domain.
Consequently, AMS stable fabric samples should reveal a harder magnetization than the reorienting ones, but this is not consistently true for the bulk of the samples. For example, the remanent magnetization at AF fields of 100 mT is between 0 and 20 % of the initial remanence magnitude in 35 of 45 samples and only 4 samples yielded residual magnetizations of 25 % or more (see Appendix 10) irre-

spective of their orientational AMS stability. Although large heterogeneities are encountered within 4 samples and may occur more often, data show that the remanent magnetization, and most probably also the induced, is rarely carried by a higher volume percentage of highly-coercive grains. Hence, the SD grains as the main or only fabric stabilisating influence can not be confirmed.

Still one question remains to be addressed: Why does the AMS fabric type often remain the same despite a reorientation of mostly 2 (or all 3) of the AMS axes? The answer has most likely to be sought in the preferred orientation of small elongate tmt grains or grain clusters/arrays. A remanence vector in elongate PSD or lower coercive SD grains has only two possible antiparallel orientations. Changing this by AFD into the reverse, antiparallel sense would not change the axis of remanence and the magnetization would remain within the previous plane. This may also be a way to explain the movement of AMS axes along great circles during successive AFD by Park et al. (1988).

In summary, NRM has an influence on AMS ellipsoid orientation and AF demagnetization eliminates this influence as far as possible, but repeated AMS measurements on AF demagnetized samples yield the same types of AMS fabric for almost every sample as before demagnetization ($AMS_{INITIAL}$). From this it is concluded that NRM influence does not explain the origin of the anomalous AMS fabrics in the HOD dyke swarm.

9.2.4 Anomalous grain orientation

As a fourth possibility besides the influence of magnetic minerals other than tmt, SD-grains or the NRM vector, anomalous AMS fabrics can arise from an anomalous, non dyke-parallel mineral orientation, which is either primary and due to magma flow, or secondary due to processes accompanying or post-dating magma emplacement. An anomalous grain orientation is suggested to be responsible for anomalous fabrics of some HOD samples (e.g. samples 18-21, 58 and 59).
In thin sections, samples 58 and 59 reveal an oblique orientation of elongate vesicles within the chilled dyke margins, which coincide in orientation roughly with the oblique AMS and AARM plane of magnetic foliation. A preferred orientation of anomalously oriented plagioclase phenocrysts, highly oblique or perpendicular to the dyke margin, is observed in HOD samples 19; 86, 87 and 93, but has not been quantified. Their fabrics are intersertal to intergranular. Among these samples, no. 19 is one with a type III magnetic fabric, in agreement with the plagioclase orientation, where no SD-influence is indicated by the AARM (AMS = AARM fabric orientation). Therefore, it is very probable, that the anomalous mineral orientation is responsible for its anomalous magnetic fabric. Since the AMS in all 4 samples of this dyke (nos. 18-21) shows a similar anomalous orientation of the long ellipsoid axis almost perpendicular to the dyke wall and AARM coincides (Figure 9-67 a), an anomalous particle orientation is inferred for all samples of this dyke.

At first glance, this appears to contradict the results of petrography and image analysis, which demonstrate dyke-parallel phenocryst orientation for sample 21. However, the thin sections represent the fabric at the dyke margin, while AMS (and AARM) specimens were taken from 2-10 cm towards the dyke centre, where the fabric may be different due to magma-internal shear. Such a fabric distribution is shown schematically in Figure 9-67 b and has been modelled by Correa-Gomes et al. (2001; Figure 4-15) for a setting, where ***tectonic shear*** occurs at the dyke walls synchronously with magma intrusion. Since tectonic shear at the dyke walls synchronously with magma intrusion is considered an important mechanism for the development of many asymmetric fabrics in the HOD swarm, this is discussed in the following subchapter (“Tectonic shear at the dyke walls during magma emplacement”) in more detail.

Alternatively, Cañón-Tapia and Chávez-Àlvarez (2004) explain all primary particle orientations, “normal and anomalous”, by the cyclic movement of ellipsoidal particles in magma flow without the influence of tectonic shear. This idea is based upon Jeffery`s model of rigid particle rotation (1922) and requires low crystal contents to enable free particle rotation in the magma. A free phenocryst rotation is likely in a narrow zone of a few centimeters at the contact with the country rock in the HOD dykes (sample 21, where plagioclase laths are well aligned and do not touch in a vitrophyric fabric;

compare chapter 7.7). In sample 19, 0.5 m more to the dyke centre plagioclase laths are touching in an intersertal fabric (ophitic fabrics in other dykes). Dragoni et al. (1997) found that the distribution of the principal susceptibility axes varies systematically as a function of the changing flow regime depending on time, shear within the magma, initial particle orientation and the particle shape ratio. It is even demonstrated by Cañon-Tapia & Pinkerton; (2000) that samples with switched susceptibility axes can coexist within only a few centimetres, a phenomenon observed in some HOD samples as well (e.g. AMS_{AFD} of samples 16, 58, 59, 77).

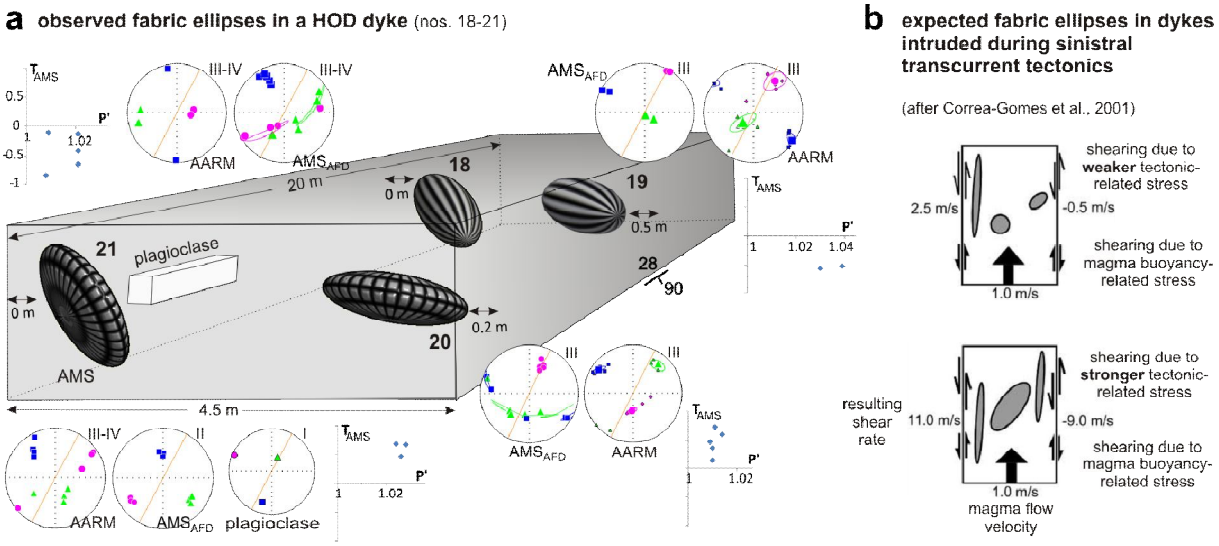

Figure 9-67. Asymmetric distribution of magnetic lineation (κ_{max}). a) at the dyke margins of dyke 18-21, Gr. Spitzkoppe region compared with the b) theoretical asymmetric fabric distribution resulting from sinistral strike-slip dyke-wall movements during magma intrusion, modelled by Correa-Gomez, 2001. Rod- and pancake-shaped ellipsoids symbolize prolate and oblate AMS fabrics. Note the rough correspondence of NW – SE oriented long magnetic axes orientation (blue squares in stereonets) of AMS and AARM of all samples. Note the varying sample distance of 0 to 0.5 m to dyke margin. Magnetic fabrics are inverse/type III or are oblique/intermediate, but tending to inverse type III. Plagioclase orientation of sample 21 in contact with the country rock is almost dyke-parallel, contrasting with the magnetic fabrics 2-10 cm away from the dyke margin.

Secondary or post-flow processes may also lead to an anomalous silicate grain orientation, such as vertical/lateral compaction in a stagnant, but still liquid magma column (Park et al., 1988; Raposo & Ernesto, 1995), gravitational mineral settling (Rochette et al., 1999), tectonics (Raposo & D'Agrella-Filho, 2000; Borradaile & Gauthier, 2001), cooling stresses, convection or hydrothermal alteration (Rochette et al., 1991). The formation of intermediate magnetic fabrics, for example, has been discussed by Hrouda (2002) to be due to vertical compaction by magma from consecutive pulses, which compresses solidifying material above. Evidence for ***consecutive magma pulses*** was found in two dykes (samples 28; 39-42), where internal chilled margins prove that magma was already solidified when a subsequent magma pulse arrived and opened the dyke along strike. However, when magma arrives before completed solidification of the prior injection, the new pulse may have rather a shearing, laterally/vertically compacting or rotating effect on the previously emplaced material. Alternatively, vertical compaction in the magma column may arise at the top end of a dyke, whose propagation up to the surface is impeded by some cap rock.

Gravitational mineral settling, or reorientation due to convection in the magma column (Rochette et al., 1999) should rather produce chaotic or random fabrics, and not alignment. Therefore, these processes are not considered to be relevant here.

Tectonic shear may produce oblique fabrics, as shown by Borradaile & Gauthier (2001). But no major tectonic event is reported from NW Namibia after dyke emplacement in early Cretaceous times. Accordingly, field examination of the HOD dykes revealed no evidence for a solid state deformation or

thermal metamorphism. Macroscopic joints and fractures are clearly related to cooling, since fracture frequency declines towards the centre in thicker dykes. Further, there are no distinct microscopic features of this kind (strongly deformed minerals or schistosity). Only very locally, bent or broken pyroxene and plagioclase crystals are observed or their undulatory extinction. These features may either point to cooling stresses within the dykes during solidification or pressures of consecutive magma pulses on already emplaced and cooling magma.

Alternatively, a primary anomalous grain orientation perpendicular to the dyke plane may result if crystallization occurs after magma flow has ceased. Then grain growth will progress from the dyke walls to the dyke centre perpendicular to the isotherms (Rochette et al. 1999), forming a ***cooling fabric***. For the HOD, cooling may have been preserved in some samples, but one would expect a symmetric cross-dyke orientation of κ_{max} at opposed dyke walls in this case rather than an asymmetric one as observed in the dykes 58-59 and 18-21.

Rochette et al. (1991) reported that anomalous fabrics are more frequently found in the ***thicker dykes*** in their study of the sheeted dyke complex of the Oman ophiolite. They speculated that this could be related to less regular magma flow in the thicker dykes and/or with an overprint by secondary processes. The comparison of HOD fabric types and dyke thickness in Appendix 19 shows that all types of fabrics occur in both thicker and thinner dykes but in fact, there is a tendency to more anomalous fabrics within the thicker dykes: among the >1.5 m thick dykes 23 of 53 samples have anomalous AMS fabric, while among the thinner dykes only 7 of 38 are anomalous. Staudigel et al. (1992) summarized that only samples from within 10 cm from the dyke margin have fabrics related to magma emplacement. Towards the dyke centre other processes may be dominant. Except to the dyke centres this may also apply to some HOD samples, which were taken from larger distances to the dyke margin (tabulated in Appendix 11; "sample position within dyke").

Rock alterations may produce fine-grained (SD + PSD) magnetite, which post-dates flow-related rock fabric acquisition, e.g. during hydrothermal alteration, when olivine breaks down (Vahle et al., 2007; e.g. samples 2, 9, 13-15, 62-64, 70, 71, 19, 94) or when tmt/tmgh is decomposing/subdividing during magma cooling (exsolution lamellae in 18 samples; see Appendix 3). All three types of alteration are observed in the HOD samples (chapters 7.1 & 7.2.1). Hydrothermal alteration is indicated by leucoxene (replacing tmt/ilm), iddingsite, opacite (both replacing olivine), chlorite, sericite, titanite and other secondary minerals. At least 14 of 34 intensively examined samples are hydrothermally altered. However, in the sample set, the AMS fabric types do not correlate with the degree of mineral alteration. All kinds of fabric types are shown by altered samples. Cooling-derived microfractures in the HOD are mostly not mineralized with iron oxides, as observed in other studies (Rochette et al., 1999; Hrouda, 2002) and can be neglected here. However, secondary SD and PSD tmt are suspected (chapter 9.2.2) to be responsible for the bulk of anomalous AARM fabric types of samples with normal AMS fabrics.

Finally, bulk fabrics may be composed of several non-coaxial ***competing subfabrics*** (e.g. Fernandez et al., 1983; Ildefonse et al. 1992; Nicolas, 1992; Ježek et al., 1996), for example a primary flow-oriented fabric may be overprinted by a secondary, non-flow controlled generation of magnetic minerals. This may apply to a few samples (86, 87, 93 and 95 for instance), where oblique silicate fabric orientation is observed, but bulk κ_{max} is dyke-parallel

In summary, non-dyke-parallel, anomalous grain orientation is suggested to be responsible for the anomalous AMS fabric of at least two HOD dykes (nos. 18-21 and 58/59), and probably also for the remaining anomalous type samples, unless evidenced otherwise. The origin of the anomalous grain orientation in the named two dykes is probably tectonic shear at the dyke walls during magma intrusion, as discussed in this and the following subchapter. For some of the remaining samples the anomalous mineral orientation may, alternatively, be primary in nature as a result of rotating particles in flowing magma.

Tectonic shear at the dyke walls during magma emplacement

Previous chapters discussed fabric types of individual specimens and failed to provide a consistent explanation for anomalous AMS fabrics. Here, the fabrics are considered from the dykes as a whole, es-

pecially comparing within-dyke profiles following the concepts of Knight and Walker (1988), Correa-Gomes et al. (2001; see chapter 4.1.1, Figure 4-15), Aubourg et al. (2002), Clemente et al. (2007), Féménias et al. (2004) and Poland et al. (2004). According to those studies, there are dykes with mirror-symmetric fabric orientations and others with asymmetrical distribution of the magnetic lineation or foliation. The referred symmetry plane is parallel with the dyke walls and located in the dyke centre. According to Correa-Gomes et al. (2001) asymmetrical configurations indicate tectonic shear located at the dyke walls during magma emplacement. According to their modeling, the fabric symmetry depends on the rate, orientation and sense of shear compared to the rate and direction of magma flow.

For the HOD despite the obvious predominance of oblate AMS fabrics, the orientation of the long and intermediate fabric axes is well defined in clusters whereas girdle arrangements are rare. Therefore, imbrication angles of the magnetic lineation at both dyke walls were compared for symmetry (and not the magnetic foliation), regardless of the fabric type. In a strict sense, only dykes which were sampled at the very margins on both sides are appropriate for this classification, because only fabrics within 10 cm or at maximum 20 cm from the dyke walls are exclusively emplacement-related (e.g. Knight and Walker, 1988; Staudigel et al. 1992). With more distance from the walls other influences become important, simple shear in the magma turns to pure shear (Féménias et al. 2004) and transcurrent wall displacement effects lose influence towards the dyke centre.
In ***23 HOD dykes sampled at both contacts with the country rock*** (see Appendix 11; "position within dyke"), a few show no imbrication of the magnetic lineation and only ***3 dykes*** reveal ***symmetrically*** imbricated magnetic lineations, as reported in chapter 7.5. The ***remaining*** have ***asymmetrical*** configurations of κ_{max} (see chapters 7.5 & 9.2.4), not caused by the SD-effect. A prominent example with homogeneous inverse-type orientation of the magnetic lineation in all 4 samples from both dyke margins is discussed in detail in the previous chapter (dykes 18-21, Figure 9-67). An asymmetric fabric is also encountered in dykes 35-36, 49-51 or 103-104 from the Gross Spitzkoppe, Omdel dam, Kalkfeld and Mt. Klein Etjo areas (see Figure 10 for sample locations). Thus, asymmetric fabrics are present in wide parts of the HOD swarm, both in areas near the coast as well as farther inland. According to Aubourg et al. (2002), Clemente et al. (2007), Féménias et al. (2004) and Poland et al. (2004) this fabric asymmetry is due to syn-emplacement tectonic shear movements of the dyke walls, which adds to the magma flow rate and potentially modifies the final imbrication angle of floating particles/crystals,especially at or near the dyke walls. The interpretation is in agreement with HOD dyke geometries and tectonic shearing in Cretaceous times along crustal-scale lineaments, which is described by various authors (see chapters 2.2 & 10 for details and references).

Summary rock magnetic fabrics

Most of the HOD samples (66%) have normal (type I) AMS fabrics with the long and intermediate fabric axis (κ_{max} and κ_{int}) parallel with the dyke plane. Their fabrics are interpreted as primary, magma flow-generated and to originate from distribution anisotropy of the late crystallizing titanomagnetite. In agreement with the literature, these fabrics are regarded appropriate to infer the magma flow direction from the long axis (κ_{max}) orientation of the AMS ellipsoid. In order to derive flow directions also from the anomalous fabric samples, at first the origin of the anomalous fabric orientation has to be understood. For 7 of the 38 (34%) anomalous AMS fabric type (II-IV) samples, a classical influence of single–domain titanomagnetite on the magnetic fabric is evidenced, which is responsible for their intermediate/inverse (II/III) AMS fabric type. Therefore, magma flow directions can be inferred from the AARM fabric orientation for these 7 samples, because the SD-effect plays no role. For the remaining samples, a non-dyke-parallel mineral orientation is suggested to generate the anomalous fabrics. No other influences, neither tmt alteration, nor the natural remanent magnetization (NRM) vector nor contributions of other magnetic minerals can be verified to provoke the anomalous fabrics here.
For 6 of these samples (2 dykes) the anomalous grain orientation is inferred from a homogeneous anomalous fabric orientation within the dyke and from stable/not reorienting AARM fabrics compared with the AMS ones. Interestingly, these dykes reveal an asymmetry of the κ_{max} imbrications at the dyke walls with a symmetry plane parallel with the dyke plane, in the centre of the dyke. An asymmetry of κ_{max} or the magnetic foliation plane in profiles across the dyke thickness is observed in 16 of the 41 HOD dykes (which were sampled directly at the dyke margins) and is interpreted to indicate tectonic shear at the dyke walls during magma intrusion. Tectonic shear may modify the originally symmetrical imbricated flow fabric, which is modeled by magma-internal shear as a consequence of

the velocity gradient between dyke wall and centre within the dyke. Cretaceous crustal scale tectonic shear is reported from diverse geological field work.

10 Interpretation

10.1 Magma flow directions and paleostress field

As reasoned in chapter 9.2, the long principal susceptibility (κ_{max}) axes of 73 samples with type I $AMS_{INITIAL}$ fabrics (66%) are interpreted in terms of magma flow orientations. For comparison: Raposo and Ernesto (1995) report fabric type I in 51 % of the Ponta Grossa dykes at the conjugate passive margin in Brazil. Among these 73 HOD samples only 51 from the dyke margins are considered, since only these may record the initial opening of the dyke fissures and early intruding magma. Additionally, magma flow orientations are interpreted from the maximum principal magnetization (M_{max}) of type I AARM fabrics of another 4 samples (again only from near the dyke margins) with anomalous $AMS_{INITIAL}$ fabrics. In total, this makes up 55% of the samples.
On the satellite image in Figure 10-68, magma flow orientations of the 51 AMS and 4 AARM type I samples are depicted as projections into the lower hemisphere stereonets as circles for steep magma flow (dip angles between 60 and 90°) and with bars giving the strike of the dykes for shallow (0 to 30°) and inclined flow (31-59°). Since the dip angle of κ_{max} is at maximum in the 3 non-vertical, inclined dykes (dykes 7-8, 68-70 and 103-104), it is classified as steep although their dip angle is < 60°.

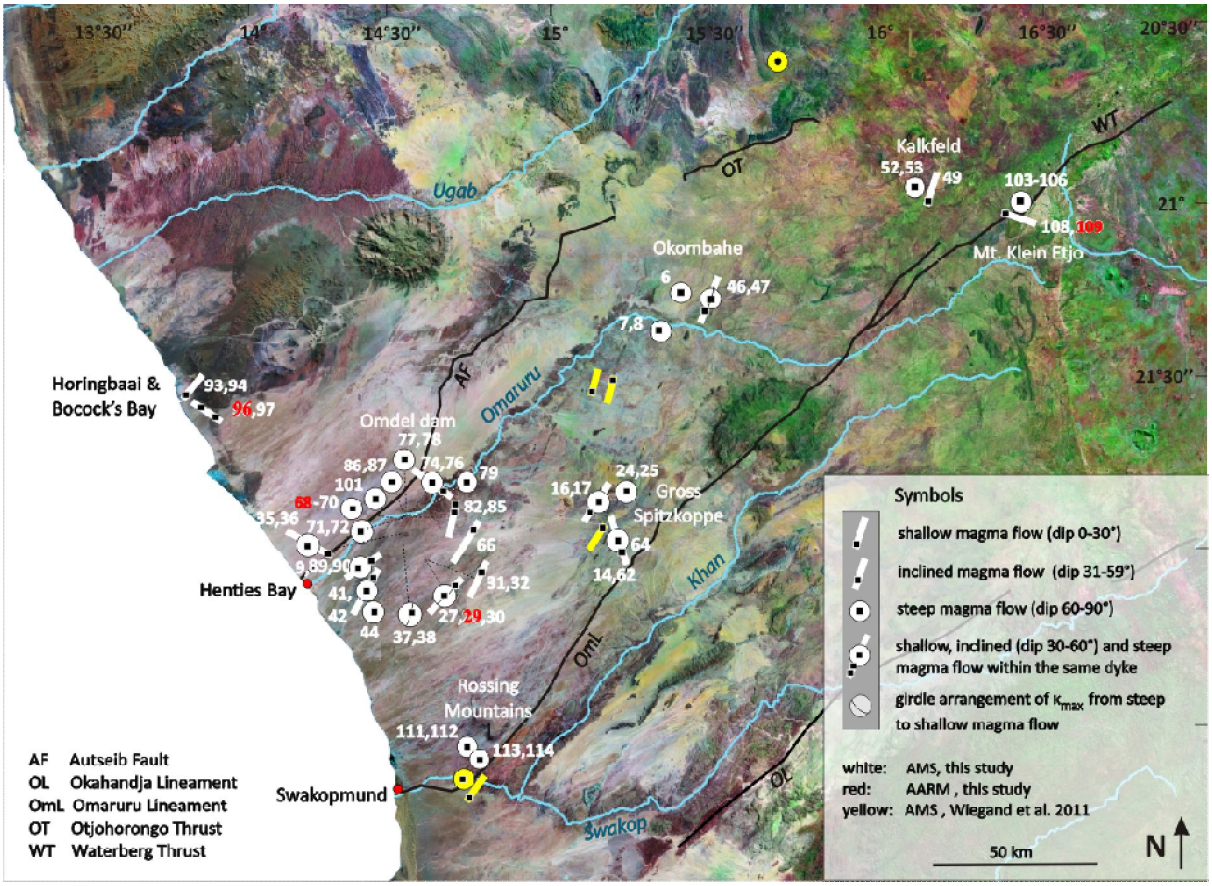

Figure 10-68. Satellite image with magma flow orientations at the dyke margins interpreted from type I AMS fabrics and from 4 type I AARM fabrics (red). Long principal fabric axes are interpreted to indicate magma flow. Circles symbolize lower hemisphere stereonets, bars give both the strike of the dyke and flow azimuth, black squares mark the dip of magma flow. Note the predominance of steep and inclined flow directions. Samples 98-99 refer to a sill.

In summary, Figure 10-68 reveals predominantly steep and inclined magma flow all across the HOD independent of dyke strike (the AMS_{AFD} derived magma flow pattern is similar). Shallow magma flow is rare, but it is indicated in almost every sampled area. In contrast, for the Brazilian Ponta Grossa dyke swarm Raposo and Ernesto (1995) inferred 58% horizontal to subhorizontal and 42% inclined to vertical magma flow sites. Samples 20, 27 and 38 have extremely oblate fabrics with κ_{max} and κ_{int} being interchanged and forming a girdle, marked with a great circle in the stereonet instead of mean κ_{max} axis. In some cases, magma flow direction locally varies within the same dyke, from steep to shallow along strike (e.g. dyke 45-47, 16-17) or across the dyke thickness (e.g. dyke 45-47, 35-36). In other dykes, κ_{max} orientation varies little along strike (samples 103-104 and 106; or 71, 72 and 86 - 88).

From the 8 dykes with roughly symmetrical fabric distribution across the dyke width, referred to in chapter 7.5, the sense of flow direction can be deduced in the sense of Knight and Walker (1988) and Clemente et al. (2007). Of these, 6 of the dykes strike NE, one N-S and one ENE-WSW. Steep, inclined and horizontal flow senses are obtained with both NE- and SW-directed magma flow. Magma flow is vertical at 3 of these dykes/locations (62/64, 79/80, 89/90), inclined and heading up to the NE at location 17, up to the SW at location 31/32), subvertical/inclined and down to the SW at location 65/66 and horizontal to the NE at locations 23/26/56 and 33/34. In other dykes, the magnetic lineation (κ_{max}) is not imbricated or samples were not taken from the dyke margins. Consequently, the sense of magma flow cannot be derived from these dykes.

An asymmetric imbrication of κ_{max} is recorded in 16 dykes, strongly asymmetric in at least 4 dykes distributed across the areas Gross Spitzkoppe, Omdel dam, Kalkfeld and Mt. Klein Etjo (see chapter 9.2.4). All of these dykes are located near or in the vicinity of (maximum 30 km) one of the Panafrican crustal-scale shear zones: Omaruru Lineament-Waterberg Fault (OmL-WT) and Autseib Fault-Otjohorongo Thrust (AF-OT). Parts of both fault zones were reactivated during early Cretaceous times (e.g. Miller, 2008; see chapter 2.1.1. for more references), and it is likely that the fabric asymmetry is the product of tectonic shear at the time of dyke emplacement. Shear localized at the dyke walls can modify the symmetrical κ_{max} imbrication produced by magma-internal shear (e.g. Clemente et al., 2007). Together, magma-internal and dyke wall shear may be responsible for the local occurrence of anomalous fabric types.

Regarding the geometries of the dykes, all three aspects sketched in Figure 10-69 are observed in the HOD: planar dykes, recording pure extensional dyke fissure opening (mode I cracks of Pollard, 1987), dykes or segments with curved tips (Figure 7-24 H) and those with an en-echelon arrangement of the segments perpendicular to the direction of least principal stress (σ_3). Curved segment tips and en-echelon geometries are both interpreted to originate from extension combined with–a strike-slip movement. A transtensional stress field during dyke emplacement explains the so-called mixed mode fractures (Pollard, 1987) in the latter two cases. A transcurrent extension mode supports the idea of dyke emplacement under shear stress which was deduced from fabric asymmetry (see above and Clemente et al., 2007 and references therein). Dyke 16-17 shows curved segment tips (Figure 7-28 H) pointing to sinistral shear movements in the Spitzkoppe area. In contrast, lateral displacements are both right- and left-stepping, as also observed elsewhere (e. g. in the Omdel Dam area, see Figure 7-26 A), not allowing to assign a shear sense. The AMS is symmetric in this narrow dyke (0.44 m) giving no indication for tectonic shear.

The idea that HOD dyke emplacement was affected by shear deformation across the dyke plane is geologically reasonable. The dykes intruded along structures of the Proterozoic Damara mobile belt with its shear zones that were reactivated as reverse and transfer faults during Gondwana breakup (see section 2.2). Miller (2008) describes the Mesozoic reactivation of these regional faults, causing uplift of the Damara Belt between them as a "pop-up" structure. Besides this evidence for shear movements, a component of horizontal shear is evidenced by the lateral offset of magnetic lineaments offshore (Bauer et al., 2000).
Steeply-dipping lineation was found on the margins of two inclined/subvertical NE-striking dykes at Omdel dam and Mt. Klein Etjo, whose orientation coincides (within 10-40°; Appendix 12) with the dyke κ_{max} axes. The lineations are defined by stretched micro-vesicles (sample 70, Figure 7-31 S) or grooves (samples 103, 104, 106, Figure 7-25 R, Q) that appear to have been generated while magma was still plastic. Both sites are located within the Autseib Fault and Waterberg Thrust zones, respec-

tively, and the lineations thus witness tectonic shear movements localized at the dyke walls during magma emplacement.

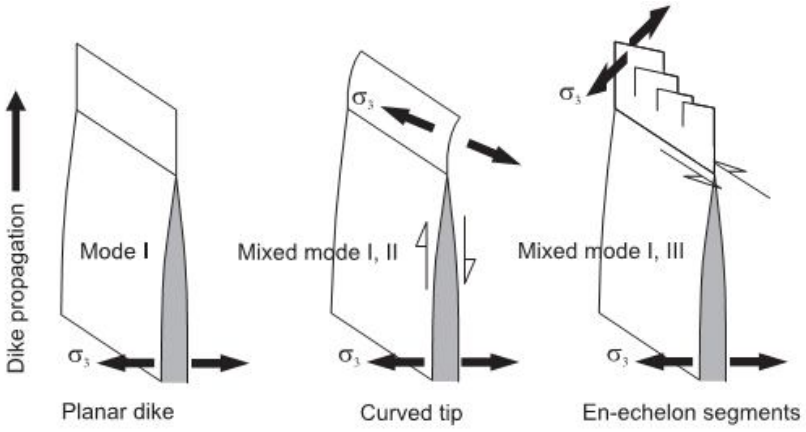

Figure 10-69. Modes of dyke propagation and dyke geometries due to the rotation of the least compressive stress at the dyke tipin response to shear stress at the dyke walls (Clemente et al., 2007; after Pollard, 1987)

An interesting question that can be addressed by dyke orientations is the evolution of the regional paleostress field at the time of emplacement, because of the different dyke trends in the HOD: a minor number of NW-striking dykes in addition to the major NE-trending ones (compare Figure 2-5). Provided that all dykes intruded during early Cretaceous times (which is suggested by dating and geological evidence, see Keiding et al 2013), at least 2 directions of extension would be needed in order to create such a pattern. Extension over a plume head is one scenario that would extend the crust in various directions, but in this case a radial dyke arrangement around the plume head is expected, which is not found in the HOD. Local peaks in dyke strike at roughly 90° to the main trend, as in the HOD (compare Figure 2-5) are common in rifted areas, for example, in a dyke swarm of the Red Sea Hills in Sudan (Babiker & Gudmundsson, 2004) or in the Tertiary paleo-rift zones in Iceland (Gudmundsson, 1990, 1995). Most of the dykes trend NE, parallel with the Panafrican lineaments and structural grain of the basement in the Damara Belt between the Kalahari and Angola/Congo Cratons, while the nearly coast-parallel NW dykes agree in strike with the orientation of the successful rifting and opening of the South Atlantic Ocean. Hahne (2004) and Trumbull et al. (2004) interpreted this orientation of dykes as a triple junction geometry of the three rift arms: the Damara Belt, Kaoko and Gariep Belts. In this case, two directions of extension could compete to open dyke fissures alternatingly in one or the other direction. Eventually, the inland (Damara) arm became inactive while rifting and dyking proceeds along the other 2 arms until finally opening the South Atlantic Ocean. This model would allow for a lack of systematic sequence of age relations between NE and NW striking dykes. Field relations in the Omdel Dam area N and S of the Omaruru river showed two cases of NE-striking dykes which are cut by the coast-parallel dykes. However, a more thorough study of cross-cutting relations of NE- and NW-striking dykes by Frei (2011) based on aerial photographs yielded ambiguous results. Out of 140 observed intersections, 85 cases showed that NE dykes are younger than the NW ones, and the opposite was true for 55 intersections. From the latter relations it is concluded that the orientation of extension or dyking alternated from NW-SE to NE-SW strike, which agrees with the 3-arm rift model. Babiker and Gudmundsson (2004) ascribe different dyke trends in the Red Sea Hills dyke swarm to abrupt stress field changes partly due to the magma overpressure in the dykes and not to a regionally variable extension direction. Their idea is that the emplacement of many NE-trending dykes generates a local and temporary alternation of the stress field by increased compression, allowing dyke emplacement in a direction perpendicular to their general trend. For the HOD, both mechanism may apply: a 3-armed rift triple junction setting evolved from 2-directional crustal extension. Since both directions are close to failure, dykes intrude alternatingly with NE or NW strike, possibly also triggered by magma overpressure in the dykes open.
Finally, of course, the pre-existing Panafrican crustal structures of the Damara Orogen are dominantly NE-striking and this likely also facilitated magma intrusion parallel with the Damara Orogen, which

explains the predominance of NE-dykes.

10.2 Dyke emplacement model

Dykes accommodate crustal extension (i.e. Paquet et al. 2007). They occur in swarms within rift zones and are arranged either radially around a centre, which is rare, or strike within a limited range of directions depending on the regional stress field and/or the pre-existing crustal anisotropy (Nakamura 1977, Walker 1999; Paquet et al. 2007). Examples of rift systems with an architecture of dykes and open fissures migrating away from an eruptive centre are found in Iceland, where a mantle plume impacts the Mid-Atlantic ridge. Paquet et al. (2007) propose an emplacement model inferred from the Icelandic dyke swarms, where magma migrates upward from depth to the magma reservoir located 3 km beneath the eruptive centre which is made up of a central volcano and cone-sheets (Figure 10-70).

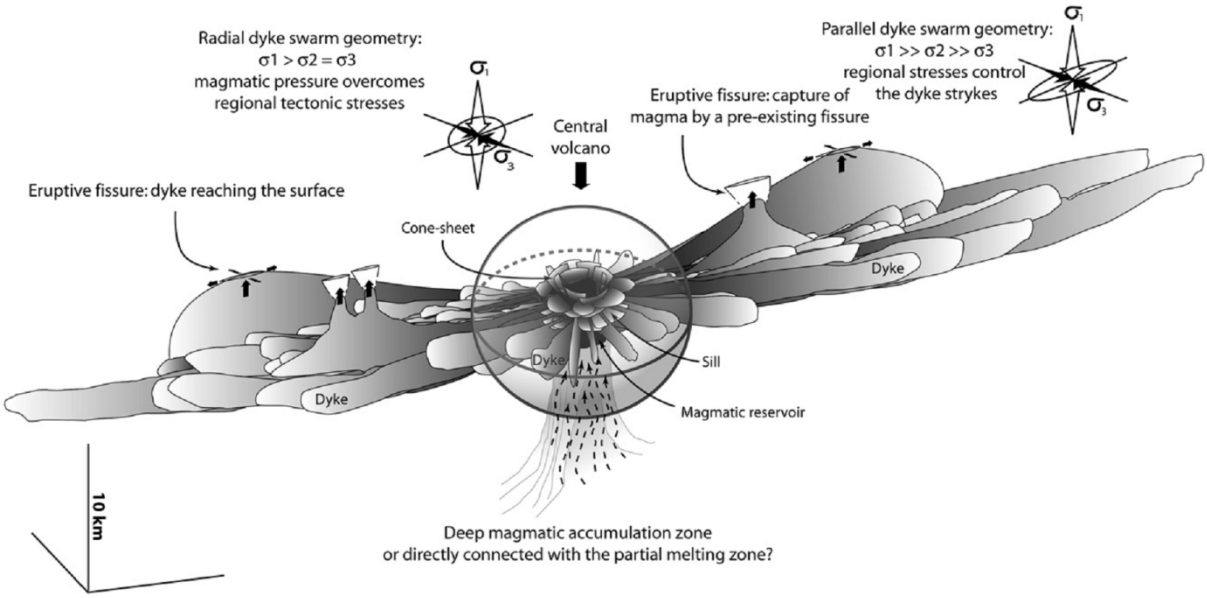

Figure 10-70. Schematic 3D model of a dyke swarm in Iceland depicting upward migration of magma from depth to the melt reservoir beneath the eruptive centre (central volcano) and mainly lateral magma transport from the reservoir away into the crust. Dykes are oriented radially near the eruptive centre, where the stress field is influenced by magma pressure. They are parallel farther away, where effects of magma pressure decrease and the regional stress field takes over control (Paquet et al. 2007).

Magma is then assumed to migrate within dykes mainly laterally away from the magma chamber (with velocities of 1-2 m/s). The average dyke trend is parallel with the plate boundary (Buck et al. 2006). While the stress field near and above the eruptive centre is modified by magma pressure, the minimum stress (σ_3) increases relatively close to the value of σ_2 and generates a radial dyke distribution and cone sheet intrusions around the eruptive centre (Paquet et al. 2007). With more distance to the eruptive centre magma pressure decreases and tectonic stresses dominate over magmatic ones (Paquet et al. 2007), dykes orient perpendicular to σ_3 of the regional extensional stress field. A similar model was proposed by Gudmundsson (2006).

AMS studies on the Mackenzie dyke swarm in the Canadian Shield by Ernst & Baragar (1992) also revealed such a flow pattern. Magma ascent is indicated for a focal point with a diameter of 500 km. The radiating dyke swarm shows a sharp transition from vertical magma flow in the focal point to horizontal flow between 500 and 600 km away from that point. The transition is interpreted to correspond to the outer boundary of melt generation in the assumed mantle plume below. Horizontal magma transport then worked over distances up to at least 2,100 km. A similar flow pattern was inferred from

AMS measurements in the Brazilian Rio Ceará-Mirim dyke swarm (Archanjo & Launeau, 2004), where again a magmatic feeder zone can be inferred from the change of horizontal to steeply plunging magnetic lineation (κ_{max}) in sites with normal AMS fabrics.

Knight and Walker (1988) developed an emplacement model for the Hawaian Koolau dyke complex with at least 3 high-level magma reservoirs distributed over about 18 km along-strike based on variations in dip angle and direction of the imbricated magnetic lineation. They considered 24 dykes with paired imbrications of κ_{max} axes. The depth of the magma reservoirs is estimated at 1 or 2 km below the present erosional surface.

For the HOD, a similar scenario as for the Koolau dyke complex is probable. Steep and subvertical/inclined magma flow orientations dominate in the areas Omdel dam, Gross Spitzkoppe, Rossing Mountains and Okombahe and are found in every area except for Horingbaai/Bocock's Bay. Horizontal or shallow magma flow (< 30°) is rare, but it also was found in all sampled areas except Okombahe. Horizontal flow over large distances can be excluded, alone from the dyke segmentation in map view. The pattern of flow orientations in the HOD suggests the existence of various mid-crustal level magma reservoirs, from which magma ascended at a steep angle, as in the sketch in Figure 10-71. Horizontal flow orientations are interpreted as local variations within a dyke segment or at the tips of a segment. Alternatively, one large reservoir may be postulated beneath the entire dyke swarm, but that is unlikely based on the presence of geochemically distinct magma types in the HOD (Trumbull et al., 2007; Keiding et al., 2013).

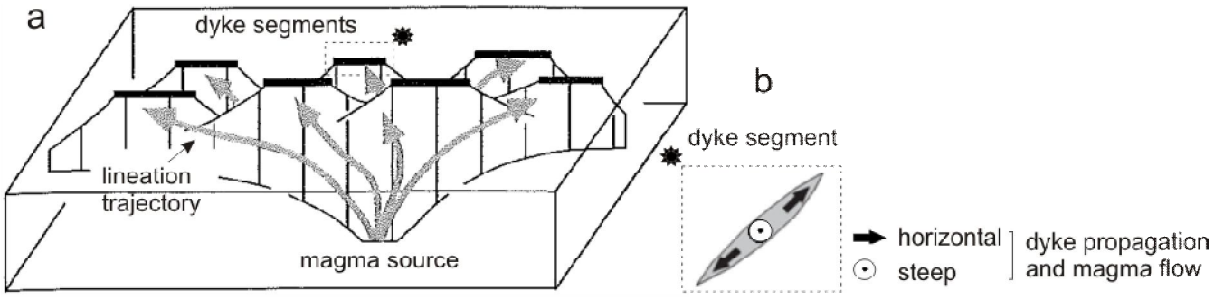

Figure 10-71. A) Simplified model of steep and inclined/subvertical magma ascent from a local mid-crustal level source/reservoir into dyke segments of the HOD swarm, Namibia (modified after Archanjo & Launeau 2004); Several of these sources may have fed the HOD. B) Dyke segment, plan view, with steep magma flow in the centre, which changes to horizontal at segment tips (modified after Clemente et al. 2007)

Apatite fission track data show that the present exposure level in NW Namibia is the product of 4 to 5 km of erosion since the Lower Cretaceous (Raab et al. 2005, see chapter 2.3), suggesting a shallow crustal level of dyke emplacement, which is in keeping with the brittle style of deformation and local presence of degassing vesicles in the dykes. The local en échelon arrangement and ubiquitous segmentation also indicates shallow crustal intrusion levels (i.e. Oliveira 1992 in Archanjo & Launeau 2004; Clemente et al. 2007). Keiding et al. (2013) estimated the depth of magma storage in the crust below the HOD from mineral-melt thermobarometry on clinopyroxene. The samples used for that study have a comparable spatial coverage as the AMS study reported here, and the results indicate a similar depth range for magma storage in all areas between 11 and 17 km. Presumably, the subvertical flow directions reflect the propagation from this mid-crustal level of magma storage. Observations of dyke segmentation on a steeply-inclined outcrop (Figure 7-26 A) also indicate both a horizontal and a vertical component of dyke fissure propagation (and magma flow) in accordance with the vertical, subvertical and horizontal flow orientation inferred from AMS (locations 77-78; 79, 82-85, Figure 10-68). Fissure propagation is accompanied by inflation of the segments due to further magma injection (e.g. Hutton, 2009). Horizontal magma flow near segment tips (e.g. in location 27), may reflect lateral propagation of a dyke segment towards an adjacent one, resulting in the final merging of segments (Clemente et al., 2007). This mode of dyke propagation was described by Currie and Ferguson (1970). Witnesses of

this propagation mode in the HOD are e.g. overlapping segment tips or broken bridges of country rock (e.g. 1.5 m x 1 m, site no. 75/76, not shown), which once separated two dyke segments. Locally, straight or bent apophyses are found, in places heading into opposite directions (i.e. dyke 16-17, Figure 7-23) and, thus, give ambiguous hints on fracture propagation direction. Magma emplacement by multiple magma pulses is evidenced in 3 dykes by dyke-internal chilled margins (nos. 28, 39-43; 111-112).

11 Conclusions

11.1 Magneto-mineralogy and magnetic fabric in the HOD dykes

The basaltic dykes of the Henties Bay-Outjo dyke swarm (HOD) in the Etendeka Province of Namibia studied here are typically fine-grained dolerites (except for glassy chilled margins) with intergranular to ophitic or subophitic magmatic textures and with phenocrysts dominated by intergrown plagioclase and clinopyroxene, minor olivine and hornblende. Late-crystallized titanomagnetite (estimated 3 to 5 vol.%) associated with ilmenohaematite is the main carrier of rock magnetism in the dykes. Strong variations of magnetic susceptibility are related to sub-solidus processes like high-temperature deuteric oxidation during magma cooling, marked by exsolution of ilmenite lamellae in tmt, and maghemitization, indicated by irreversible kappa-T curves. Both alterations are typically associated with tmt grain-size reduction. Common secondary mineralization by carbonate, and sericite, or different degrees of pseudomorphic replacement of tmt and ilmenite by leucoxene are regarded as the products of hydrothermal alteration.

The magnetic fabric in the HOD dykes was studied by a combination of anisotropy of magnetic susceptibility (AMS) and anisotropy of anhysteritic remanent magnetization (AARM). A mixture of single-domain (SD), pseudo-single domain (PSD) and multi-domain (MD) grains in variable proportions is inferred from hysteresis properties, alternating field demagnetization curves and the comparison of AMS with AARM fabric orientation.

Owing to the alignment of tmt along previously crystallized silicate phases (plagioclase and pyroxene) and its clustering in their interstices, the origin of magnetic rock anisotropy is basically distributional in nature with magnetic interactions between close tmt grains. Occasionally, anisotropic tmt grains, such as elongate dendrites, dominate and may add shape anisotropy of the tmt grains. Depending on the orientation of the dendrites, this may enhance the distribution anisotropy or reduce it.

A primary magmatic origin of the rock fabrics is consistent with the generally low P' values. 66% of the 111 investigated samples show "normal" AMS fabric type I with the long and intermediate principal fabric ellipsoid axis κ_{max} and κ_{int} within the dyke plane, suggesting that the early crystallized minerals acquired their orientation by magma flow and this state is preserved. From these normal fabrics magma flow directions are deduced from the orientation of κ_{max}. Vertical to subvertical orientations of κ_{max} axes dominate and indicate a mostly steep magma flow in the dyke swarm, which is supported by dyke segmentation in map view and on a steeply-inclined outcrop. Horizontal κ_{max} orientations also occur, and are interpreted as local flow variations within a dyke segment or at the tips of the segment.

In order to understand the nature of the 38 anomalous, non-dyke-parallel AMS fabrics (types II-IV), diverse hypothetical mineralogical and geological scenarios were investigated. For 7 anomalous AMS fabric samples that reveal normal type AARM fabrics, an influence of a higher proportion of primary single-domain titanomagnetite is concluded, which is known as the classical SD-effect. In these cases, magma flow directions can be inferred from the long axis orientation of their AARM fabric. The high number of anomalous AARM fabrics, where surprisingly, the AMS fabric is of normal type, may be due to secondary, non-flow-oriented and non-dyke parallel tmt.

11.2 Tectonic interpretation and dyke emplacement

For the interpretation of magma flow directions in the dykes, the fabric orientation across the dyke width is important, especially the orientation of κ_{max} near the dyke margins, where the flow direction of the initial magma intrusion is best recorded. Within the sample set, only 3 dykes show the classical symmetrical or conjugate imbrication of κ_{max} axes on opposing margins. It is suggested that the κ_{max} asymmetry is due to tectonic shearing at the dyke walls during magma intrusion. Field observations and satellite images of segmented dykes as well as dyke geometries including locally curved segments, en-echelon arrangements and left/right-stepping lateral displacements support the suggestion from asymmetric AMS fabrics for magma intrusion into rocks undergoing shear stress. This tectonic influence is related to the well-documented reactivation of Neoproterzoic crustal-scale shear zones in the basement which hosts the HOD swarm.

Provided that all dykes intruded during early Cretaceous times, at least 2-directional crustal extension must have occurred to open all the dyke fissures with almost perpendicular trends. Since most of the dykes trend NE, it is suggested that the time-averaged direction of the minimum compressive stress

(σ_3) during dyke emplacement of the HOD was oriented NW-SE. The predominance of NE-striking dykes relates at least in part to the orientation of pre-existing Panafrican crustal structures of the old Damara Orogen. Mutually cross-cutting relations of NE and NW trending dykes do not support consistent age differences between the dyke trends, but rather suggest that local magma pressure triggered failure (dyking) alternatingly in one or the other direction. Such a scenario is in agreement with a triple junction geometry of rift segments, where, the inland (Damara) segment becomes inactive while rifting and dyking proceeds along the other two (Gariep and Kaoko Belt), finally opening the South Atlantic Ocean.

The predominantly vertical and subvertical magma flow orientations throughout the HOD area imply a wide distribution of magma sources below the region instead of dominantly at the coastal rift. This is consistent with the petrologic evidence of Keiding et al. (2013) for mid-crustal magma storage zones at 11-17 km depth in the HOD area. The magnetic fabric studies suggest magma ascent sub-vertically from these storage zones to the present outcrop level, which fission-track evidence places at 4-5 km depth. Fissure propagation presumably was accompanied by inflation of the segments due to further magma injection. Minor components of horizontal magma flow are also indicated by the magnetic fabrics and this may reflect lateral propagation of one dyke segment towards an adjacent one. Observations of overlapping segment tips or broken bridges of country rock, which once separated two dyke segments are evidence for this mode of dyke propagation.

12 References

AGICO Advanced Geoscience Instruments Co., 2009. MFK1-FA/CS4/CSL, MFK1-B, User's Guide. Vers. 4.0, Brno.

Arbaret, L., Diot, H., Bouchez, J.L., 1996. Shape fabrics of particles in low concentration suspensions: 2D analogue experiments and application to tiling in magma. Journal of Structural Geology, 18, 941-950.

Arbaret, L., Diot, H., Bouchez, J.L., Lespinasse, P., De Saint-Blanquat, M., 1997. Analogue 3D simple-shear experiments of magmatic biotite subfabrics. In: Bouchez, J.L., Hutton, D.H.W. & Stephens, W.E. (eds). Granite: From Segregation of Melt to Emplacement Fabrics. Kluwer Academic Publishers, Dordrecht, 129-143.

Archanjo, C.J., Araujo, M.G.S., Launeau, P., 2002. Fabric of the Rio Ceara-Mirim mafic dike swarm (northeastern Brazil) determined by anisotropy of magnetic susceptibility and image analysis. Journal of Geophysical Research 107, 2046. doi:10.1029/2001JB000268.

Archanjo, C.J. & Launeau, P., 2004. Magma flow inferred from preferred orientations of plagioclase of the Rio Ceará-Mirim dyke swarm (NE Brazil) and its AMS significance. In Martín-Hernández, F., Lüneburg, C.M., Aubourg, C. & Jackson, M. (eds). Magnetic Fabric: Methods and Applications. Geological Society, London, Special Publications, 238, 285-298.

Aubourg, C., Giordano, G., Mattei, M., Speranza, F., 2002. Magma flow in sub-aqueous rhyolitic dikes inferred from magnetic fabric analysis (Ponza Island, W. Italy). Physics and Chemistry of the Earth, Parts A/B/C 27 (25-31), 1263-1272.

Babiker, M., Gudmundsson, A., 2004. Geometry, structure and emplacement of mafic dykes in the Red Sea Hills, Sudan. Journal of African Earth Sciences, Vol. 38, No. 3, 02.2004, 279-292.

Backeberg, N.R., Reid, D.L., Trumbull, R.B., Romer, R.L., 2011. Petrogenesis of the False Bay dyke swarm, Cape Peninsula: Evidence for Basement Assimilation. South African Journal of Geology, 114, 3-4, 335-352. DOI:10.2113/gssajg.114.3-4.335.

Bauer, K., Neben, S., Schreckenberger, B., Emmermann, R., Hinz, K., Fechner, N., Gohl, K., Schulze, A., Trumbull, R.B., Weber, K., 2000. Deep structure of the Namibia continental margin as derived from integrated geophysical studies. Journal of Geophysical Research 105, 25829–25853.

Borradaile, G.J. & Gauthier, D., 2003. Interpreting anomalous magnetic fabrics in ophiolite dikes. Journal of structural Geology, 25, 171-182.

Borradaile, G.J. & Gauthier, D., 2001. AMS-detection of inverse fabrics without AARM, in ophiolite dikes. Geophysical Research Letters, 28, 18, 3517-3520.

Bowles, J., Jackson, M., Banerjee, S.K., IRM, 2010. Interpretation of low-temperature data part II: The haematite Morin transition. The IRM Quarterly, vol. 20, no.1, ISSN: 2152-1972.

Buck, W. R., Einarsson, P. & Brandsdóttir, B., 2006. Tectonic stress and magma chamber size as controls on dike propagation: Constraints from the 1975–1984 Krafla rifting episode. Journal of Geophysical Research, Vol. 111, B12404, 15 p.

Butler, R.F., 1998. Paleomagnetism: Magnetic Domains to Geologic Terranes. Electronic Edition, www.geo.arizona.edu/Paleomag/book/. 238 p.

Butler, R.F. and Banerjee, S.K., 1975. Theoretical single-domain grain size range in magnetite and titanomagnetite. Journal of Geophysical Research, 80, 4049. 4058.

Cañón-Tapia, E., 2004. Anisotropy of magnetic susceptibility of lava flows and dykes: A historical account. In Martín-Hernández, F., Aubourg, C. And Jackson, M. (eds) 2004. Magnetic fabrics: Methods and applications. Geological Society, London, Special Publications, 238, 205-225.

Cañón-Tapia, E., 1996. Single-grain versus distribution anisotropy: a simple three-dimensional model. Physics of the Earth and Planetary Interiors, 94, 149-158.

Cañón-Tapia, E. & Chávez-Àlvarez, M. J., 2004. Theoretical aspects of particle movement in flowing magma: implications for the anisotropy of magnetic susceptibility of dykes. In: Martín-Hernández, F. Aubourg, C., Jackson, M. & Luneburg, C. (eds). Magnetic fabric: Methods and applications. Geological Society, London, Special Publications, 238, 227-249.

Cañon-Tapia, E. & Pinkerton, H., 2000. The anisotropy of magnetic susceptibility of lava flows: an experimental approach. Journal of Volcanology and Geothermal Research, 98, 219-233.

Chevallier, L. and Woodford, A., 1999. Morpho-tectonics and mechanism of emplacement of the dolerite rings and sills of the western Karoo, South Africa. South African Journal of Geology, 102, 43-54.

Clemente, C.S., Amorós, E.B. & Crespo, M.G., 2007. Dike intrusion under shear stress: Effects on magnetic and vesicle fabrics in dikes from rift zones on Tenerife (Canary Islands). Journal of Structural Geology, 29, 1931-1942.

Clemson, J., Cartwright, J., Booth, J., 1997. Structural segmentation and the influence of basement structure on the Namibian passive margin. Journal of the Geological Society (London) 154, 477– 482.

Clemson, J., Cartwright, J., Swart, R., 1999. The Namib Rift: a rift system of possible Karoo age, offshore Namibia. In: Cameron, M.J. Raab et al. / Tectonophysics 349 (2002) 75–92 90N.R., Bate, R.H., Clure, V.S. (Eds.), The Oil and Gas Habitats of the South Atlantic. Geological Society Special Publication Vol.153, 381– 402.

Correa-Gomes, L.C., Souza-Filho, C.R., Martins, C.J.F.N., Oliveira, E.P., 2001. Development of symmetrical and asymmetrical fabrics in sheet-like igneous bodies: the role of magma flow and wall-rock displacements in theoretical and natural cases. Journal of Structural Geology, 23, 1415-1428.

Coward, M.P., Daly, M.C., 1984. Crustal lineaments and shear zones in Africa: their relationships to plate movements. Precambrian Research 24, 27– 45.

Cui, Y., Verosub, K.L., Roberts, A.P., 1994. The effect of low-temperature oxidation on large multidomain magnetite. Geophysical Research Letters, 21, 9, 757-760.

Daly, M. C., 1989. Rift basin evolution in Africa: the influence of reactivated steep basement shear zones. In: G. D. W. M. A. Cooper (ed.), Inversion Tectonics. Special Publications Geological Society London 44: 309-334.

Daly, M. C., 1986. Crustal shear zones and thrust belts: their geometry and continuity in Central Africa. Philosophical Transactions Royal Society 317: 111-128.

Daly, L., 1970. Etude des propriétés magnétiques des roches métamorphiques ou simplement tectonisées, thesis, Univ. of Paris, Paris. 340 p.

Day, R., Fuller, M. & Schmidt, V. A., 1977. Hysteresis properties of titanomagnetites: grain size and compositional dependence. Physics of the Earth and Planetary Interiors, 13, 260 -267.

DeWall, H., 2005. Die Anisotropie der magnetischen Suszeptibilität - eine Methode zur Gefügeanalyse. Zeitschrift der Deutschen Geologischen Gesellschaft. 155/2-4, 287–298.

DeWall, H., 2000. The Field-Dependence of AC Susceptibility in Titanomagnetites: Implications for the Anisotropy of Magnetic Susceptibility. Geophysical Research Letters, 27, 16. 2409–2411.

De Wit M.J., de Brito Neves B.B., Trouw R., Allard J., Pankhurst R.J., 2008. West-Gondwana: Pre-Cenozoic Correlations Across the South Atlantic Region; "the Ties that Bind", Special Publication, vol 294. Geological Society, London: 1–8.

Dingle, R.V., Siesser,W.G.&Newton, A.R., 1983. Mesozoic and Tertiary Geology of Southern Africa. Balkema, Rotterdam.

Dragoni, M., Lanza, R. & Tallarico, A., 1997. Magnetic anisotropy prodiced by magma flow: theoretical model and experimental data from Ferrar dolerite sills (Antarctica). Geophysical Journal International, 128, 230-240.

Dunlop, D.J., 1983. Determination of domain structure in igneous rocks by alternating field and other methods. Earth and Planetary Science Letters, 63, 353-367.

Dunlop, D.J. and Özdemir, Ö., 1997. Rock Magnetism: Fundamentals and frontiers. Cambridge University Press, Cambridge. 573 p.

Erlank, A. J., Marsh, J. S., Duncan, A. R., Miller, R. McG., Hawkesworth, C. J., Betton, P. J. & Rex, D. C., 1984. Geochemistry and petrogenesis of the Etendeka volcanic rocks from SWA/Namibia. In: Erlank, A. J. (ed.) Petrogenesis of the Volcanic Rocks of the Karoo Province. Geological Society of South Africa, Special Publication 13, 195-245.

Ernst, R.E. & Baragar, W.R.A., 1992. Evidence from magnetic fabric for the flow pattern of magma in the MacKenzie giant radiating dyke swarm. Nature, 356, 511-513.

Ewart, A., Milner, S.C., Armstrong, R.A., Duncan, A.R., 1998. Etendeka volcanism of the Goboboseb Mountains and Messum Igneous Complex, Namibia. Part I: Geochemical evidence of Early Cretaceous Tristan plume melts and the role of crustal contamination in the Paraná-Etendeka CFB. Journal of Petrology, 39, 2, 191-225.

Féménias, O., Diot, H., Berza, T., Gauffriau, A. & Demaiffe, D., 2004. Asymmetrical to symmetrical magnetic fabrics of dikes: Paleo-flow orientations and Paleo-stress recorded on feeder-bodies from the Motru Dike Swarm (Romania). Journal of Structural Geology, 26, 1401-1418.

Ferré, E.C., 2002. Theoretical models of intermediate and inverse AMS fabrics. Geophysical Research Letters, 29, 7.

Florisbal L, Janasi V., Bitencourt M.D.F. & Heaman L. (O) 2013. Precise U-Pb ID-TIMS baddeleyite and zircon ages for the Florianópolis Dyke Swarm and its correlation to Paraná-Etendeka mafic to intermediate magmatism. *Mineralogical Magazine*, 77, 5**.** 1095 p. Goldschmidt2013 Conference Abstracts.

Frei, O., 2011. Petrological and geochemical investigation of mafic dykes of the Henties Bay - Outjo dyke swarm, Etendeka igneous province, Namibia. Msc-Thesis, TU Bergakademie Freiberg, M. sc. thesis, unpublished. 93 p.

Gaillot, P., de Saint-Blanquat, M., Bouchez, J.-L., 2006. Effects of magnetic interaction in anisotropy of magnetic susceptibility: Models, experiments and implications for igneous rock fabrics quantification. Tectonophysics, 418, 3-19.

Gaucher C., Frimmel H.E., Germs G.J.B., 2009. Tectonic events and palaeogeographic evolution of southwestern Gondwana in the Neoproterozoic and Cambrian. In: Gaucher C, Sial AN, Halverson GP, Frimmel HE (eds) Neoproterozoic-Cambrian Tectonics, Global Change and Evolution: A Focus on Southwestern Gondwana. Developments in Precambrian Geology 16, Elsevier, Amsterdam, 295–316.

Geoffroy, L., Callot, J.P., Aubourg, C. & Moreira, M., 2002. Magnetic and plagioclase linear fabric discrepancy in dykes: a new way to define the flow vector using magnetic foliation. Terra Nova, 14, 183-190.

Gladczenko, T.P., Hinz, K., Eldhol, O., Meyer, H., Neben, S. & Skogseid, J., 1997. South Atlantic volcanic margins. Journal of the Geological Society, London 154, 465-470.

Gray, D.R., Foster, D.A., Meert, J.G., Goscombre, B.D., Armstrong, R., Trouw, R.A.J. & Passchier, C.W. A damara orogen perspective on the assembly of southwestern Gondwana. In Pankhurst, R.J., Trouw, R.A.J., Brito Neves, B.B. & deWit, M.J., (eds), 2008. West Gondwana: pre-Cenozoic correlations across the South Atlantic region, Geological Society, London, Special Publications, 294, 257-278.

Grégoire, V., Darrozes, J., Gaillot, P., Nédélec, A. & Launeau, P., 1998. Magnetite grain shape fabric and distribution anisotropy vs. Rock magnetic fabric: A three-dimensional case study. Journal of Structural Geology, 20, 937-944; Amsterdam.

Grégoire, V., de Saint-Blanquat, M., Nédélec, A. & Bouchez, J.L., 1995. Shape anisotropy versus magnetic interactions of magnetite grains: experiments and application to AMS in granitic rocks. Geophysical Research Letters, 20, 2765-2768.

Gudmundsson, A., 2006. How local stresses control magma-chamber ruptures, dyke injections, and eruptions in composite volcanoes. Earth Science Reviews 79, 1-31.

Gudmundsson, A., 1990. Emplacement of dikes, sills and crustal magma chambers at divergent plate boundaries. Tectonophysics 176, 257–275.

Gudmundsson, A., 1995. Infrastructure and mechanics of volcanic systems in Iceland. Journal of Volcanology and Geothermal Research 64, 1–22.

Günther, A., 2003. Magnetische Anisotropie gebänderter Eisenerze und deren Beziehung zu kristallographischen Vorzugsorientierungen. GKSS 2003/35, TU Clausthal, Dissertation, 140 p.

Hahne, K., 2004. Detektierung eines mesozoischen Gangschwarmes in NW Namibia und Rekonstruktion regionaler Spannungszustände während der Südatlantiköffnung. Dissertation, University of Potsdam, 125 p.

Halvorsen, E., 1974. The magnetic fabric of some dolerite intrusions, northeast Spitzbergen; implications for their mode of emplacement. Earth and Planetary Science Letters, 21, 127-133.

Hargraves, R.B., Johnson, D. & Chan, C.Y., 1991. Distribution anisotropy: The cause of AMS in igneous rocks. Geophysical Research Letters, 18, 2193-2196.

Hegenberger, W., 1988. Karoo Sediments of the Erongo Mountains, their environmental setting and correlation. Communications of the Geological Survey of Namibia 4, 51 p.

Heit, B., Yuan, X., Geissler, W., Lushetile, B.. Weber, M. & Jokat, W., 2013. Crustal thickness and lithospheric structure in Northwestern Namibia from the WALPASS experiment. Geophysical Research Abstracts, Vol. 15, EGU2013-1233, EGU General Assembly 2013.

Heit, B., Yuan, X., Weber, M., Geissler, W., Jokat, W., Lushetile, B. & Hoffmann, K.-H., 2015. Crustal thickness and V_p/V_s ratio in NWNamibia from receiver functions: Evidence for magmatic underplating due to mantle plume-crust interaction. Geophysical Research Letters, 42, 3330–3337, doi:10.1002/2015GL063704.

Herrero-Bervera, E., Walker, G.P.L., Cañon-Tapia, E., Garcia, M.O., 2001. Magnetic fabric and inferred flow direction of dikes, conesheets and sill swarms, Isle of Skye, Scotland. Journal of Volcanology and Geothermal Research, 106, 3-4, 195-210.

Hinz, K. 1981. A hypothesis on terrestrial catastrophes; wedges of very thick oceanward dipping layers beneath passive continental margins; their origin and paleoenvironmental significance. Geologisches Jahrbuch. Reihe E: Geophysik. 22, 28 p.

Hirt, A.M., Lanci, L., Dobson, J., Weidler, P., Gehring, A.U., 2002. Low-temperature magnetic properties of lepidocrocite. Journal of Geophysical Research, 107, B1.

Holzförster, F., Stollhofen, H., Stanistreet, I.G., 1999. Lithostratigraphy and depositional environments in the Waterberg-Erongo area, central Namibia, and correlation with the main Karoo Basin, South Africa. Journal of African Earth Sciences 29, 105–123.

Hrouda, F., 2009. Determination of field-independent and field-dependent components of anisotropy of susceptibility through standard AMS measurement in variable low fields I: Theory. Tectonophysics, 466, 114-122

Hrouda, F., 1994. A technique for the measurement of thermal changes of magnetic susceptibility of weakly magnetic rocks by the CS-2 apparatus and KLY-2 Kappabridge. Geophysical Journal International 118: 604–612.

Hunter D.R., Reid D.L., 1987. Mafic dike swarms in Southern Africa. In: Halls HC, Fahrig WF (eds) Mafic Dike Swarms, Special Paper, vol 34. Geological Association Canada, St. Johns: 445–456.

Ildefonse, B., Launeau, P., Bouchez, J.L. & Fernandez, A., 1992.a. Effect of mechanical interactions on the development of shape preferred orientation: a two-dimensional experimental approach. Journal of Structural Geology, 14, 73-83.

Ildefonse, B., Sokoutis, D. & Mancketelow, N.S., 1992b. Mechanical interactions between rigid particles in a deforming ductile matrix. Analogue experiments in simple shear flow. Journal of Structural Geology, 14, 1253-1266.

Jackson, M., 1991. Anisotropy of magnetic remanence: A brief review of mineralogical sources, physical origins, and geological applications, and comparison with susceptibility anisotropy. Pure and Applied Geophysics,Vol. 136, No 1, p. 1-28, DOI: 10.1007/BF00878885.

Jackson, M., Moskowitz, B., Bowles, J., 2011. Interpretation of low-temperature data part III: The magnetite Verwey transition (Part A). The IRM Quarterly, Vol. 20, 4, 2011.

Jefferey, G.B., 1922. The motion of ellipsoidal particles immersed in a viscous fluid. Proceedings of the Royal Society of London, 102, 161-179.

Jelinek, V., 1980. Kappabridge KLY-2. A precision laboratory bridge for measuring magnetic susceptibility of rocks and its application (including anisotropy). In: Leaflet, Geofyzika, Brno.

Jelinek, V., 1981. Characterization of the magnetic fabrics of rocks. – Tectonophysics, 79: 63-67.

Jelinek, V., 1993. Theory and measurement of the anisotropy of isothermal remanent magnetization of rocks, Trav. Geophys., 37, 124–134.

Jeppe, J. F. B., 1952. The geology of the area along the Ugab River, west of the Brandberg, Ph.D. thesis (unpubl.), Univ. Witwatersrand, Johannesburg, 224 p.

Just, J. & Kontny, A., 2012. Thermally induced alterations of minerals during measurements of the temperature dependence of magnetic susceptibility: a case study from the hydrothermally altered Soultz-sous-Forêts granite, France. International Journal of Earth Sciences, 101, 3, 819-839.

Keiding, J.K., Frei, O., Renno, A., Veksler, I.V., Trumbull, R.B., 2013. Conditions of magma crystallization in the Henties Bay-Outjo dyke swarm, Namibia: Implications for the feeder system of continental flood basalts. Lithos 179, 16-27.

Ketteler, G., 2002. Präparation und Charakterisierung von epitaktischen Oxidfilmen für modellkatalytische Untersuchungen. Dissertation. Universitätabibliothek der Freien Universität Berlin. 201 p.

Knight, M.D. and Walker, G.P.L., 1988. Magma flow directions in dikes of the Koolau Complex, Oahu, determined from magnetic fabric studies. Journal of Geophysical Research, 93(B5): 4301-4319.

Lattard, D., Engelmann, R., Kontny, A., Sauerzapf, U., 2006. Curie temperatures of synthetic titanomagnetites in the Fe-Ti-O system: Effects of composition, crystal chemistry, and thermomagnetic methods. Journal of Geological Research 111: B12S28.

Launeau, P. & Robin, P.-Y., 2005. Determination of fabric and strain ellipsoids from measured sectional ellipses – implementation and applications. Journal of Structural Geology, 27, 2223-2233.

Light, M.P.R., Maslanyj, M.P., Greenwood,R.J. & Banks, N.L., 1993. Seismic sequence stratigraphy and tectonics offshore Namibia. In: Williams,G.D. & Dobb, A. (eds) Tectonics and Seismic Sequence Stra-tigraphy. Geological Society, London, Special Publications, 71, 163–191.

Mang, C.& Kontny, A., 2013. Origin of two Verwey transitions in different generations of magnetite from the Chesapeake Bay impact structure, USA. Journal of Geophysical Research: Solid Earth, 118, 1-13.

Martín-Hernández, F., Aubourg, C. And Jackson, M. (eds), 2004. Magnetic fabrics: Methods and applications. Geological Society, London, Special Publications, 238, 1-7.

Marzoli, A., Melluso, L., Morra, V., Renne, P.R., Sgrosso, I., D'Antonio, M., Duarte Morais, L., Morais, E.A.A. and Ricci, G., 1999. Geochronology and petrology of Cretaceous basaltic magmatism in the Kwanza basin (western Angola), and relationships with the Paraná-Etendeka continental flood basalt province. Journal of Geodynamics, 28, 341-356.

Miller, R. M., 1980. Geology of a portion of central Damaraland, South West Africa/Namibia. Memoirs Geological Survey of South Africa, South West African Series 6, 78 p.

Miller, R.McG., 2008. The Geology of Namibia. Volume 3: Palaeozoic to Cenozoic. Ministry of Mines and Energy, Windhoek, Namibia. (no continuous page numbering).

Miller, R. M., 1983. The Pan-African Damara Orogen of South West Africa/Namibia. In Miller, R. M.: Evolution of the Damara Orogen of South West Africa/Namibia. Special Publications of the Geological Society of South Africa 11, 431-515.

Miller, R. M., 1983a. Tectonic Implications of the contrasting geochemistry of Damaran mafic volcaniclastic rocks, South West Africa/Namibia. In Miller, R. M.: Evolution of the Damara Orogen of South West Africa/Namibia. Special Publications of the Geological Society of South Africa, 11, 115-138.

Miller, 1973. Geological map 2013 - Cape Cross, scale 1:250 000. Geol. Surv. S. W. Afr./Namibia (unpubl.).

Milner S. C., Ewart A., 1989. The geology of the Goboboseb Mountain volcanics and their relationship to the Messum Complex, Namibia. Communications of the Geological Survey of Namibia, 5, 31-40.

Milner, S.C., le Roex, A.P., O'Connor, J.M., 1995. Age of Mesozoic igneous rocks in northwestern Namibia, and their relationship to continental breakup. Journal of the Geological Society (London) 152, 97– 104.

Mohriak, W.U., Rosendahl, B.R., Turner, J.P. and Valente, S.C., 2002. Crustal architecture of South Atlantic volcanic margins. In: M.A. Menzies, S.L. Klemperer, C.J. Ebinger and J. Baker (Editors), Volcanic rifted margins. Geological Society of America Special Paper, 362, 159-202.

Moore, A., Blenkinsop, T. & Cotterill, F. W., 2009. Southern African topography and erosion history: plumes or plate tectonics? Terra nova, 21, 4, 310-315.

Moskowitz, B.M., Banerjee, S.K., 1979. Grain size limits for pseudo-single domain behavior in magnetite: implications for paleomagnetism, I.E.E.E. Transactions on Magnetics, 15, 1241-1246.

Moskowitz, B.M., 1980. Theoretical grain size limits for single-domain, pseudo-single domain and multi-domain behavior in titanomagnetite (x = 0.6) as a function of low-temperature oxidation. Earth and Planetary Science Letters, 47, 285-293.

Moskowitz, B.M., Jackson, M. & Kissel, C., 1998. Low-temperature magnetic behavior of titanomagnetites. Earth and Planetary Science Letters, 157, 141-149.

Muxworthy, A.R., 1999. Low-temperature susceptibility and hysteresis of magnetite. Earth and Planetary Science Letters, 169, 51-58.

Muxworthy, A.R., Williams, W., 2004. Distribution anisotropy: the influence of magnetic interactions on the anisotropy of magnetic remanence. In: Martín-Hernández, F., Lüneburg, F., Aubourg, C & Jackson, M. (eds). 2004. Magnetic Fabric: Methods and Applications. Geological Society, London, Special Publications, 238, 37-47.

Nagata, T., 1961. Rock Magnetism, Maruzen, Tokyo, 350 p.

Nagel, R. 1999. Eine Milliarde Jahre geologischer Entwicklung am NW-Rand des Kalahari Kratons. Dissertation, GA-University, Göttingen. 169 p.

Nakamura, K., 1977. Volcanoes as possible indicators of tectonic stress orientation: principle and proposal. Journal of Volcanology and Geothermal Research 2, 1-16.

O'Connor, J.M., Duncan, R.A., 1990. Evolution of the Walvis Ridge-Rio Grande Rise hot spot system; implications for African and South American Plate motions over plumes. Journal of Geophysical Research 95, 17475–17502.

Oliva-Urcia, B., Kontny, A., Vahle, C. & Schleicher, A.M., 2011. Modification of the magnetic mineralogy in basalts due to fluid-rock interactions in a high-temperature geothermal system (Krafla, Iceland). Geophysical Journal International, 186, 155-174. doi: 10.1111/j.1365-246X.2011.05029.x.

Oliver, G. J. H., 1994. Mid-crustal detatchment and domes in the central zone of the Damaran orogen, Namibia. Journal of African Earth Sciences 19, 4: 331-344.

O'Reilly, W., 1984. Rock and Mineral Magnetism, Blackie, Glasgow. 220 p.

Özdemir, Ö., Dunlop, D.J., Moskowitz, B. M., 1993. The effect of oxidation on the Verwey transition in magnetite. Geophysical Research Letters, 20, 16, 1671 p.

Paquet, F., Dauteuil, O., Hallot, E. & Moreau, F., 2007. Tectonics and magma dynamics coupling in a dyke swarm of Iceland. Journal of Structural Geology, 29, p.1477-1493.

Park, J.K., Tanczyk, E.I. Desbarats, A., 1988. Magnetic fabric and its significance in the 1400 Ma Mealy diabase dikes of Labrador, Canada. Journal of Geophysical Research, 93;13, 689-13,704.

Peate, D.W., 1997. The Paraná-Etendeka Province. In: Large Igneous Provinces: Continental, Oceanic, and Planetary Flood Volcanism. Geophysical Monograph 100, American Geophysical Union. 217-245.

Perroud, H., Calza, F. & Khattach, D., 1991. Paleomagnetism of the Silurian volcanism at Almaden, southern Spain. Journal of Geophysical Research, 96, 1949-1962.

Pichler, H.& Schmitt-Riegraf, C., 1993. Gesteinsbildende Minerale im Dünnschliff. Ferdinand Enke Verlag Stuttgart, 233 p.

Pisarevsky, S.A., Murphy, J.B., Cawood, P.A. & Collins, A.S., 2008. Late Neoproterozoic and Early Cambrian palaeogeography: models and problems. In: Pankhurst, R.J., Trouw, R.A.J., Brito Neves, B.B. & deWit, M.J., (eds) 2008. West Gondwana: pre-Cenozoic correlations across the South Atlantic region, Geological Society, London, Special Publications, 294, 9-31.

Poland, M.P., Fink, J.H., Tauxe, L., 2004. Patterns of magma flow in segmented silicic dikes at Summer Coon volcano, Colorado: AMS and thin section analysis. Earth and Planetary Science Letters 219, 155-169.

Pollard, D.D., 1987. Elementary fracture mechanics applied to the structural interpretation of dykes. In: Halls, H.C., Fahrig, W.F. (Eds.), Geological Association of Canada Special Paper 34. Mafic Dyke Swarms, 5-24.

Porada, H., 1979. The Damara-Ribeira orogen and the Pan-African-Brasiliano cycle in Namibia (Southwest Africa) and Brazil as interpreted in terms of continental collision. Tectonophysics 57, 237-265.

Porada, H., 1989. Pan-African Rifting and Orogenesis in Southern to Equatorial Africa and Eastern Brazil. Precambrian Research 44: 103-136.

Potter, D.K., 2004. A comparison of anisotropy of magnetic remanence methods – a user's guide for application to paleomagnetism and magnetic fabric studies. In.: *Magnetic fabric: Methods and Applications.* Geological Society, London, Special Publications, 238, 21-35.

Potter, D.K. and Stephenson, A., 1988. Single-domain particles in rocks and magnetic fabric analysis. Geophysical Research Letters, 15, 10, 1097-1100.

Raab, M. J., R. W. Brown, K. Gallagher, A. Carter, and K. Weber, 2002. Late cretaceous reactivation of major crustal shear zones in northern Namibia: Constraints from apatite fission track analysis, Tectonophysics, 349, 75 – 92.

Raab M.J., Brown R.W., Gallagher K., Weber K., Gleadow A.J.W., 2005. Denudational and thermal history of the Early Cretaceous Brandberg and Okenyenya igneous complexes on Namibia's Atlantic passive margin. Tectonics 24, TC3006.

Raposo, M.I.B. and Berquo, T.S. 2008. Tectonic fabric revealed by AARM of the proterozoic mafic dike swarm in the Salvador city (Bahia State): São Francisco Craton, NE Brazil. Physiscs of Earth and Planetary Interiors, 167, 179-194.

Raposo, M.I.B., Ernesto M., Renne, P.R., 1998. Paleomagnetism and $^{40}Ar/^{39}Ar$ dating of the early Cretaceous Florianópolis dike swarm (Santa Catarina Island), Southern Brazil. Physics of the Earth and Planetary Interiors, 108, 4, p. 275-290.

Raposo, M. I. B., 1997. Magnetic fabric and its significance in the Florianópolis dyke swarm, southern Brasil. Geophysical Journal International, 1997, 131, 159-170.

Raposo M.I.B., Ernesto M., 1995. Anisotropy of magnetic susceptibility in the Ponta Grossa dyke swarm (Brazil) and its relationship with magma flow direction. Physics and Earth Planetary Interiors 87:183–196.

Raposo, M.I.B., 1992. Paleomagnetismo do enxame de diques do Arco de Ponta Grossa. Ph.D. Thesis, University of São Paulo, 105 p. unpublished.

Raposo, M.I.B. and Ernesto, M., 1989. Rochas intrusivas basicas do Arco de Ponta Grossa: resultados paleomagnéticos preliminares. Rev. Bras. Geocienc., 19: 393-400. unpublished.

Rasband, W.S., 1997-2012. ImageJ, U. S. National Institutes of Health, Bethesda, Maryland, USA, http://imagej.nih.gov/ij/.

Reid, D.L., Erlank, A.J. and Rex, D.C., 1991. Age and correlation of the False Bay dolerite dike swarm, south-western Cape, Cape Province. South African Journal Geology, 94, 155-158.

Reid, D.L. and Rex, D.C., 1994. Cretaceous dikes associated with the opening of the South Atlantic: the Mehlberg dike, northern Richtersveld. South African Journal of Geology, 97, 135-145.

Renne, P.R., Ernesto, M.I.G., Pacca, R.S.C., Glen, J.M., Prevot, M., Perrin, M., 1992. The age of Paraná flood vocanism, rifting of Gondwanaland, and the Jurassic–Cretaceous boundary. Science 258, 975–979.

Renne, P. R., Glen, J. M., Milner, S. C. & Duncan, A. R., 1996. Age of Etendeka flood volcanism and associated intrusions in southwestern Africa. Geology 24, 659-662. Stanistreet, I.G., Kukla, P.A. & Henry, G. 1991. Sedimentary basinal responses to a Late Precambrian Wilson Cycle: the Damara Orogen and Nama Foreland, Namibia. Journal of African Earth Sciences, 13, 1, 141-156.

Robin, P.-Y.F., 2002. Determination of fabric and strain ellipsoids from measured sectional ellipses – Theory. Journal of Structural Geology, 24, 531-544.

Rochette, P., 1988. Inverse magnetic fabric in carbonate-bearing rocks. Earth and Planetary Science Letters, 90, 229-237.

Rochette P., Jenatton L., Dupuy C., Boudier F., Reuber J., 1991. Diabase dikes emplacement in the Oman Ophiolite: a magnetic fabric study with reference to geochemistry. In: Peters T (ed) Ophiolite Genesis and Evolution of the Oceanic Lithosphere. Ministry of Petroleum and Minerals, Sultanate of Oman.

Rochette P., Jackson M., Aubourg C., 1992. Rock magnetism and the interpretation of the anisotropy of magnetic susceptibility. Reviews of Geophysics 30: 209–226.

Rochette P., Aubourg C., Perrin M., 1999. Is this magnetic fabric normal? A review and case studies in volcanic formations. Tectonophysics 307(1-2): 219–234.

Ryall, P.J.C., Hall, J.M., Clark, J., Milligan, T., 1977. Magnetization of oceanic crustal layer 2 – results and thoughts after DSDP Leg 37, Canadian Journal of Earth Sciences, 14, 684-706.

Schneider, G., 2008. The Roadside Geology of Namibia. 2nd edn. Gebrüder Bornträger, Stuttgart, p 294.

Schöbel, S., de Wall. ,2013. AMS–NRM interferences in the Deccan basalts: Toward an improved understanding of magnetic fabrics in flood basalts. Journal of Geophysical Research: Solid Earth, 119, 4, 2651-2678.

Schöbel, S., de Wall, H., Rolf, C., 2013. AMS in basalts: is there a need for prior demagnetization? Geophysical Journal International, 195, 1509–1518.

Shaar, R. & Feinberg, J.M., 2013. Rock magnetic properties of dendrites: insights from MFM imaging and implications for paleomagnetic studies. Geochemistry Geophysics Geosystems, 14, 2, 407- 421.

Siedner, G., Mitchell, J.G., 1976. Episodic Mesozoic volcanism in Namibia and Brazil; K-Ar isochron study bearing on the opening of the South Atlantic. Earth and Planetary Science Letters 30, 292–302.

Soffel, H. C., 1991. Paläomagnetismus und Archäomagnetismus. Eine Einführung für Geowissenschaftler. Heidelberg, Springer Verlag 1991, 276 p.

Soffel, H.C., 1971. The single domain-multidomain transition in natural intermediate titanomagnetites. Zeitschrift für Geophysik, 37, 451-470.

Stacey, F. D., 1960. Magnetic anisotropy of igneous rocks. Journal of Geophysical Research. 65, 2429-2442.

Stacey, F. D., Banerjee, S.K., 1974. The Physical Principles of Rock Magnetism. Elsevier Scientific Publishing Company, Amsterdam, 195 p.

Stephenson, A., Sadikun, S., and Potter, D.K., 1986. A theoretical and experimental comparison of the anisotropies of magnetic susceptibility and remanence in rocks and minerals. Geophysical Journal of Royal Astronomical Society 84, 185-200.

Stephenson, A., 1994. Distribution anisotropy: two simple models for magnetic lineation and foliation. Physics of the Earth and Planetary Interiors, 82, 49-53.

Stewart, K.S., Turner, S., Kelly, S., Hawkesworth, C.J., Kirstein, L., Mantovani, M.S.M., 1996. 3D $^{40}Ar–^{39}Ar$ geochronology in the Paraná flood basalt province. Earth and Planetary Science Letters 143, 95– 110.

Tankard, A., Eriksson, M., Hobday, D., Hunter, D., Minter, E., 1982. Crustal Evolution of southern Africa: 3.8 billion years of Earth history. New York, Springer, 523 p.

Tarling, D.H. and Hrouda, F., 1993. The Magnetic Anisotropy of Rocks. Chapman and Hall, London. 217 p.

Tauxe, L., 2002. Paleomagnetic Principles and Practice. Kluwer Academic Publishers. 299 p.

Tauxe, L., 2013. Essentials of Paleomagnetism: Second Web Edition. https://earthref.org/MagIC/books/Tauxe/Essentials/, (22.03.2017).

Trumbull, R.B., Sobolev, S.V. and Bauer, K., 2002. Petrophysical modelling of high seismic velocity crust at the Namibian volcanic margin. In: M.A. Menzies, S.L. Klemperer, C.J. Ebinger and J. Baker (Editors), Volcanic Rifted Margins, Geologic Society of America Special Paper, 362, 221-230.

Trumbull R.B., Vietor T., Hahne K., Wackerle R., Ledru P., 2004. Aeromagnetic mapping and reconnaissance geochemistry of the Early Cretaceous Henties Bay-Outjo mafic dike swarm, Etendeka Igneous Province, Namibia. J Afr Earth Sci 40: 17–29.

Trumbull, R.B., Reid, D.L., de Beer, C., van Acken, D., Romer, R.L., 2007. Magmatism and continental breakup at theWest Margin of Southern Africa: a geochemical comparison of dolerite dikes from NW Namibia and the Western Cape. South African Journal of Geology 110, 477–502.

Tucker, P. and O'Reilly, W., 1980. The laboratory simulation of deuteric oxidation of titanomagnetites: effect on magnetic properties and stability of thermoremanence. Phys. Earth Planet. Inter., 23: 112-133.

Turner, S., Regelous, M., Kelly, S., Hawkesworth, C. & Mantovani, M.S.M., 1994. Magmatism and continental break-up in the South Atlantic: High precision Ar-40Ar-39 geochronology, Earth and Planetary Science Letters, 121, 333-348.

Vahle, C., Kontny, A., Gunnlaugsson, H.P. & Kristjansson, L., 2007. The Stardalur magnetic anomaly revisited - new insights into a complex cooling and alteration history. Physics of the Earth and Planetary Interiors 164, 119-141.

Vietor, T. and Weber, K., 1999. Orientation and density distribution of Cretaceous dikes in central Namibia from high resolution aeromagnetics. European Union of Geosciences conference abstracts; EUG 10. Journal of Conference Abstracts. 4, 1, 347.

Walker, G.P.L., 1999. Volcanic rift zones and their intrusion swarms. Journal of Volcanology and eothermal Research 94, 21-34.

Wang, L., Pan, Y.X., Li, J.H., Quin, H.F., 2008. Magnetic properties related to thermal treatment of pyrite. Science in China Series D: Earth Sciences, 2008, 51, 8, 1144-1153.

Wigand, M., Schmitt, A.K., Trumbull, R.B., Villa, I.M. and Emmermann, R., 2004. Short-lived magmatic activity in an anorogenic subvolcanic complex: $^{40}Ar-^{39}Ar$ and ion microprobe U-Pb zircon dating of the Erongo, Damaraland Province, Namibia. Journal of Volcanology and Geothermal Research 130, 285-305.

Wiegand, M., Trumbull, R.B., Greiling, R.O., Vietor, T., 2011. Magnetic Fabric Studies on Mafic Dykes at a Volcanic Rifted Margin in the Henties Bay – Outjo Dyke Swarm, NW Namibia. R.K. Srivastava (ed.), Dyke Swarms: Keys for Geodynamic Interpretation, Springer, Berlin Heidelberg.

Wiegand, M., Trumbull, R. B., Kontny, A., Greiling, R. O., 2016. An AMS study of magma transport and emplacement mechanisms in mafic dykes from the Etendeka Province, Namibia, Tectonophysics, http://dx.doi.org/10.1016/j.tecto.2016.08.016. (in press).

Wolff, J.A., Ellwood, B.B. & Sachs, S.D., 1989. Anisotropy of magnetic susceptibility in welded tuffs: application to a welded tuff dyke in the tertiary Trans-Pecos Texas volcanic province. Bulletin of Volcanology, 51, 299-310.

13 Appendices

Appendix 1. Sample list with field data and dyke properties

Appendix 2. Geochemical data

Appendix 3. Microscopic observations

Appendix 4: Temperature-dependent susceptibility (κ–T) curves

Appendix 5. Results of temperature-dependent susceptibility (κ-T) curves)

Appendix 6. Hysteresis loops

Appendix 7. Hysteresis data

Appendix 8. NRM data and Koenigsberger ratio (Q)

Appendix 9. Alternating Field Demagnetization (AFD) curves and median destructive field (MDF) values

Appendix 10. Alternating Field Demagnetization (AFD) data

Appendix 11. Anisotropy of magnetic susceptibility (AMS) data and sample locations with dyke parameters

Appendix 12. AMS fabric ellipsoids

Appendix 13 (&13a). Anisotropy of anhysteretic remanent magnetization (AARM) data

Appendix 14. AARM fabric ellipsoids

Appendix 15. Image analysis data

Appendix 16. Results of fabric ellipsoid determination with the program 'Ellipsoid'(Image analysis)

Appendix 17. Comparison of fabric ellipsoids: $AMS_{INITIAL}$ vs. AARM vs. AMS_{AFD}

Appendix 18. Parameters and comparison of image analysis, AMS and AARM fabric ellipsoids

Appendix 19. Comparison of AMS fabric type versus the mean susceptibility and versus dyke thickness

Appendix 20. Compilation of most important data